Aus der Medizinischen Klinik mit Schwerpunkt

Kardiologie und Angiologie CCM

der Medizinischen Fakultät Charité – Universitätsmedizin Berlin

DISSERTATION

Identification of stability- and instability-associated proteoglycan/ glycosaminoglycan patterns in human atherosclerotic lesions

zur Erlangung des akademischen Grades

Doctor medicinae (Dr. med.)

vorgelegt der Medizinischen Fakultät

Charité – Universitätsmedizin Berlin

von

Vasileios Karampelas

aus Cholargos, Griechenland

Datum der Promotion: 26.06.2022

Table of contents

Abbreviations

Abbreviation	Full name
PG	Proteoglycan
GAG	Glycosaminoglycan
VSMC	Vascular smooth muscle cell
AIT	Adaptive intimal thickening
DIT	Diffuse intimal thickening
ECM	Extracellular matrix
LP	Lipoprotein
LDL	Low density lipoprotein
DAMP	Damage-associated molecular pattern
PIT	Pathological intimal thickening
EFA	Early fibroatheroma
FC	Fibrous cap
NC	Necrotic core
LFA	Late fibroatheroma
TCFA	Thin cap fibroatheroma
PR	Plaque rupture
TAL	Thrombus-associated lesion
PE	Plaque erosion
CN	Calcified nodule
FCP	Fibrocalcific plaque
SLRP	Small leucine-rich proteoglycan
GPI	Glycophosphatidylinositol
CS	Chondroitin sulfate
DS	Dermatan sulfate
HS	Heparan sulfate
Hep	Heparin
KS	Keratan sulfate
HA	Hyaluronic acid
GCX	Glycocalyx
CT	Computed tomography
MRI	Magnetic resonance imaging

α-SMA	Alpha smooth muscle cell actin
HPLC	High-performance liquid chromatography
CEA	Carotid endarterectomy
CCM	Campus Charité Mitte
CBF	Campus Benjamin Franklin
CVK	Campus Virchow Klinikum
NaOH	Sodium hydroxide
EDTA	Ethylenediamine tetraacetic acid
H_2O_2	Hydrogen peroxide
HCl	Hydrochloric acid
TBST	Tris buffered saline-Tween
FFPE	Formalin-fixed paraffin embedded tissue
cDNA	Complementary DNA
$Na_2HPO_4 * 2 H_2O$	di-Sodium hydrogen phosphate dihydrate
$NaH_2PO_4 * H_2O$	Sodium hydrogen phosphate monohydrate
$NaBH_4$	Sodium borohydride
TCA	Trichloracetic acid
CH_3COOK	Potassium acetate
SD	Standard deviation
AHA	American Heart Association
LV	Low vulnerability
MV	Medium vulnerability
HV	High vulnerability
p.	Points
FDR	False discovery rate
FNR	False negative rate
HI	High inflammation
LI	Low Inflammation
RIN	RNA integrity number
FU	Fluorescent units

List of figures

List of tables

Zusammenfassung

Hintergrund: Proteoglykane (PG) und ihre Glukosaminoglykan (GAG)-Seitenketten sind Hauptbestandteile der Extrazellulärmatrix atherosklerotischen Läsionen und spielen eine wichtige Rolle bei der Krankheitsprogression. Methoden zur Erkennung von stabilen und instabilen atherosklerotischen Plaques sind für die Verbesserung der kardiovaskulären Diagnostik wünschenswert. Aktuelle Forschungsergebnisse identifizierten GAGs als potenzielle Ziele für die nicht-invasiven Bildgebung der Atherosklerose.

Hypothese und Ziel: Es wird vermutet, dass humane atherosklerotische Plaques durch spezifische PG/GAG-Muster charakterisiert sind. Das Ziel dieser Pilotstudie war die Erstellung einer methodischen Plattform zur Erfassung histologischer, glykoanalytischer und genexpressionanalytischer Daten aus kleinen Segmenten menschlicher atherosklerotischer Plaques, um stabilitäts- und instabilitätsassoziierten PG/GAG-Muster zu identifizieren.

Methoden: 30 Karotisendarteriektomie-Proben wurden asserviert. Nach Formalin-Fixierung und Dekalzifizierung folgte die Einbettung in Paraffin. Serielle 6 μm-Schnitte wurden für die Histologie und Immunhistochemie angefertigt. Movat-Pentachrom-, Alzianblau- und Picro-Sirius Rot-Färbungen dienten zur Bestimmung der Plaquemorphologie, des GAG- und des Kollagengehalts. Immunfärbungen mit Antikörpern gegen CD68, α-SMA und CD34 wurden zur Detektion von Makrophagen, zur Detektion der Verteilung von glatten Muskelzellen und zur Darstellung von Neovaskularization durchgeführt. Anhand der Histologie wurden die Proben klassifiziert und die räumliche Verteilung der GAG mit stabilitäts- und instabilitätsassoziierten morphologischen Merkmalen korreliert. Von 16 Proben wurde RNA aus 30 μm-Schnitten isoliert und mittels Microarray-Technologie analysiert. GAGs wurden aus benachbarten 200-μm-Schnitten extrahiert und nach einem enzymatischen Aufschluss der Polysaccharidketten zu Disaccharideinheiten mittels Hochleistungsflüssigkeitschromatographie analysiert.

Ergebnisse: Histologisch zeigte sich eine Anreicherung von GAGs in Bereichen mit vielen glatten Muskelzell-, sowie in kalzifizierten und kollagenreichen Arealen, während sich durch Inflammation gekennzeichnete Regionen GAG-arm erwiesen. Die mRNA Expressionsanalyse ergab PG-/GAG-assoziierte Kandidatengene, deren Expressionsmuster mit erhöhter Plaquevulnerabilität und Inflammation assoziiert sein könnte. Die auf Basis der Expressionsdaten durchgeführten Power Analysen ergaben, dass eine Stichprobenanzahl von 60-70 notwendig wäre, um statistisch gesicherte Ergebnisse zu erhalten. Präliminäre Glykoanalytikergebnisse zeigten, dass CS/DS-4S und -6S in atherosklerotischen Läsionen in großer Menge vorhanden sind und dass

Alterationen in ihrer Relation mit der Morphologie und Instabilität der Plaques korrelieren könnten.

Schlussfolgerung: In dieser Arbeit wird eine geeignete Forschungsplattform für die künftige Identifizierung stabilitäts- und vulnerabilitätsassoziierter PG-/GAG-Muster in humanen atherosklerotischen Plaques vorgestellt. Die Analyse histologischer, glykoanalytischer und genexpressionsanalytischer Daten aus einer kleinen Stichprobenzahl lieferte erste Hinweise darauf, dass stabile- und vulnerable atherosklerotische Plaques charakteristische PG/GAG Muster aufweisen, aus denen neue Bildgebungstargets generiert werden könnten. Die Erhöhung des Stichprobenumfangs auf 60-70 wäre notwendig, um statistisch gesicherte Ergebnisse zu erhalten.

Abstract

Background: PG core proteins and their GAG side chains are major constituents of the extracellular matrix of atherosclerotic plaques and play important pathophysiological roles. Non-invasive methods to identify stable and vulnerable atherosclerotic plaques are desirable for improving cardiovascular diagnostics. Recent studies have identified GAGs as potential targets for non-invasive imaging of atherosclerosis.

Hypothesis and objective: It is assumed that human atherosclerotic plaques are characterized by specific PG/GAG patterns. The aim of this pilot study was to establish a platform for the acquisition of histological, glycoanalytical and gene expression data from within μm-thick segments of human atherosclerotic specimens, in order to identify stability- and instability-associated PG/GAG patterns.

Methods: 30 carotid endarterectomy samples were collected, formalin fixed, decalcified and embedded in paraffin. Serial 6-μm sections were prepared for histology and immunohistochemistry. Movat pentachrome, alcian blue and picro-sirius red stainings were used to determine plaque morphology, GAG and collagen content. Immunostaining using antibodies against CD68, α-SMA and CD34 aimed to delineate macrophages, vascular smooth muscle cells and neovascularization. The samples were classified and the spatial distribution of GAGs was correlated to stability- and instability-associated morphological features. RNA was isolated from 30 μm sections and analyzed using microarray technology. GAGs were extracted from adjacent 200 μm sections, and after an enzymatic digestion of the polysaccharide chains to disaccharide units, high-performance liquid chromatography was performed.

Results: GAGs were abundant in smooth muscle cell-, collagen- and calcification-rich areas, whereas inflamed regions were GAG-poor. The mRNA expression analysis revealed PG/GAG-related candidate genes whose expression patterns may associate with plaque vulnerability and inflammation. Based on these results, power analyses revealed the need to increase the sample size to 60-70 in order to achieve statistical significance. Preliminary glycoanalytical results suggested that CS/DS-4S and -6S are abundant in atherosclerotic lesions, and that alterations in their ratio may correlate with plaque morphology and instability.

Conclusions: This thesis presents a research platform for the identification of PG/GAG patterns in human atherosclerotic plaques. Histological, glycoanalytical and gene expression data from a small number of samples provided first indications that stable and vulnerable atherosclerotic plaques exhibit characteristic PG/GAG patterns, out of which novel imaging targets may arise. Increasing the sample size to 60-70 would be required to statistically empower these results.

1.   Introduction

1.1   The pathobiology of atherosclerosis and the vulnerable plaque

1.1.1   The epidemiology of atherosclerosis and the nature of the disease

Cardiovascular diseases are still the number one cause of death globally. According to the World Health Organization, 17.7 million people died in 2015 because of cardiovascular diseases, out of which 14.1 million died due to atherosclerosis-related pathologies, mainly coronary artery disease and stroke[1]. In fact, the epidemic of obesity, type 2 diabetes, and the changes driven by population growth and aging have accelerated the progression of atherosclerosis, and by 2030 the number of deaths is expected to rise up to 23.6 million per year[2], with an expected economic burden exceeding 1 trillion United States dollars[3]. This versatile disease is influenced by both modifiable (e.g. physical inactivity, smoking, dietary habits etc.) and non-modifiable (e.g. age, male gender, genetic predisposition etc.) factors that over decades trigger subclinical pathological changes[4,5].

1.1.2   Endothelial dysfunction, changes in vascular smooth muscle cell behavior and the formation of atherosclerosis-prone sites

The dysfunctional activation of endothelial cells and the processes involved in the behavioral change of media-derived vascular smooth muscle cells (VSMC) are pivotal for the formation of atherosclerosis-susceptible regions throughout the vascular bed[6,7]. Known as adaptive- (AIT) or diffuse (DIT) intimal thickenings, these pre-atherosclerotic areas arise adjacent to arterial branch points or curvatures as a response to alternating hemodynamics[8]. Especially low shear stress forces acting upon these regions, together with a variety of factors such as pro-inflammatory mediators, reactive oxygen species, hormones and toxins, foster the gradual transition of the endothelial cell phenotype from athero-resistant to athero-prone[6]. This initial activation promotes certain populations of myeloid cells to become resident in the sub-endothelial space[9] and causes tunica media-derived VSMCs to "switch" their phenotype, allowing them to proliferate, migrate and secrete various extracellular matrix (ECM) molecules and cytokines[7].

1.1.3   Lipid accumulation and the induction of a chronic inflammatory response as key pathogenic events in atherosclerosis

These events are not capable of initiating lesion formation without the aggrandizing effect of sub-endothelial lipid retention[10]. The excess of apolipoprotein-containing lipoproteins (LP) and especially low density lipoproteins (LDL) in the blood circulation is essential for their

entrapment[11-13]. In the vessel walls, LPs undergo various modifications, particularly oxidation and aggregation, acquiring properties of damage-associated molecular patterns (DAMP)[11]. As a result, resident myeloid cells and monocyte-derived macrophages start to internalize LPs via scavenger receptors[14]. Under homeostatic conditions, these cells possess refined mechanisms to process ingested cholesterol. Nonetheless, in a sustained hypercholesterolemic setting, cholesterol metabolism loses its fine tuning and the cells gradually acquire "foam cell" morphology and undergo a pro-inflammatory activation via Toll-like receptor signaling and inflammasome assembly[14,15]. Hypercholesterolemia not only influences the phenotype of immune cells that already abide in lesions - increasing evidence strongly connects cholesterol excess with a pro-atherogenic effect on immune cell progenitors produced and differentiated in primary and secondary lymphatic organs[16]. Augmented endothelial stimulation, additional rounds of immune cell recruitment, enhanced LP retention[17], amplification of VSMC-phenotypic modulation[7], apoptosis and early post-apoptotic necrosis[18] are only some of the consequences. At the same time, endogenous lipids (e.g. resolvins, lipoxins, protectins and maresins), proteins (e.g. transforming growth factor-β), gas molecules (e.g. nitric oxide) and immune cells (e.g. regulatory T-cells and pro-resolving macrophages) orchestrate an inflammatory resolution response as part of the physiological inflammatory cascade[19]. The interplay between inflammation and inflammation resolution might frame the histological correlates of early and intermediate human atherosclerotic lesions, from AIT and pathological intimal thickening (PIT) to early fibroatheromas (EFA)[8]. The formation of a thick, VSMC- and ECM-rich fibrous cap (FC) that confines necrotic core (NC) areas, the expansive remodeling of the vessel wall and intimal calcification are thought to prevent contact of the thrombogenic plaque material with the blood, preserve blood flow and sustain tissue architecture[17,20].

1.1.4 The transition towards a defective immune response and the progression into more advanced stages

A progressive tipping between pro-resolving and pro-inflammatory responses towards the latter is suggested to trigger the transition into more advanced lesions[19]. The combination of persistent LP-derived DAMP generation with continuous immune cell infiltration, intensified apoptosis[19], and most importantly acquired deficiency in the efferocytotic[21] and autophagocytotic capacity[22] of various cell types, promotes an augmented inflammatory response. This is accompanied by aggravated cell death, not only via post-apoptotic necrosis, but also through pyroptosis and active necroptosis[18], stress-induced, premature cellular senescence[23] and protease-driven ECM degradation in both NCs and FCs[24]. Additionally, the evolving hypoxic microenvironment induces

immature neoangiogenesis and subsequent intra-plaque hemorrhage. This leads to an increase in lesion size, followed by an accumulation of free cholesterol, hemoglobin-related degradation products, immune cells and coagulation factors (e.g. tissue factor and fibrinogen), all of which boost oxidative stress and NC thrombogenicity[25]. Conclusively, these events shape the morphology of late- (LFA) and thin cap fibroatheromas (TCFA)[8].

1.1.5 Pathomechanisms of plaque destabilization, thrombosis and the vulnerable plaque concept

Over the last few decades, several histopathological and clinical studies have identified three mechanisms of plaque destabilization that are associated with intraluminal thrombosis[8]. Plaque ruptures (PR) are the most common thrombus-associated lesions (TAL). They arise from highly inflamed TCFAs whose thin FCs cannot withstand the biomechanical forces acting upon them (e.g. due to acute intra-plaque hemorrhages with sudden increase in lesion size) and rupture, allowing the thrombogenic NC to come into contact with the blood's coagulation system. Plaque erosions (PE) and calcified nodules (CN) most likely evolve from lesions with lower inflammatory burden such as PITs and EFAs or fibrocalcific plaques (FCP), respectively[8]. PEs are thought to occur as a result of a denuded tunica intima, the pathophysiology of which most likely involves gradual steps towards increased endothelial activation prior to an unpredictable desquamation phase[26]. Regarding CNs, which represent the least frequent thrombus-related lesions, the precise mechanism is unidentified, but it is proposed that mechanical stress might fragment sheets of calcified matrix, giving rise to nodules that may erupt with time through the plaque surface and activate the coagulation cascade[8].

Finally, it is the degree of thrombus formation (occlusive versus non-occlusive) that determines the patient's clinical presentation (e.g. stable angina versus acute coronary syndrome)[27]. Therefore, in an attempt to detect patients at high risk, the "vulnerable plaque/vulnerable patient" concept has been introduced[28].

1.2 PGs and GAGs

1.2.1 PG diversity and classification:

PGs and their GAG side chains are major constituents of the ECM, and they consist of a core protein on which GAG chains may attach covalently on specific amino acid sequences[29,30].

The structural variety of PGs is enormous and numerous factors contribute to this variance. Approximately 45 core proteins have been identified over the past few decades, some of which exist in various isoforms (e.g. versican isoforms V_0-V_3) due to alternative splicing[29-32]. In addition, core proteins can carry from one to more than a hundred GAG chains (e.g. biglycan with two versus aggrecan with more than a hundred GAG attachment sites, respectively), and the diversity increases even more taking into account "hybrid-PGs" that can carry GAG chains of more than one type, with different lengths and a highly heterogeneous composition[33]. "Part-time-PGs", which only carry GAGs under certain conditions, have been under surveillance for a long time[34].

PGs can be divided into four major groups (intracellular-, cell surface-, pericellular- and extracellular PGs) (Figure 1)[32]. Extracellular PGs represent the largest class, including families such as the hyalectans (also known as lecticans), and the small leucine-rich proteoglycans (SLRP) with more than twenty five members and important regulatory roles in cell-/matrix assembly and signaling[35-37]. The hyalectans, as their name implies, bind to HA and lectin forming viscous conglomerates, while serving as links between cell membranes and the ECM[32]. Additionally, SLRPs are characterized by a small core protein that embodies an area of leucine-rich repeats and can be further grouped into five classes (SLRP I-V). Classes I-III, as opposed to classes IV and V, are considered canonical and their members are able to carry GAG chains, although exceptions to the rule (e.g. asporin) are known[32]. Moreover, cell surface proteoglycans serve as receptors or co-receptors affecting the bioavailability of a variety of ligands and form the second biggest group. This group is represented by thirteen members, six existing as glycophosphatidylinositol (GPI)-anchored PGs, and seven with transmembrane domains. The pericellular PGs, comprised of four members, are closely related to the cell surface and are part of basement membranes. Lastly, serglycin is the only known intracellular PG and is responsible for the assembly and storage of proteases and other molecules inside secretory granules.
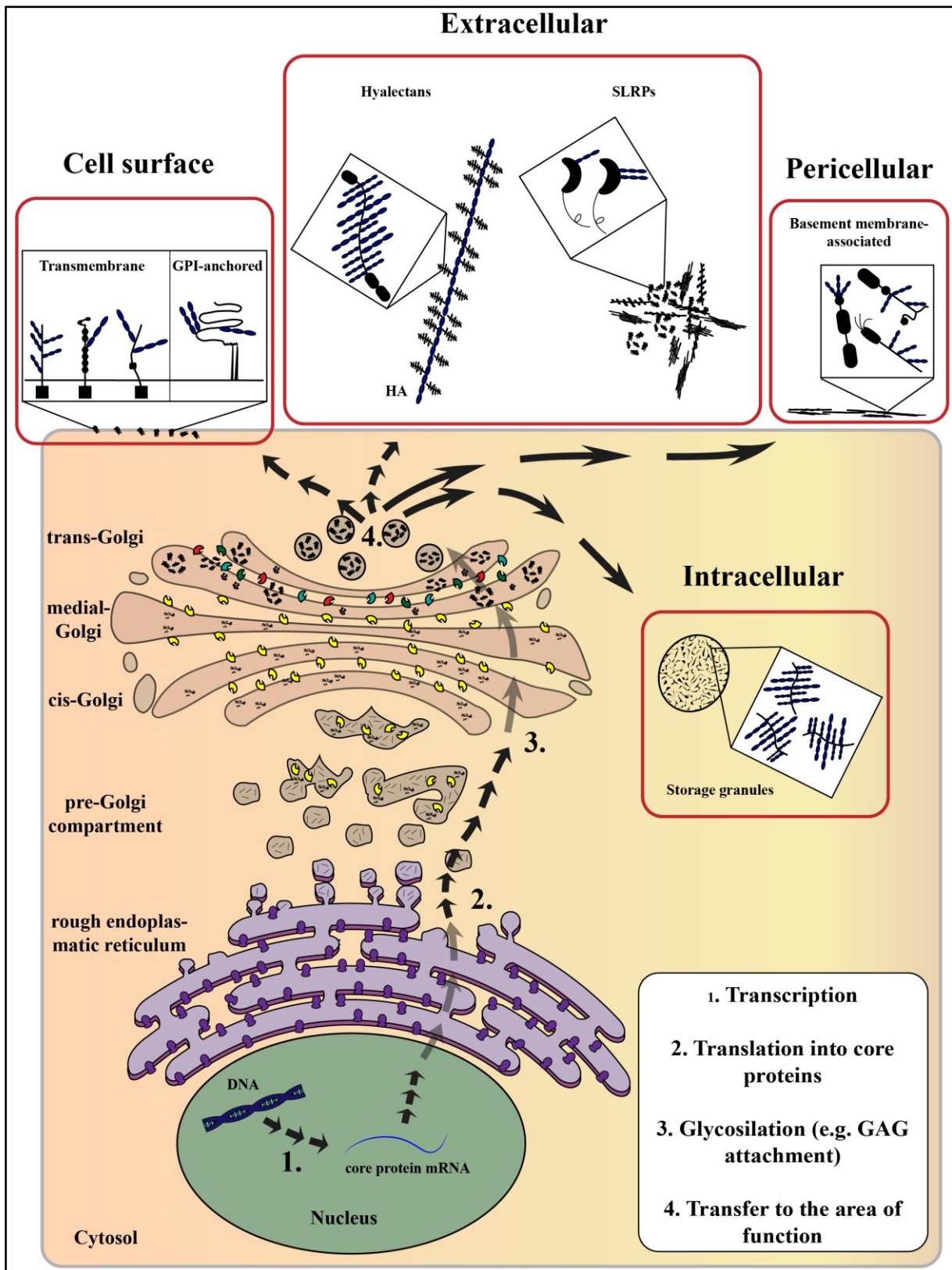
Figure 1. Classification and schematic representation of PGs and their biosynthesis pathway. Inspired and based on theory and figures in Iozzo et al.[32] and Theocharis et al.[286]. Abbreviations: GPI= glycophosphatidylinositol, HA= hyaluronic acid, SLRPs= small leucine-rich repeat proteoglycans.

1.2.2 GAG architecture and metabolism

GAGs are defined as long unbranched polysaccharides, of various sizes, consisting of repeating disaccharide units that are shaped by the linkage of a uronic acid (D-glucuronic- or L-iduronic acid) or a galactose moiety with an N-acetylated hexosamine (N-acetylgalactosamine or N-acetylglucosamine). The additional modification of these units in terms of epimerization, deacetylation and sulfation frames the basis for the formation of five distinct classes: chondroitin sulfate (CS), dermatan sulfate (DS), heparan sulfate/heparin (HS/Hep), keratan sulfate (KS) and hyaluronic acid (HA) (Figure 2)[38].

The generation of certain linker sequences is a prerequisite for the initiation of CS/DS-, HS/Hep- and KS chain synthesis, and the process occurs in a pre-Golgi compartment. While CS, DS and HS/Hep share the same tetrasaccharide linker that binds on serine residues of the core protein, KS has been found to attach via distinct N- or O-glycan oligosaccharides onto asparagine- or serine/threonine residues[38]. The subsequent polymerization and modification reactions that mark the final composition and length of the GAG chains take place inside the cisternal spaces of the Golgi network. This process involves more than 50 enzymes, capable of producing at least 66 unique disaccharide units (Figure 1)[39-42]. In addition, HS chains may undergo post-synthetic modifications, mainly by the action of two sulfatases (Sulfatase-1 and -2) and a heparanase[43]. HA is assembled at the plasma membrane by the action of three hyaluronan synthases[44], and unlike the other GAG types, it is not substituted with sulfate groups[30]. It mainly exists as a free form that can non-covalently attach to core proteins via hyaluronan-binding motifs of the hyaladherin protein family[30].

Similarly to GAG biosynthesis, the process of GAG degradation is strictly regulated and involves at least 17 different enzymes, the majority of which act inside acidic lysosomes (Figure 1)[29,45,46]. The pattern of action of these enzymes is comparable between the different GAG types and includes the cleavage of the polysaccharides into smaller parts with the help of specific endoglycosidases, followed by the action of type-specific (e.g. arylsulfatase B in CS/DS-catabolism) or shared (e.g. hexosaminidases A and B in all GAG types) groups of exoglycosidases and sulfatases. Only in the case of HA does degradation already begin at the plasma membrane, before the produced fragments are internalized and transferred to the lysosomes for a complete breakdown into monosaccharide units[45,47].
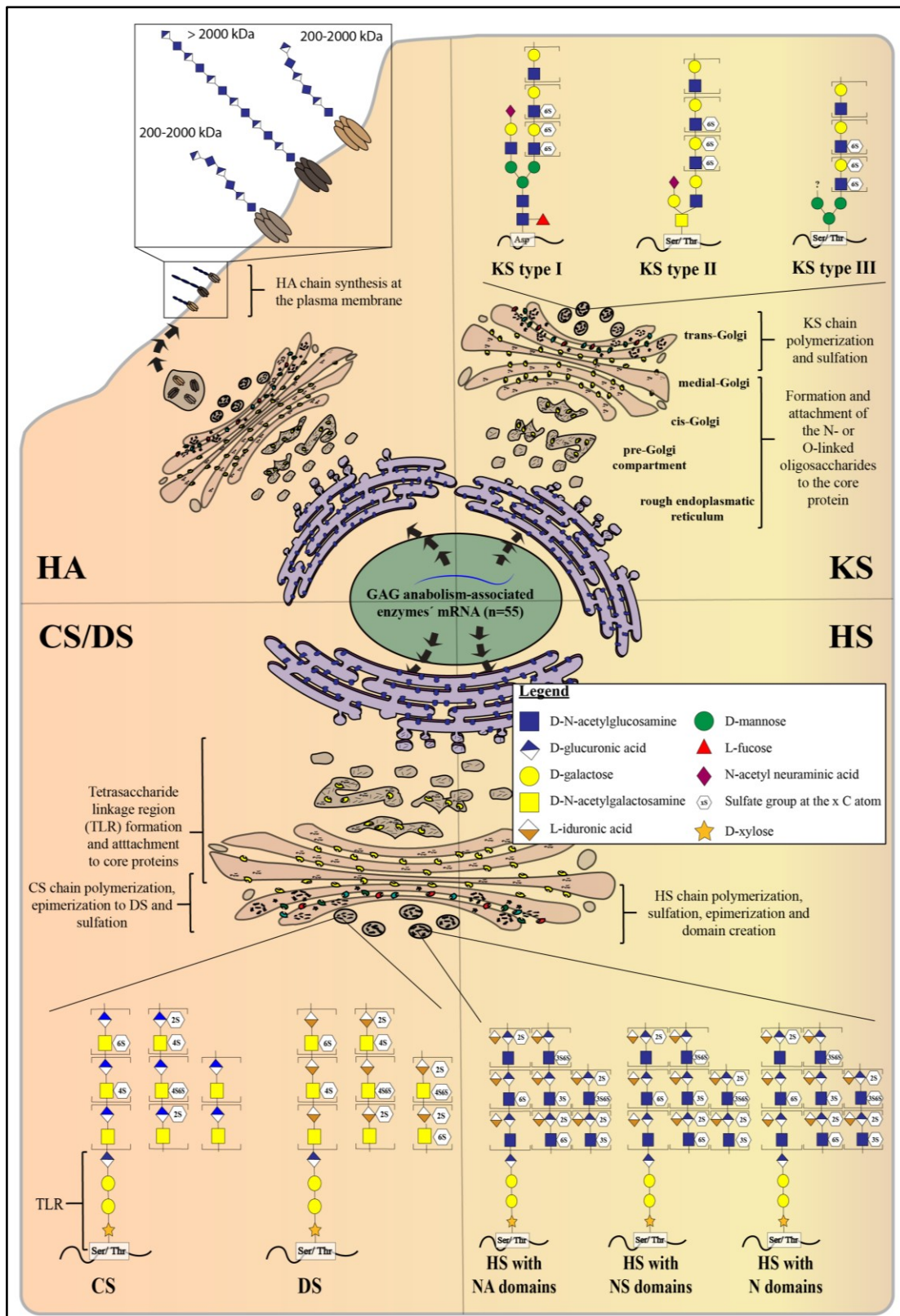
Figure 2. Schematic representation of the GAG classes and -subtypes, depiction of the chemical diversity of the disaccharide units (within the brackets) and display of their biosynthesis pathway. Inspired and based on theory and figures in Caterson et al.[39], Itano et al.[44], Mikami et al.[40] and Li et al.[41]. Abbreviations: HA: Hyaluronic acid, CS: Chondroitin sulfate, DS: Dermatan sulfate, HS: Heparan sulfate, Ser/ Thr: Serine/ Threonine, Asp: Asparagine.

1.3 The multiple roles of PGs and GAGs in atherosclerosis

1.3.1 PGs and GAGs as major structural components of disease-free arteries

The ECM of normal, heart-proximal arteries is distributed throughout three concentric layers. The tunica intima is the innermost layer and the endothelial cell lining is its major component. Its surface is covered by the glycocalyx (GCX), a network that along with glycoproteins and other molecules (e.g. coagulation-associated factors, cell adhesion molecules, albumin and enzymes) is composed of various PGs with their GAG chains and HA. HS is the most prominent GAG type, followed by CS, HA and to a lesser extent by DS and KS. The majority of the HS and CS chains are part of the transmembrane syndecans-1 (HS and CS), -2 and -4 (mainly HS) as well as GPI-anchored glypican-1 (only HS)[48,49]. On the other hand, HA is non-covalently bound to the cell surface and to CS chains of the GCX via hyaladherins (e.g. CD44)[49]. Additionally, a small part of secreted PGs carrying CS, DS and KS chains may also reside in the GCX[48]. At the abluminal side, HS-carrying PGs (perlecan, collagen type XV, -XVIII and agrin) together with other ECM components (mainly laminins, nidogens and collagen type IV) form the endothelial basement membrane[50]. Underlying elastic fibers, collagen type I and III, and to a much lesser extent PGs (e.g. versican, biglycan and decorin) and HA create the scaffold of the tunica media, in which VSMCs are embedded[50]. Each VSMC is encapsulated by a basement membrane that has a very similar structure to the one underlying the endothelial cells. The adjacent tunica adventitia contains an abundancy of collagen and elastic fibers, as well as significant amounts of PGs that are mainly produced by fibroblasts. These structures surround nervi- and vasa vasorum that innervate the vessel wall and supply it with oxygen and other metabolites[50,51].

1.3.2 PGs and GAGs as key players in vascular endothelial dysfunction

Under homeostatic conditions and favorable hemodynamics, the mechanosensitive GCX coordinates vascular permeability and tone, controls endothelial-blood cell interactions, regulates blood coagulability and promotes an anti-atherosclerotic cell phenotype[48].

In murine models of atherosclerosis, GCX thickness was found to be decreased at regions of high disease predilection[52,53]. At corresponding areas, van den Berg et al. observed an enhanced LDL uptake, linking the GCX loss with defective endothelial barrier properties[52]. Experiments using 3D endothelial cell cultures under flow revealed that GCX degradation leads to an enhanced nuclear factor kappa B pathway activation, which in turn promotes leukocyte adhesion and inflammation[54]. Similar results were observed in other in vitro models that studied the effect of

depletion of syndecan-1 and -4 on vascular endothelial cells[55,56]. Silencing of glypican-1, another major component of the endothelial GCX, has led to reduced endothelial nitric oxide synthase activation in bovine aortic endothelial cells, suggesting a tight relation of this PG with the atheroprotective nitric oxide synthesis[6,57]. Increased levels of reactive oxygen- and nitrogen species, secreted matrix metalloproteinases, as well as glycosidases (e.g. heparanases and hyaluronidases) in a pro-atherogenic milieu, contribute both directly and indirectly to shedding of the GCX, fragments of which (e.g. low molecular weight HA) can then act in a pro-inflammatory way[58]. These findings support the notion that GCX impairment and endothelial dysfunction are tightly connected, forming "vicious circle relations" that drive disease progression[59].

Apart from the GCX, the endothelial basement membrane components are equally vital for a proper endothelial function[50]. Only a few studies have been conducted to associate basement membrane PGs with endothelial dysfunction in the context of atherosclerosis. Nonaka et al. showed that perlecan is involved in vascular tone regulation by increasing nitric oxide bioavailability, and that both in vivo and in vitro its deficiency resulted in endothelial dysfunction[60]. Two other studies using human coronary endothelial cells, further displayed that reactive nitrogen species modify the composition of perlecan and other basement membrane components in a way where endothelial cell adhesion and proliferation is altered[61,62]. In fact, proteolytic cleavage of perlecan can release C-terminal domains such as endorepellin that have been found amongst other things to influence endothelial cell adhesion and apoptosis[63]. Lastly, in a murine model of atherosclerosis, loss of collagen XVIII increased LP deposition, suggesting a regulatory role of this PG in vascular permeability[64].

1.3.3 PGs and GAGs in vascular smooth muscle cell phenotypic switching and intimal thickening

HS-PGs play an important role in regulating and maintaining the cells in a quiescent and contractile state. Both in vitro and in vivo experiments have provided evidence regarding the inhibitory potency of HS-PGs (mainly perlecan and syndecan-1) towards VSMC proliferation and migration[65-70]. Other studies additionally underlined the significance of the HS chains in this process, suggesting that their structure is essential in regulating VSMC behavior[71-73]. Paradoxically, HS-carrying syndecan-4 has been found to be involved in growth factor-induced VSMC proliferation, and syndecan-4 deficient mice showed reduced neointimal formation upon wire-evoked arterial injury[74]. Consistent with these results, another in vitro study using human VSMCs showed that syndecan-4 is important in thrombin-induced migration and mitogenesis[75].

In an atherosclerotic microenvironment with increasing amounts of secreted proteases (e.g. metalloproteinase-1,-2,-3 and -9) and glycosidases (e.g. heparanase), some molecules (e.g. perlecan) are partly degraded and others (e.g. syndecan-4) are overexpressed. Hence, these events promote the phenotypic transition of VSMCs, which abandon their contractile state, become resident in the sub-endothelial space, and by producing substantial amounts of PGs and GAGs contribute to the thickening of the intima[8,76].

The newly synthesized PGs and GAGs are part of a "provisional matrix" that is postulated to further expedite vascular remodeling and VSMC phenotypic modulation[63]. Whereas HS-carrying PGs are the main group found in the intima and the media of human non-atherosclerotic arteries[50], the matrix generated by dedifferentiated VSMCs is based on a mixture of CS/DS-carrying PGs, mainly the V1 isoform of versican (CS) and biglycan (CS/DS), as well as HA[51,77-81]. The viscoelastic coat formed by these molecules facilitates further VSMC migration and proliferation, and influences cell adhesion and ECM assembly[82-88]. These abilities are thought to be transfused by the CS/DS chains attached on the core proteins, as indirectly suggested by several studies that examined the effect of GAG-deficient biglycan and the GAG-free variant of versican (V3) on VSMC behavior and elastogenesis[89-91]. Conversely, decorin (CS/DS) that is present throughout the thickened intima[51] has been shown to negatively influence the response of VSMCs towards mitogens, thus dampening their migro-proliferative response[92,93].

Recent immunohistochemical- and proteomics-based studies on human aortic, coronary and CEA specimens presenting with intimal thickening revealed further PG family members such as prolargin (KS), aggrecan (CS), mimecan (KS), fibromodulin (KS), lumican (KS), asporin (-) and podocan (-) to be present[94-96]. Some of these molecules, such as podocan and mimecan, have already been found to alter VSMC behavior[97-100], although results were not always consistent[101].

1.3.4 The "response-to-retention" hypothesis and the association of PGs and GAGs with lipid accumulation

Following the differentiation of CS subtypes and the characterization of DS, HS, HA and KS by Meyer and colleagues between 1930 and 1953[102], substantial experimental work demonstrated that these principle GAG types, back then referred to as acidic mucopolysaccharides, are present in the human vasculature, increase in the early stages of atherosclerosis and are able to interact with LPs that usually accumulate in GAG-rich areas[63]. Based on these and other observations, back in 1995 Kevin Jon Williams and Ira Tabas proposed the "response-to-retention" hypothesis, suggesting that as a pathogenic event, PG-mediated LP retention fulfills both the "necessity" and the

"sufficiency" criterion to initiate atherosclerotic lesion formation on an otherwise disease-free vessel[103].

In vitro and transgenic mice-based studies reinforced this notion[10,104] and several extracellular (biglycan, decorin, versican, perlecan, fibromodulin) and cell surface (syndecan-4 and NG2) PGs together with HA were found to be associated with lipid retention[77,105-114]. Differences in the composition of arterial walls between humans and rodents (e.g. regarding versican and perlecan)[115-118], and the fact that the distribution of vascular PGs such as versican and decorin in human coronary arteries does not always follow that of apolipoproteins/lipids[78-81,119], have raised questions with regard to the extent to which the investigated PGs are involved in vascular lipid accumulation in humans[63]. Nevertheless, there is no uncertainty that the existence[106,109,110], composition[120,121], length[122,123], charge[124] and number of GAG chains per core protein[63] are definitely involved in the process of LP retention.

It is possible that numerous PGs, with their highly complex GAG chains, can bind with different affinities to LPs, and as recently suggested, "it might not be important which type of PG is present during lipid retention", but "it is rather the where and how much" of these molecules are present to facilitate this process[63]. It is now accepted that PG/GAG-mediated LP retention is causatively linked to atherogenesis[11].

1.3.5 The involvement of PGs and GAGs in plaque neoangiogenesis

The ECM, including PGs with their GAG chains, is strongly related to the process of angiogenesis under both physiological and pathological conditions. Basement membrane-associated PGs such as perlecan and collagen XV, and XVIII have been found to promote neovessel formation, while their proteolytically-derived fragments restin, endostatin and endorepellin are suggested to inhibit endothelial cell migration and facilitate angiostasis[125-129]. Decorin, fibromodulin and HA can exert both pro- and anti-angiogenic features, depending on the composition of the microenvironment and their structural characteristics[130-134]. Other PGs such as the SLRPs biglycan, lumican, versican and the cell-surface associated syndecans-1, -2, -4 and glypican-1 have also been found to operate as regulators of blood vessel formation by regulating either the stimulation or the inhibition of the process[130-134].

Although several of the aforementioned PGs (e.g. biglycan, decorin, perlecan, collagen XVIII, collagen XV and agrin) have been found in microvessel-rich areas in human atherosclerotic lesions[78,126,135], few experimental studies have focused on the potency of such PGs as regulators of angiogenesis in a vascular disease-/atherosclerosis-related context. Three in vivo-based

experiments using murine, porcine and rabbit models of atherosclerosis showed that endostatin treatment inhibited neovascularization and plaque progression[128,129,136]. Perlecan has also been found to regulate neovessel formation as shown in an in vivo model of hind-limb induced ischemia. The authors additionally observed that the HS chains in perlecan are decisive for its pro-angiogenic character under hypoxic conditions[125]. Using a similar study model, Wu and colleagues suggested a new role for osteoglycin as a negative regulator of ischemia-induced angiogenesis[137]. Supporting this notion, Shen et al. showed that patients suffering from coronary artery disease with poor coronary collateralization presented with increased serum concentrations of osteoglycin, while Kampmann and colleagues found osteoglycin to be downregulated in collateral arteries after rabbit femoral artery ligation[137].

1.3.6 PGs and GAGs as regulators of vessel wall thrombogenicity

It has long been suspected that PGs and GAGs are capable of regulating hemostasis. Hep is the most known GAG with strong anticoagulant properties, and together with its chemical derivatives it remains one of the pharmacological pillars regarding prophylaxis and treatment of thrombus-related conditions[138]. However, the relevance of endogenously produced Hep in controlling physiological coagulation remains controversial[139].

During the 1960s, '70s and '80s, various studies examined the ability of other GAG types to regulate the coagulation process and showed that CS, DS and HS possess anticoagulant properties that vary according to their biochemistry[140-144]. Similar results were reported by other groups testing GAG extracts from bovine blood vessels with respect to this issue. GAGs obtained from the adventitia, containing mainly DS and HS, exerted the biggest anticoagulant activity among all layers[145-147]. Izuka et al. and Tover et al. were able to show that GAGs isolated from human blood vessels prolonged the thrombus formation time and reduced clot weight. At the same time, higher anti-thrombogenic properties of DS in comparison to CS and HS were noticed, although small amounts of Hep-like HS chains with high antithrombin III affinity were also detected[148,149]. It is now known that these molecules can bind with varying affinities to antithrombin III and heparin cofactor II, as shown in vitro and in vivo, thereby functioning as endogenous inhibitors of the coagulation cascade[150,151].

Kolodgie and colleagues demonstrated differences in the distributions of versican, biglycan, decorin and HA at the plaque/thrombus interface of TALs as compared to stable plaques. More specifically, plaque erosions showed intense immunostaining for HA and versican, and barely detectable staining for biglycan, while stable plaques presented with intense versican and biglycan

staining, but were negative for HA. Decorin immunostaining was weak to mild in both cases. Conversely, immunostaining for all these molecules was very weak to non-existent at the plaque/thrombus interface of plaque ruptures. These observations indicate a possible regulatory function of these PGs in thrombus formation, suggesting that their presence or absence may shift the plaque microenvironment towards a pro- or anti-thrombotic state[152]. Indeed, a HA-rich matrix can alter endothelial cell viability and promote platelet attachment via CD44, the major HA cell surface receptor that was found to colocalize with specific subsets of VSMCs at the plaque/thrombus interface of eroded plaques[26,152,153]. The accumulation of versican at these sites might play an integral role in promoting platelet adhesion under low shear stress forces, as implied by a study using real-time analysis to examine the binding capabilities of human platelets on vascular PGs[154]. The G3 domain of versican was found to inhibit the activity of tissue factor pathway inhibitor-1, an important actor of the fibrinolytic system, thereby enhancing the pro-coagulant abilities of activated factors VIIa and Xa[155]. McGee et al. demonstrated that advanced type IV lesions (representing EFAs and LFAs) from human aortas contained versican with significantly reduced CS chain sulfation relative to that of adjacent, healthy segments. The decrease of sulfation led to a reduction in CS′s anticoagulant activity via disruption of water transfer homeostasis and subsequent compromise of antithrombin-factor Xa complex formation[156]. Loss of other PGs such as biglycan from erosion- and rupture-prone plaques might also contribute to the creation of a pro-thrombotic milieu[86]. In a very recent study, Grandoch et al. reported higher thrombin activity and increased thrombocyte activation and adhesion in ApoE/Biglycan double-deficient mice, suggesting an anticoagulant character for this SLRP[157]. It was reported that biglycan isolated from human atherosclerotic lesions has a reduced ability to promote heparin cofactor II-dependent thrombin inhibition compared to biglycan isolated from healthy vessels. This reduction was attributed to compositional changes of the molecule, which presented with undersulfated and mainly CS-containing GAG chains[158].

1.3.7 PGs and GAGs as modulators of vascular inflammation

PGs and their GAG side chains have been found to be related to inflammatory processes in atherosclerotic lesions. Many of the PGs, such as biglycan, fibromodulin, lumican and the GAG HA, have been located inside or adjacent to macrophage-rich areas in atherosclerotic lesions[63]. Biglycan is known for its ability to act as a DAMP, promoting the activation of inflammatory cascades and the secretion of pro-inflammatory cytokines. Indirectly biglycan is supposed to facilitate further DAMP generation by improving the catalytic activity of lipid metabolism-associated enzymes, the products of which act in a pro-inflammatory manner[159]. Lumican was

found to interact with surface molecules of immune cells, possibly promoting the chemotaxis of further immune cells in the atherosclerotic lesions. It has been found to be increasingly produced by cells that undergo inflammatory activation via interleukin-1β, tumor necrosis factor α and lipopolysaccharide[159]. Leukocyte attraction to the inflammation site is also influenced by the actions of fibromodulin, which has been found to modulate the complement system[63]. More recently, HA has gained increased attention regarding its association with inflammation and as a putative target for modulation of the immune response[86]. Due to its size and its numerous non-covalent interaction sites, HA functions as a "linker" and is capable of forming so called "HA cables", which were first found in an experimental model of intestinal inflammation. These formations attach to monocytes, macrophages and lymphocytes, promoting their pro-inflammatory activation[86].

1.4   Imaging in atherosclerosis: Current tools and the emerging role of magnetic resonance imaging

Clinically-based cardiovascular risk assessment algorithms (e.g. SCORE, Framingham risk score etc.) allow physicians to roughly estimate the patient´s risk for future cardiovascular events. Different imaging modalities have come to play an important role in the management of patients presenting with various atherosclerosis phenotypes. This is reflected in the European Society of Cardiology guidelines, according to which risk stratification and diagnosis, therapeutic decision making, interventional planning and estimation of prognosis is connected to the results of non-invasive and/or invasive imaging[160-165].

The current imaging-based algorithms rely on the estimation of total plaque burden and the detection of potential vessel obstructions with downstream organ ischemia[160-165]. However, these measurements provide unspecific and inaccurate predictions of future adverse events[166]. Over the last few decades, efforts have been undertaken to assess alternative factors that may facilitate a more efficient prediction of such events[166].

The first approach is based on the identification of vulnerable plaques that are characterized by particular histopathological features, namely thin FCs, high inflammatory burden, large NCs, high amount of neovessels, intraplaque hemorrhage, positive remodeling and FC-associated microcalcification[167]. The clinical significance of this concept has not been proven yet and doubts have been raised in the cardiological community[168]. Several prospective study results (e.g. PROSPECT, VIVA and ATHEROMO-IVUS) have provided evidence that the identification and treatment of individual high-risk plaques has a low positive predictive value regarding major adverse cardiovascular events[168,169]. Patients may remain asymptomatic even after the destabilization of such high-risk plaques, possibly due to clinically silent rupture and/or erosion with subsequent healing[168,169]. On the other hand, computed tomography (CT)- and magnetic resonance imaging (MRI)-based studies showed that patients carrying plaques with features of instability in both the carotid and coronary arteries are at increased risk for cerebrovascular and cardiovascular events, respectively[170-181]. Thus, it might be the detection and treatment of vulnerable patients carrying a plethora of instability-related plaque characteristics, instead of the detection of individual unstable plaques, that might prove to play a role in clinical practice[182].

The second approach was inspired by clinical trial observations focusing on the dynamic nature of atherosclerotic plaques, which may alternate their phenotype within months, transiting from low-

to high-risk and vice versa[168,169]. The visualization and monitoring of what was termed "disease activity" led scientists to form new strategies against atherosclerosis[166]. In this way, molecular imaging is emerging as a promising way of using various imaging modalities in order to depict disease pathophysiology[182].

At the moment, CT is the non-invasive imaging modality with the widest use, being able to assess total plaque burden and to identify luminal obstruction and high-risk plaque characteristics[183]. CT-based coronary angiography even allows fractional flow reserve measurements, although this is still far from being part of the clinical workflow[184-186], and it is expected to have increased representation in upcoming clinical guidelines[187]. In particular, the use of hybrid techniques that combine the aforementioned approaches in one imaging session are expected to accurately prognosticate patients at high risk with unstable plaque features and an active disease state[188].

MRI is a rapidly emerging technology that offers the advantages of enhanced soft-tissue contrast, a lack of radiation and good spatial resolution values[188]. For conditions that are accompanied by the formation of cardiac edema and/or scar tissue (e.g. cardiomyopathies, myocarditis etc.), MRI is considered as a first-line imaging procedure[189]. MRI is strongly represented as a diagnostic procedure in the clinical guidelines of atherosclerosis-related vascular diseases[160-165]. For peripheral arterial diseases including the extracranial carotid and vertebral-, mesenteric-, renal- and lower extremity vascular bed, MRI angiograms are recommended as second-line imaging modalities for stenosis severity estimation and intervention planning[161]. Compared to CT and ultrasound, carotid MR angiography is considered more suitable for detecting high-risk plaque features such as thin FCs and intraplaque hemorrhage[180], while providing a higher sensitivity and specificity in the detection of vertebral artery disease[161]. Furthermore, although MRI angiograms of the coronary arteries provided inferior results in the detection of coronary artery stenosis in comparison to CT-based angiography, ongoing technical advancements are already narrowing this gap[183]. Apart from the visualization and characterization of atherosclerotic plaques, MRI scans, usually performed as stress MRIs, provide additional information regarding cardiac viability, structure and left/right ventricular function, and are recommended as part of the diagnostic workflow for the management of patients with coronary artery disease[162-165].

Non-invasive imaging may revolutionize the way cardiologists assess and treat their patients, while giving deeper insights into the pathophysiology of atherosclerosis. MRI is one of these emerging modalities and is expected to play a more central role in the very near future[189].

1.5 Aims of the project

It is becoming clear that the ECM is a highly active network that is involved in the regulation of human organ homeostasis and plays a central role in human disease pathophysiology[190].

PGs and GAGs are important constituents of the vasculature in healthy and diseased blood vessels[63], but the exact atherosclerosis-related changes and patterns have still not been completely clarified. The lack of methods to fully characterize chemically modified GAGs from atherosclerotic tissue, along with their highly complex nature, has impeded an in-depth investigation of their role in the disease. The mechanisms that regulate the elongation of GAG chains and control sulfation, including the activity of their metabolism-related enzymes in atherosclerotic sites, are largely unknown.

Various ECM-related tracers (e.g. against elastin, collagen, fibrin, matrix metalloproteinases etc.) have been tested for molecular imaging in the context of atherosclerosis[191]. Tracers that specifically target PGs and their GAG side chains are so far not available[191]. GAGs have been identified as novel targets for non-invasive atherosclerotic plaque imaging, e.g. as binding partners to gadolinium and iron oxide nanoparticles[192-196]. These molecules possess a dual capability of being highly negative and biochemically highly variable. In other words, these molecules simultaneously possess "general-" and "target-specific" traits, which makes them attractive as imaging targets[196].

Against this background, it is of interest to investigate whether specific PG/GAG patterns are associated with instability-related morphological features and processes (e.g. inflammation) as identified in atherosclerotic plaque sections.

Thus, the aim of this pilot study was to introduce an experimental platform and establish a methodology that allows for the acquisition and examination of histological, glycoanalytical and gene expression analysis data from within μm-sections of human atherosclerotic samples in order to identify instability-related PG/GAG patterns.

1.6 Experimental design

The following experimental procedures were conducted in the study (Figure 3):

(1) Specimen acquisition and pre-analytical preparation (i.e., segmentation, documentation, decalcification and paraffin embedding).

(2) Establishment of a vulnerability scoring system according to well-known, instability-related plaque features, which were visualized via conventional histology (i.e., Movat pentrachrome) and immunohistochemistry [i.e., anti-CD68, anti-α-smooth muscle cell actin (α-SMA) and anti-CD34].

(3) Morphometrical analysis using the sections stained with alcian blue, anti-CD68, anti-α-SMA and picro-sirius red, in order to investigate the GAG distribution, particularly in relation to instability-associated plaque features (i.e., NCs, macrophage-rich areas and VSMC-sparse regions), but also in regions with signs of calcification and collagen deposition.

(4) RNA extraction, microarray analysis, investigation of differential mRNA expression levels of core proteins and GAG anabolism-/catabolism-related enzymes between low-/high vulnerability lesions and between sections of low- and high anti-CD68 immunoreactivity. The mRNA expression levels of the core protein and GAG anabolism-/catabolism-related enzymes were correlated with the mRNA expression levels of (in) stability-associated markers.

(5) Extraction of GAGs, enzymatic digestion into disaccharide units and analysis via high-performance liquid chromatography (HPLC), with emphasis on pattern alterations between low- and high vulnerability sections, as well as sections with low- and high anti-CD68 immunoreactivity.

(6) Conducting of a sample size estimation for future project organization.
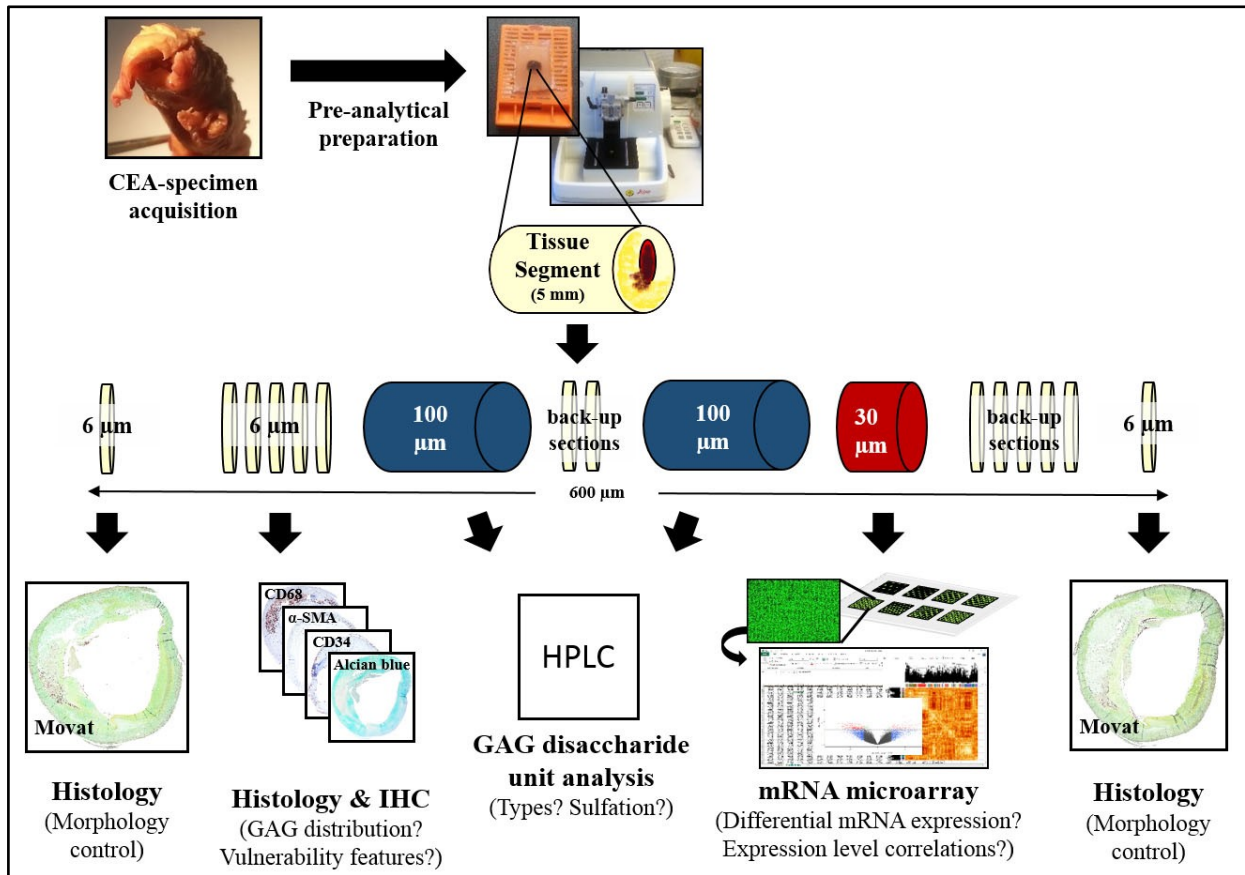
Figure 3. Schematic representation of the workflow. For each tissue segment the first and last sections served as controls in order to assure a constant plaque morphology.

2.   Materials and methods

2.1   Ethics committee approval and informed consent

The implementation of the project was approved by the ethics committee of the Charité – Universtitätsmedizin Berlin (EA 1/188/15). An information sheet signed by the patients served as their written consent to participation and was archived. All of the experiments were undertaken in accordance with the Helsinki Declaration of 1975, as revised in 2013 and with conformation to the Charité – Universitätsmedizin Berlin Statute Ensuring Good Scientific Practice of 2012, as revised in 2016.

2.2   Eligibility criteria and specimen acquisition

Patients diagnosed with symptomatic or asymptomatic carotid artery stenosis with an indication for carotid endarterectomy (CEA) were included in the study. The indication was set according to the S3 guidelines for diagnosis, treatment and aftercare of extracranial carotid artery stenosis by the physicians of the surgical and neurological departments of the Charité – Universitätsmedizin Berlin Campus Charité Mitte (CCM), Campus Benjamin Franklin (CBF) and Campus Virchow Klinikum (CVK). Patients under 18 years old, and/or with unclear past medical history, and/or with reduced cognitive faculty were excluded from the study. Between October 2015 and April 2017, 30 CEA specimens were collected and were initially included in the pilot study.

2.3   Pre-analytical specimen processing: Fixation, decalcification and tissue segment embedding

Table 1. Material used for the pre-analytical specimen preparation

Material	Supplier
Roti®-Histofix 4 %, pH 7	Roth, Karlsruhe, Germany
Tissue Marking Dye Kit	Sigma Aldrich, St. Louis, USA
Camera: 8.0 megapixel Sony CMOS-Sensor 1/3.2" IMX175	Sony Europe Limited, Companies House Cardiff, Great Britain
Sartorius Balance BP 610	Sartorius, Göttingen, Germany
pH portable meter, pH 330i pH electrode SenTix ® 51	WTW, Weilheim, Germany
Sodium hydroxide (NaOH) solution (2.5 M):	Merck, Darmstadt, Germany

10 g Sodium hydroxide pellets for analysis Emsure ® ad 100 mL Aqua destillata	
Ethylenediaminetetraacetic acid (EDTA) solution (0.27 M, pH =7.40-7.44): 10 g EDTA disodium salt dihydrate ad 80 mL Aqua destillata ad 20 mL NaOH solution	Roth, Karlsruhe, Germany
Universal embedding cassettes, 4.2 x 2.9 cm	R. Langenbrinck, Emmendingen, Germany
Leica TP1020 Semi-enclosed Benchtop Tissue Processor Leica TP1020 Tissue Basket, Standard	Leica Microsystems, Wetzlar, Germany
Ethanol absolute, J.T. Baker ®	Avantor, Pennsylvania, USA
Xylenes, Baker Analyzed ®	Avantor, Pennsylvania, USA
Paraffin, Surgipath ®, Paraplast Plus ®	Leica Microsystems, Wetzlar, Germany
Leica EG1150 H Heated Paraffin Embedding Module Leica EG1140 C Cold Plate	Leica Microsystems, Wetzlar, Germany
Metal Base Mold 15 x 15, 24 x 24, 30 x 24	Leica Microsystems, Wetzlar, Germany

Upon CEA specimen acquisition, the material was fixated with 4 % (v/v) formaldehyde (=10 % neutrally buffered formalin) for a maximum of 24 hours at 4°C. A code name was applied to every CEA specimen indicating the collection order and the patient's initials. The specimens were dissected into 5 mm-thick segments, which were numbered and photographically documented. A tissue marking dye was applied at the distal surface of each segment in order to assure the correct order of the segments. A total of 120 tissue segments were obtained.

Decalcification was performed using a 0.27 M EDTA aqueous solution (pH= 7.40-7.44) for seven days at room temperature. The solution was substituted daily. On the eighth day, the decalcified segments were washed using distilled water and enclosed in embedding cassettes. The cassettes were transferred into the "first position" container of a TP1020 tissue processor, which was set to run a 12 h program overnight.

Finally, the tissue segments were embedded with paraffin on the top of the cassettes using the EG1150H embedding module and the EG1140 cooling plate. The segments were stored at 4°C.

2.4 Histology and immunohistochemistry

2.4.1 Tissue segment sectioning

Table 2. Material used for the sectioning of the tissue segments

Material	Supplier
Leica RM2245 Rotatory Microtome	Leica Microsystems, Wetzlar, Germany
Low disposable blades 819	Leica Microsystems, Wetzlar, Germany
Disposable blade N35	Feather, Osaka, Japan
Leica HI1210 Water bath for paraffin sections	Leica Microsystems, Wetzlar, Germany
Adhesion microscope slides SuperFrost Plus ®	R. Langenbrinck, Emmendingen, Germany

The embedded segments were cut with a RM2245 microtome (clearance angle was set at 4-5 °; a thickness of 6 µm was chosen). Three tissue sections were mounted on each slide and were air dried at room temperature for 24 h.

2.4.2 Conventional histology

Table 3. Material used for conventional histological staining methods

Material	Supplier
EasyDip™ Slide Staining Jar M900 EasyDip™ Slide Staining Rack M905-12DGY	Simport, Beloeil, Canada
Xylenes, Baker Analyzed ®	Avantor, Pennsylvania, USA
Ethanol absolute, J.T. Baker ®	Avantor, Pennsylvania, USA
Acetic acid (glacial) 100 %, Emsure ®	Merck, Darmstadt, Germany
2-propanol, Emplura ®	Merck, Darmstadt, Germany
Movat pentachrome (Verhoeff) staining kit -Alcian blue 1 % (pH 2.5, 1 % acetic acid) -Verhoeff stock solution A, B and C -Ferric chloride 1 % -Phosphotungstic acid 2 % -Safran du Gâtinais -Brilliant crocein-acid fuchsin	Morphisto, Frankfurt am Main, Germany

Parafilm ® M, roll size 4 in. x 125 ft.	Sigma Aldrich, St. Louis, USA
Whatman ® prepleated qualitative filter paper, Grade 595 ½, circles, diam. 240 mm Whatman ® Puradisc disposable filter units, cellulose acetate, 0.2 μm	Sigma Aldrich, St. Louis, USA

Alcian blue/nuclear fast red stain (pH 2.5):
    - 5 g Alcian blue 8GX ad 485 mL Aqua destillata ad 15 mL acetic acid 100 %
    - Nuclear fast red-aluminium sulfate solution
	Sigma Aldrich, St. Louis, USA
	Roth, Karlsruhe, Germany

Picro-sirius red stain:
    - 0.2 g Direct Red 80 ad 200 mL picric acid solution 1.3 % in H_2O (saturated)
    - Weigert stock solution A, B
	Sigma Aldrich, St. Louis, USA
	Morphisto, Frankfurt am Main, Germany

Rapid mounting medium, Entellan®	Merck, Darmstadt, Germany
Microscopical cover slips, 24 x 46/24 x 32 mm, glass thickness: 0.13-0.17 mm	R. Langenbrinck, Emmendingen, Germany

2.4.2.1 Modified Verhoeff´s Movat pentachrome stain:

The modified Verhoeff´s version of the original Movat pentachrome stain was chosen[197]. Staining was performed at room temperature and the volumes used were 100 mL unless otherwise stated. The selected slides were deparaffinized twice using a fresh xylene solution for 10 min each time. The sections were hydrated using 96 %, 80 %, 70 % and 60 % ethanol and Aqua destillata for 2 min, and were pretreated with 3 % acetic acid for 30 s prior to staining with 1 % alcian blue (pH 2.5) for 30 min. The slides were washed using running tap water for 2 min and were incubated with a Verhoeff solution for 8 min. The solution was freshly prepared by mixing the three Verhoeff stock solutions (A: B: C) at a ratio of 3: 2: 1. A step using 1 % ferric chloride for pickling was performed to stabilize the staining. After a rinsing step with running tap water for 10 min, the slides were placed into a brilliant crocein-acid fuchsin solution and incubated for 6 min. The subsequent differentiation step included a fast treatment with 1 % acetic acid for 30 s, and the latter stain was stabilized by the use of 2 % phosphotungstic acid as a mordant for 15 min. Next, the slides were differentiated with 1 % acetic acid for 1 min and dehydrated twice in 99 % ethanol for 3 min and 15 min, respectively. The excess ethanol was shaken off and the tissue sections were

stained with Safran du Gâtinais for 15 min. The excess Safran du Gâtinais was washed out by rinsing the sections twice in 99 % ethanol for 2 min and once in 2-propanol for 3 min. Lastly, the slides were cleared twice using xylene for 10 min and mounted with Entellan ® and cover slips.

2.4.2.2 Alcian blue/nuclear fast red stain:

The staining procedure was performed according to the protocol of Carson et al.[198] at room temperature and the volumes used were always 100 mL unless otherwise stated. The selected tissue sections were deparaffinized and hydrated as described above. A short rinsing in 3 % acetic acid for 3 min protected the subsequent alcian blue staining step from gross pH changes. The alcian blue solution was freshly prepared by adding 5 g Alcian blue 8GX to 485 mL Aqua destillata, while adjusting the pH with approximately 15 mL of 100 % acetic acid at a level of 2.5. The solution was filtered with a Whatman ® filter paper before use. Next, the slides were incubated in the 1 % alcian blue solution (pH 2.5) for 30 min and the excess dye was removed by rinsing in 3 % acetic acid for 1 min followed by a washing step in Aqua destillata for 10 min. The slides were counterstained with nuclear fast red for 4 min and dehydrated using 60 %, 70 %, 80 % and 96 % ethanol for 2 min each time. They were finally cleared twice with xylene for 10 min and mounted with Entellan ® and cover slips.

2.4.2.3 Picro-sirius red stain:

The procedure was performed according to the protocol of Junqueira et al.[199] at room temperature and the volumes used were always 100 mL unless differently stated. The selected tissue sections were deparaffinated and hydrated as described above. The slides were stained with a Weigert´s hematoxylin solution for 8 min. The solution was prepared by mixing the two Weigert´s stock solutions A and B at a ratio of 1:1. After a short washing step of 10 min with running tap water, the tissue sections were stained with picro-sirius red for 60 min. The picro-sirius red was composed of 0.2 g sirius-red powder in 200 mL picric acid. The solution was firmly stirred with a magnetic stir bar for 20 min and left covered with Parafilm ® for 1 h, before being filtrated with a Whatman ® filter paper and filter unit. After a brief rinsing with acidified water (1.25 ml acetic acid (100 %) in 250 mL Aqua destillata) to wash off the excess dye, the slides were dehydrated using 60 %, 70 %, 80 % and 96 % ethanol for 2 min and cleared twice with xylene for 10 min. Finally, they were mounted with Entellan ® and cover slips.

2.4.2.4 Alizarin red stain:

The staining procedure was performed according to the protocol described by Carson et al.[201] at room temperature and the volumes used were always 100 mL unless differently stated. The selected tissue sections were deparaffinized and hydrated as described above. The slides were stained with alizarin red for 15 min. The solution was freshly prepared by dissolving 2 g of Alizarin Red S in 80 mL of Aqua destillata and the pH was adjusted to 4.5-4.6 by using 28-30 % NH_4OH. Aqua destillata was then added to a final volume of 100 mL. Next, the excess dye was gently shaken off and the sections were dry blotted using thin filter paper. The tissues were rinsed in acetone for 1 min twice and in xylene/acetone (1: 1) for 30 s, before being cleared two times with xylene for 10 min. Finally, the sections were mounted with Entellan ® and cover slips.

2.4.3 Immunohistochemistry

Table 4. Material used for immunohistochemistry

Material	Supplier
Xylenes, Baker Analyzed ®	Avantor, Pennsylvania, USA
Ethanol absolute, J.T. Baker ®	Avantor, Pennsylvania, USA
Hydrogen peroxide (H_2O_2) 30 %, Baker ®	Avantor, Pennsylvania, USA
Citrate buffer stock solution (2mM citric acid, 7 mM sodium citrate, pH 6.0): -Citric acid stock solution (0.1M): 21.04 g citric acid ad 1 L Aqua destillata -Sodium citrate stock solution (0.1M): 29.4 g tri-sodium citrate dehydrate 1000 mL Aqua destillata -Hydrochloric acid (HCl) 1 N Titripur ®	Merck, Darmstadt, Germany
Perfect Plus Pressure Cooker, 4.5 Qts	WMF, Geislingen an der Steige, Germany
Tris buffered saline-Tween stock solution (TBST) (pH 7.6): 1 tablet Roti ®fair TBST 7.6 ad 500 mL Aqua destillata	Roth, Karlsruhe, Germany
PAP pen, LP0001	Zytomed Systems, Berlin, Germany

Monoclonal Mouse Anti-Human CD68, Concentrated, Clone KP1, Unconjugated, DAKO®	Agilent Technologies, Waldbronn, Germany
Monoclonal Mouse Anti-Human Hematopoietic Cell, CD34, Class II, Clone QBEnd 10, Unconjugated, DAKO ®	Agilent Technologies, Waldbronn, Germany
Monoclonal Mouse anti-Actin, smooth muscle, Clone 1A4	Zytomed Systems, Berlin, Germany
ProTaqs ® Antibody Diluent, pH 7.4	Quartett, Berlin, Germany
ZytoChem-Plus HRP Kit, Broad Spectrum, HRP008AEC: - 8 mL blocking solution - 8 mL biotinylated secondary antibody - 8 mL Streptavidin-HRP-conjugate - 7 x 5 mL AEC substrate buffer - 3 mL AEC concentrate	Zytomed Systems, Berlin, Germany
Hematoxylin solution, Gill No. 1	Thermo Fisher Scientific, Waltham, USA
Aqueous mounting agent, Aquatex®	Merck, Darmstadt, Germany
Microscopical cover slips, 24 x 46/24 x 32 mm, glass thickness: 0.13-0.17 mm	R. Langenbrinck, Emmendingen, Germany

The immunohistochemical staining methods were performed in collaboration with the Laboratory Habedank, Berlin, Germany.

2.4.3.1 Deparaffinization and heat-induced epitope retrieval:

Slides adjacent to the ones used for conventional histology were selected for immunostaining with anti-CD68, anti-CD34 and anti-α-SMA. The slides were deparaffinized three times with xylene (10 min each time) and rehydrated in 100 % ethanol for 1 min, in a 3 % H_2O_2/ethanol solution (3 mL 30 % H_2O_2 in 100 mL 100 % ethanol) for 8 min, and in 80 % and 70 % ethanol solutions for 2 min each. Lastly, the slides were rinsed three times with Aqua destillata for 1 min.

The slides selected for anti-CD68 and anti-CD34 staining were processed with a heat-induced epitope retrieval method using a citrate buffer stock solution (2mM citric acid, 7mM sodium citrate, pH 6.0). Initially, the slides were inserted in a pressure cooker with a staining dish

containing the citrate buffer and were incubated for 8 min at maximum power, then left to cool down for 13 min at room temperature. Shortly after, the sections were rinsed in TBST before continuing with the immunostaining. As the supplier suggested, no antigen retrieval pretreatment was undertaken for the anti-α-SMA staining.

2.4.3.2 Primary antibody dilutions:

The optimal primary antibody concentrations were determined using a series of dilutions. Anti-CD68-, anti-CD34- and anti-α-SMA-antibodies were diluted 1: 400, 1: 200 and 1: 500, respectively.

2.4.3.3 CD68-, CD34- and α-smooth muscle cell actin staining:

The microscope slides were taken out of the TBST solution (for CD68 and CD34) or distilled water (for α-SMA) and were blotted dry with a filter paper. Using a hydrophobic PAP pen, the sections were circled and were incubated with the protein blocking medium for 10-20 min. Next, the diluted primary antibody solutions were added on the respective slides and were incubated at room temperature for 45 min, then thoroughly washed with TBST. The sections were next incubated for 10 min with the respective biotinylated, secondary antibodies and were washed with TBST again. The Streptavidin-HRP-conjugate was added and incubated for 10 min. After a short washing step with TBST, the AEC-chromogen solution (50 µl AEC substrate buffer, 50 µl AEC concentrate, 50 µl 0.6 % H_2O_2 in 1 mL Aqua destillata) was added for 5-15 min (under light microscopy control) until the desired color precipitation was reached. The slides were subsequently washed with Aqua destillata and counterstained with Gills hematoxylin for 20 s. The color tone was then intensified ("blueneed") by a final washing step for 10 min under running tap water before being mounted with Aquatex ® and cover slips.

2.4.4 Microscopy, image digitization and processing

Table 5. Material for microscopy and digital image processing

Material	Manufacturer
Microscope HS - BZ9000 (Biorevo)	Keyence, Osaka, Japan
Microscope Objectives - CFI Plan Apochromat Lambda Series (2 x-, 10 x-Plan Apo)	Nikon, Düsseldorf, Germany

BZ H2AE-Analysis software
    - BZ-II Viewer
    -BZ-II Analyzer v. 2.1
	Keyence, Osaka, Japan

Precision T3500 Tower-Workstation, W3503 Intel ® Xeon ® 2.4 GHz Dual Core Processor, 64 - bit system, Windows 7 Professional	Dell, Frankfurt am Main, Germany
Adobe ® Bridge ® CC 2017-v. 7.0.0.93 x 64 Adobe ® Photoshop CC 2017-v.1.1 x 64	Adobe Systems Incorporated, San Jose, USA
Image Composite Editor 2.0	Microsoft, Redmond/Washington, USA

Using the Continuous Image Capturing tool of the BZ-II Viewer software, individual images of each plaque section were acquired with high spatial accuracy and were stitched into a panorama image via the BZ-II Analyzer. Using Adobe Camera Raw and the "Lens Correction" tool, the vignette phenomenon was removed from every image and the vignette-free images were reconstructed to a panorama image using Microsoft's Image Composite Editor Software. The exported image was resized to the dimensions of the original panorama image using Adobe ® Photoshop. Particles that would interfere with the analysis tools (e.g. dirt particles, trapped air bubbles, slide edges etc.) were removed via Adobe Photoshop. The morphology of the tissue sections remained unaffected throughout the whole modification process and the final panorama images were controlled for similarity with the originals before subsequent analysis. Polarized light microscopy of the picro-sirius red images was conducted at the institution of Ipath Berlin – Core Unit Immunopathology for Experimental Models of the Charité – Universitätsmedizin Berlin with the kind assistance and support of PD Dr. rer. nat. Anja Kühl.

2.4.5 Image analysis:

Prior to image analysis, it was tested whether the first and the last section of each stack showed high morphological similarity. Only then was the stack considered for further investigation (see Figure 3). Image analysis was then performed using both quantitative (Image J/Fiji v.1.8.0[201]) and semi-quantitative (observational evaluation) methods, as detailed below:

Quantification of alcian blue- and picro-sirius red-positive area:

1. Image file opening (Alcian blue- and picro-sirius red-stained sections), 2. Background subtraction, 3. Identification of alcian blue positive area using color thresholding values from three independent observers, 4. Area measurement, 5. Plaque area measurement, 6. Procedure repetition for all images (applies for all further described quantification methods), 7. Calculation of the alcian blue-/picro-sirius red-positive area as percentage of the whole plaque area.

Quantification of mean- and minimum FC-thickness:

1. Image file opening (Movat- and alcian blue-stained sections), 2. Marking of the FC by setting pairs of points using the "Multi-point tool", 3. Retrieval of the x and y coordinates for each point, 4. Measurement of the FC thickness between the paired points according to the Euclidean distance formula $d((x_1, y_1), (x_2, y_2)) = \sqrt[2]{(x_1 - x_2)^2 + (y_1 - y_2)^2}$, where (x_1, y_1) and (x_2, y_2) are the coordinates of the paired points, 5. Identification of the minimum FC thickness and calculation of the mean FC thickness (individually for each stain), 6. Calculation of the mean values from step 5.

Quantification of NC size:

1. Image file opening (Movat- and alcian blue-stained sections), 2. Specification and measurement of the necrotic core areas, 3. Plaque area measurement (as described above), 4. Calculation of the necrotic areas as a percentage of the whole plaque area (repeated individually for each staining), 5. Calculation of the mean necrotic core size value.

Quantification of total and FC-specific CD68- as well as FC-specific α-SMA-positive area:

The FC areas were isolated and measured (μm^2) prior to quantification. A similar procedure to the one used for the quantification of alcian blue-/picro-sirius red- positive areas was followed.

Semi-quantitative comparison of alcian blue staining intensity with anti-CD68-, anti-α-SMA- and Movat pentachrome (identification of calcification sites) staining results:

The alcian blue staining intensity was correlated using an ordinal scale (+: non-existent/very weak, ++: weak, +++: mild, ++++: strong, or "unclear"). For this purpose, three independent reviewers filled pre-formed Excel sheets.

Quantification of anti-CD34 immunostaining:

The amount of anti-CD34 positively stained neovessels was determined via the Trainable Weka Segmentation plugin of Fiji. The number of neovessels was then related to the plaque area that was measured after removal of tunica media rests. Only the anti-CD34-positive regions with a vascular-like morphology were identified as neovessels.

2.5 mRNA expression analysis

2.5.1 RNA extraction

Table 6. Material used for RNA extraction

Material	Supplier
Eppendorf Safe-Lock Tubes, 1.5 mL/2 mL	Eppendorf, Hamburg, Germany
Eppendorf research ® plus pipettes, single channel, 10-100/20-200/100-1000 µL	Eppendorf, Hamburg, Germany
SafeSeal Tips Professional, sterile, 10/20/100/200/1000 µl	Biozym Scientific, Hessisch Oldendorf, Germany
Sterican ® Hypodermic needles, 0.4 x 20 mm	B. Braun, Hessen, Germany
Ethanol absolute, J.T. Baker ®	Avantor, Pennsylvania, USA
Xylenes, Baker Analyzed ®	Avantor, Pennsylvania, USA
Thermomixer 5436 and 5437, Eppendorf ®	Eppendorf, Hamburg, Germany
Eppendorf ® Microcentrifuge 541R	Eppendorf, Hamburg, Germany

RNeasy FFPE Kit (50)
  - 50x RNeasy MinElute ® spin columns
  - 100x collection tubes (1.5 mL/2 mL)
  - 45 mL buffer RBC
  - 15 mL buffer PKD
  - 1.25 mL proteinase K
  - 1500 units RNase-free DNase I
  - 2 mL DNase booster buffer
  - 11 mL buffer RPE (concentrate)
  - 10 mL RNase-free water
	Qiagen, Hilden, Germany

NanoDrop™ 2000/2000c Spectrophotometer	Thermo Fischer Scientific, Waltham, USA

The RNeasy FFPE Kit was chosen for the RNA extraction from formalin-fixed paraffin embedded tissue (FFPE)[202-204]. Three adjacent 10 µm-thick tissue sections were retrieved and pooled for RNA extraction. The sections were deparaffinized via xylene, both at room temperature and at 56°C, before rinsing with 100 % ethanol twice. After centrifugation and discarding of the supernatant, the deparaffinized tissue sections were air dried for 1 h. Following a double protein digestion via the action of 150 µl PKD buffer and 10 µl of proteinase K at 56°C and 80°C respectively, the

solution was centrifuged and the supernatant was treated for 15 min at room temperature with a DNase-containing buffer solution for DNA degradation. After the addition of an RBC buffer and the admixture with 100 % ethanol, the lysate was filtered using RNease MinElute spin columns via centrifugation at 13,200 rpm. The same procedure was repeated using RPE buffer solution. Each time, the collection tubes with the flow troughs were discarded and replaced by new ones. Finally, RNase-free water was added in the spin column membranes and the eluted RNA was collected after a short centrifugation step. The RNA concentration and purity ratios were measured via the NanoDrop 2000/2000c Spectrophotometer and the samples were stored at - 80°C until further use.

2.5.2 RNA microarray

The mRNA microarray analysis (experimental procedure and raw data retrieval) was performed by OakLabs (Henningsdorf, Germany) on the 16 above-mentioned 16 samples using ArrayXS Human FFPE that was specifically developed for RNA acquired from FFPE tissue.

2.5.2.1 RNA quality control:

The quality and quantity of the extracted RNA was evaluated using the 2100 Bioanalyzer (Agilent Technologies, Santa Clara, USA). The Agilent 2100 Bioanalyzer calculates the RNA integrity value and displays the individual electropherograms. RNA concentration, purity and integrity measurements were documented.

2.5.2.2 Labelling, hybridization and microarray scanning:

The Transplex Whole Transcriptome Amplification Kit (Sigma Aldrich, St. Louis, USA) was used to generate complementary DNA (cDNA). Briefly, the total amount of extracted RNA from each sample was initially reverse transcribed using primers composed of random 3´-ends and universal 5´-ends, and subsequently amplified by polymerase chain reaction with a universal primer to produce a whole transcriptome amplification. The cDNA yield was measured with the Nanodrop 2000 spectrophotometer. Next, fluorescent cDNA was generated using the SureTag DNA Labeling Kit (Agilent Technologies, Santa Clara, USA), with cyanine 3-deoxyuridine triphosphate being incorporated in the nucleotide sequence. For the labelling reaction, 1.8 µg of cDNA was used from each sample. The labelled DNA was purified (by size exclusion principle) using the purification columns of the kit and the cyanine-3 incorporation rate was measured spectrophotometrically. The subsequent hybridization step was carried out using the Agilent Gene Expression Hybridization Kit (Agilent Technologies, Santa Clara, USA), SurePrint G3 Custom GE 8 x 60 K microarrays

(Agilent Technologies, Santa Clara, USA), an Agilent G2534A Hybridization Chamber (Agilent Technologies, Santa Clara, USA) and an Agilent G2545A Hybridization Oven (Agilent Technologies, Santa Clara, USA). After a short washing step, the fluorescent signals on the microarrays were detected and scanned with the SureScan Microarray Scanner (Agilent Technologies, Santa Clara, USA). The raw data were provided as Excel files.

2.5.2.3 TIFF processing and mRNA expression analysis strategy:

The Agilent Feature Extraction Software v.11 (Agilent Technologies, Santa Clara, USA) was used for raw image file-based data extraction.

Prior to differential expression analysis, a wide literature-[29-32,38-41,47,205-211] and database-dependent[31,216] approach was undertaken, and a list with known PG core proteins as well as enzymes involved in GAG biosynthesis and degradation was created. The final register included 148 entities, taking mRNA splice variants into account.

Using RStudio[213] and the R packages 'limma'[214], 'vsn'[215], 'ggplot2'[216] and 'EnhancedVolcano'[217], microarray preprocessing, quality control and subsequent differential expression analysis were performed. The R code can be found together with the session information in Chapter 2.5.2.4.1. Correlation analysis was performed via GraphPad Prism v.7.03. Correction for multiple hypothesis testing was implemented when necessary. Results with FDR-adjusted p values (q-values) < 0.05 were considered a discovery. The online platform ClustVis was accessed in order to display the correlation analysis results between the different mRNA signal intensities via heatmapping[218].

Sample size estimation was performed according to a permutation-based methodology[219] that was implemented via the R package 'samr'[220]. The R code can be found together with the session information in Chapter 2.5.2.4.2.

2.5.2.4 R code

2.5.2.4.1 R code: Comparison of HV versus LV

```
> library(limma)
> library(openxlsx)
> library(vsn)
> library(ggplot2)
> library(EnhancedVolcano)
> library(ggpubr)
> library(tidyr)
```

```
> sessionInfo()

R version 3.6.3 (2020-02-29)

Platform: x86_64-w64-mingw32/x64 (64-bit)

Running under: Windows 10 x64 (build 18363)

Matrix products: default

locale:
[1] LC_COLLATE=German_Germany.1252  LC_CTYPE=German_Germany.1252    LC_MON
ETARY=German_Germany.1252
[4] LC_NUMERIC=C                LC_TIME=German_Germany.1252

attached base packages:
[1] parallel  stats    graphics grDevices utils    datasets  methods  base

other attached packages:
 [1] tidyr_1.1.1        ggpubr_0.4.0       EnhancedVolcano_1.2.0 ggrepel_0.8.2
 [5] ggplot2_3.3.2      vsn_3.52.0         Biobase_2.44.0     BiocGenerics_0.30.0
 [9] openxlsx_4.1.5     limma_3.40.6

loaded via a namespace (and not attached):
 [1] tidyselect_1.1.0   purrr_0.3.4        haven_2.3.1        lattice_0.20-38
 [5] carData_3.0-4      colorspace_1.4-1   vctrs_0.3.2        generics_0.0.2
 [9] rlang_0.4.7        pillar_1.4.6       foreign_0.8-75     glue_1.4.1
[13] withr_2.2.0        affy_1.62.0        readxl_1.3.1       affyio_1.54.0
[17] lifecycle_0.2.0    zlibbioc_1.30.0    munsell_0.5.0      ggsignif_0.6.0
[21] gtable_0.3.0       cellranger_1.1.0   zip_2.0.4          rio_0.5.16
[25] forcats_0.5.0      curl_4.3           preprocessCore_1.46.0 broom_0.7.0
[29] Rcpp_1.0.5         scales_1.1.1       backports_1.1.7    BiocManager_1.30.10
[33] abind_1.4-5        hms_0.5.3          stringi_1.4.6      rstatix_0.6.0
[37] dplyr_1.0.1        grid_3.6.3         tools_3.6.3        magrittr_1.5
[41] tibble_3.0.3       crayon_1.3.4       car_3.0-9          pkgconfig_2.0.3
[45] ellipsis_0.3.1     data.table_1.13.0  rstudioapi_0.11    R6_2.4.1
[49] compiler_3.6.3
 > setwd("F:/3A. Array Ergebnisse 15 OLD FIRST SAMPLES/limma")
> memory.limit(size=50000)
> targetsHVLV <- readTargets("TargetsHVLV.txt")
> targetsHVLV <- readTargets("TargetsHVLV.txt", row.names="Name") #OR
```

```
> View(targetsHVLV)
> intensities <- read.maimages(targetsHVLV, source="agilent.mean",path=NULL,ext=NULL,na
mes=targetsHVLV$Name,columns=NULL, other.columns=list("Vulnerability_Class", "Chromo
somal_Location", "gIsWellAboveBG","gProcessedSignal","gBGMeanSignal","gBGMedianSign
al", "gMeanSignal", "gMedianSignal", "gBGSubSignal","gIsPosAndSignif", "NCBI_Entrez_ID"
, "Gene_Type", "Ensembl_Gene_ID", "EC_Number", "UniGene_ID", "UniProt_Accession", "Bi
ocarta_Pathway_Name", "GO_ID", "KEGG_Gene_ID", "KEGG_Pathway_ID", "KEGG_Pathw
ay_Title", "Reactome_ID", "Reactome_Pathway_ID", "PositionX", "PositionY"),annotation=NU
LL,wt.fun=NULL,verbose=TRUE,quote=NULL, green.only=TRUE, na.strings="NA") ##--> E:
gMeanSignal and Eb:gBGMedianSignal
> names(intensities$targets)
> names(intensities$genes)
> names(intensities$other)
> ### Background correction (normexp) and normalization (CLN):
> normexp50BCintensities <- backgroundCorrect(intensities, method="normexp", offset=50, pri
nter=NULL, normexp.method="saddle", verbose=TRUE)
> CLNnormexp50BCintensities <- normalizeBetweenArrays(normexp50BCintensities, method=
"cyclicloess", targets=NULL, cyclic.method="fast", weights=NULL, span=0.7, iterations=3)
> ### Creation of an appropriate design matrix:
> HVLV <- factor(targetsHVLV$Vulnerability_Class, levels=c("HV","LV"))
> designHVLV <- model.matrix(~0+HVLV)
> colnames(designHVLV) <- c("HV", "LV")
> rownames(designHVLV) <- c("P1", "P3", "P7", "P8", "P9", "P14", "P15", "P18","P20","P25",
"P26", "P27", "P28", "P33", "P34")
> ### Array Quality Weight calculation based on all genes:
> AWCLNnormexp50BCintensitiesHVLV <- arrayWeights(CLNnormexp50BCintensities, desig
n=designHVLV, method="reml") # design NOT default (comparison to the other arrays of the gr
oup)
> barplot(AWCLNnormexp50BCintensitiesHVLV, xlab="Arrays", ylab="Weight", col="coral2"
, las=2, ylim=c(0,6), family="serif", names.arg=CLNnormexp50BCintensities$targets$Name) +
abline(h=1, lwd=1, lty=2)
numeric(0)
> ### Summarization process: Functions for handling of within array duplicate spots (Averaging
versus Duplicate spot strength correlation via linear models):
```

```
> # Averaging
> setwd("F:/3A. Array Ergebnisse 15 OLD FIRST SAMPLES/limma")
> CLNnormexp50BCintensities <- avereps.EList(CLNnormexp50BCintensities, ID=CLNnorme
xp50BCintensities$genes$SystematicName)
> ### Filtering (removal of control spots, removal of all genes with a IsWellAboveBG=0 AND r
emoval of all genes with a RefSeq NR_, XR_ and XM_) unexpressed probes:
> ### + removal of columns no longer needed and creation of the final file "eset":
> noXMXRNRCLNnormexp50BCintensities <- CLNnormexp50BCintensities[!grepl("XM_|NR
_|XR_",CLNnormexp50BCintensities$genes$SystematicName),]
> controlnoXMXRNRCLNnormexp50BCintensities <- noXMXRNRCLNnormexp50BCintensiti
es$genes$ControlType==1L
> noSymbolnoXMXRNRCLNnormexp50BCintensities <- is.na(noXMXRNRCLNnormexp50B
Cintensities$genes$GeneName)
> IsExprnoXMXRNRCLNnormexp50BCintensities <- rowSums(noXMXRNRCLNnormexp50B
Cintensities$other$gIsWellAboveBG > 0) >=8 # do not forget to change the number of arrays he
re depending on the design matrix
> esetCLN <- noXMXRNRCLNnormexp50BCintensities[!controlnoXMXRNRCLNnormexp50
BCintensities&!noSymbolnoXMXRNRCLNnormexp50BCintensities&IsExprnoXMXRNRCLN
normexp50BCintensities,]
> dim(esetCLN)
> ### Change the gene names manually after writing the files into the folder and reread the file
within R:
> setwd("F:/3A. Array Ergebnisse 15 OLD FIRST SAMPLES/limma/Text Files of BC Normaliz
ed and Filtered Data")
> write.xlsx(esetCLN$genes, file="esetCLNgenesHVLV.xlsx", colNames=TRUE, borders="col
umns")
> esetCLNgenes <- read.xlsx("esetCLNgenesHVLV.xlsx")
> esetCLN$genes$GeneName <- esetCLNgenes$GeneName
> setwd("F:/3A. Array Ergebnisse 15 OLD FIRST SAMPLES/limma")
> ### Fitting of linear model and differential expression analysis between the different groups:
> ## with weights
> setwd("F:/3A. Array Ergebnisse 15 OLD FIRST SAMPLES/limma/13. Model fitting and DE/
HV vs. LV with weights")
```

```
> fitesetCLNHVLVls <- lmFit(esetCLN, design=designHVLV, weights=AWCLNnormexp50BC
intensitiesHVLV, method="ls")
> contrast.matrixHVLV <- makeContrasts(HV-LV, levels=c("HV","LV"))
> ContrastCLNHVLVls <- contrasts.fit(fitesetCLNHVLVls, contrasts=contrast.matrixHVLV, co
efficients=NULL)
> DEGzCLNHVLVlsNoRobust <- eBayes(ContrastCLNHVLVls, proportion=0.01, stdev.coef.li
m = c(0.1,4), trend=TRUE, robust=FALSE)
> # Summary table of all/ top-ranked genes from a linear model fit for all genes OR for PG-/GA
G-specific:
> setwd("F:/3A. Array Ergebnisse 15 OLD FIRST SAMPLES/limma/13. Model fitting and DE/
HV vs. LV with weights")
> OverviewDEGzCLNHVLVlsNoRobust <- topTable(DEGzCLNHVLVlsNoRobust, coef=1, nu
mber=Inf, genelist=DEGzCLNHVLVlsNoRobust$genes, adjust.method="BH", p.value=1, sort.b
y="p", resort.by=NULL, confint=TRUE)
> OverviewDEGzCLNHVLVlsNoRobustPGGAG <- topTable(DEGzCLNHVLVlsNoRobust[c(
"NM_001711.4","NM_004370.5","NM_001199080.1","NM_178232.2","NM_001126336.2","N
M_002727.2","NM_002023.4","NM_030582.3","NM_001291860.1","NM_005529.6","NM_01
4654.3","NM_198576.3","NM_001195683.1","NM_002999.3","NM_002725.3","NM_0011344
34.1","NM_001244950.1","NM_001193335.1","NM_001135.3","NM_001146254.1","NM_001
920.3","NM_001024629.2","NM_003873.5","NM_001024628.2","NM_002998.3","NM_02300
2.2","NM_001852.3","NM_002081.2","NM_198427.1","NM_021948.4","NM_001127708.1","
NM_005014.2","NM_001197295.1","NM_001135604.1","NM_004386.2","NM_001267.2","N
M_001897.4","NM_001855.4","NM_021817.2","NM_005708.3","NM_002345.3","NM_00120
2557.1","NM_001001392.1","NM_022567.2","NM_001243245.2","NM_001448.2","NM_0140
57.3","NM_001258210.1","NM_152742.1","NM_001206838.1","NM_001166103.1","NM_138
481.1","NM_001164617.1","NM_016247.3","NM_004598.3","NM_001146289.1","NM_00100
6946.1","NM_001282368.1","NM_004466.5","NM_014359.3","NM_001884.3","NM_007035.3
","NM_004950.4","NM_001851.4","NM_006093.3","NM_001040159.1","NM_022166.3","NM
_022167.3","NM_007255.2","NM_080605.3","NM_018644.3","NM_014864.3","NM_004273.4
","NM_004854.4","NM_014918.4","NM_175856.4","NM_019015.2","NM_001284295.1","NM
_001195731.1","NM_018590.4","NM_001080976.1","NM_032160.2","NM_019886.3","NM_0
31422.5","NM_001173982.1","NM_001243794.1","NM_152889.2","NM_130468.3","NM_005
715.2","NM_015892.4","NM_001270765.1","NM_004455.2","NM_001033025.2","NM_00144
0.3","NM_000127.2","NM_000401.3","NM_001543.4","NM_003635.3","NM_004784.2","NM
```

_022569.1","NM_015554.1","NM_001134492.1","NM_004807.2","NM_001077188.1","NM_1
53456.3","NM_005114.2","NM_006043.1","NM_006041.1","NM_153612.3","NM_001009606.
3","NM_001297436.1","NM_005328.2","NM_001199280.1","NM_138612.2","NM_003654.5",
"NM_004267.4","NM_024533.4","NM_021615.4","NM_006577.5","NM_014256.3","NM_030
765.2","NM_145236.2","NM_003778.3","NM_212543.1","NM_198709.2","NM_000046.3","N
M_001128204.1","NM_001161841.1","NM_198596.2","NM_014960.4","NM_001098540.2","
NM_000199.3","NM_152419.2","NM_000263.3","NM_033159.3","NM_003773.4","NM_0012
00029.1","NM_000404.2","NM_000512.4","NM_000202.6","NM_006123.4","NM_000203.4","
NM_000520.4","NM_000521.3","NM_001284290.1","NM_000181.3","NM_002076.3","NM_1
98150.2"),], coef=1, number=Inf, adjust.method="BH", p.value=1, sort.by="p", resort.by=NULL
, confint=TRUE)

> ### Volcano plots of all genes (without names/identifiers):

> setwd("F:/3A. Array Ergebnisse 15 OLD FIRST SAMPLES/limma/13. Model fitting and DE/
HV vs. LV with weights")

> EnhancedVolcano(OverviewDEGzCLNHVLVlsNoRobust, lab=NA, x='logFC', y='adj.P.Val',
xlim=c(min(OverviewDEGzCLNHVLVlsNoRobust[,11], na.rm=TRUE), max(OverviewDEGzC
LNHVLVlsNoRobust[,11], na.rm=TRUE)), ylim =c(0, max(-log10(OverviewDEGzCLNHVLVl
sNoRobust[,17]), na.rm=TRUE) + 1), xlab = bquote(~Log[2]~ "fold change (HV-LV)"), ylab =
bquote(~-Log[10]~(FDR)), axisLabSize = 10, pCutoff = 0.05, FCcutoff = 1.0, transcriptPointSiz
e = 0.9, transcriptLabSize = 2.4, col=c("grey30", "royalblue", "forestgreen", "red2"), colAlpha =
1/3, legend = c("q value > 0.05 and \n |log2FC| < 1", "q value > 0.05 and \n |log2FC| > 1", "q val
ue < 0.05 and \n |log2FC| < 1", "q value < 0.05 and \n |log2FC| > 1"), legendPosition = "bottom",
legendLabSize = 10, legendIconSize = 3.0, cutoffLineType = "dashed",cutoffLineWidth= 0.3, cu
toffLineCol="gray35", gridlines.major=FALSE, gridlines.minor=FALSE, border="partial", title
=NULL, subtitle=NULL, caption=NULL, shape=16)

> ### Volcano plots of PGs and GAGs with weights:

> setwd("F:/3A. Array Ergebnisse 15 OLD FIRST SAMPLES/limma/13. Model fitting and DE/
HV vs. LV with weights")

> EnhancedVolcano(OverviewDEGzCLNHVLVlsNoRobustPGGAG, lab=OverviewDEGzCLN
HVLVlsNoRobustPGGAG$GeneName, x='logFC', y='adj.P.Val', xlim=c(min(OverviewDEGzC
LNHVLVlsNoRobustPGGAG[,11], na.rm=TRUE), max(OverviewDEGzCLNHVLVlsNoRobus
tPGGAG[,11], na.rm=TRUE)), ylim =c(0, max(-log10(OverviewDEGzCLNHVLVlsNoRobustP
GGAG[,17]), na.rm=TRUE) + 1), xlab = bquote(~Log[2]~ "fold change (HV-LV)"), ylab = bquo
te(~-Log[10]~(FDR)), axisLabSize = 10, pCutoff = 0.05, FCcutoff = 1.0, transcriptPointSize = 2.

0, transcriptLabSize = 3.0, col=c("grey70", "royalblue", "forestgreen", "red2"), colAlpha = 4/5, l
egend = c("q value > 0.05 and \n |log2FC| < 1", "q value > 0.05 and \n |log2FC| > 1", "q value <
0.05 and \n |log2FC| < 1", "q value < 0.05 and \n |log2FC| > 1"), legendPosition = "bottom", lege
ndLabSize = 10, legendIconSize = 3.0, cutoffLineType = "dashed", cutoffLineWidth= 0.3, cutoff
LineCol="gray35", gridlines.major=FALSE, gridlines.minor=FALSE, border="partial", shape=1
6, title=NULL, subtitle=NULL, caption=NULL, drawConnectors=TRUE, widthConnectors=0.2,
colConnectors='gray30', boxedlabels=FALSE, selectLab=c("IMPG1","CHSY3","HAPLN1","E
XTL2","CHPF2v1","CHADL","DSEL","CHST10","HAS3v3","ASPN","PODNL1","CHST12",
"HS6ST3","NRP1v2","B3GNT3","NDST3","ARSK","SRGN","HEXA"))

The code that was used for the comparisons of HI vs. LI groups is identical to this code, except
for the different grouping of the microarrays and the difference in the target files, contrast
matrices and design matrix.

2.5.2.4.2 R code: Sample size estimation

```
> ### Load required packages:
> library(samr)
> library(openxlsx)
> library(limma)
> library(dplyr)
> sessionInfo()
R version 3.6.3 (2020-02-29)
Platform: x86_64-w64-mingw32/x64 (64-bit)
Running under: Windows 10 x64 (build 18363)
Matrix products: default
locale:
[1] LC_COLLATE=German_Germany.1252  LC_CTYPE=German_Germany.1252    LC_MON
ETARY=German_Germany.1252
[4] LC_NUMERIC=C              LC_TIME=German_Germany.1252
attached base packages:
[1] stats    graphics grDevices utils    datasets methods  base
other attached packages:
[1] dplyr_1.0.1   limma_3.40.6   openxlsx_4.1.5 samr_3.0
loaded via a namespace (and not attached):
```

[1] zip_2.0.4   Rcpp_1.0.5   pillar_1.4.6   compiler_3.6.3   later_1.1.0.1

 [6] tools_3.6.3   digest_0.6.25   jsonlite_1.7.0   lifecycle_0.2.0   tibble_3.0.3

[11] pkgconfig_2.0.3   rlang_0.4.7   shiny_1.5.0   rstudioapi_0.11   fastmap_1.0.1

[16] generics_0.0.2   fs_1.5.0   vctrs_0.3.2   shinyFiles_0.8.0   tidyselect_1.1.0

[21] glue_1.4.1   impute_1.58.0   R6_2.4.1   GSA_1.03.1   purrr_0.3.4

[26] magrittr_1.5   promises_1.1.1   ellipsis_0.3.1   htmltools_0.5.0   matrixStats_0.56.0

[31] mime_0.9   xtable_1.8-4   httpuv_1.5.4   stringi_1.4.6   crayon_1.3.4

> # Increase memory limit:

> memory.limit(size=50000)

> ### Set the working directory:

> setwd("F:/3A. Array Ergebnisse 15 OLD FIRST SAMPLES/SAM")

> ### Reading the data/objects (target file, expression set file):

> targetsHVLV <- readTargets("TargetsHVLV.txt")

> targetsHVLV <- readTargets("TargetsHVLV.txt", row.names="Name")

> intensities <- read.maimages(targetsHVLV, source="agilent.mean",path=NULL,ext=NULL,na
mes=targetsHVLV$Name,columns=NULL, other.columns=list("Vulnerability_Class", "Chromo
somal_Location", "gIsWellAboveBG","gProcessedSignal","gBGMeanSignal","gBGMedianSign
al", "gMeanSignal", "gMedianSignal", "gBGSubSignal","gIsPosAndSignif", "NCBI_Entrez_ID"
, "Gene_Type", "Ensembl_Gene_ID", "EC_Number", "UniGene_ID", "UniProt_Accession", "Bi
ocarta_Pathway_Name", "GO_ID", "KEGG_Gene_ID", "KEGG_Pathway_ID", "KEGG_Pathw
ay_Title", "Reactome_ID", "Reactome_Pathway_ID", "PositionX", "PositionY"),annotation=NU
LL,wt.fun=NULL,verbose=TRUE,quote=NULL, green.only=TRUE, na.strings="NA") ##--> E:
gMeanSignal and Eb:gBGMedianSignal

> ### Background correction (normexp) and normalization (CLN):

> normexp50BCintensities <- backgroundCorrect(intensities, method="normexp", offset=50, pri
nter=NULL, normexp.method="saddle", verbose=TRUE)

> CLNnormexp50BCintensities <- normalizeBetweenArrays(normexp50BCintensities, method=
"cyclicloess", targets=NULL, cyclic.method="fast", weights=NULL, span=0.7, iterations=3)

> ### Creation of an appropriate design matrix:

> HVLV <- factor(targetsHVLV$Vulnerability_Class, levels=c("HV","LV"))

> designHVLV <- model.matrix(~0+HVLV)

> colnames(designHVLV) <- c("HV", "LV")

> rownames(designHVLV) <- c("P1", "P3", "P7", "P8", "P9", "P14", "P15", "P18","P20","P25",
"P26", "P27", "P28", "P33", "P34")

> ### Filtering (removal of control spots, removal of all genes with a IsWellAboveBG=0 AND removal of all genes with a RefSeq NR_, XR_ and XM_) unexpressed probes:

> ### + removal of columns no longer needed and creation of the final file "eset":

> noXMXRNRCLNnormexp50BCintensities <- CLNnormexp50BCintensities[!grepl("XM_|NR_|XR_",CLNnormexp50BCintensities$genes$SystematicName),]

> controlnoXMXRNRCLNnormexp50BCintensities <- noXMXRNRCLNnormexp50BCintensities$genes$ControlType==1L

> noSymbolnoXMXRNRCLNnormexp50BCintensities <- is.na(noXMXRNRCLNnormexp50BCintensities$genes$GeneName)

> IsExprnoXMXRNRCLNnormexp50BCintensities <- rowSums(noXMXRNRCLNnormexp50BCintensities$other$gIsWellAboveBG > 0) >=8

> esetCLN <- noXMXRNRCLNnormexp50BCintensities[!controlnoXMXRNRCLNnormexp50BCintensities&!noSymbolnoXMXRNRCLNnormexp50BCintensities&IsExprnoXMXRNRCLNnormexp50BCintensities,]

> ### Change the gene names manually after writing the files into the folder and reread the file within R:

> setwd("F:/3A. Array Ergebnisse 15 OLD FIRST SAMPLES/SAM/Renaming_SpecialAnnotation")

> write.xlsx(esetCLN$genes, file="esetCLNgenesHVLV.xlsx", colNames=TRUE, borders="columns")

> esetCLNgenes <- read.xlsx("esetCLNgenesHVLV.xlsx")

> esetCLN$genes$GeneName <- esetCLNgenes$GeneName

> setwd("E:/3A. Array Ergebnisse 15 OLD FIRST SAMPLES/SAM")

> ### Procedure prior to implementation of the following code:

> # 1. Perform background correction, normalization, summarization and filtering and create Excel files containing following columns: "GeneName", "SystematicName" and the columns containing the final gene expression values (see above)

> # 2. Especially for the PG/GAG-specific probes replace the GeneNames with those to depict the isoforms (see "For renaming the gene names of the upper files.txt")

> # 3. Create the subset (after transofrming the EList into a matrix via as.matrix and adding the column GeneName from the EList that is going to be on position 1) via ...PGGAG <- subset(...matrix,rownames(...matrix)%in%c(PGGAG--> see end of page!))

> # Code: ...matrix <- as.matrix(esetCLN); ...matrix <- cbind(...matrix,...$genes$GeneName,...$genes$SystematicName); colnames(...matrix)[11] <- "GeneName" ; colnames(...matrix)[12] <- "S

ystematicName"; ...matrix <-...matrix[,c("GeneName","SystematicName","P7","P8","P15","P18","P25","P26","P27","P28","P33","P34")]

> ### Read the files for the comparison groups and create the matrices and vectors prior to SAM analysis:

> setwd("F:/3A. Array Ergebnisse 15 OLD FIRST SAMPLES/SAM/HV vs. LV")

> HVLVvector <- c(2,2,1,2,2,2,2,2,2,1,1,1,2,2,2)

> library(readxl)

> HVvsLVCLNallforR <- read_excel("HVvsLVCLNallforR.xlsx")

> HVvsLVCLNall <- HVvsLVCLNallforR[,-c(1,2)]

> HVvsLVCLNall <- as.matrix(HVvsLVCLNall)

> HVvsLVCLNPGGAGforR <- read_excel("HVvsLVCLNPGGAGforR.xlsx",

+   col_types = c("text", "text", "numeric",

+   "numeric", "numeric", "numeric", "numeric", "numeric",

+   "numeric", "numeric", "numeric", "numeric", "numeric",

+   "numeric", "numeric", "numeric", "numeric"))

> HVvsLVCLNPGGAG <- HVvsLVCLNPGGAGforR[,-c(1,2)]

> HVvsLVCLNPGGAG <- as.matrix(HVvsLVCLNPGGAG)

> ### Significance analysis of microarrays:

> # HV vs. LV

> ResultsHVLVCLNPGGAG <- SAM(x=HVvsLVCLNPGGAG, y=HVLVvector, censoring.status=NULL, genenames=HVvsLVCLNPGGAGforR$GeneName, geneid=HVvsLVCLNPGGAGforR$SystematicName,resp.type=c("Two class unpaired"),nperms=3000, testStatistic="standard", knn.neighbors = 10, random.seed=696389, logged2=TRUE, fdr.output=0.05)

> ## Compute delta table for SAM analysis:

> # HV vs. LV

> DeltaTableHVLVCLNPGGAG <- samr.compute.delta.table(ResultsHVLVCLNPGGAG$samr.obj, min.foldchange = 1.0)

> myDeltaHVLVCLNPGGAG <- min(DeltaTableHVLVCLNPGGAG[which(DeltaTableHVLVCLNPGGAG[,"median FDR"]<0.05), "delta"])

> ## Estimate the miss rate table for the SAM analysis:

> # HV vs. LV:

> MissRateTableHVLVCLNPGGAG <- samr.missrate(ResultsHVLVCLNPGGAG$samr.obj, myDeltaHVLVCLNPGGAG, DeltaTableHVLVCLNPGGAG)

> ## Assess sample size for a SAM analysis (assess current sample size AND the effect of doubling sample size) + make a plot of the results:

> # HV vs. LV

> SampleSizeHVLVCLNPGGAG <- samr.assess.samplesize(ResultsHVLVCLNPGGAG$samr.obj, data=list(x=HVvsLVCLNPGGAG, y=HVLVvector, genenames=HVvsLVCLNPGGAGforR$GeneName, geneid=HVvsLVCLNPGGAGforR$SystematicName, logged2=TRUE), dif=1.0, samplesize.factors = c(1,2,4,5))

> par(family="serif", cex.main=1.2)

> samr.assess.samplesize.plot(SampleSizeHVLVCLNPGGAG, logx=TRUE)

The code that was used for the comparisons of HI vs. LI groups is identical to this code, except for the different grouping of the microarrays and the difference in the target files, contrast matrices and design matrix.

2.6 GAG quantification and disaccharide unit analysis

2.6.1 GAG extraction and quantification

Table 7. Material used for the glycosaminoglycan extraction

Material	Supplier
Xylenes, Baker Analyzed ®	Avantor, Pennsylvania, USA
Eppendorf Safe-Lock Tubes, 2 mL/5 mL	Eppendorf, Hamburg, Germany
Falcon™ Conical Tubes, 15 mL/50 mL	Fisher Scientific, Schwerte, Germany
Pasteur pipettes, PE-LD	Brand, Wertheim, Germany
Eppendorf research ® plus pipettes, single channel, 10-100/20-200/100-1000 µL epT.I.P.S. ® Standard, Eppendorf Quality ™	Eppendorf, Hamburg, Germany
pH portable meter, pH 330i pH electrode SenTix ® 51	WTW, Weilheim, Germany
Di-sodium hydrogen phosphate (Na$_2$HPO$_4$) stock solution (1 M): - 142 g di-sodium hydrogen phosphate (Na$_2$HPO$_4$) ad 1 L Aqua destillata *Sodium hydrogen phosphate (NaH$_2$PO$_4$) stock solution (1 M):* - 138 g sodium hydrogen phosphate (NaH$_2$PO$_4$) ad 1 L Aqua destillata *PBS stock solution (1 M, pH 6.5):* - 685 mL NaH$_2$PO$_4$ * H$_2$O - 315 mL Na$_2$HPO$_4$ * 2 H$_2$O	Merck, Darmstadt, Germany
L-Cysteine, BioUltra	Sigma Aldrich, St. Louis, USA
EDTA disodium salt dihydrate	Roth, Karlsruhe, Germany
Papain from papaya latex - buffered aqueous suspension, 2 x Crystallized, 100 mg, 100 U/mL	Sigma Aldrich, St. Louis, USA
Weighing paper MN226, 9 x 11.5 cm	Macherey Nagel, Düren, Germany
Sartorius Basic BA 110 Analytical Balance Sartorius Balance BP 610	Sartorius, Göttingen, Germany
Thermomixer 5436, Eppendorf ®	Eppendorf, Hamburg, Germany

Eppendorf ® Microcentrifuge 541R	Eppendorf, Hamburg, Germany
NaOH stock solution (0.5 M) 2 g sodium hydroxide pellets for analysis Emsure ® ad 100 mL Aqua destillata	Merck, Darmstadt, Germany

Sodium borohydride (NaBH₄) digestion buffer (1 M NaBH₄, 0.5 M NaOH):
     - 10 mL NaOH stock solution
     - 0.36 g NaBH₄ powder
	Sigma Aldrich, St. Louis, USA

HCl 1 N Titripur ®	Merck, Darmstadt, Germany
Trichloroacetic acid (TCA) solution (100 % w/v): 100 g TCA BioUltra ad 45.4 mL Aqua destillata	Sigma Aldrich, St. Louis, USA
Potassium Acetate (CH_3COOK) Extra Pure	Merck, Darmstadt, Germany
Ethanol absolute, J.T. Baker ®	Avantor, Pennsylvania, USA
Vivaspin ® 20 Ultrafiltration Spin Columns, MWCO 3000	Sartorius, Göttingen, Germany
Milli-Q ® Direct Water Purification System	Merck, Darmstadt, Germany

The GAG extraction method combined the protocols published by van Wijk et al.[221] and Ambrosius et al.[222]. Two 100 µm-thick slices from 20 selected tissue segments were deparaffinized. A 500 µl mixture containing the enzyme papain (10 U/mL) and a papain digestion buffer (50 mM PBS, pH 6.5, 2 mM cysteine and 2 mM EDTA) was added, and the tissue digestion was performed at 65°C overnight. The lysate was then centrifuged at 13,200 rpm for 5 min at 25°C, and the supernatant was collected and stored at 4°C. Next, the tissue pellet was digested at 37°C for 1 h using 250 µl of a 1M NaBH₄ digestion buffer. In the case of tissue remnants, an extra 200 µl NaBH₄ would be added for another 1 h. The supernatant of the papain digestion was added together with the solutions from the NaBH₄ digestion and was placed on ice. Subsequently, NaBH₄ was inactivated by HCl (1N) and the solutions were centrifuged for 5 min at 5,000 rpm at 4°C. The protein precipitation was carried out by using 100 % w/v TCA to a final concentration of 10 % for 30 min. The solutions were centrifuged at 13,200 rpm for 6 min at 4°C. The supernatants were then admixed with CH_3COOK and ethanol (5 g CH3COOK in 100 mL 99 % ethanol) and were left overnight at - 20°C for the GAGs to precipitate. After centrifugation at 5,000 rpm and 4°C, the supernatant was discarded and the precipitated GAGs were air dried. Subsequently,

Vivaspin ® 20 spin columns were used for the desalting process. The desalted GAGs were stored at - 20°C until further use.

2.6.2 GAG digestion and disaccharide unit analysis

The further processing and analysis of the extracted GAGs was performed by the AG Blanchard research group of the Institute of Laboratory Medicine, Clinical Chemistry and Pathobiochemistry, CVK. The procedures were performed according to the protocol of Takegawa et al.[223], which was modified by AG Blanchard for the project's purposes. Briefly, the extracted GAGs were enzymatically digested into their disaccharide unit constituents using a dual digestion with Chondroitinase ABC from Proteus vulgaris (Sigma Aldrich, St. Louis, USA) and Heparinase I, II and III from Flavobacterium heparinum (Sigma Aldrich, St. Louis, USA). Commercially acquired disaccharide units served as standards. After a vacuum drying step, the acquired samples and the standards were derivatized with the fluorophore 2-aminobenzamide, and purified using PD MiniTrap[TM] G-10 Sephadex preparation columns (GE Healthcare, Little Chalfont, UK). The subsequent 2-aminobenzamide-labeled disaccharide separation was performed on an Ultimate 3000 HPLC-System (Dionex, Idstein, USA) using a SeQuant zwitterionic type of hydrophilic interaction chromatography column (Merck, Darmstadt, Germany). The 2-aminobenzamide-labeled disaccharide units were detected UV-spectrometrically (λ_{ex}= 330 nm, λ_{em}= 420 nm) and the data analysis was performed using Chromeleon software v.6.8 SR12 (Dionex, Idstein, USA). Manual correction of the peak assignment was undertaken in cases of imprecise peak identification. The integrated peak areas were calculated and the values were summed up to a value that was set to 100 %. The disaccharide units from each sample were then reported and compared to each other as a relative amount (in percentage).

2.7 Statistical analysis, figure- and graph creation

The statistical analyses were performed using GraphPad Prism v.8.0.1 and RStudio. Figures were created via Adobe ® Illustrator- and Photoshop CC 2017 v.1.1 x 64. Continuous variables with normal distribution were expressed as mean ± standard deviation (SD). Continuous variables with non-normal distribution were expressed as median and 25th to 75th percentiles. Violin plots were used in order to visualize the distribution of the sample data. Correlation analyses were performed using Pearson's r and Spearman's ρ correlation coefficients. P values < 0.05 were considered statistically significant. For multiple hypothesis testing correction, a false discovery rate methodology was applied. Results with FDR-adjusted p values (q-values) < 0.05 were considered a discovery. The 95% confidence intervals of the individual measurements were calculated.

3. Results

3.1 Dropout rate

From the initial amount of 30 CEA specimens (n= 30 patients), 120 tissue segments were obtained and were initially included in the analysis. Due to insufficient decalcification (high calcification burden of the tissue), intraoperative tissue wear (impossible morphometrical analysis) and high analysis costs, the pilot study was initially conducted using 24 tissue segments from 15 CEA specimens (n= 15 patients). The patients' baseline characteristics were archived for future correlation analyses.

3.2 Distribution of alcian blue staining and its relation towards necrotic-, anti-CD68- and α-smooth muscle cell actin-positively stained regions

In order to identify and estimate the amount and distribution of GAGs in atherosclerotic lesions of human carotid arteries, sections were stained with alcian blue (pH 2.5).

The individual relation of alcian blue staining towards necrotic regions, anti-CD68-rich areas, as well as regions with low anti-α-smooth muscle cell actin immunoreactivity was investigated. For this purpose an ordinal scaling system was established, based on the characterization of the alcian blue staining intensity as very week/non-existent, weak, moderate and strong. The individual scores that were given by the raters, together with representative histological/immunohistochemical images, are presented in Figures 4-6.

Figure 4A shows the semi-quantitative analysis results of the alcian blue staining intensity inside NCs as evaluated by the three observers. Observers 1, 2 and 3 did not identify NC areas in 6, 6 and 7 plaques, respectively, out of a total sum of 24 analyzed sections. Accordingly, observers 1 and 2 found a very weak to weak staining intensity in 15 and 14 atherosclerotic plaques. In only three (Observer 1) or four (Observer 2) sections, the intensity was rated as moderate to strong. Observer 3 presented similar results, evaluating the staining intensity as very weak to weak in 16 plaques, while in only one case was the alcian blue staining intensity reported to be moderate within a NC. Representative histological examples of NC areas with very weak/non-existent, weak and moderate alcian blue staining intensities are shown in Figure 4B.

The evaluation of the alcian blue staining intensity in CD68-rich regions is depicted in Figure 5A. A very weak to weak alcian blue staining intensity was detected in most of the CD68-rich areas.

More specifically, all observers rated the alcian blue staining intensity in CD68-abundant areas as very weak to weak in 18 plaque sections, while observing a moderate to strong intensity in three (Observer 2) to four (Observer 1 and -3) atherosclerotic lesions. In two cases, the evaluation was termed as unclear due to strong histological artifacts that impeded the identification of the anti-CD68 staining distribution. Histological sections of two exemplary cases stained with alcian blue and immunostained with anti-CD68 are shown in Figure 5B.

Next, the observers investigated the alcian blue staining intensity in areas presenting with a weak anti-α-SMA immunostaining. The summary of the results is presented in Figure 6A. Observer 1 found a very weak to weak staining intensity in 21 (15 very weak and 6 weak) out of 24 plaques, while the intensity was rated as moderate in three sections. Observers 2 and 3 detected a very weak to weak intensity in 16 and 17 sections, respectively, while finding that the alcian blue staining intensity in 6 (Observer 2) and 7 (Observer 3) plaques was moderate. In contrast to the evaluation of the first observer, observers 2 and 3 noticed in one case a strong alcian blue staining intensity within an α-SMA-weakly stained site. Representative histological sections from two plaques stained with alcian blue and immunostained with anti-α-SMA illustrate these observations and are shown in Figure 6B.
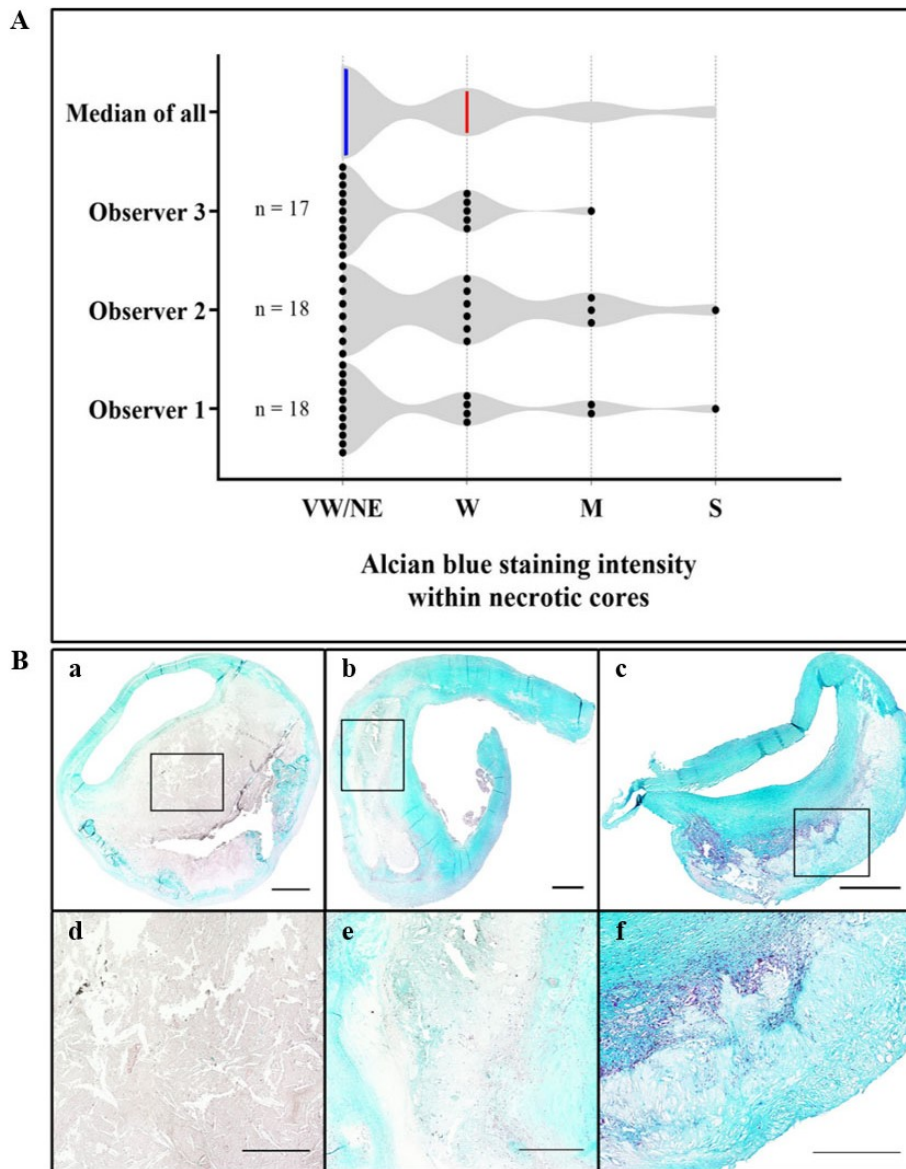
Figure 4. Alcian blue staining intensity in NC areas. (A) Violin plots presenting the semi-quantitative analysis results of alcian blue staining intensity inside necrotic cores. The upper violin plot presents the summary of the individual rater results after calculation of the median values. The blue and red lines represent the median and the 75th percentile, respectively. In this case, the 25th percentile overlaps with the minimum value and is not displayed here. **(B)** Representative histological sections of atherosclerotic plaques with necrotic cores showing differences in the alcian blue staining intensity (a-c). High magnification images (d-f) of the areas annotated with boxes are shown exemplarily. Images were stained with alcian blue and counterstained with nuclear fast red. Scale bars: 1 mm. Abbreviations: VW/NE= very weak/non-existent, W= weak, M= moderate, S= strong.
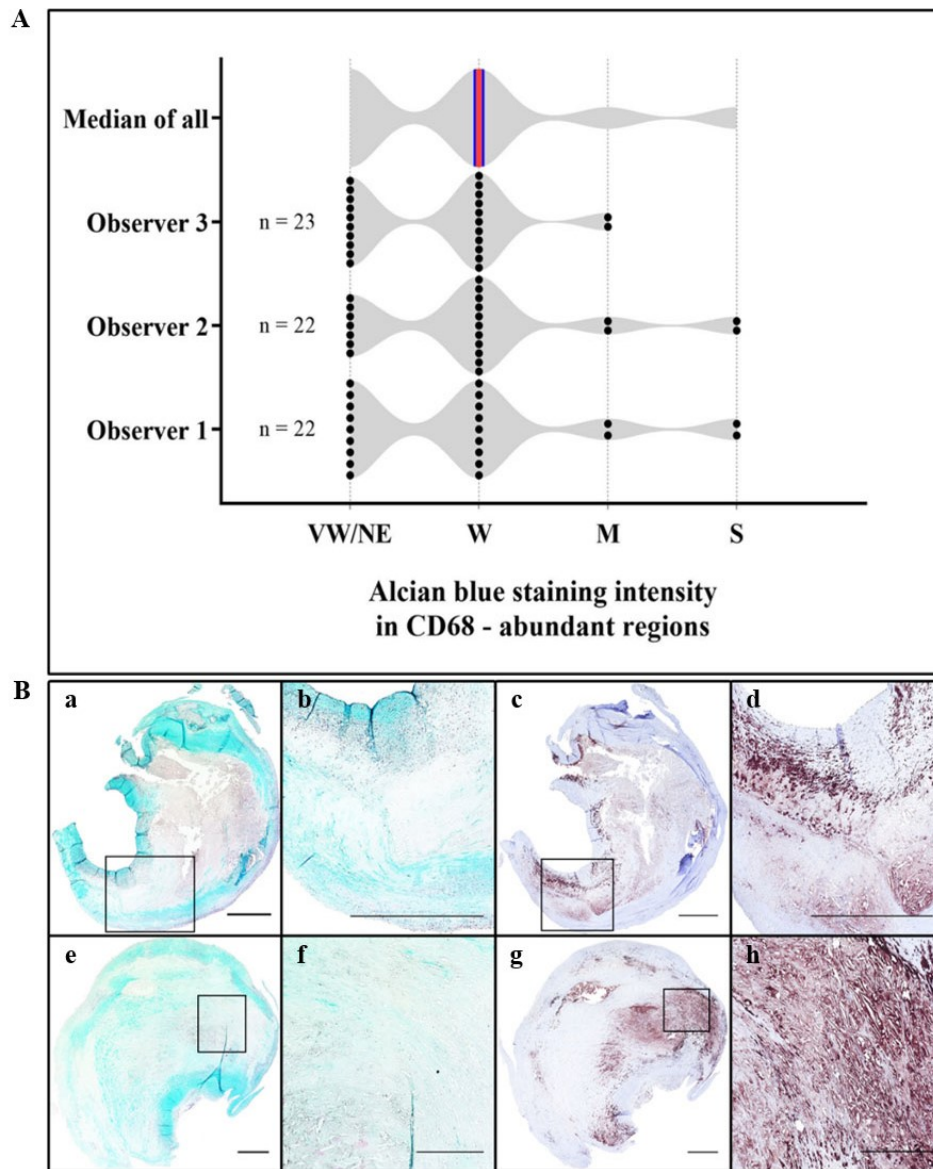
Figure 5. Alcian blue staining intensity in CD68-abundant regions. (A) Violin plots presenting the semi-quantitative analysis results of alcian blue staining intensity in CD68-abundant regions as assessed by three independent observers. The upper violin plot presents the summary of the individual rater results after calculation of the median. The blue and red lines in the plots represent the median and the 25th /75th percentiles, respectively. **(B)** Representative histological images of two plaque sections stained with alcian blue/nuclear fast red (a, e) and immunostained with anti-CD68 antibodies (c, g) to detect macrophages and cells of the monocyte lineage. High magnification images (b, f and d, h) of the areas annotated with boxes are shown exemplarily. Scale bars: 1 mm. Abbreviations: VW/NE= very weak/non-existent, W= weak, M= moderate, S= strong.
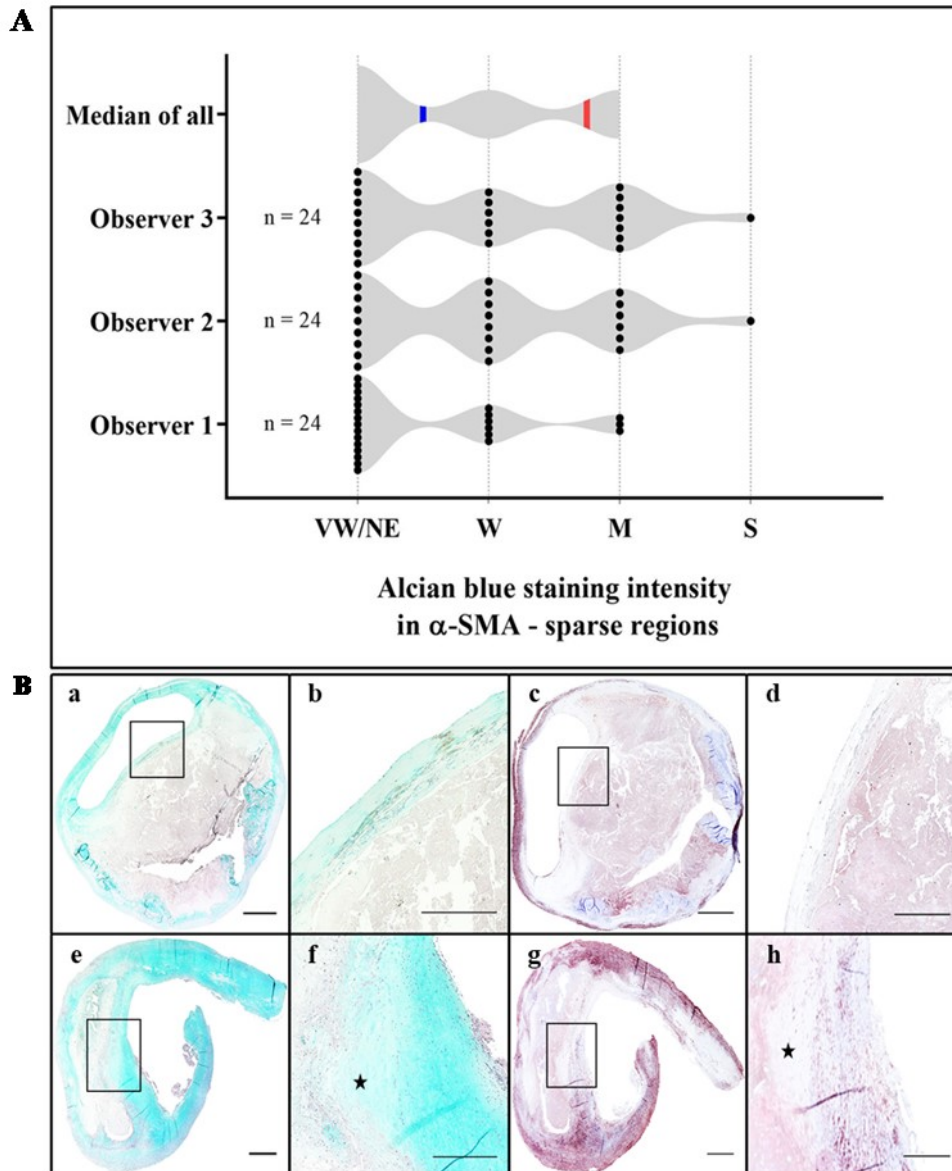
Figure 6. Alcian blue staining intensity in α-SMA-sparse regions. (A) Violin plots presenting the semi-quantitative analysis results of alcian blue staining intensity in α-SMA-sparse regions as assessed by three independent observers. The upper violin plot presents the summary of the individual rater results after calculation of the median. The blue and red lines within the plots represent the median and the 75th percentile, respectively. In this case, the 25th percentile overlaps with the minimum value and is not displayed here. **(B)** Representative histological images of two plaque sections stained with alcian blue/nuclear fast red (a, e) and immunostained with anti-α-SMA antibodies to detect VSMCs (c, g). High magnification images of the areas annotated with boxes are presented in b, f, d and h. Please note the analogy of weak alcian blue staining intensity and low α-SMA immunostaining in the areas marked with a star, while the overlying region is strongly stained with alcian blue and shows a high α-SMA immunostaining. Scale bars: 1 mm. Abbreviations: VW/NE= very weak/non-existent, W= weak, M= moderate, S= strong.

3.3 Relation of picro-sirius red- and alcian blue staining distribution and -intensity

25 sections were stained with collagen-targeting picro-sirius red, while 24 adjacent sections were stained with alcian blue before morphometric and semi-quantitative analysis.

The results are shown in Figure 7. Figure 7A shows the correlations of picro-sirius red- and alcian blue-positive areas determined by three independent observers. All three observers detected a positive correlation between the area covered by picro-sirius red- and alcian blue staining (Observer 1: Pearson´s r = 0.7130/p ≤ 0.0001/95% confidence interval = 0.4346 to 0.8670, observer 2: Pearson´s r = 0.7160/p <0.0001/95% confidence interval = 0.4395 to 0.8685, observer 3: Pearson´s r = 0.8169/p <0.0001/95% confidence interval = 0.6167 to 0.9178).

Next, the staining intensities were compared between the adjacent sections using an ordinal scaling system and the results of the semi-quantitative analysis are presented in Figure 7B. In the majority of cases, the observers rated the alcian blue staining intensity in picro-sirius red strongly stained regions as moderate to strong. In regions with a weak alcian blue staining intensity, the intensity of picro-sirius red was also weak, especially when observing the necrotic areas of the plaques.

In four atherosclerotic plaques, the intensities between the two stainings showed an opposite behavior. This discrepancy was observed mainly in FC areas and in regions adjacent to the NCs. Here, picro-sirius red staining was more intense, while the alcian blue staining intensity was weak. In one case, representing a healing plaque rupture with an intra-luminal thrombus, this incongruence was also observed inside the area of the thrombus. The thrombus presented with a strong alcian blue staining intensity, while being intensely stained by picro-sirius red. Histological images of the latter case are presented exemplarily in Figure 7C. High power view images point out locations where the incongruence in staining intensity is noticeable.

The picro-sirius red stained sections were observed under polarized light that takes advantage of the birefringence properties of certain collagen fibers. Regarding the four atherosclerotic sections that showed an obvious discrepancy between the staining intensities, two main conclusions could be drawn. The regions with weak alcian blue staining intensity corresponded to fluorescent-like, yellow-orange areas that most likely depict thick collagen fibers, while the opposite was the case with respect to the thrombus (Figures 8A-D).
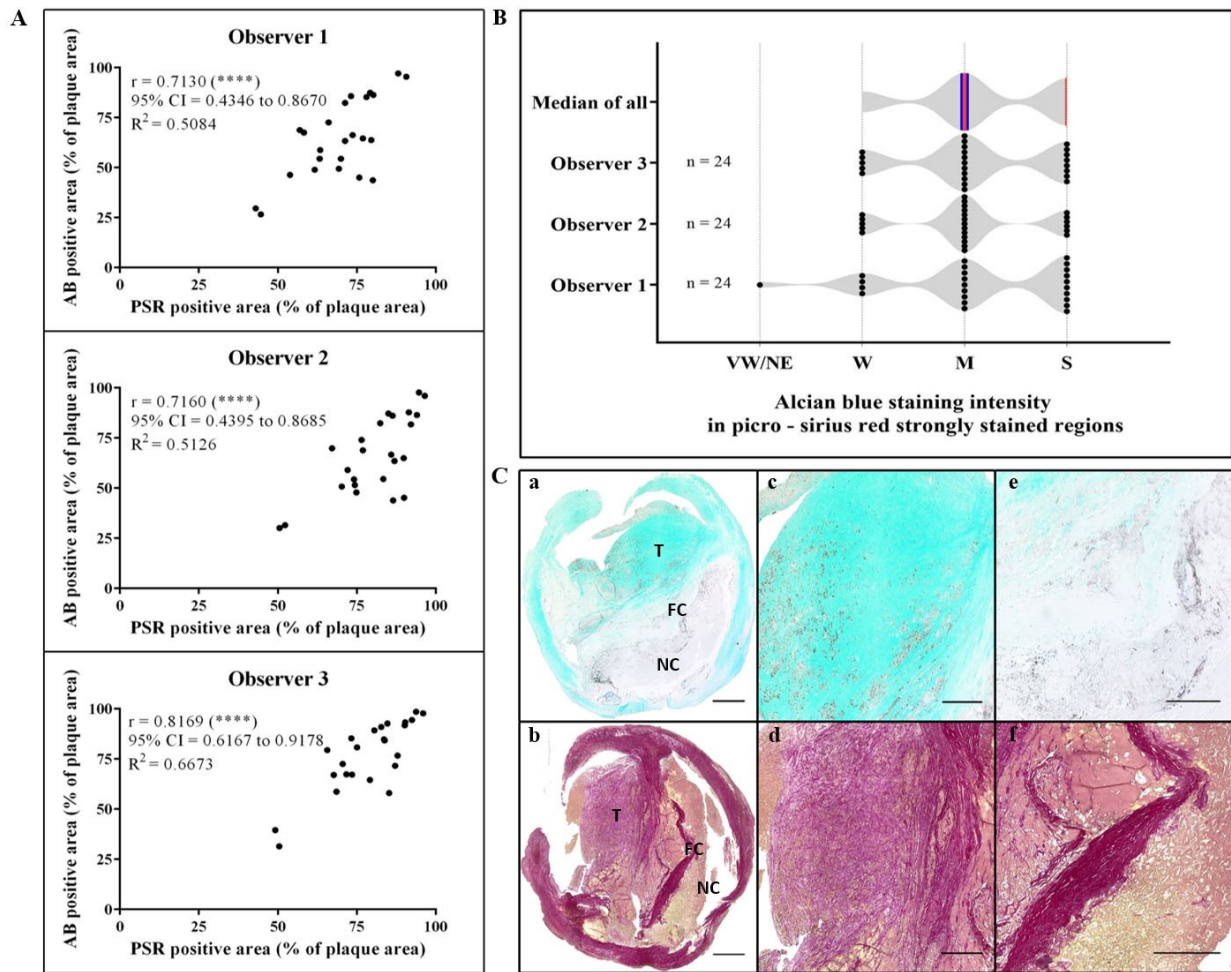
Figure 7. Correlation of alcian blue- and picro-sirius red staining coverage and -intensity in atherosclerotic lesions. (A) Scatterplots presenting the correlation results of the alcian blue- and picro-sirius red positive areas as measured by three independent observers via color thresholding. **(B)** Violin plots presenting the semi-quantitative analysis results of alcian blue staining intensity in picro-sirius red intensely stained regions, as assessed by three independent observers. The upper violin plot presents the summary of the individual rater results after calculation of the median. The blue and red lines inside the plots represent the median and the 75th percentile, respectively. In this case, the 25th percentile overlaps with the minimum value and is not displayed here. **(C)** Representative histological images of two adjacent sections stained with alcian blue/nuclear fast red (a) and picro-sirius red (b) (Collagen fibers: intense red; cytoplasm and muscle fibers: yellow; cell nuclei: blue-black). High power images show corresponding areas of the thrombus (c, d) and the fibrous cap (e, f). Scale bars: 1 mm. Abbreviations: AB= alcian blue, r= Pearson´s correlation coefficient, ****= $p \leq 0.0001$, 95 % CI= 95 % confidence interval, R^2= coefficient of determination, VW/NE= very weak/non-existent, W= weak, M= moderate, S= strong, T= thrombus, FC= fibrous cap, NC= necrotic core, AB= alcian blue.
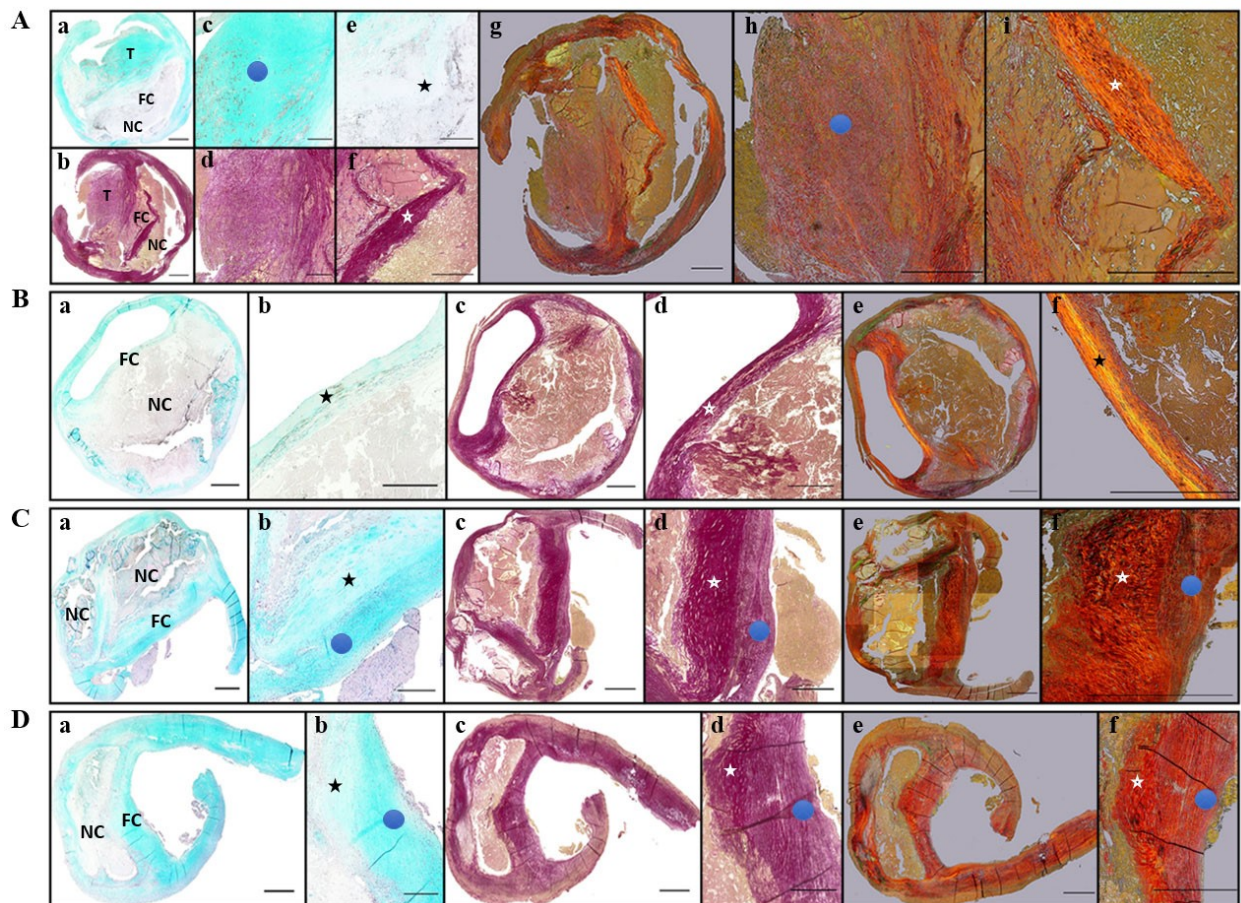
Figure 8. Correlation of alcian blue- and picro-sirius red staining intensity in atherosclerotic lesions using polarized light microscopy. (A) – (D) Histological images of the four sections that showed a discrepancy between alcian blue- (Figures Aa, -Ba, -Ca and -Da) and picro-sirius red (Figures Ab, -Ad, -Af, -Bc, -Bd, -Cc, -Cd, -Dc and -Dd) staining (Collagen fibers: intense red; cytoplasm and muscle fibers: yellow; cell nuclei: blue-black) of the fibrous caps and the thrombus region. The results of the observation of the picro-sirius red stained sections under polarized light (Large/type I collagen fibers: bright, fluorescent-like yellow-orange; thin/type III collagen fibers: green; blunt yellow: cytoplasm and muscle fibers; blunt red: non-birefringence showing material such as collagen type IV) are shown in Figures Ag, -Be, -Ce and -De. High power images show corresponding areas of the thrombus (Figures Ac and -Ad) and the fibrous cap (Figures Ae, -Af, -Ah, -Ai, -Bb, -Bd, -Bf, -Cb, -Cd, -Cf, -Db, -Dd and -Df). Please note the analogy of weak alcian blue staining (regions are annotated with a black or white star) intensity, intense picro-sirius red staining intensity (regions annotated with a black or white star) and the fluorescent-like orange-yellow color that these regions exhibit under polarized light. Note the reverse behavior of the intensity of the two stainings in adjacent FC regions or inside the thrombus (annotated with a blue circle), where the alcian blue staining intensity is strong, while the picro-sirius red staining intensity is weak and presents under polarized light with a blunt, red-orange color tone. Scale bars: 1 mm. Abbreviations: T= thrombus, FC= fibrous cap, NC= necrotic core.

3.4 Alcian blue staining affinity towards calcified areas

The relation between alcian blue staining intensity and the presence of calcification was investigated. Despite the fact that all sections underwent previous decalcification, it was still possible to indirectly detect regions of macrocalcification (in the form of sheets and nodules), but not microcalcification. The areas were found in typical locations (near the intimo-medial border or diffusely distributed throughout the intimal layer with respect to nodular calcification) and showed a polycyclic/irregular shape with prominent borders, as identified with Movat pentachrome. In total, the observers identified areas with probable calcification in 10 to 11 plaques (total plaque number: 24).

The first step was to evaluate the intensity of alcian blue staining in close proximity to calcification sites by using the same ordinal scaling system as described in Chapter 3.3. The results are presented in Figure 9A. Observer 1 found a moderate to strong staining intensity in 10 out of 11 cases, while observing a weak staining intensity in one plaque. Correspondingly, observers 2 and 3 found that the alcian blue staining intensity was moderate to strong in 10 out of 11 and 8 out of 10 cases, respectively. Observers 2 and 3 identified a very weak to weak staining intensity in one and two cases, respectively. Representative histological examples are shown in Figure 9Ab and 9Ad. The high power images (Figure 9Ac and 9Ae) focus on the sites with assumed calcification. Next, the alcian blue staining intensity inside sites with probable calcification was evaluated. All observers found a very weak to weak alcian blue staining intensity inside these sites (analysis graph not shown) (Figure 9Ab-Ae). In one of the cases, observers found remainings of a nodular calcification site that was prominently stained with alcian blue (Figure 9Ba and 9Bb). The existence of calcium in this area was confirmed by positive staining with alizarin red (Figure 9Bc and 9Bd).
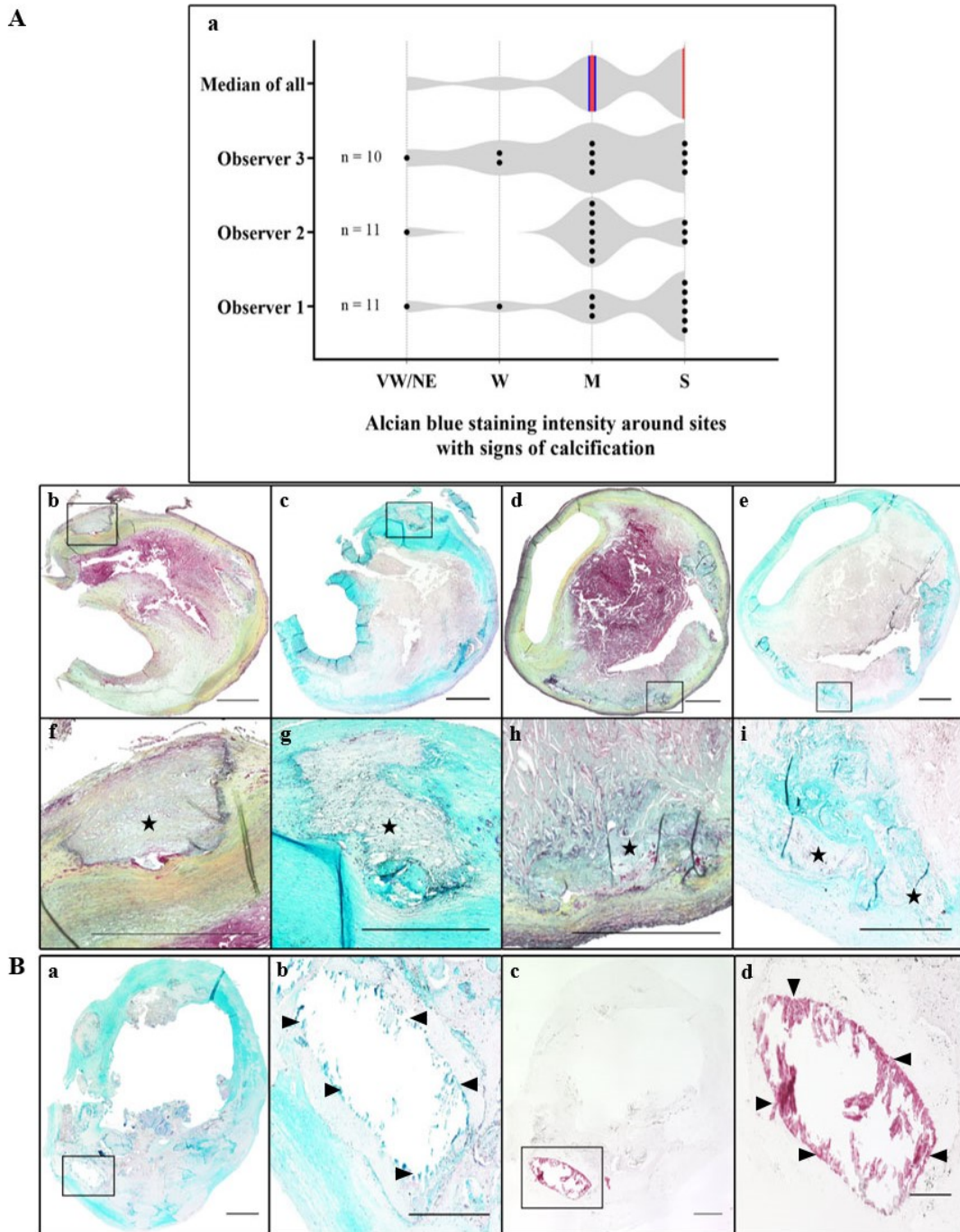
Figure 9. Affinity of alcian blue staining towards calcified areas. (A) Violin plots (a) and representative histological images stained with alcian blue/nuclear fast red (c, e) and Movat pentachrome (b, d). The violin plots present the semi-quantitative analysis results of alcian blue staining intensity around areas with signs of calcification, as assessed by three independent evaluators. The upper plot presents the summary of the individual rater´s results after calculation of the median. The blue and red lines inside the plot represent the median and the 25th /75th percentiles, respectively. High magnification images (f-i) focus on the regions with assumed calcification (stars). **(B)** Representative histological images of two adjacent sections stained with alcian blue/nuclear fast red (a) and alizarin red (c) (Calcium deposits: red-violet), respectively. High magnification images (b, d) show remainings (arrowheads) of a calcification nodule. Scale bars: 1 mm. Abbreviations: VW/NE= very weak/non-existent, W= weak, M= moderate, S= strong.

3.5 Establishment of a vulnerability scoring system and lesion categorization in low-, medium- and high vulnerability/-anti-CD68 immunoreactivity groups

Despite the variety of lesions that were identified during the processing of the 15 CEA specimens, the number (n= 24) of sections available did not allow the implementation of the widely accepted Modified American Heart Association (AHA) Classification as a reference system[8]. In order to make the various sections comparable for the upcoming microarray and disaccharide unit analysis, a scoring system based on the quantitative and semi-quantitative measurements of well-known stability- and instability-associated morphological features was established. The maximum vulnerability score that could be assigned was 24 points. Plaque sections that gathered a score of between 0 and 4 points were enclosed in the low vulnerability (LV) group. The medium vulnerability (MV) group included lesions with a score of between 5 and 10 points, while all lesions that were assigned 11-24 points comprised the high vulnerability (HV) group.

Table 8 presents the parameters that frame the basis of the vulnerability scoring system and outlines the specifications according to which vulnerability points were assigned. An example of the assignment procedure is schematically visualized in Figure 10. The vulnerability points for each of the twenty four sections are presented in Table 9.

7 plaques were classified as LV (mean acquired points: 3.14, SD: ± 0.89). 6 plaques were included in the MV group (mean acquired points: 9.0, SD: ± 1.5), while 11 plaques were catalogued as HV (mean acquired points: 14.54, SD: ± 2.20). Histological sections and corresponding macroscopical images of the lesions and their affiliation to the vulnerability groups are presented in Figure 11.

The plaques were also categorized according to their anti-CD68 immunoreactivity (Anti-CD68 immunoreactivity in Table 8) in high-, medium- and low- immunoreactivity groups. 10 plaques were included in the high anti-CD68 immunoreactivity group, while 9 sections displayed low anti-CD68 immunoreactivity. The remaining 5 plaques were included in the medium anti-CD68 immunoreactivity group. Histological sections and corresponding macroscopical images of the lesions and their affiliation to the anti-CD68 immunoreactivity groups are shown in Figure 12.

Table 8. Vulnerability scoring system

Criteria	Points	Specifications
Minimum FC thickness	0 - 3	**3:** < 120 μm **2:** 120-240 μm **1:** 240-360 μm **0:** >360 μm or no FC present
Mean FC thickness	0 - 3	**3:** < 120 μm **2:** 120-240 μm **1:** 240-360 μm **0:** > 360 μm or no FC present
NC size (% of total plaque area)	0 - 3	**3:** large (> 40 %) **2:** medium (25-40 %) **1:** small (< 25 %) **0:** no NC present
Anti-CD68 immunoreactivity (% of total plaque area)	0 - 3	**3:** > 5 % **2:** 2.5-5 % **1:** 0-2.5 % **0:** 0 %
FC-associated anti-CD68 immunoreactivity (% of total FC area)	0 - 3	**3:** > 20 % **2:** 10-20 % **1:** 0-10 % **0:** 0 % or no FC present
FC-associated anti-α-SMA immunoreactivity (% of total FC area)	0 - 3	**3:** 0-10 % **2:** 10 - 20 % **1:** > 20 % **0:** 0 no FC present
Neovessel-like stuctures	0 - 3	**3:** > 50/mm^2 **2:** 25-50/mm^2 **1:** 0-25/mm^2 **0:** no
Hemorrhage	0 or 1	**1:** hemorrhage present **0:** not existent
Cap rupture/ulceration	0 or 1	**1:** probably ruptured/ulcerated **0:** not existent
Thrombus	0 or 1	**1:** presence of thrombus **0:** not existent

NC size

Mean = 30.56 %

2 p.

Anti-CD68 immunoreactivity

3.05 %

2 p.

Min. and mean FC thickness

Mean of Mins= 86 μm,
Mean of Means= 295 μm

3 p. + 1p.

Score = 18

FC-associated anti-CD68 immunoreactivity

5.77 %

1 p.

FC-associated anti-α-SMA immunoreactivity

2.37 %

3 p.

Hemorrhage?
Cap rupture/ ulceration?
Thrombus?

Yes,
Yes,
Yes

1 p. + 1 p. + 1 p.

Neovessel-like structures

56.28/mm²

3 p.
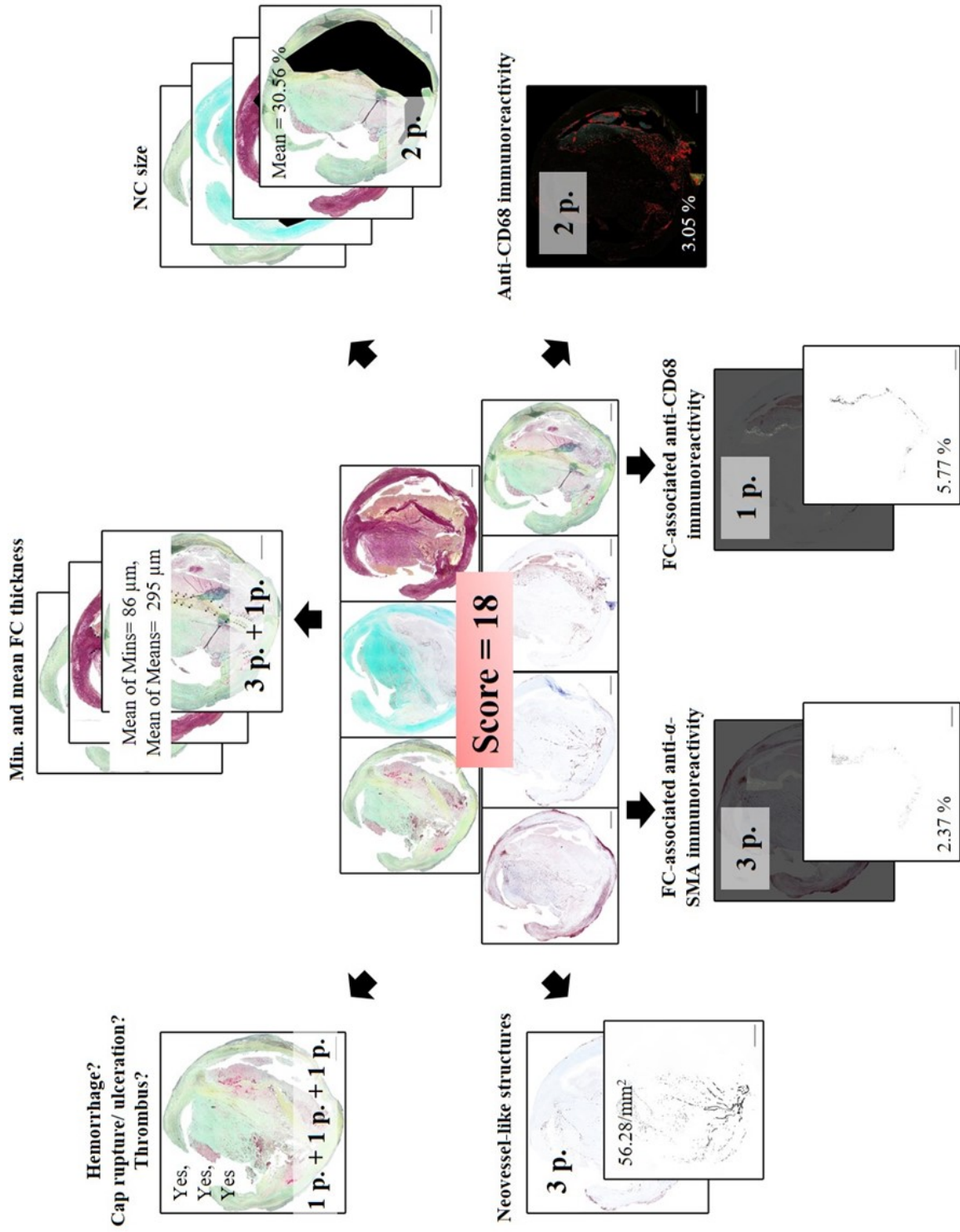
Figure 10. Exemplary visualization of the scoring process as conducted on one of the samples. Abbreviations p.= points

71

Table 9. Summary of the vulnerability points awarded for each criterion and final score of the plaques.

Criteria / Plaques	P1	P3	P5	P7	P8	P9	P14	P15	P17	P18	P19	P20	P21	P23	P25	P26	P27	P28	P29	P30	P32	P33	P34	PT12
Minimum FC thickness	2	3	0	0	0	0	3	2	0	1	0	1	0	0	0	0	0	3	2	0	0	2	2	1
Mean FC thickness	0	1	0	0	0	0	1	0	0	0	0	0	0	0	0	0	0	2	0	0	0	0	0	0
NC size (% of total plaque area)	3	2	1	0	3	2	3	3	1	3	1	2	0	0	0	0	0	2	1	1	0	1	1	3
Anti-CD68 immunoreactivity (% of total plaque area)	1	2	3	1	3	2	2	3	3	3	2	3	1	1	1	1	1	3	1	2	1	3	3	1
FC-associated anti-CD68 immunoreactivity (% of total FC area)	2	1	1	0	1	3	3	2	2	1	0	3	0	0	0	0	0	2	1	1	0	2	1	1
FC-associated anti-α-SMA immunoreactivity (% of total FC area)	3	3	2	0	2	2	3	2	2	3	0	3	0	0	0	0	0	3	2	3	0	3	3	3
Neovessel-like stuctures	1	3	2	3	3	3	1	2	2	1	3	3	1	2	3	3	2	2	2	3	1	1	2	0
Hemorrhage	1	1	0	0	1	1	1	1	0	1	0	0	0	0	0	0	0	0	0	0	0	0	0	1
Cap rupture/ulceration	0	1	0	0	0	0	1	0	0	0	0	0	0	0	0	0	0	0	0	0	0	0	0	0
Thrombus	0	1	0	0	0	0	0	0	0	0	0	0	0	0	0	0	0	0	0	0	0	1	0	0
Score	**13**	**18**	**9**	**4**	**13**	**13**	**18**	**15**	**10**	**13**	**6**	**15**	**2**	**3**	**4**	**4**	**3**	**17**	**9**	**10**	**2**	**13**	**12**	**10**
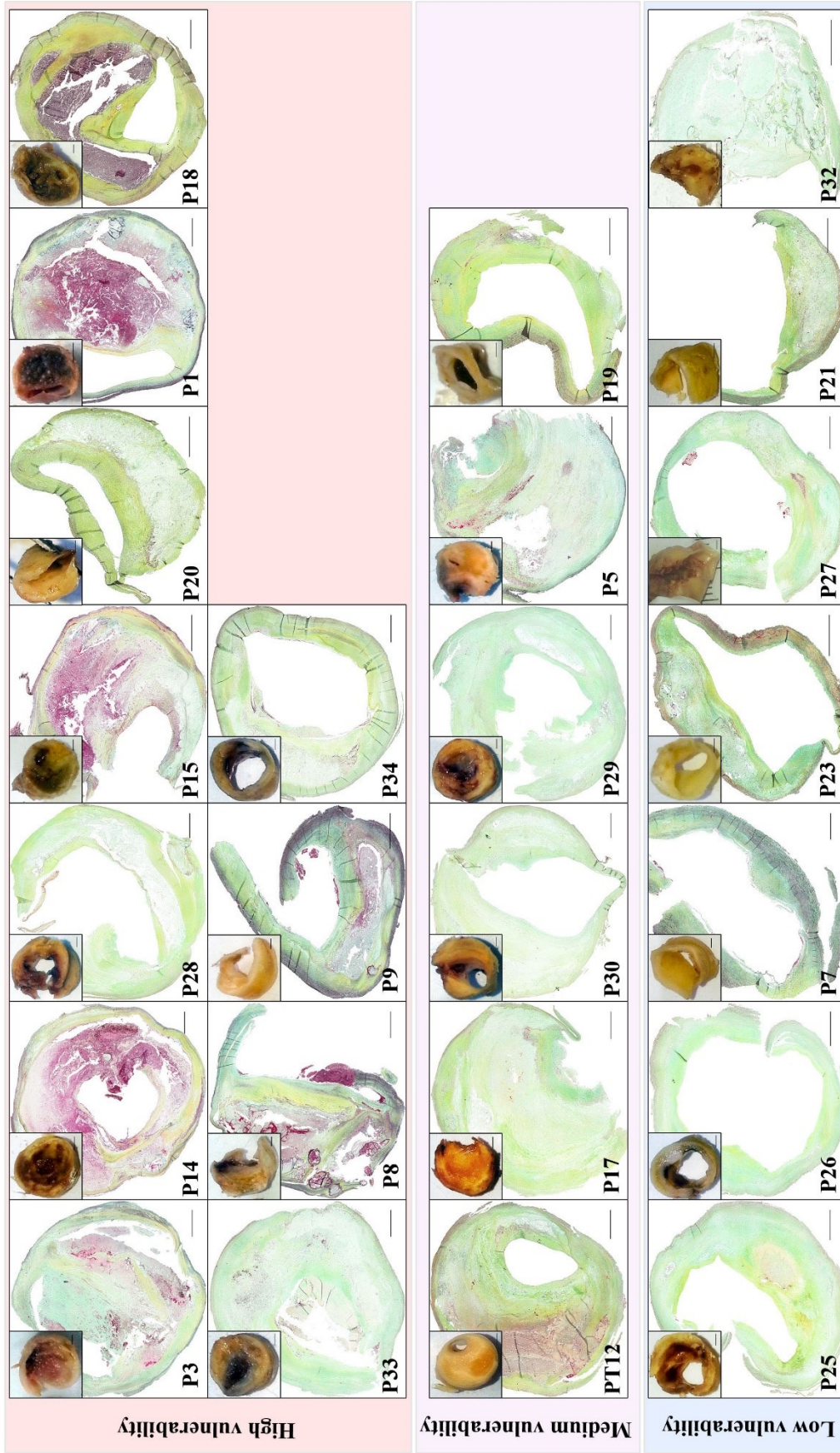
Figure 11. Histological sections and corresponding macroscopical images of the analyzed atherosclerotic sections and their categorization in high-, medium- and low vulnerability groups. Images were stained with Movat pentachrome (Dark blue-black: cell nuclei and elastic fibers; Red-light brown: vascular smooth muscle cells; Intense red: erythrocytes/ hemorrhage area; Pale red-pink: fibrin/ fibrinoid substance; Yellow: collagen fibers; Light blue: acidic mucopolysaccharides/ GAGs; Light yellow-green/ light blue-green: colocalization of colagen fibers with GAGs). The samples to which the images correspond to are are shown. Scale bars 1 mm (histological images) and 0.2 cm (macroscopical images).

73
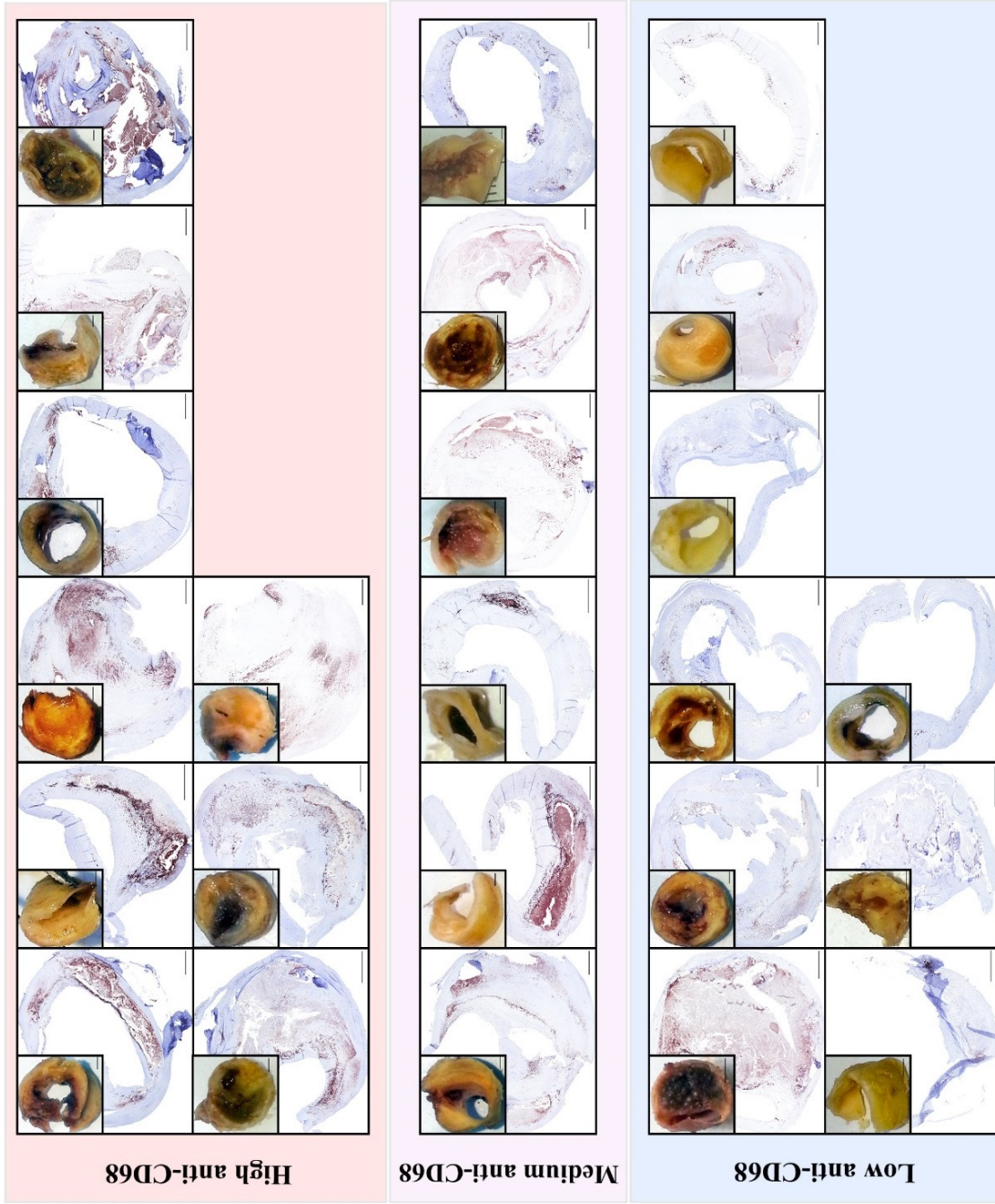
Figure 12. Histological sections and corresponding macroscopical images of the analyzed atherosclerotic sections and their categorization in high-, medium- and low anti-CD68 groups. Images were immunostained with anti-CD68 antibodies. Scale bars 1 mm (histological images) and 0.2 cm (macroscopical images).

3.6 Differential mRNA expression profile between low- and high vulnerability lesions and between lesions with low- and high anti-CD68 immunoreactivity

For investigation of mRNA expression level variations between LV- and HV-classified atherosclerotic sections, as well as between lesions presenting with low- and high anti-CD68 immunoreactivity, RNA amounts were extracted from 16 tissue sections adjacent to the ones used for histological and biochemical examination and were analyzed using mRNA microarray technology (sample numbers P1, P3, P7, P8, P9, P14, P15, P18, P20, P25, P26, P27, P28, P30, P33 and P34 in Table 9).

Briefly, the raw data were preprocessed and quality assessed in order to potentially identify technical outlier samples. No samples were classified as a technical outlier and all samples were considered for further preprocessing. The signals were background corrected and out of 5 normalization methods (none, cyclic loess-, quantile-, variance stabilizing- and median normalization) "cyclic loess" was chosen, according to the criteria proposed by Bolstad et al.[224]. Figure 13 shows the summary statistics of the intensity values prior to and after normalization.

After passing quality control and after normalization, the microarrays representing 9 HV- and 4 LV lesions as well as 9 high- and 9 low anti-CD68 immunoreactivity lesions were subjected to differential expression analysis. The focus was placed on 140 genes that are involved in PG/GAG metabolism. The results of the analyses are displayed in Figures 14 and 15. A complete list of the gene full names and analytical fold change results are available in Table 11 at the end of this chapter.

Of the 65 core protein-coding mRNAs and the 83 GAG metabolism-associated enzyme-coding mRNAs, 12 candidates showed a $\geq$ 2-fold change in their signal intensity both between HV- and LV sections, as well as between lesions with high- and low anti-CD68 immunoreactivity (Table 10). A fold change of < 2 was calculated for the remaining mRNAs. The mRNA signal intensities of SRGN and ARSK showed a positive three- to four–fold change between sections with a high vulnerability score and a high anti-CD68 immunoreactivity versus sections with a low vulnerability score and a low anti-CD68 immunoreactivity. Conversely, PODNL1, ASPN, CHADL, HAPLN1, IMPG1, DSEL, CHST10, EXTL2, CHPF2v1 and CHSY3 were found with a two- to four-fold decrease in their mRNA expression levels when comparing the same groups as above. NRP1v2, HPSE, NDST3, B3GNT3, HS6ST3, CHST12, HAS3v3 and HAS2 showed concomitant changes when observing the analysis results of the above comparisons.
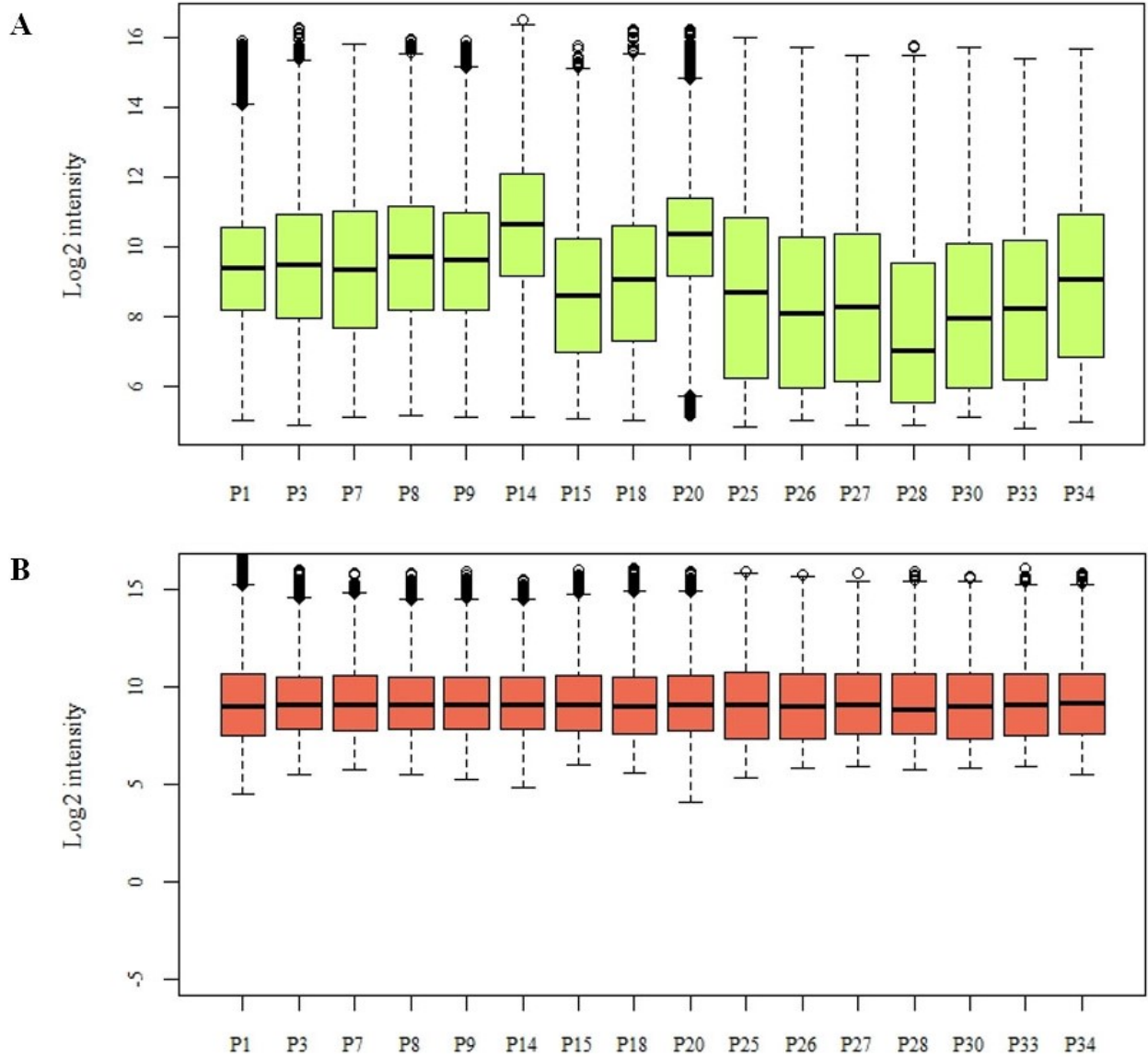
Figure 13. Boxplots of the log2 raw- and normalized signal intensities. (A) Foreground signal intensities prior to normalization. **(B)** Foreground signal intensities after normalization. The bold lines within the boxplots correspond to the median values; boxes extend from the 25th to the 75th percentile of the values. Outlier values are denoted as a circle.
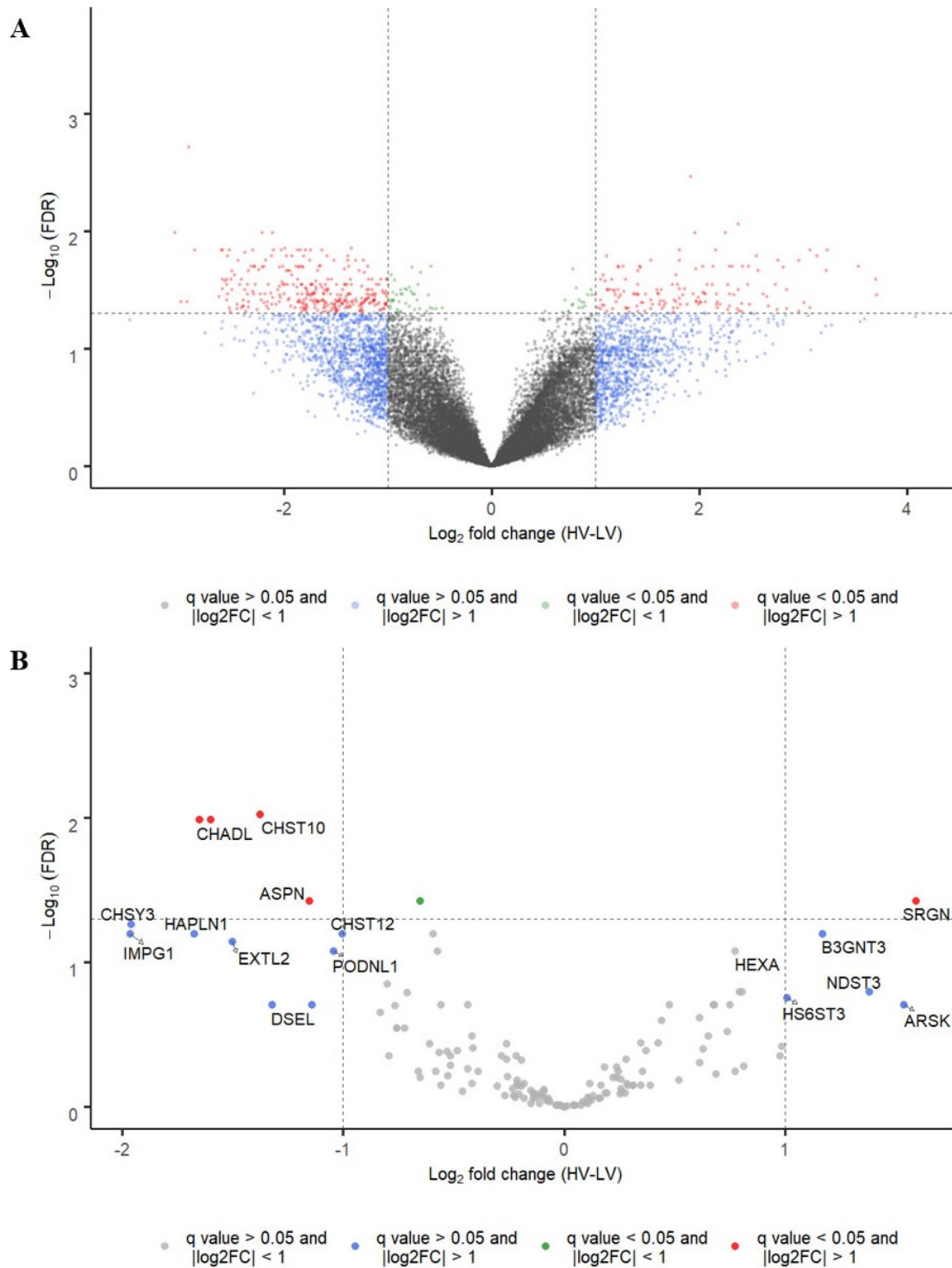
Figure 14. Differential mRNA expression analysis between HV- and LV lesions. (A) Volcano plot depicting the mRNA expression analysis results between HV- and LV-groups for all mRNA transcripts. **(B)** Volcano plot depicting the mRNA expression analysis results between the two groups, emphasized on 148 mRNAs involved in PG-/GAG metabolism. The negative logarithms (base 10) of the calculated q values are plotted on the y-axis, while the logarithm (base 2) of the fold change is displayed on the x-axis. The red and blue points represent mRNAs with ≥ 2-fold change and q values < 0.05. The grey points represent mRNAs with < 2-fold change and q values > 0.05. The full names of the acronyms and the detailed results for all mRNAs can be found in Chapter 3.6, Table 11. Abbreviations: LV: low vulnerability, HV: high vulnerability, FDR: false discovery rate.
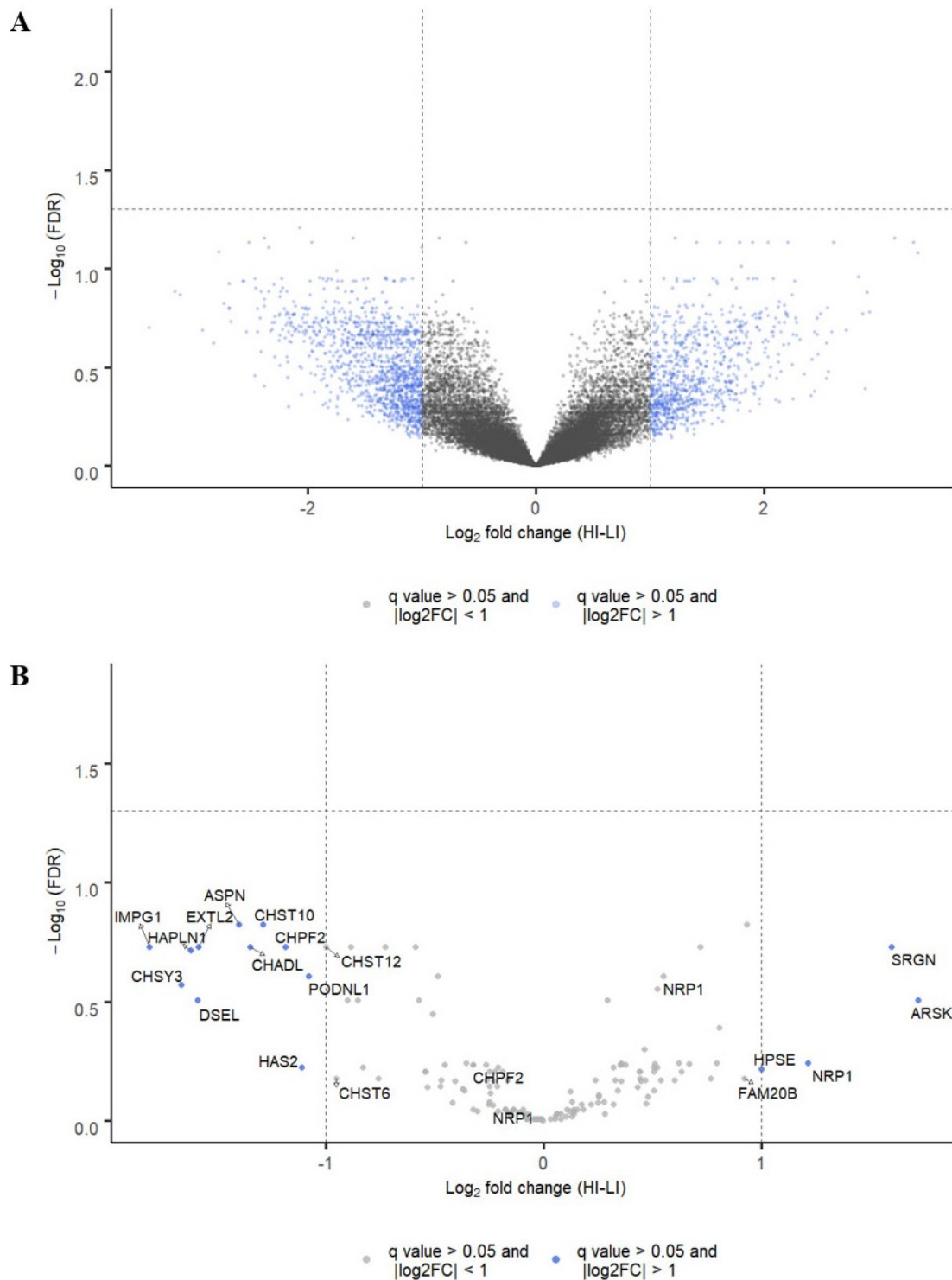
Figure 15. Differential mRNA expression analysis between HI- and LI lesions. (A) Volcano plot depicting the mRNA expression analysis results between HI- and LI-groups for all mRNA transcripts **(B)** Volcano plot depicting the mRNA expression analysis results between the two groups emphasized on 148 mRNAs involved in PG-/GAG metabolism. The negative logarithms (base 10) of the calculated q values are plotted on the y-axis, while the logarithm (base 2) of the fold change is displayed on the x-axis. The red- and blue points represent mRNAs with ≥ 2-fold change and q values < 0.05. The grey points represent mRNAs with < 2-fold change and q values > 0.05. The full names of the acronyms and the detailed results for all mRNAs can be found in Chapter 3.6, Table 11. Abbreviations: LI: low anti-CD68 immunoreactivity, HI: high anti-CD68 immunoreactivity, FDR: false discovery rate.

Table 10. mRNA expression levels of core proteins and GAG metabolism-associated enzymes with ≥ 1 log2 fold change between the two comparison groups. Abbreviations: CI= confidence interval.

	Log2 fold change (p-, q value, 95% CI) *	
	High vs. Low vulnerability score	High- vs. Low anti-CD68
Core proteins		
SRGN	+ 1.590 (p= 0.0014, q= 0.037, 95% CI= + 0.70 to + 2.47)	+ 1.599 (p= 0.009, q= 0.185, 95% CI= + 0.458 to + 2.739)
NRP1v2	+ 0.983 (p= 0.117, q= 0.377, 95% CI= - 0.274 to + 2.241)	+ 1.215 (p= 0.118, q= 0.571, 95% CI= -0.350 to + 2.781)
PODNL1	- 1.043 (p= 0.008, q= 0.08, 95% CI= - 1.785 to – 0.301)	- 1.075 (p= 0.028, q= 0.247, 95% CI= -2.021 to – 0.129)
ASPN	- 1.154 (p= 0.001, q= 0.037, 95% CI= -1.800 to – 0.508)	- 1.398 (p= 0.001, q= 0.149, 95% CI= - 2.125 to – 0.672)
CHADL	- 1.650 (p= 0.0002, q= 0.010, 95% CI= - 2.388 to - 0.911)	- 1.345 (p= 0.005, q= 0.185, 95% CI= - 2.226 to – 0.464)
HAPLN1	- 1.675 (p= 0.005, q= 0.063, 95% CI= - 2.777 to – 0.573)	- 1.617 (p= 0.018, q= 0.192, 95% CI= - 2.917 to – 0.316)
IMPG1	- 1.963 (p= 0.004, q= 0.063, 95% CI= - 3.232 to – 0.695)	- 1.806 (p= 0.012, q= 0.185, 95% CI= - 1.806 to – 3.163)
GAG anabolism-associated enzymes		
NDST3	+ 1.379 (p= 0.021, q= 0.160, 95% CI= + 0.227 to + 2.53)	+ 0.751 (p= 0.236, q= 0.666, 95% CI= - 0.251 to + 1.115)
B3GNT3	+ 1.165 (p= 0.004, q= 0.063, 95% CI= + 0.416 to + 1.914)	+ 0.809 (p= 0.07, q= 0.407, 95% CI= - 0.09 to + 1.712)
HS6ST3	+ 1.005 (p= 0.026, q= 0.177, 95% CI= + 0.133 to + 1.878)	+ 0.432 (p= 0.196, q= 0.628, 95% CI= - 0.251 to + 1.115)
CHST12	- 1.006 (p= 0.005, q= 0.06, 95% CI= - 1.666 to - 0.346)	- 0.998 (p= 0.009, q= 0.242, 95% CI= - 1.716 to – 0.280)
HAS3v3	- 1.141 (p= 0.034, q= 0.195, 95% CI= - 2.187 to – 0.095)	- 0.473 (p= 0.373, q= 0.755, 95% CI= - 1.576 to 0.630)
DSEL	- 1.323 (p= 0.037, q= 0.195, 95% CI= - 2.560 to - 0.085)	- 1.586 (p= 0.043, q= 0.312, 95% CI= - 3.121 to – 0.051)
CHST10	- 1.285 (p= 0.002, q= 0,009, 95% CI= - 2.013 to - 0.557)	- 1.285 (p= 0.002, q= 0.149, 95% CI= - 2.013 to – 0.557)
EXTL2	- 1.502 (p= 0.006, q= 0.071, 95% CI= - 2.518 to - 0.486)	- 1.582 (p= 0.015, q= 0.185, 95% CI= - 2.814 to – 0.351)
CHPF2v1	- 1.601 (p= 0.0002, q= 0.010, 95% CI= - 2.321 to – 0.881)	- 1.182 (p= 0.014, q= 0.185, 95% CI= - 2.088 to – 0.277)
CHSY3	- 1.961 (p= 0.002, q= 0.054, 95% CI= - 3.132 to – 0.789)	- 1.662 (p= 0.033, q= 0.269, 95% CI= - 1.662 to – 3.171)
HAS2	- 0.461 (p= 0.546, q= 0.778, 95% CI= - 2.045 to + 1.122)	- 1.107 (p= 0.195, q= 0.594, 95% CI= - 2.855 to + 0.641)
GAG catabolism-associated enzymes		
ARSK	+ 1.535 (p= 0.038, q= 0.195, 95% CI= + 0.09 to 2.98)	+ 1.720 (p= 0.05, q= 0.312, 95% CI= - 0.03 to + 3.47)
HPSE	+ 0.809 (p= 0.220, q= 0.518, 95% CI= - 0.534 to 2.153)	+ 1.002 (p= 0.203, q= 0.605, 95% CI= -0.61 to + 2.61)

2- to 3-fold		
3- to 4-fold		

* For a better interpretation of the results the colors display the non-logarithmic fold changes according to the color legend.

Table 11. Total mRNA differential expression analysis results between high- and low vulnerability lesions (upper row) and between lesions with high- and low anti-CD68 immunoreactivity (lower row).

Acronym	Eponym	Reference number	log2FC	p value	q value	95 % CI* (Lower/ Upper)	
BGN	Biglycan	NM_001711.4	-0.596	0.004	0.057	-0.967	-0.224
			-0.588	0.015	0.164	-1.042	-0.134
COL12A1	Collagen 12α1	NM_004370.5	0.277	0.185	0.524	-0.146	0.699
			0.109	0.621	0.907	-0.353	0.571
PODN	Podocan	NM_001199080.1	0.750	0.035	0.209	0.060	1.440
			0.357	0.341	0.736	-0.421	1.136
HAPLN3	Hyaluronan and proteoglycan link protein 3	NM_178232.2	-0.195	0.191	0.524	-0.497	0.107
			-0.208	0.185	0.613	-0.529	0.112
VCANv3	Versican	NM_001126336.2	-0.416	0.123	0.427	-0.957	0.125
			-0.571	0.049	0.294	-1.138	-0.003
SRGN	Serglycin	NM_002727.2	1.590	0.001	0.033	0.708	2.473
			1.599	0.009	0.164	0.459	2.739
FMOD	Fibromodulin	NM_002023.4	-0.714	0.023	0.169	-1.317	-0.111
			-0.885	0.012	0.164	-1.542	-0.229
COL18A1	Collagen 18α1/XVIII (Endostatin)	NM_030582.3	-0.152	0.520	0.779	-0.640	0.336
			-0.212	0.381	0.785	-0.715	0.291
HSPG2	Heparan sulfate proteoglycan 2 (Perlecan)	NM_001291860.1	-0.565	0.147	0.461	-1.349	0.219
			-0.162	0.319	0.736	-0.500	0.175
SDC3	Syndecan 3	NM_014654.3	-0.080	0.783	0.876	-0.682	0.522
			0.176	0.572	0.907	-0.477	0.829
AGRN	Agrin	NM_198576.3	0.220	0.325	0.632	-0.239	0.679
			0.321	0.179	0.613	-0.166	0.808
TGFBR3	Transforming growth factor beta receptor 3 (Betaglycan)	NM_001195683.1	-0.527	0.301	0.602	-1.570	0.516
			-0.829	0.194	0.613	-2.132	0.474
SDC4	Syndecan 4 (Amphiglycan)	NM_002999.3	-0.230	0.638	0.827	-1.243	0.783

			-0.046	0.926	0.976	-1.094	1.001
PRELP	Proline/arginine-rich end leucine-rich repeat protein (Prolargin)	NM_002725.3	0.251	0.593	0.827	-0.722	1.225
			0.321	0.579	0.907	-0.892	1.534
SPOCK2v2	Sparc/osteonectin, cwcv and kazal-like domains proteoglycan 2 (Testican 2)	NM_001244950.1	0.261	0.537	0.785	-0.613	1.134
			-0.073	0.879	0.976	-1.086	0.939
SPOCK2v1	,,	NM_001134434.1	-0.213	0.358	0.638	-0.688	0.263
			-0.010	0.966	0.976	-0.497	0.477
ASPN	Asporin	NM_001193335.1	-1.155	0.002	0.033	-1.800	-0.509
			-1.399	0.001	0.069	-2.126	-0.672
ACAN	Aggrecan	NM_001135.3	-0.418	0.089	0.346	-0.907	0.071
			-0.509	0.063	0.347	-1.049	0.032
PODNL1	Podocan-like 1	NM_001146254.1	-1.043	0.009	0.081	-1.785	-0.302
			-1.075	0.029	0.211	-2.021	-0.129
DCN	Decorin (Dermatan sulfate proteoglycan II)	NM_001920.3	-0.759	0.070	0.321	-1.588	0.069
			-0.852	0.048	0.294	-1.698	-0.007
NRP1v1	Neuropilin 1	NM_003873.5	-0.235	0.495	0.763	-0.946	0.476
			-0.232	0.588	0.907	-1.131	0.667
NRP1v2	,,	NM_001024628.2	0.984	0.117	0.427	-0.274	2.242
			1.215	0.118	0.579	-0.351	2.782
NRP1v3	,,	NM_001024629.2	0.473	0.040	0.221	0.024	0.922
			0.550	0.028	0.211	0.069	1.031
SDC2	Syndecan 2 (Fibroglycan)	NM_002998.3	-0.022	0.946	0.960	-0.686	0.643
			0.141	0.710	0.907	-0.655	0.936
HAPLN4	Hyaluronan and proteoglycan link protein 4	NM_023002.2	0.790	0.021	0.169	0.132	1.448
			0.505	0.186	0.613	-0.275	1.286
COL9A2	Collagen 9α2	NM_001852.3	0.122	0.770	0.876	-0.746	0.990
			-0.030	0.953	0.976	-1.120	1.059
GPC1	Glypican 1	NM_002081.2	-0.136	0.689	0.842	-0.840	0.568
			0.035	0.930	0.976	-0.797	0.867
BCANv1	Brevican	NM_021948.4	0.677	0.032	0.209	0.064	1.291
			0.328	0.324	0.736	-0.361	1.017

BCANv2	´´	NM_021948.4	-0.035	0.912	0.960	-0.685	0.616
			-0.011	0.976	0.976	-0.748	0.727
PRG4	p53-responsive gene 4 (Lubricin)	NM_001127708.1	-0.212	0.431	0.712	-0.766	0.343
			-0.014	0.963	0.976	-0.658	0.630
OMD	Osteomodulin (Osteoadherin)	NM_005014.2	0.612	0.203	0.536	-0.363	1.587
			0.600	0.315	0.736	-0.636	1.836
ECM2i2	Extracellular matrix protein 2	NM_001197295.1	-0.660	0.261	0.562	-1.858	0.538
			-0.418	0.539	0.907	-1.842	1.007
ESM1	Endothelial cell-specific molecule 1 (Endocan)	NM_001135604.1	0.253	0.338	0.638	-0.289	0.796
			0.141	0.664	0.907	-0.540	0.821
NCAN	Neurocan (Chondroitin sulfate proteoglycan 3)	NM_004386.2	-0.018	0.945	0.960	-0.562	0.526
			-0.009	0.976	0.976	-0.672	0.653
CHAD	Chondroadherin	NM_001267.2	-0.722	0.073	0.321	-1.520	0.075
			-0.361	0.427	0.853	-1.308	0.586
CSPG4	Chondroitin sulfate proteoglycan 4	NM_001897.4	-0.269	0.645	0.827	-1.482	0.943
			-0.154	0.829	0.976	-1.659	1.352
COL15A1	Collagen 15α1/XV (Restin)	NM_001855.4	0.157	0.728	0.857	-0.778	1.091
			0.466	0.305	0.736	-0.475	1.408
HAPLN2	Hyaluronan and proteoglycan link protein 2	NM_021817.2	-0.105	0.653	0.827	-0.589	0.379
			0.063	0.797	0.976	-0.452	0.578
GPC6	Glypican 6	NM_005708.3	0.773	0.264	0.562	-0.640	2.186
			0.473	0.550	0.907	-1.188	2.134
LUM	Lumican	NM_002345.3	0.108	0.744	0.862	-0.580	0.796
			-0.175	0.622	0.907	-0.924	0.573
CD44i8	CD44 Molecule (Indian Blood Group)	NM_001202557.1	0.241	0.273	0.562	-0.208	0.690
			0.359	0.167	0.613	-0.169	0.886
CD44i5	´´	NM_001001392.1	-0.534	0.141	0.461	-1.262	0.195
			-0.145	0.714	0.907	-0.981	0.691
NYX	Nyctalopin	NM_022567.2	-0.039	0.898	0.960	-0.673	0.595
			0.157	0.648	0.907	-0.568	0.883

Gene	Description	Accession					
PRG2	Proteoglycan 2	NM_001243245.2	-0.213	0.431	0.712	-0.769	0.344
			-0.136	0.672	0.907	-0.814	0.542
GPC4	Glypican 4	NM_001448.2	0.516	0.355	0.638	-0.629	1.661
			0.480	0.483	0.907	-0.951	1.912
OGN	Osteoglycin (Mimecan)	NM_014057.3	0.161	0.713	0.856	-0.750	1.073
			0.105	0.843	0.976	-1.009	1.218
TSKU	Tsukushin	NM_001258210.1	0.281	0.397	0.690	-0.402	0.965
			0.054	0.889	0.976	-0.761	0.868
GPC2	Glypican 2	NM_152742.1	0.737	0.079	0.325	-0.094	1.569
			0.797	0.123	0.579	-0.245	1.838
PTPRZ1	Protein Tyrosine Phosphatase, Receptor Type Z1 (Phosphacan)	NM_001206838.1	0.049	0.942	0.960	-1.350	1.447
			-0.302	0.701	0.907	-1.960	1.356
SPINT2	Serine peptidase inhibitor, Kunitz type 2 (Bikunin)	NM_001166103.1	-0.583	0.271	0.562	-1.664	0.498
			-0.208	0.708	0.907	-1.374	0.958
CHADL	Chondroadherin-like	NM_138481.1	-1.650	0.000	0.013	-2.389	-0.911
			-1.345	0.006	0.164	-2.226	-0.464
GPC3	Glypican 3	NM_001164617.1	-0.392	0.266	0.562	-1.111	0.327
			-0.172	0.673	0.907	-1.028	0.684
IMPG2	Interphotoreceptor matrix proteoglycan 2	NM_016247.3	-0.142	0.610	0.827	-0.719	0.435
			-0.039	0.900	0.976	-0.695	0.618
SPOCK1	Sparc/osteonectin, cwcv and kazal-like domains proteoglycan 1 (Testican 1)	NM_004598.3	-0.208	0.616	0.827	-1.065	0.650
			-0.404	0.346	0.736	-1.292	0.485
P3H1	Prolyl 3-hydroxylase 1 (Leprecan)	NM_001146289.1	-0.515	0.217	0.551	-1.364	0.333
			-0.253	0.574	0.907	-1.196	0.690

Gene	Name	Accession					
SDC1	Syndecan 1	NM_001006946.1	0.106	0.865	0.952	-1.193	1.405
			0.769	0.276	0.736	-0.688	2.226
IMPG1	Interphotoreceptor matrix proteoglycan 1	NM_001282368.1	-1.964	0.005	0.057	-3.233	-0.695
			-1.807	0.013	0.164	-3.164	-0.450
GPC5	Glypican 5	NM_004466.5	0.610	0.056	0.282	-0.016	1.236
			0.378	0.152	0.613	-0.157	0.913
OPTC	Opticin (Oculoglycan)	NM_014359.3	-0.125	0.664	0.827	-0.719	0.470
			0.120	0.692	0.907	-0.518	0.758
HAPLN1	Hyaluronan and proteoglycan link protein 1	NM_001884.3	-1.675	0.005	0.057	-2.777	-0.573
			-1.617	0.019	0.174	-2.918	-0.316
KERA	Keratocan	NM_007035.3	-0.193	0.472	0.759	-0.748	0.361
			-0.258	0.321	0.736	-0.797	0.281
EPYC	Epiphycan (Dermatan sulfate proteoglycan III)	NM_004950.4	-0.794	0.170	0.511	-1.964	0.376
			-0.757	0.272	0.736	-2.178	0.665
COL9A1	Collagen 9α1	NM_001851.4	0.000	0.998	0.998	-0.447	0.448
			-0.012	0.943	0.976	-0.364	0.340
PRG3	Proteoglycan 3	NM_006093.3	0.235	0.236	0.562	-0.169	0.638
			0.131	0.514	0.907	-0.288	0.549
SPOCK3	Sparc/osteonectin, cwcv and kazal-like domains proteoglycan 3 (Testican 3)	NM_001040159.1	0.255	0.497	0.763	-0.520	1.029
			0.521	0.195	0.613	-0.301	1.344
XYLT1	Xylosyltransferase I	NM_022166.3	0.074	0.905	0.954	-1.208	1.355
			0.081	0.916	0.968	-1.555	1.718

Gene	Description	Accession					
XYLT2	Xylosyltransferase II	NM_022167.3	0.308	0.429	0.732	-0.494	1.110
			0.279	0.524	0.752	-0.637	1.196
B4GALT7	Xylosylprotein beta 1.4-galactosyltransferase. polypeptide 7	NM_007255.2	-0.833	0.049	0.190	-1.663	-0.003
			-0.541	0.234	0.635	-1.475	0.393
B3GALT6	UDP-Gal:betaGal beta 1.3-galactosyltransferase polypeptide 6	NM_080605.3	-0.417	0.400	0.732	-1.435	0.602
			-0.160	0.789	0.892	-1.417	1.097
B3GAT1	Beta-1.3-glucuronyltransferase 1	NM_018644.3	0.013	0.959	0.993	-0.499	0.525
			0.080	0.774	0.892	-0.509	0.670
FAM20B	Family with sequence similarity 20, member B	NM_014864.3	0.974	0.163	0.418	-0.435	2.384
			0.920	0.277	0.639	-0.828	2.669
CHST3	Carbohydrate (chondroitin 6) sulfotransferase 3	NM_004273.4	-0.091	0.748	0.886	-0.681	0.499
			-0.245	0.450	0.720	-0.922	0.432
CHST10	Carbohydrate sulfotransferase 10	NM_004854.4	-1.377	0.000	0.004	-1.927	-0.826
			-1.285	0.002	0.115	-2.014	-0.557
CHSY1	Chondroitin sulfate synthase 1	NM_014918.4	-0.076	0.796	0.908	-0.690	0.537
			-0.089	0.788	0.892	-0.784	0.607
CHSY3	Chondroitin sulfate synthase 3	NM_175856.4	-1.961	0.003	0.050	-3.133	-0.790
			-1.663	0.033	0.266	-3.172	-0.153
CHPF2v1	Chondroitin polymerizing factor 2	NM_019015.2	-1.601	0.000	0.006	-2.322	-0.881
			-1.183	0.014	0.154	-2.088	-0.277
CHPF2v2	,,	NM_001284295.1	-0.573	0.009	0.075	-0.983	-0.163
			-0.322	0.163	0.610	-0.792	0.148
CHPF	Chondroitin polymerizing factor	NM_001195731.1	-0.561	0.038	0.159	-1.087	-0.036
			-0.726	0.017	0.154	-1.297	-0.154
CSGALNACT2	Chondroitin sulfate N-acetylgalactosaminyltransferase 2	NM_018590.4	0.165	0.420	0.732	-0.256	0.586
			0.240	0.327	0.675	-0.268	0.748

DSE	Dermatan sulfate epimerase	NM_001080976.1	0.129	0.655	0.883	-0.470	0.729
			0.256	0.464	0.722	-0.474	0.985
DSEL	Dermatan sulfate epimerase-like	NM_032160.2	-1.323	0.038	0.159	-2.561	-0.086
			-1.587	0.044	0.306	-3.122	-0.052
CHST7	Carbohydrate (N-acetylglucosamine 6-O) sulfotransferase 7	NM_019886.3	0.274	0.568	0.804	-0.720	1.268
			-0.078	0.870	0.937	-1.084	0.928
CHST9	Carbohydrate (N-acetylgalactosamine 4-0) sulfotransferase 9	NM_031422.5	-0.073	0.713	0.886	-0.487	0.340
			-0.094	0.674	0.859	-0.564	0.376
CHST11	Carbohydrate (chondroitin 4) sulfotransferase 11	NM_001173982.1	0.345	0.451	0.732	-0.597	1.287
			0.540	0.320	0.675	-0.583	1.663
CHST12	Carbohydrate (chondroitin 4) sulfotransferase 12	NM_001243794.1	-1.006	0.005	0.059	-1.666	-0.346
			-0.999	0.010	0.154	-1.717	-0.281
CHST13	Carbohydrate (chondroitin 4) sulfotransferase 13	NM_152889.2	0.310	0.451	0.732	-0.538	1.158
			0.669	0.138	0.610	-0.243	1.580
CHST14	Carbohydrate (N-acetylgalactosamine 4-0) sulfotransferase 14	NM_130468.3	0.686	0.290	0.674	-0.640	2.011
			0.506	0.423	0.706	-0.812	1.824
UST	Uronyl-2-sulfotransferase	NM_005715.2	-0.261	0.110	0.319	-0.586	0.065
			-0.265	0.156	0.610	-0.644	0.114
CHST15v1	Carbohydrate (N-acetylgalactosamine 4-sulfate 6-O) sulfotransferase 15	NM_015892.4	-0.213	0.398	0.732	-0.733	0.306
			0.057	0.820	0.901	-0.474	0.588
CHST15v4	,,	NM_001270765.1	-0.002	0.995	0.995	-0.717	0.713
			0.219	0.570	0.779	-0.591	1.029
EXTL1	Exostosin-like glycosyltransferase 1	NM_004455.2	-0.139	0.562	0.804	-0.636	0.358
			-0.015	0.957	0.991	-0.605	0.575
EXTL2	Exostosin-like glycosyltransferase 2	NM_001033025.2	-1.503	0.006	0.060	-2.519	-0.487
			-1.583	0.016	0.154	-2.814	-0.352

Gene	Description	Accession					
EXTL3	Exostosin-like glycosyltransferase 3	NM_001440.3	-0.612	0.108	0.319	-1.372	0.149
			-0.370	0.407	0.706	-1.300	0.559
EXT1	Exostosin glycosyltransferase 1	NM_000127.2	-0.438	0.038	0.159	-0.849	-0.026
			-0.356	0.127	0.610	-0.826	0.115
EXT2	Exostosin glycosyltransferase 2	NM_000401.3	-0.094	0.507	0.795	-0.385	0.198
			-0.187	0.233	0.635	-0.508	0.135
NDST1	N-deacetylase/N-sulfotransferase (heparan glucosaminyl) 1	NM_001543.4	-0.182	0.399	0.732	-0.626	0.262
			-0.008	0.973	0.991	-0.486	0.471
NDST2	N-deacetylase/N-sulfotransferase (heparan glucosaminyl) 2	NM_003635.3	-0.761	0.073	0.266	-1.602	0.080
			-0.545	0.244	0.635	-1.506	0.416
NDST3	N-deacetylase/N-sulfotransferase (heparan glucosaminyl) 3	NM_004784.2	1.380	0.022	0.140	0.228	2.532
			-	-	-	-	-
NDST4	N-deacetylase/N-sulfotransferase (heparan glucosaminyl) 4	NM_022569.1	0.285	0.453	0.732	-0.497	1.067
			0.509	0.229	0.635	-0.359	1.377
GLCE	Glucuronic acid epimerase	NM_015554.1	-0.284	0.166	0.418	-0.698	0.130
			-0.228	0.338	0.675	-0.722	0.265
HS2ST1	Heparan sulfate 2-O-sulfotransferase 1	NM_001134492.1	-0.221	0.687	0.886	-1.362	0.919
			-0.531	0.389	0.703	-1.815	0.752
HS6ST1	Heparan sulfate 6-O-sulfotransferase 1	NM_004807.2	-0.182	0.719	0.886	-1.231	0.868
			-0.001	0.999	0.999	-1.289	1.288
HS6ST2	Heparan sulfate 6-O-sulfotransferase 2	NM_001077188.1	0.192	0.582	0.804	-0.529	0.912
			0.250	0.541	0.757	-0.606	1.106
HS6ST3	Heparan sulfate 6-O-sulfotransferase 3	NM_153456.3	1.006	0.026	0.153	0.133	1.879
			-	-	-	-	-
HS3ST1	Heparan sulfate (glucosamine) 3-O-sulfotransferase 1	NM_005114.2	0.387	0.454	0.732	-0.680	1.454
			0.634	0.246	0.635	-0.491	1.758

HS3ST2	Heparan sulfate (glucosamine) 3-O-sulfotransferase 2	NM_006043.1	0.650	0.088	0.301	-0.108	1.408
			0.809	0.075	0.469	-0.094	1.712
HS3ST3B1	Heparan sulfate (glucosamine) 3-O-sulfotransferase 3B1	NM_006041.1	0.048	0.896	0.954	-0.717	0.813
			0.343	0.429	0.706	-0.562	1.249
HS3ST4	Heparan sulfate (glucosamine) 3-O-sulfotransferase 4	NM_006040.2	-	-	-	-	-
			-	-	-	-	-
HS3ST5	Heparan sulfate (glucosamine) 3-O-sulfotransferase 5	NM_153612.3	-0.262	0.185	0.448	-0.663	0.139
			-0.247	0.250	0.635	-0.689	0.195
HS3ST6	Heparan sulfate (glucosamine) 3-O-sulfotransferase 6	NM_001009606.3	0.002	0.993	0.995	-0.427	0.431
			0.061	0.796	0.892	-0.438	0.560
HAS1	Hyaluronan synthase 1	NM_001297436.1	-0.065	0.817	0.908	-0.649	0.519
			-0.247	0.378	0.703	-0.830	0.336
HAS2	Hyaluronan synthase 2	NM_005328.2	-0.461	0.547	0.804	-2.045	1.122
			-1.107	0.196	0.635	-2.856	0.641
HAS3v2	Hyaluronan synthase 3	NM_138612.2	-0.802	0.016	0.116	-1.435	-0.169
			-0.452	0.157	0.610	-1.100	0.196
HAS3v3	,,	NM_001199280.1	-1.141	0.034	0.159	-2.187	-0.095
			-0.473	0.373	0.703	-1.577	0.631
CHST1	Carbohydrate (keratan sulfate Gal-6) sulfotransferase 1	NM_003654.5	0.105	0.698	0.886	-0.455	0.664
			-0.074	0.779	0.892	-0.625	0.478
CHST2	Carbohydrate (N-acetylglucosamine-6-O) sulfotransferase 2	NM_004267.4	0.182	0.577	0.804	-0.495	0.859
			0.443	0.283	0.639	-0.409	1.296
CHST5		NM_000046.3	0.082	0.809	0.908	-0.621	0.784

Gene	Description	Accession					
	Carbohydrate (N-acetylglucosamine 6-O) sulfotransferase 5		0.256	0.481	0.729	-0.505	1.018
CHST6	Carbohydrate (N-acetylglucosamine 6-O) sulfotransferase 6	NM_001128204.1	-0.559	0.442	0.732	-2.055	0.938
			-0.950	0.285	0.639	-2.788	0.887
B3GNT2	UDP-GlcNAc:betaGal beta-1.3-N-acetylglucosaminyltransferase 2	NM_001161841.1	0.425	0.103	0.319	-0.096	0.945
			0.721	0.014	0.154	0.169	1.272
B3GNT3	UDP-GlcNAc:betaGal beta-1.3-N-acetylglucosaminyltransferase 3	NM_014960.4	1.166	0.004	0.059	0.417	1.915
			0.809	0.075	0.469	-0.094	1.712
B3GNT4	UDP-GlcNAc:betaGal beta-1.3-N-acetylglucosaminyltransferase 4	NM_001098540.2	-0.515	0.164	0.418	-1.261	0.232
			-0.249	0.519	0.752	-1.058	0.560
B3GNT7	UDP-GlcNAc:betaGal beta-1.3-N-acetylglucosaminyltransferase 7	NM_000199.3	-0.140	0.740	0.886	-1.020	0.739
			0.184	0.671	0.859	-0.726	1.094
B4GALT4v2	UDP-Gal:betaGlcNAc beta 1.4-galactosyltransferase. polypeptide 4	NM_152419.2	0.094	0.830	0.908	-0.815	1.003
			0.141	0.779	0.892	-0.917	1.198
B4GALT4v1	´´	NM_000263.3	-0.654	0.326	0.728	-2.019	0.712
			-0.323	0.675	0.859	-1.942	1.296
ARSBv1	Arylsulfatase B	NM_000046.3	-0.303	0.471	0.565	-1.172	0.565
			-0.155	0.755	0.840	-1.199	0.890
ARSBv2	´´	NM_198709.2	-0.151	0.862	0.899	-1.955	1.653
			0.282	0.770	0.840	-1.747	2.311
SULF1	Sulfatase 1	NM_003773.4	-0.112	0.613	0.700	-0.570	0.346
			-0.324	0.146	0.350	-0.775	0.128
SULF2v2	Sulfatase 2	NM_198596.2	-0.766	0.043	0.172	-1.506	-0.027
			-0.900	0.052	0.214	-1.809	0.009
SULF2v3	´´		0.437	0.059	0.203	-0.019	0.894

		NM_00116184 1.1	0.523	0.036	0.214	0.038	1.009
ARSG	Arylsulfatase G	NM_000404.2	-0.259	0.311	0.434	-0.782	0.264
			-0.137	0.663	0.837	-0.799	0.525
HPSE	Heparanase	NM_000512.4	0.809	0.221	0.385	-0.534	2.153
			1.002	0.203	0.392	-0.610	2.615
SGSH	N-sulfoglucosamine sulfohydrolase	NM_000202.6	0.353	0.273	0.410	-0.304	1.010
			0.512	0.136	0.350	-0.182	1.205
HGSNAT	Heparan-alpha-glucosaminide N-acetyltransferase	NM_000203.4	-0.438	0.240	0.385	-1.197	0.322
			-0.028	0.941	0.941	-0.817	0.762
NAGLU	N-acetylglucosaminidas e, alpha	NM_000520.4	0.345	0.104	0.300	-0.079	0.769
			0.357	0.129	0.350	-0.118	0.832
HYAL1	Hyaluronidase 1	NM_000521.3	0.237	0.325	0.434	-0.257	0.731
			0.355	0.165	0.360	-0.165	0.874
HYAL2	Hyaluronidase 2	NM_000181.3	-0.114	0.856	0.899	-1.412	1.185
			0.131	0.840	0.876	-1.233	1.495
HYAL3	Hyaluronidase 3	NM_002076.3	0.672	0.041	0.172	0.031	1.312
			0.446	0.222	0.392	-0.303	1.195
GLB1	Galactosidase, beta 1	NM_198150.2	0.040	0.942	0.942	-1.106	1.186
			0.434	0.394	0.557	-0.626	1.494
GALNS	Galactosamine (N-acetyl)-6-sulfatase	NM_000046.3	-0.484	0.138	0.300	-1.139	0.171
			-0.114	0.730	0.840	-0.810	0.582
IDSv1	Iduronate 2-sulfatase	NM_000202.6	-0.221	0.158	0.316	-0.536	0.095
			-0.223	0.245	0.392	-0.618	0.172
IDSv2	ʹʹ	NM_006123.4	-0.652	0.001	0.034	-1.014	-0.291
			-0.485	0.027	0.214	-0.907	-0.063
IDUA	Iduronidase, alpha-L-	NM_00116184 1.1	0.801	0.020	0.162	0.141	1.461
			0.440	0.241	0.392	-0.332	1.211
HEXA	Hexosaminidase A	NM_014960.4	0.771	0.008	0.101	0.225	1.318
			0.935	0.003	0.074	0.374	1.496
HEXB	Hexosaminidase B	NM_00109854 0.2	0.182	0.227	0.385	-0.125	0.489
			0.294	0.052	0.214	-0.003	0.590
GUSBv1	Glucuronidase, beta	NM_000181.3	0.115	0.398	0.503	-0.165	0.394
			0.123	0.438	0.584	-0.208	0.453
GUSBv2	ʹʹ	NM_00128429 0.1	0.369	0.136	0.300	-0.128	0.866
			0.466	0.096	0.329	-0.094	1.026

GNS	Glucosamine (N-acetyl)-6-sulfatase	NM_152419.2	0.628	0.128	0.300	-0.200	1.456
			0.448	0.348	0.523	-0.543	1.439
ARSK	Arylsulfatase K	NM_000263.3	1.536	0.039	0.172	0.091	2.981
			1.720	0.054	0.214	-0.030	3.470

* Abbreviations: FC=fold change, CI=confidence interval.

Core proteins	
GAG anabolism-associated enzymes	
GAG catabolism-associated enzymes	

3.7 Co-expression analysis of mRNA signal intensities of core proteins and GAG metabolism-associated enzymes with inflammation-, smooth muscle cell-, collagen- and calcification-related markers

It was further investigated whether the signal intensity levels of the 148 mRNAs coding for PG core proteins and GAG metabolism-associated enzymes correlate with those of markers representing (I) Pro-inflammatory cytokines and immune cell markers, (II) VSMCs (contractile phenotype), (III) Calcification and (IV) Collagen types (Figure 16).
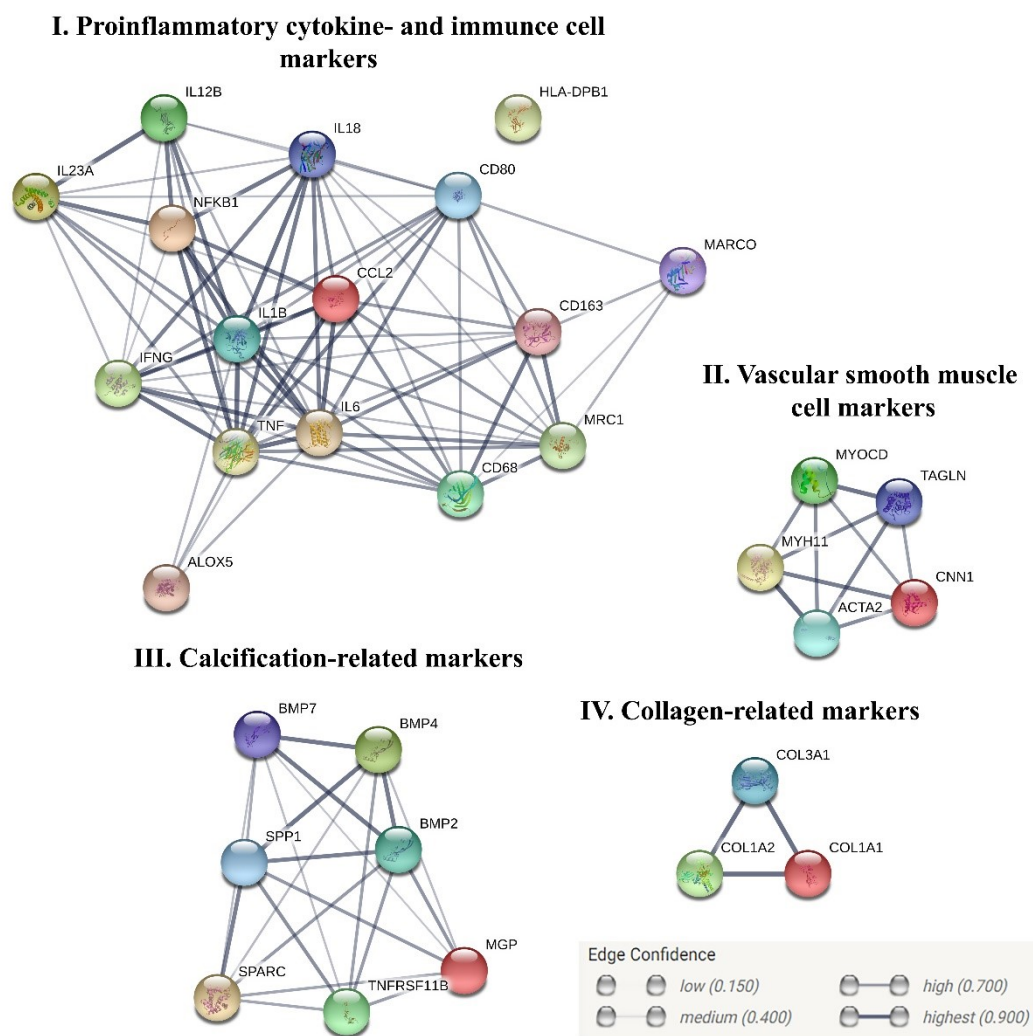

Figure 16. Protein-protein interaction networks of markers chosen to represent inflammation, vascular smooth muscle cells, the calcification process and collagens. Nodes indicate the selected markers with their name. The edges represent protein-protein associations. Line thickness indicates the strength of data support (e.g. text mining, model simulations, experiments etc.) as expressed in terms of confidence measures. Networks and legend were

constructed using the STRING database (https://string-db.org/). Abbreviations: IL12B= Interleukin 12 beta, IL23A= Interleukin 23A, IL18= Interleukin 18, NFKB1= Nuclear factor kappa B Subunit 1, IL1B= Interleukin 1 beta, IFNG= Interferon γ, CCL2= C-C Motif Chemokine Ligand 2 (known as Monocyte Chemoattractant Protein-1=MCP1), CD80= CD80 Antigen (CD28 Antigen Ligand 1, B7-1 Antigen), HLA-DPB1= Major Histocompatibility Complex, Class II, DP Beta, TNF= Tumor Necrosis Factor, IL6= Interleukin 6, CD163= CD163 Molecule/Hemoglobin Scavenger Receptor, ALOX5= Arachidonate 5-Lipoxygenase, CD68= Macrophage Antigen CD68, MRC1= Mannose Receptor C-Type 1, MARCO= Macrophage Receptor With Collagenous Structure, MYOCD= Myocardin, TAGLN= Transgelin/Smooth Muscle Protein 22-Alpha, CNN1= Calponin 1, ACTA2= Actin Alpha 2, Smooth Muscle, MYH11= Myosin Heavy Chain 11, BMP7= Bone Morphogenetic Protein 7, BMP4= Bone Morphogenetic Protein 4, BMP2= Bone Morphogenetic Protein 2, SPP1= Secreted Phosphoprotein 1/Osteopontin, SPARC= Secreted Protein Acidic And Cysteine Rich/Osteonectin, MGP= Matrix Gla Protein, TNFRSF11B= TNF Receptor Superfamily Member 11b/Osteoprotegerin, COL3A1= Collagen Type III Alpha 1 Chain, COL1A1= Collagen Type I Alpha 1 Chain, COL1A2= Collagen Type I Alpha 2 Chain.

Correlation analyses with subsequent agglomerative hierarchical clustering were performed using the mRNA signal intensities from all 13 samples. The results are presented as heatmaps with integrated dendrograms (Figures 17-19).

According to their coefficients, the markers clustered in two or three groups, respectively.

53 members of the core protein-coding mRNAs associated to inflammation-related markers (clusters A1, B1-B4 in Figure 17.). In particular, COL15A1, SRGN, EPYC and CD44i8 clustered together with the majority of inflammation-related markers forming cluster B3.

From the remaining groups, cluster A1 (containing the immune cell-associated CD80 and the core proteins AGRN, NRP1, GPC4, GPC6, GPC3, ECM2i2, CD44i5 and SDC3) showed an antithetical behavior towards cluster B4 (containing the inflammation marker-associated IL23A and the core proteins COL9A2, SPOCK2v3, HAPLN1, HAPLN4, BCAN, COL12A1, PODN, TGFBR3, LUM, DCN, IMPG1, COL9A3, TSKU, SPINT2, ESM1 and GPC5) and towards clusters B1 (containing the inflammation marker-associated IFNG and the core proteins CSPG4, GPC2, GPC1, SDC1, PTPRZ1v2 and SPOCK1) and -B2 (containing the inflammation marker-associated NFKB1i2, IL12B and the core proteins SDC2, HAPLN2, SPOCK3, CHAD, NYX, SPOCK2v1, PRG4, OPTC, IMPG2, NCAN, PRG2, COL9A1, PRG3, P3H1, PODNL1, KERA and CHADL).

12 core protein-coding mRNAs (ACAN, ASPN, BGN, HAPLN3, SDC4, HSPG2, FMOD, COL18A1, VCAN3v3, PRELP, OMD and OGN) were found to cluster together with the majority of VSMC-, calcification- and collagen-associated markers in cluster A2.
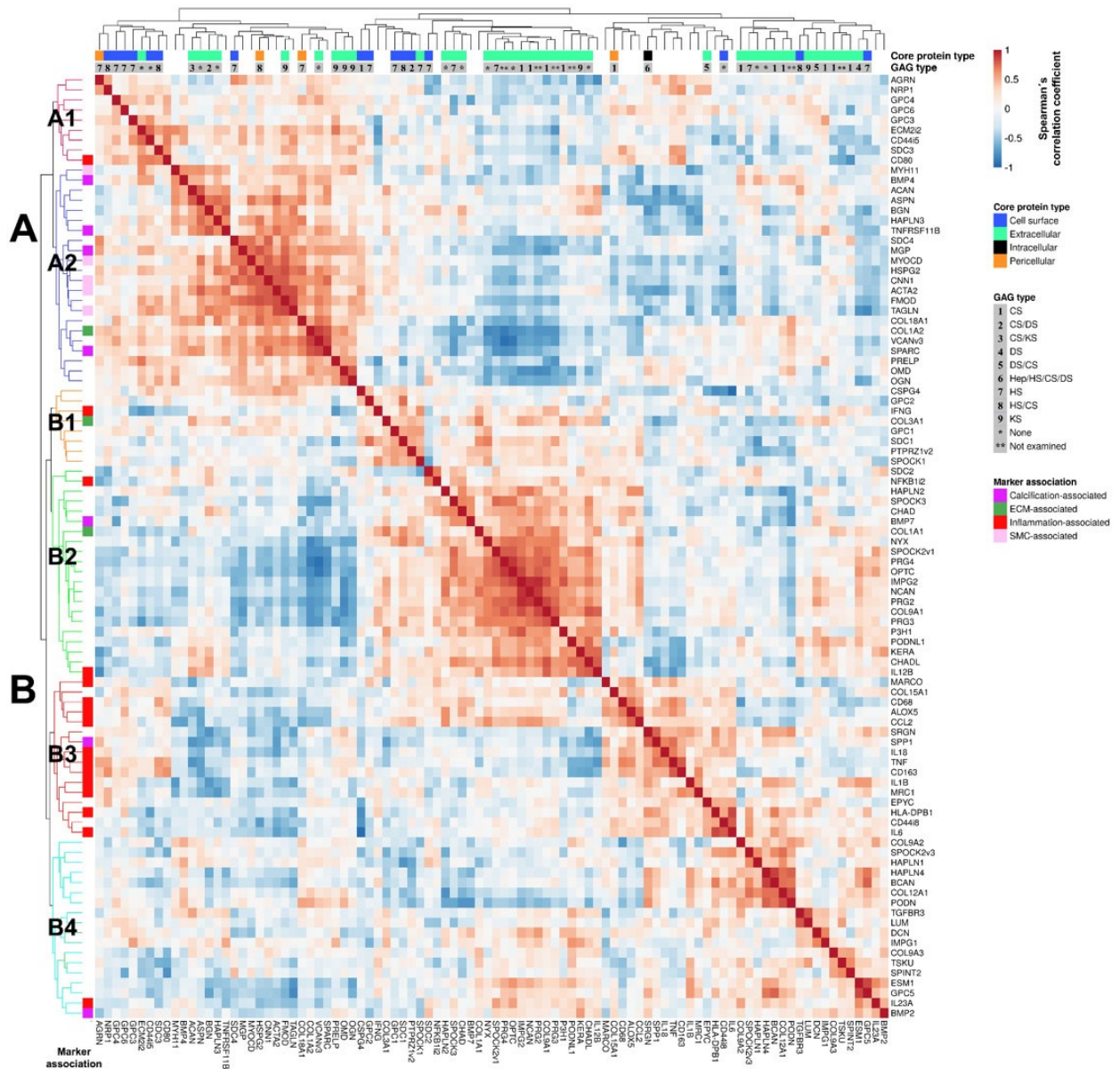
Figure 17. Correlation between mRNA expression levels of PG core proteins and inflammation-/VSMC-/collagen- and calcification-associated markers. Heatmap showing the correlations between the signal intensities of 63 mRNAs coding for PG core proteins and 30 representative mRNAs related to inflammation, VSMCs, collagen and calcification. The coefficients are displayed as different color tones according to the color key. The dendrograms were created by using the average linkage/Euclidean distance metric clustering methodology. Letters A and B denote the major clustering groups, while subgroups carry an additional number. The core protein- (blue=cell surface, turquoise= extracellular, black= intracellular and orange= pericellular) and GAG type (1: CS, 2: CS/DS, 3: CS/KS, 4: DS, 5: DS/CS, 6: Hep/HS/CS/DS, 7: HS, 8: HS/CS, 9: KS, *: no chains, **: not examined) is depicted underneath the upper dendrogram. The marker's category (purple: calcification, dark green: ECM-/collagen, red: inflammation, pink: VSMCs) is shown underneath the side dendrogram.

94

Correlation analyses of the GAG anabolism-associated enzymes with the aforementioned markers revealed the formation of three major groups (Figure 18).

Clusters A and -C2 contained all the inflammation-associated markers except for CD80, which is found in cluster B.

Cluster B contains most of the VSMC- and calcification-related markers and shows an opposing behavior towards cluster A.

In cluster A the signal intensity of the markers IL23A, ALOX5, CCL2, NFKB1i2, IL12B and IFNG correlated positively with B3GAT1, B4GALT7 and FAM20B (tetrasaccharide linker region biosynthesis), with CHST15, CHST9, CHSY3, CHPF2 and CHSY1 (CS/DS biosynthesis), with HS3ST3B1, HS3ST5, EXTL1, HS3ST6, NDST1, HS6ST2 and GLCE (HS/Hep biosynthesis), with CHST2, B4GALT4 and CHST5 (KS biosynthesis), as well as with HAS1 (HA biosynthesis). Cluster C2 contained the rest of the inflammation-associated markers, namely MRC1, MARCO, TNF, CD163, CD68, IL18, IL1B, IL6 and HLA-DPB1. These clustered together with XYLT2 (tetrasaccharide linkage region synthesis), DSE, CHST13, CSGALNACT2, CHST11 (CS/DS anabolism), HS3ST1, NDST4, HS3ST2, HS2ST1 (HS/Hep anabolism), as well as B3GNT2 and B3GNT7 (KS biosynthesis).

The majority of the remaining GAG anabolism-associated enzymes (XYLT1, CHST6, B3GALT6, HAS3, NDST2, B3GNT4, B4GALT4v2, B3GAT1v2, HS6ST1, HAS2, EXT2, EXTL3, CHST12, EXTL2, CHPF, DSEL, HS3ST4, UST, EXT1 and CHST10) formed cluster B together with the VSMC-, collagen- and calcification-related markers.

Collagen markers COL1A1 and -COL3A1 clustered with the inflammation-associated cluster A, while COL1A2 was grouped together with CHST1, CHST7, CHST3, HS6ST3, B3GNT3 and NDST3 in cluster C1.

The correlation analyses between the signal intensities of the markers and the GAG catabolism-associated enzymes revealed a clustering into two major groups (see Figure 19).

Cluster A included all the VSMC-, collagen- and calcification- related markers except for SPP1, BMP7, BMP2, COL3A1 and COL1A1. Inside this group, only 2 GAG-catabolism associated enzymes were present, namely SULF1 (HS post-synthetic modification/-catabolism) and IDS (unspecific; involved in more than one catabolism pathway).
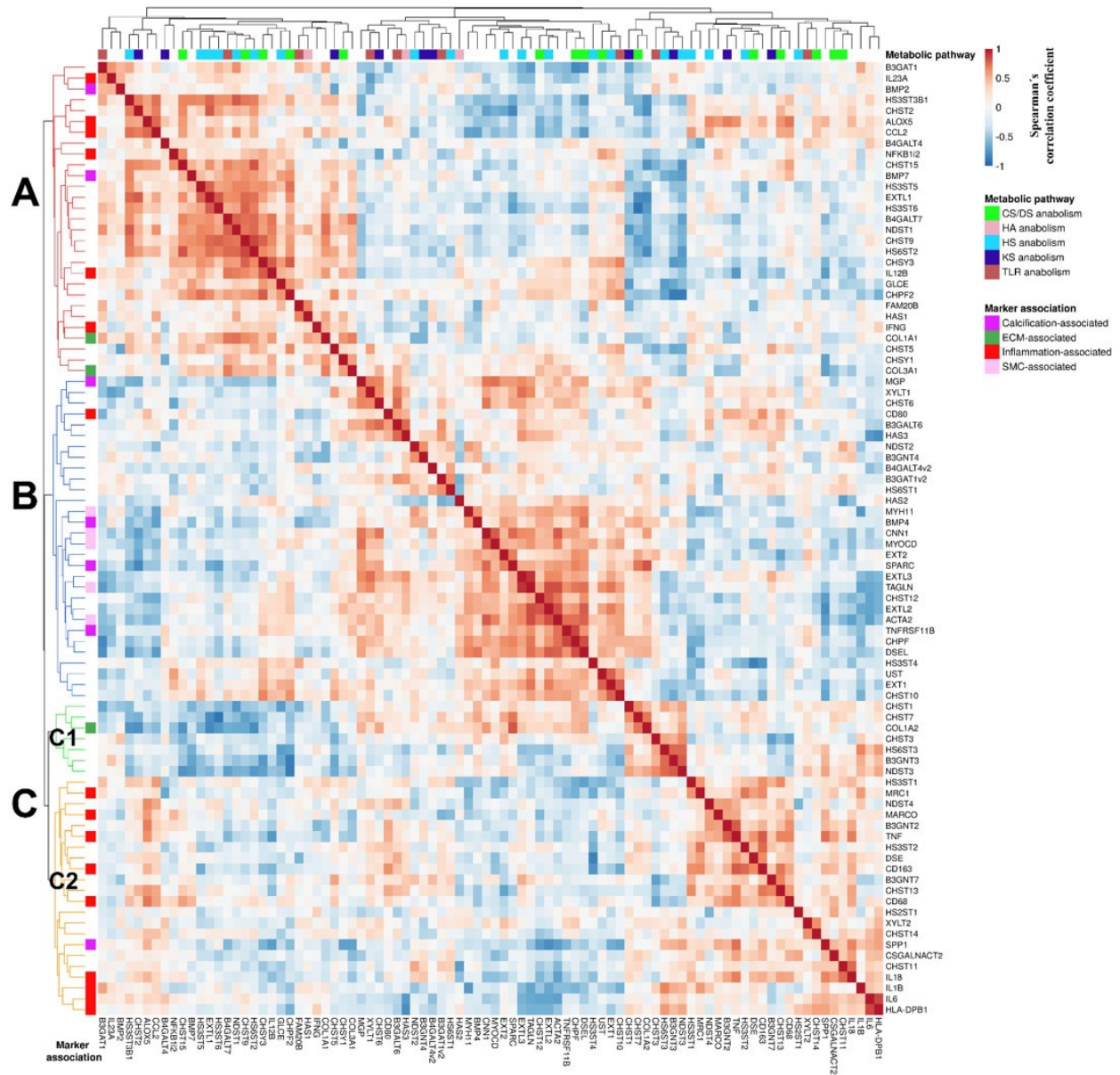
Figure 18. Correlation between mRNA expression levels of GAG-anabolism related enzymes and inflammation-/macrophage-/VSMC-/collagen- and calcification-associated markers. Heatmap showing the correlations between the signal intensities of 63 mRNAs coding for GAG anabolism-related enzymes and 30 representative mRNAs related to inflammation-/macrophages, smooth muscle cells, collagen and calcification. The coefficients are displayed as different color tones according to the provided color key. The dendrograms were created by using the average linkage method/Euclidean distance metric clustering methodology. Letters A, B and C denote the major clustering groups, while subgroups are annotated with an additional number. The GAG anabolism pathways in which the enzymes are involved (light green= CS/DS, salmon= HA, light blue= HS/Hep, dark blue= KS, brown= tetrasaccharide linkage region synthesis), are depicted underneath the upper dendrogram. The marker's category (purple: calcification, dark green: extracellular matrix-/collagen, red: inflammation- /macrophages, pink: VSMCs) is shown underneath the side dendrogram.

Cluster B contained 5 sub-clusters, which included all inflammation-related markers.

In sub-cluster B1 (containing the inflammation markers IL12B and IFNG, the collagen-related COL3A1 and COL1A1, as well as the calcification-related markers BMP2 and BMP7) three GAG catabolism-related enzymes were included, namely HGSNAT (HS catabolism), GUSB (CS-, DS- and HS-catabolism) and GALNS (unspecific; involved in more than one catabolism pathway). Sub-cluster B2 contained the markers IL6, HLA-DPB1, IL23A and IL1B, along with the HA catabolism-related HYAL1 and HYAL3, as well as GNS and IDUA, which are involved in multiple catabolism pathways. Sub-clusters B1 and -B2 showed a more similar clustering pattern as compared to sub-clusters B3, B4 and B5. Sub-cluster B3 was a small cluster containing NFKB1i2 and the CS/DS- and HS catabolism-related ARSB and ARSG respectively. Sub-clusters B4 and -B5 seemed to be more tightly connected. Sub-cluster B4 contained the inflammation-associated CD163, TNF, IL18 and MARCO, as well as the GAG catabolism-related NAGLU, SGSH, HPSE (HS catabolism), HYAL2 (HA catabolism) and HEXA (unspecific; involved in more than one catabolism pathways). The last sub-cluster (B5) included the markers CD80, MRC1, CD68, ALOX5 and CCL2, together with GLB1 (KS catabolism), SULF2 (HS catabolism) and ARSK, HEXB (unspecific; involved in more than one catabolism pathways).

The 20 mRNAs that showed higher intensity levels when comparing HV versus LV and HI versus LI lesions (Chapter 3.6) were found to cluster in the following groups: SRGN was part of sub-cluster B3 that included the markers MARCO, CD68, ALOX5, CCL2, IL18, TNF, CD163, IL1B, MRC1, HLA-DPB1, IL6 and SPP1, while ASPN was part of sub-cluster A2, together with MYH11, BMP4, TNFRSF11B, MGP, MYOCD, CNN1, ACTA2, TAGLN, SPARC and COL1A2. PODNL1 and CHADL were included in cluster B2, together with NFKB1i2, BMP7, COL1A1, and IL12B. HAPLN1 and IMPG1 were part of the cluster B4, together with COL9A3, IL23A and BMP2 (see Figure 17). Regarding the GAG anabolism-associated enzymes, CHSY3 was found inside cluster A, together with IL23A, ALOX5, CCL2, IL12B, IFNG, BMP7, BMP2, COL1A1 and COL3A1. CHST12, EXTL2, DSEL, CHST10 and HAS3 clustered together with the smooth muscle cell-/calcification-associated markers MYH11, BMP4, CNN1, MYOCD, TAGLN, ACTA2, SPARC and TNFRSF11B (see Figure 18). The GAG catabolism-related HPSE was found in sub-cluster B4, together with the macrophage-/inflammation-associated CD163, TNF, IL18 and MARCO. ARSK clustered together with CD80, MRC1, CD68, ALOX5 and CCL2 (see Figure 19). A summary of the correlation results between the mRNA signal intensities of these 20 molecules and the markers are shown in Tables 12 and -13.

Thus, the differential expression analysis results are in line with the correlation analyses and may indicate the existence of instability- and stability-related PG/GAG-associated patterns.
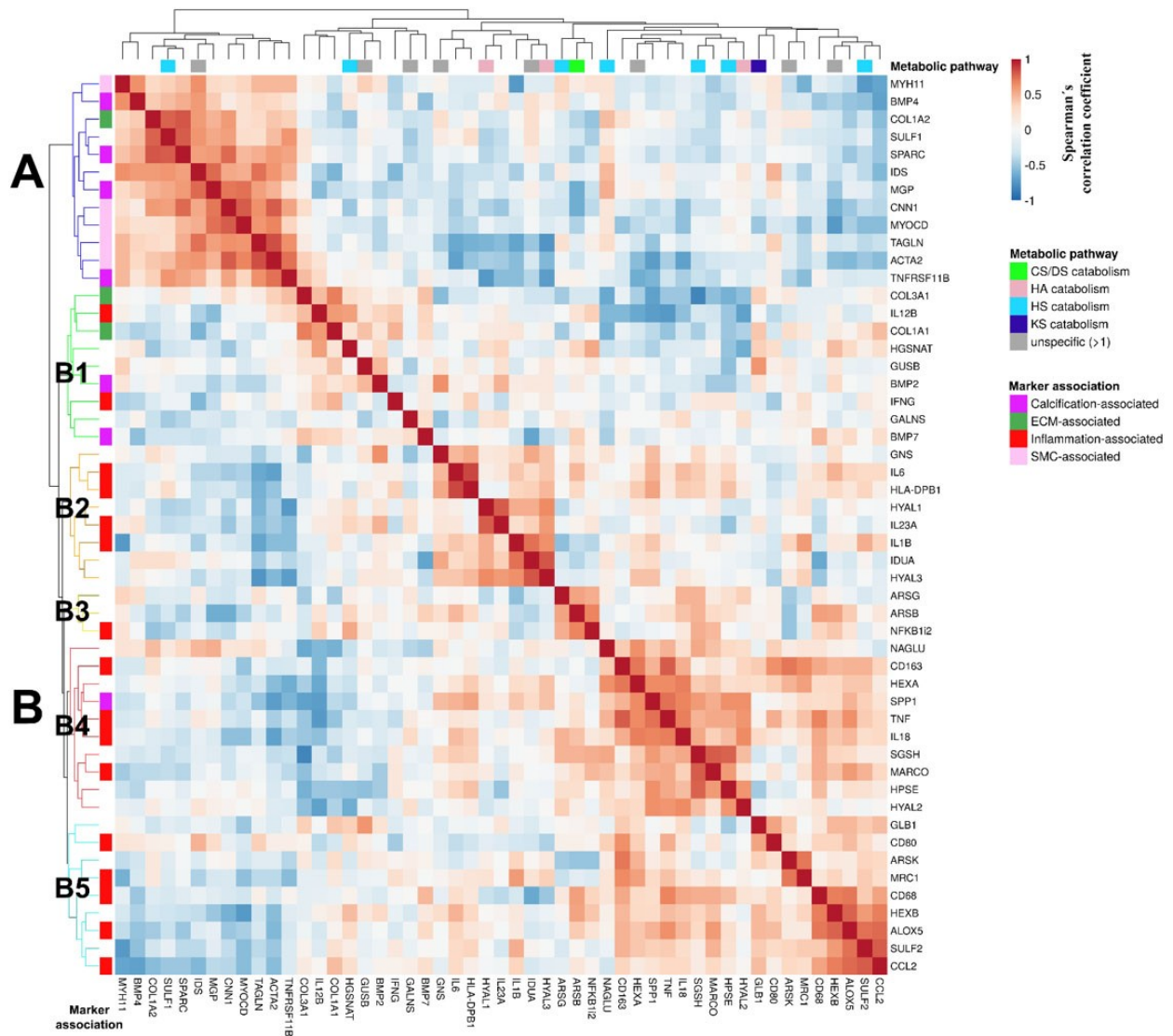
Figure 19. Correlation between mRNA expression levels of GAG-catabolism related enzymes and inflammation-/macrophage-/VSMC-/collagen- and calcification-associated markers. Heatmap showing the correlations between the signal intensities of 24 mRNAs coding for GAG catabolism-related enzymes and 30 representative mRNAs related to inflammation-/macrophages, smooth muscle cells, collagen and calcification. The coefficients are displayed as different color tones according to the provided color key. The dendrograms were created by using the average linkage method/Euclidean distance metric clustering methodology. Letters A, B and C denote the major clustering groups, while subgroups are annotated with an extra number. The GAG catabolism pathways in which the enzymes are involved (light green= CS/DS, salmon= HA, light blue= HS/Hep, dark blue: KS, grey: multiple pathways/unspecific) are depicted underneath the upper dendrogram. The markers' category (purple: calcification, dark green: extracellular matrix-/collagen, red: inflammation-/macrophages, pink: VSMCs) is presented underneath the side dendrogram.

Table 12. mRNA correlation analysis results between the core proteins and GAG metabolism-associated enzymes that showed a ≥ 1 log2 fold change in the differential expression analysis results of chapter 3.6. and the proinflammatory and immune cell markers group. The red colored boxes depict correlations with Spearman´s ρ ≥ + 0.5. The light green colored boxes display correlations with Spearman´s ρ ≤ - 0.5. Bold characters point out correlations with q values ≤ 0.05.

	ALOX5	CCL2	IL6	IL1B	TNF	IL12B	IL23A	IFNG	IL18	NFKB1i2	CD68	CD163	HLADPB1	MARCO	CD80	MRC1
SRGN	0.29	0.14	0.51	0.56	0.47	-0.50	0.25	-0.22	0.48	-0.34	0.01	0.53	0.61	0.08	0.11	0.43
NRP1v2	-0.07	-0.05	-0.17	-0.08	0.52	-0.42	-0.33	-0.06	0.35	-0.48	0.31	0.63	-0.07	-0.16	0.29	0.50
NDST3	-0.24	-0.33	0.36	0.48	0.12	-0.50	0.04	-0.12	0.16	-0.40	-0.41	0.04	0.53	-0.02	-0.20	0.06
B3GNT3	-0.14	-0.33	0.29	0.51	0.07	-0.39	0.40	-0.09	0.20	-0.19	-0.49	0.13	0.44	0.05	-0.01	0.25
HS6ST3	-0.11	-0.06	0.41	0.67	0.01	-0.24	0.05	0.27	0.08	-0.24	-0.42	0.00	0.59	0.24	-0.24	0.25
ARSK	0.15	0.34	-0.28	0.36	0.28	-0.27	-0.02	0.04	0.10	-0.52	0.07	0.71	-0.13	-0.10	0.26	0.70
HPSE	0.27	0.15	0.35	0.05	0.53	-0.49	-0.50	0.18	0.45	0.01	0.45	0.13	0.43	0.60	-0.16	0.02
PODNL1	-0.38	-0.11	-0.07	-0.05	-0.62	0.49	0.33	0.18	-0.35	-0.12	-0.51	-0.62	-0.13	-0.49	-0.47	-0.40
ASPN	-0.64	-0.66	-0.24	-0.53	-0.69	0.45	-0.23	0.16	-0.58	0.16	-0.35	-0.69	-0.17	-0.37	-0.26	-0.61
CHADL	-0.20	0.08	-0.18	-0.33	-0.64	0.78	0.24	0.20	-0.39	0.32	-0.13	-0.67	-0.40	-0.33	-0.37	-0.41
HAPLN1	-0.24	-0.52	0.26	0.01	-0.01	0.15	0.24	-0.29	-0.16	0.30	-0.17	-0.40	0.07	0.05	-0.12	-0.16
IMPG1	-0.06	0.15	0.06	0.03	-0.21	0.20	-0.01	-0.30	-0.27	-0.39	-0.16	-0.28	-0.13	-0.55	-0.11	-0.38
CHST12	-0.60	-0.64	-0.67	-0.49	-0.42	0.29	0.00	-0.05	-0.57	-0.15	-0.35	-0.21	-0.60	-0.56	0.10	-0.17
HAS3v3	-0.05	0.12	-0.73	-0.20	0.09	-0.16	-0.13	-0.35	-0.09	-0.36	-0.03	0.29	-0.78	-0.31	0.50	0.06
DSEL	-0.42	-0.72	-0.45	-0.51	-0.20	0.02	-0.31	-0.22	-0.41	0.06	-0.24	-0.18	-0.32	-0.16	0.40	-0.39
CHST10	-0.42	-0.22	-0.19	-0.61	-0.52	0.46	-0.25	0.20	-0.26	0.26	0.00	-0.63	-0.31	-0.31	-0.36	-0.56
EXTL2	-0.44	-0.49	-0.66	-0.64	-0.31	0.29	-0.32	-0.01	-0.45	0.16	-0.07	-0.15	-0.61	-0.25	0.32	-0.22
CHPF2v1	0.05	0.16	-0.39	-0.51	-0.20	0.43	-0.07	0.03	-0.25	0.31	0.24	-0.33	-0.61	-0.06	-0.01	-0.35
CHSY3	-0.13	0.11	-0.09	-0.38	-0.46	0.78	-0.12	0.39	-0.40	0.50	0.14	-0.54	-0.24	-0.02	-0.33	-0.28
HAS2	-0.27	-0.36	0.00	-0.04	-0.38	0.37	-0.18	0.35	-0.53	0.24	-0.21	-0.20	0.20	0.09	-0.05	-0.05

Table 13. mRNA correlation analysis results between the core proteins and GAG metabolism-associated enzymes that showed a ≥ 1 log2 fold change in the differential expression analysis results of chapter 3.6. and the VSMC-, calcification and collagen-related markers group. The red colored boxes depict correlations with Spearman´s ρ ≥ + 0.5. The light green colored boxes display correlations with Spearman´s ρ ≤ - 0.5. Bold characters point out correlations with q values ≤ 0.05.

	ACTA2	CNN1	MYH11	MYOCD	TAGLN	SPARC	BMP4	BMP2	MGP	TNFRSF11B	BMP7	SPP1	COL1A1	COL1A2	COL3A1
SRGN	-0.67	-0.38	-0.20	-0.56	-0.66	-0.13	-0.10	0.38	-0.12	-0.48	-0.29	0.76	-0.20	0.26	-0.45
NRP1v2	0.02	0.13	-0.05	-0.14	0.20	0.28	0.10	-0.33	0.15	0.00	0.15	0.09	-0.31	0.45	0.03
NDST3	-0.20	0.12	0.00	0.02	-0.29	0.29	0.25	0.08	0.27	-0.17	-0.71	0.54	-0.41	0.53	-0.53
B3GNT3	-0.35	-0.18	0.01	-0.20	-0.48	0.08	0.36	0.13	0.13	-0.49	-0.67	0.49	-0.19	0.29	-0.41
HS6ST3	-0.28	-0.13	-0.43	-0.21	-0.48	-0.01	0.04	-0.07	-0.06	-0.28	-0.60	0.45	0.01	0.14	-0.29
ARSK	-0.18	0.06	-0.37	-0.33	-0.20	-0.02	-0.31	0.13	0.04	-0.40	0.07	0.13	0.30	0.18	0.17
HPSE	-0.24	-0.02	-0.34	0.11	0.00	-0.18	-0.40	-0.46	0.05	-0.09	-0.01	0.62	-0.50	-0.03	-0.61
PODNL1	0.07	-0.13	-0.01	0.02	-0.23	-0.31	0.05	0.28	-0.40	0.17	0.28	-0.36	0.31	-0.34	0.42
ASPN	0.76	0.58	0.64	0.70	0.57	0.60	0.49	-0.16	0.33	0.68	-0.07	-0.69	-0.04	0.26	0.26
CHADL	0.19	-0.13	0.10	0.11	0.06	-0.31	-0.05	0.20	-0.44	0.23	0.50	-0.66	0.44	-0.57	0.48
HAPLN1	0.05	-0.20	0.31	0.13	0.03	0.15	0.50	0.12	-0.04	0.10	-0.20	0.04	-0.56	0.24	-0.42
IMPG1	0.12	0.08	0.01	-0.02	0.04	0.09	0.10	0.30	-0.05	0.54	0.20	-0.28	0.06	0.08	0.48
CHST12	0.71	0.46	0.56	0.48	0.52	0.44	0.50	-0.02	0.31	0.39	0.24	-0.71	-0.02	0.34	0.47
HAS3v3	0.30	0.20	0.07	0.03	0.48	0.08	0.21	-0.04	0.28	0.11	0.02	-0.39	-0.05	0.09	0.35
DSEL	0.77	0.45	0.66	0.49	0.73	0.61	0.72	-0.20	0.55	0.60	-0.28	-0.47	-0.44	0.51	0.10
CHST10	0.55	0.44	0.40	0.56	0.58	0.33	0.20	-0.32	0.10	0.58	0.20	-0.67	0.10	-0.10	0.32
EXTL2	0.83	0.50	0.56	0.47	0.83	0.55	0.51	-0.27	0.38	0.55	0.02	-0.78	-0.08	0.29	0.36
CHPF2v1	0.33	0.03	0.05	0.26	0.41	-0.24	-0.14	-0.17	-0.13	0.31	0.64	-0.54	0.20	-0.49	0.45
CHSY3	0.36	0.02	-0.02	0.16	0.24	-0.13	-0.23	-0.04	-0.42	0.42	0.48	-0.60	0.42	-0.42	0.38
HAS2	0.50	0.34	0.15	0.22	0.15	0.42	0.10	-0.03	0.10	0.37	-0.15	-0.29	0.27	0.27	0.20

3.8 Alterations in the distribution of glycosaminoglycans between atherosclerotic lesions of varying instability and morphology

In an attempt to biochemically characterize the GAG molecules and their disaccharide units, adjacent sections to those used for histology/immunohistochemistry (Figure 3) were obtained for GAG extraction, subsequent enzymatic digestion into disaccharide units and HPLC analysis. Figure 20 shows the cumulative results of the disaccharide unit analyses of 21 carotid atherosclerotic plaques.

Peaks 5 (Median: 40.08, $25^{th}/70^{th}$ percentile: 35.66/43.49) and 7 (Median: 27.59, $25^{th}/70^{th}$ percentile: 23.27/29.89) were the most prominent ones, followed by peaks 9 (Median: 12.12, $25^{th}/70^{th}$ percentile: 10.82/13.89), 10 (Median: 5.36, $25^{th}/70^{th}$ percentile: 4.35/6.45) and 8 (Median: 4.70, $25^{th}/70^{th}$ percentile: 4.17/5.83). The rest of the peaks had values below 5 % and were not taken into account in the upcoming comparison results.
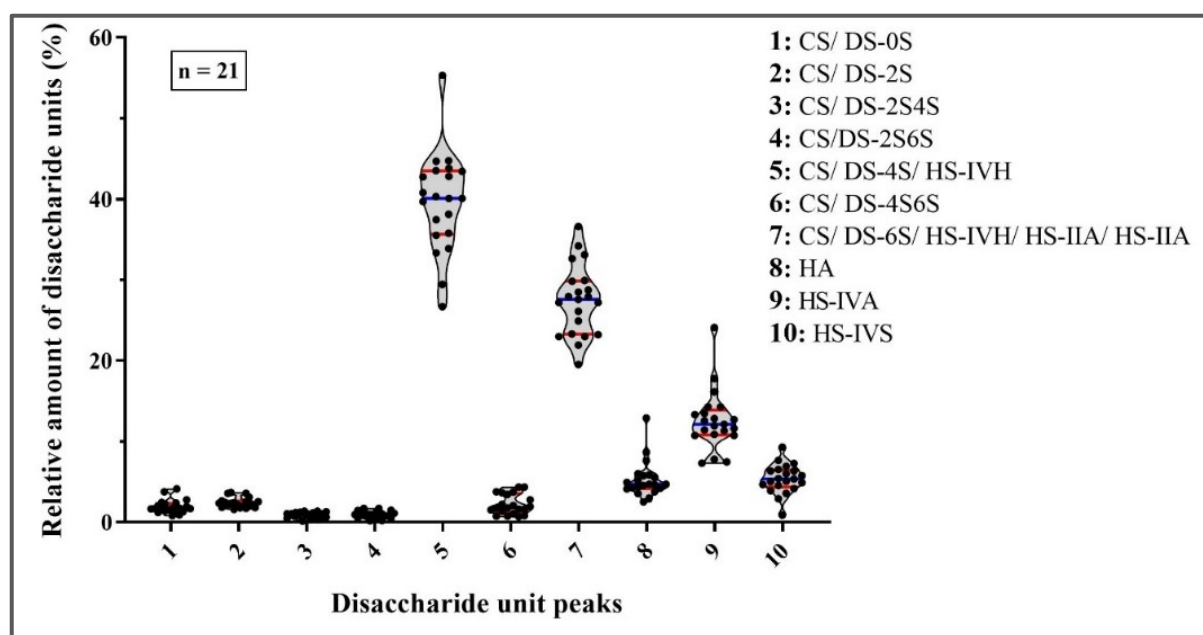

Figure 20. Disaccharide unit peaks detected inside atherosclerotic lesions. Violin plots showing the cumulative results of the disaccharide unit analyses of 21 atherosclerotic plaques irrespective of plaque morphology. The different peaks (x axis) portray different types of disaccharide units. Blue and red lines of the plots represent median and $25^{th}/75^{th}$ percentiles, respectively. The plot borders depict the 10th and 90th percentiles. Abbreviations: CS/DS: chondroitin/dermatan sulfate, HS: heparan sulfate, HA: hyaluronic acid, xS: sulfate group on the carbohydrate atom x of the respective monosaccharide unit, HS-IIA: HS unit with acetylated N-domain and sulfated on the 6th carbohydrate molecule of the hexosamine moiety, HS-IIIA: HS unit with acetylated N-domain and sulfated on the 2nd carbohydrate molecule of the uronic acid moiety, HS-IVA: HS unit with acetylated N-domain and no sulfation, HS-IVH: HS unit with naked N-domain and no sulfation, HS-IVS: HS unit with sulfated N-domain and no sulfation.

The lesions were grouped according to their vulnerability score and according to their anti-CD68 immunoreactivity in HV versus LV and HI versus LI. Peaks 5, -8, -9 and -10 were compared for differences between the comparison groups. The results are depicted in Figures 21 and -22.

No significant differences were detected between the peaks of HV versus LV and HI versus LI. In both comparisons, peak 9 had slightly higher values in sections that were classified LV and LI. Peak 5 showed slightly increased values in LI sections versus HI plaques. This was not the case when HV- and LV sections were compared.
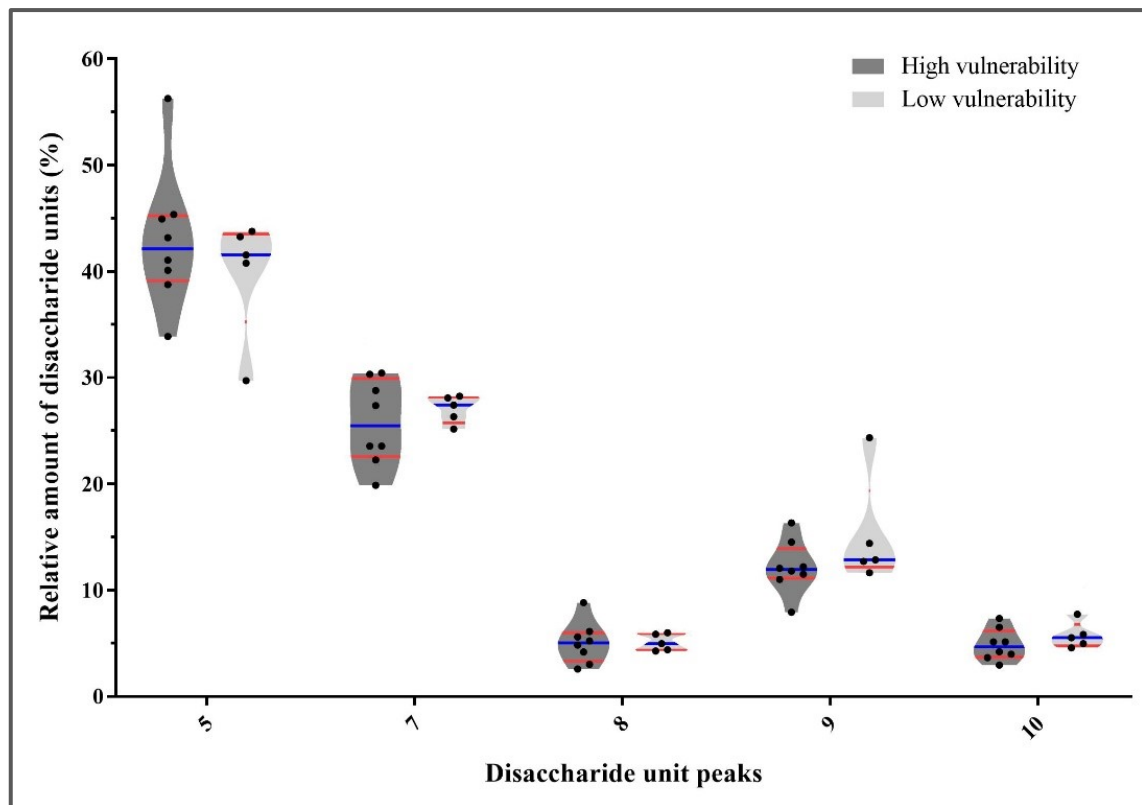
Figure 21. Differences in disaccharide unit peaks in LV- and HV lesions. Violin plots showing differences in the values of the disaccharide unit peaks 5, 7, 8, 9 and 10 between LV- and HV lesions. Blue and red lines inside the plots represent median and $25^{th}/75^{th}$ percentiles, respectively. The borders of the plots depict the 10th and 90th percentiles. Abbreviations: LV= low vulnerability, HV= high vulnerability.
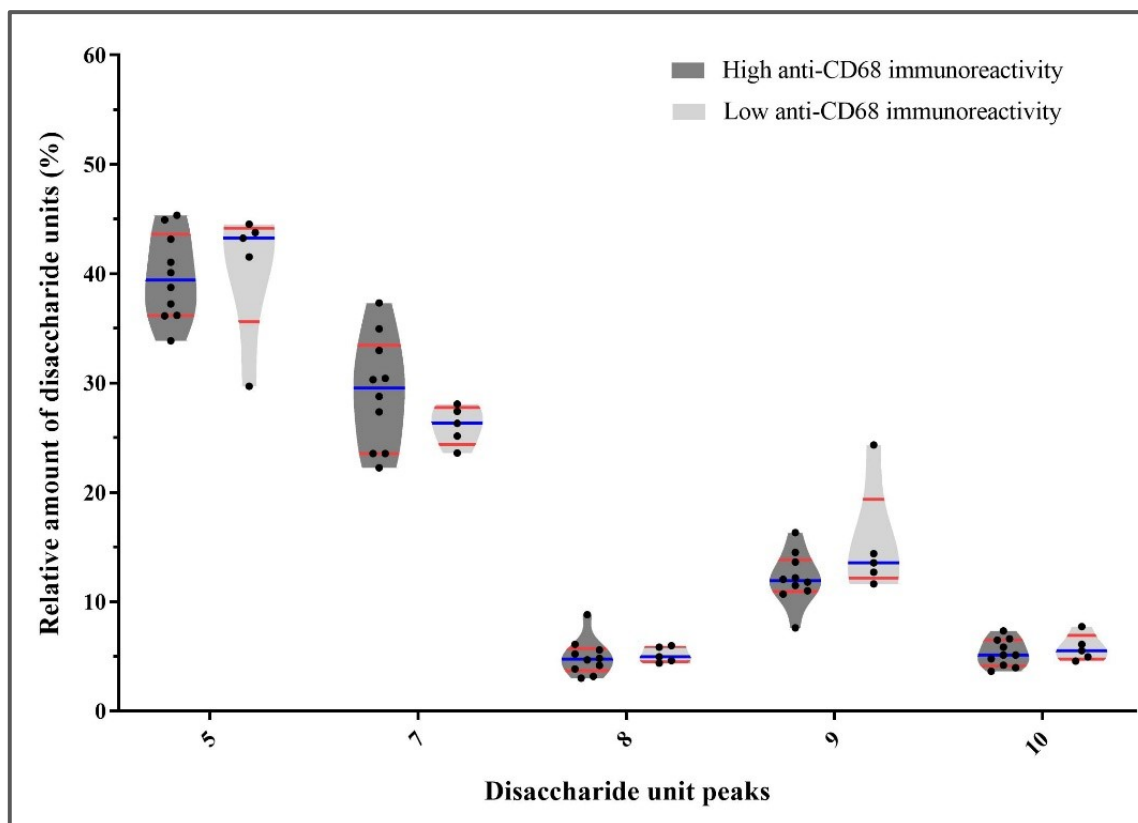
Figure 22. Differences in disaccharide unit peaks in lesions with high- and low anti-CD68 immunoreactivity. Violin plots showing differences in the values of the disaccharide unit peaks 5, 7, 8, 9 and 10 between lesions with high- and low anti-CD68 immunoreactivity. Blue and red lines inside the plots represent median and $25^{th}/75^{th}$ percentiles, respectively. The borders of the plots depict the 10th and 90th percentiles.

Out of the 21 sections that were used for GAG extraction and subsequent disaccharide unit analysis, five pairs and one triplet of sections were obtained from segments of the same CEA specimen. Figures 23 and 24 show the individual HPLC results. In all the examples, peaks 5 and -7 possessed the highest values, followed by peaks 9, -10 and -8, respectively.

Figure 23A represents the HPLC analysis results of the sections P18, P19 and P20. P18 and P20 were classified as HV and HI, while P19 was classified as MV and MI. The ratio of peak 5/peak 7 was the highest for P18, followed by P20. The ratio of P19 was almost equal to one. Peak 9 of P19 was the highest, followed by those of P20 and P18. Peaks 8 and -10 did not show any trends between the three sections.

Figure 23B displays the results of sections P5 and P17 that represent lesions with the same vulnerability level (MV) and the same anti-CD68 immunoreactivity (HI). The ratio of peak 5/peak 7 was almost one for P5, but showed an increase when observing the peaks corresponding to P17. Peaks 8, -9 and -10 did not show any trends.

Figure 23C shows the HPLC measurements of sections P8 and P9. Both lesions were classified as HV, but they differed in terms of their anti-CD68 immunoreactivity, with P8 presenting as a HI lesion, while P9 was classified as a MI. The peak 5/peak 7 ratio was slightly higher for P8 in comparison to P9. Peaks 8 and -9 showed an almost negligible increase in P8 as compared to P9. Peak 10 had the same value between both sections.

Figure 24D depicts the results of the HPLC analysis for P14 and P15. The lesions depict HV lesions, although P14 exhibited lower levels of anti-CD68 immunoreactivity as compared to P15. The ratio of peak 5/peak 7 was considerably higher in P14 in comparison to the ratio of P15. Peak 8 was slightly higher in P14 as compared to P15, while the opposite was observed for peak 10. Peak 9 showed no inclination or declination trend between the two sections.

Figure 24E shows the HPLC results for the sections P25 and P26, which are identical in terms of vulnerability score and anti-CD68 immunoreactivity. There were no trends observed for all peaks.

Figure 24F presents the HPLC results of the sections P33 and P34. Both sections were classified as HV and HI respectively. The ratio of peak 5/peak 7 had higher values in P33, as compared to the almost identical peaks 5 and -7 in P34. Peaks 8 and -10 showed slightly higher values in P34 as compared to P33. No trend was observed between the two sections with respect to peak 8.
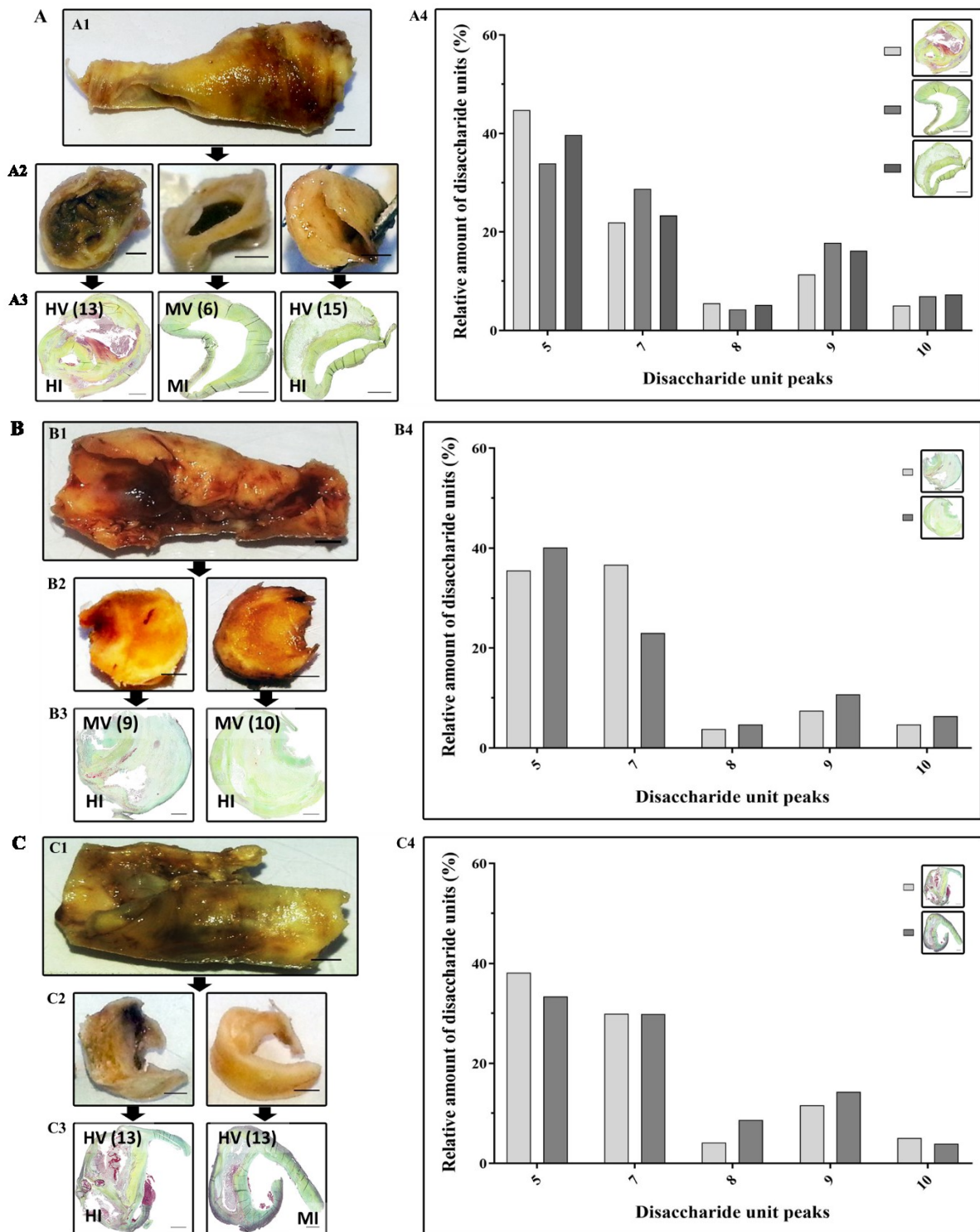
Figure 23. Intra-specimen disaccharide unit analysis (Part 1). Macroscopical images of representative CEA specimens **(A1, B1, C1)** with subsequent dissection and presentation of the transverse plaque surfaces **(A2, B2, C2)**, and as microscopically observable after Movat pentachrome staining **(A3, B3, C3)**. Scale bars: 1 mm (histological images), 0.2 cm (macroscopical images). The samples presented in A3, B3 and C3 are: P18, P19, P20, P5, P17, P8 and P9 (see Table 8). The bar plots **(A4, B4, C4)** depict the disaccharide unit analysis results. The vulnerability scores are presented inside the parentheses. Abbreviations: HV=high vulnerability, MV= medium vulnerability, HI= high anti-CD68 immunoreactivity, MI= medium anti-CD68 immunoreactivity.
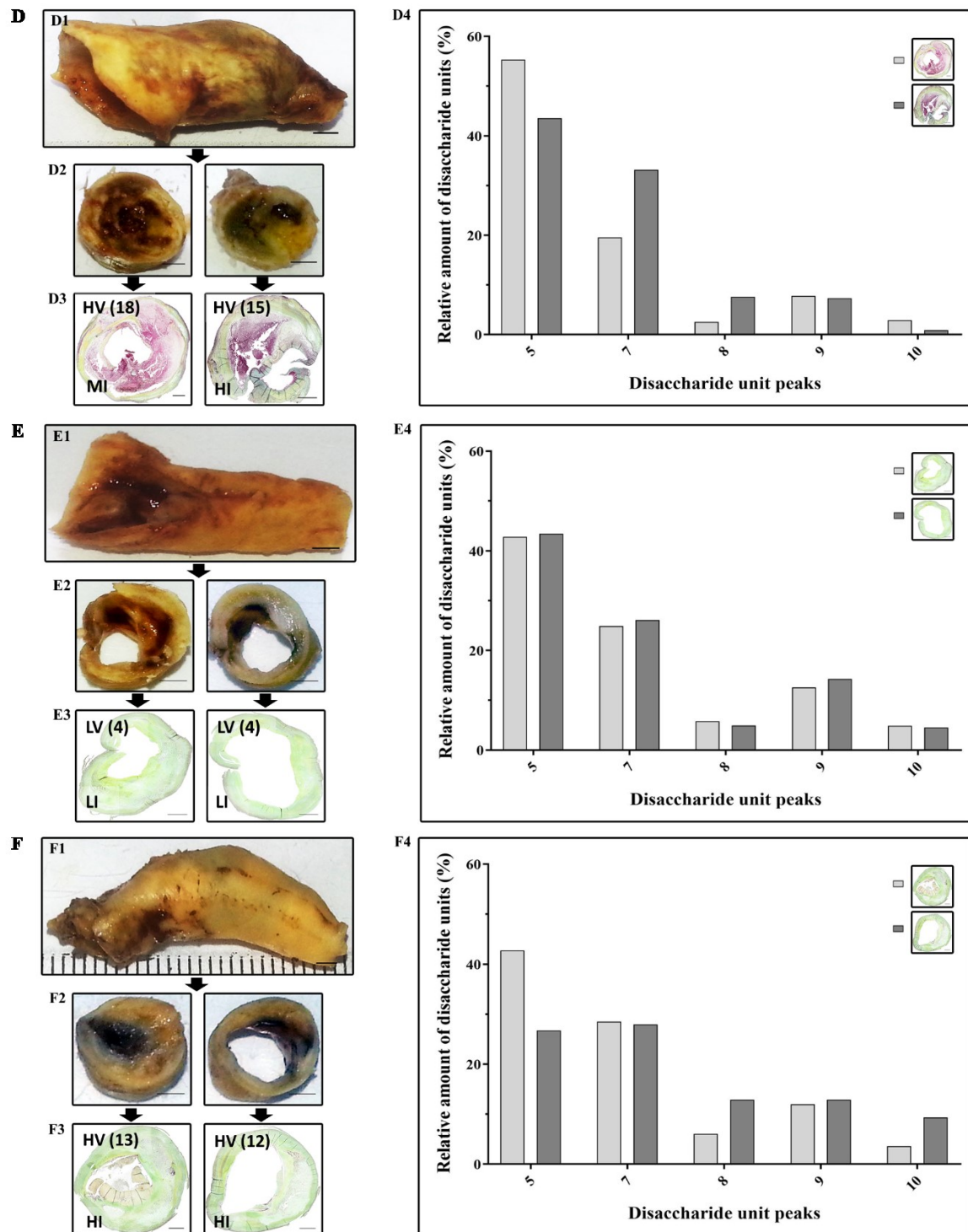
Figure 24. Intra-specimen disaccharide unit analysis (Part 2). Macroscopical images of representative CEA specimens **(D1, E1, F1)** with subsequent dissection and presentation of the transverse plaque surfaces **(D2, E2, F2)** and as microscopically observable after Movat pentachrome staining **(D3, E3, F3)**. Scale bars: 1 mm (histological images), 0.2 cm (macroscopical images). The samples presented in D3, E3 and F3 are: P14, P15, P25, P26, P33 and P34 (see Table 8). The bar plots **(D4, E4, F4)** depict the disaccharide unit analysis results. The vulnerability scores are presented inside the parentheses. Abbreviations: HV=high vulnerability, LV= low vulnerability, HI= high anti-CD68 immunoreactivity, LI= low anti-CD68 immunoreactivity.

3.9 Sample size estimation

Sample size determination was performed on the basis of differential expression analysis results in order to approximate the number of sections that are required to be analyzed via this multi-omics approach for future planning and cost estimation.

The chosen methodology is based on the R package 'samr' that incorporates the "Significance analysis of microarrays" methodology as proposed by Tusher et al.[220] as well as the microarray sample size estimation method of Robert Tibshirani[219]. Briefly, the fold changes are calculated in terms of a gene score that depicts the relative expression difference between two conditions. Using a permutation-based statistical approach, the observed and expected relative differences are compared. A pre-defined threshold value classifies a gene to have a potentially significant gene score alteration or not. Based on the permutation analysis data, the FDR (=ratio of false positives among all positives) and the false negative rate (=ratio of false negatives among all negatives) (FNR) for a hypothesized mean difference of each of the genes of interest is calculated. The process is repeated as a function of sample size in order to evaluate the change in the FDR and FNR values. For simplification, the authors assumed that the sum of positives identified through the test equals the number of the positives of the general population, and thus the FDR is equivalent to 1 – power (=ratio of true positives devided by the sum of true positives and false negatives), while the FNR is equal to the false positives.

Figures 25 and 26 display the results of the sample size estimation analysis for the two comparison groups (Figure 25: high- versus low vulnerability and Figure 26: high- versus low anti-CD68 immunoreactivity). The calculations were performed with a focus on the 148 mRNAs coding for PG core proteins and GAG metabolism-associated enzymes. The given hypothesized log2 mean difference was chosen to be 1, corresponding to a two-fold change in expression.

In both cases, and in order to acquire a differential expression analysis that would offer approximately 70-80 statistically significant candidates, while having a FDR of around 5-10 % and an equivalently low FNR, the final sample size should be increased to 60-70 probes.
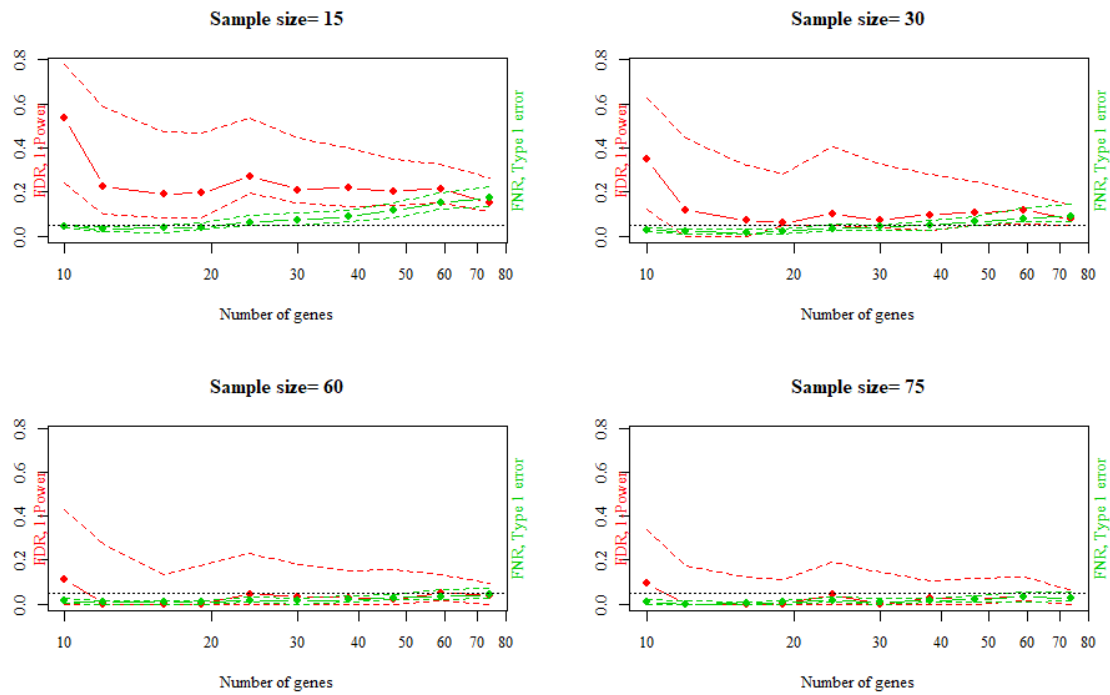
Figure 25. Sample size determination plots for the comparison of high- versus low vulnerability sections. The y-axes represent the FDR and FNR values. The x-axes represent the number of genes (mRNAs) that have a given hypothesized log2 FC > 1 and would be considered significant taking sample size into account. The continuous red and green lines display the FDR and FNR values. The dotted lines graphically display the 95 % confidence intervals.
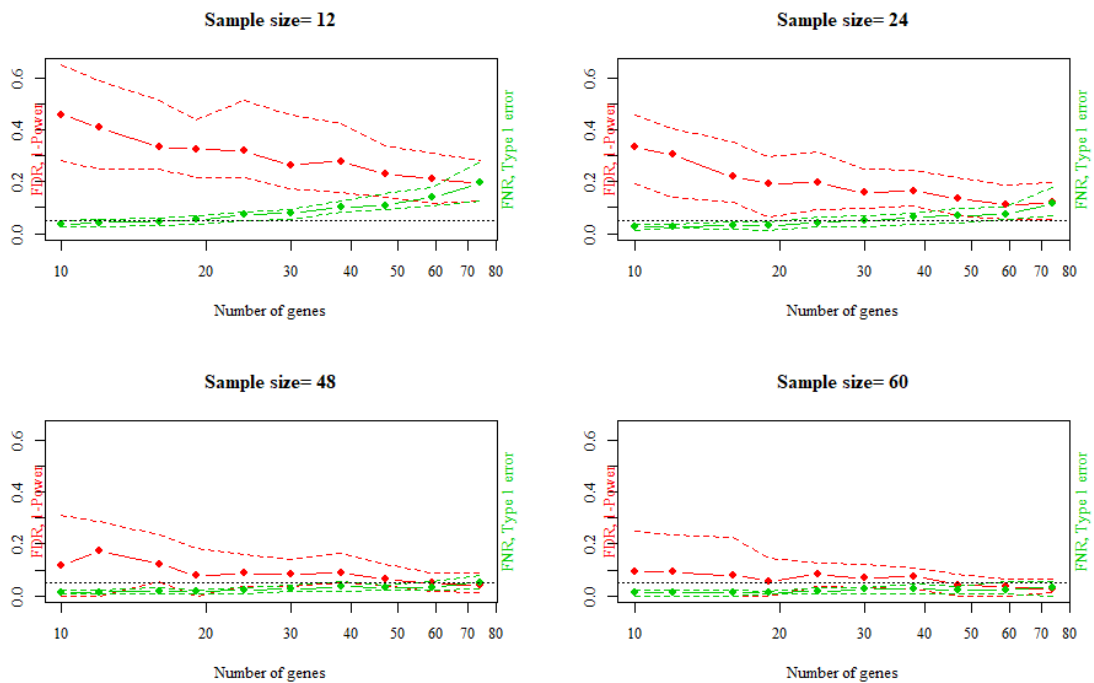

Figure 26. Sample size determination plots for the comparison of high- versus low anti-CD68 immunoreactivity. The y-axes represent the false discovery rate and false negative rate values. The x-axes represent the number of genes (mRNAs) that have a given hypothesized log2 FC > 1 and would be considered significant taking sample size into account. The continuous red and green lines display the FDR and FNR values. The dotted lines graphically display the 95 % confidence intervals.

108

4. Discussion

The purpose of the current pilot study was to establish a research platform that would allow the acquisition and examination of histological, glycoanalytical and molecular biological information from within a few μms of human carotid endarterectomy specimens, to characterize the distribution of GAGs in sections of the specimens, and in relation to stability-/instability-related morphological features, as well as to identify instability-related PG/GAG patterns. Sample size estimations were conducted for future study planning.

Attempts have been made to identify histological differences in the distribution of GAGs, and later on between PG core proteins in various stages of atherosclerosis[77-80,96,113,118,135,152,225-227]. Glycoanalytically, some groups focused on examining biochemical differences in the GAG composition of atherosclerotic lesions[158,228-250], while microarray technology was performed in order to identify genes and pathways linked to atherosclerosis, which could potentially serve as a source of biomarkers and pharmacotherapy targets[251-275]. An approach combining histological, glycoanalytical and molecular biology-based methods within 600 μm-thick sections of atherosclerotic specimens under continuous plaque-morphology control has not been conducted.

4.1 Summary of the results

1. Establishment of a platform that allows small amounts of FFPE-atherosclerotic specimens to be processed with histological, glycoanalytical and molecular biological techniques under continuous plaque morphology control.

2. The main preliminary findings presented in this pilot study are the following:

> 2a. The distribution of GAGs is inversely correlated to inflammation, necrosis, loss of vascular smooth muscle cells, and positively relates to collagen and calcified regions.
>
> 2b. mRNA expression levels of PG-/GAG-metabolism-related proteins and enzymes associate to stable or unstable atherosclerotic plaque characteristics.
>
> 2c. CS/DS-4S and -6S units seem to be abundant in atherosclerotic lesions and alterations in their ratio might signal changes in plaque morphology and stability.

3. An analysis of 60-70 atherosclerotic plaque sections could provide the necessary statistical power to consolidate the working hypotheses.

4.2 Assessment of the spatial distribution of GAGs in human atherosclerotic lesions via alcian blue staining

In the last few decades, a plethora of information with respect to PGs and their association with stability- or instability-associated components inside atherosclerotic lesions has been gained by the immunohistochemical identification of PG core proteins[78,80,96,113,119,152,227,227]. However, this does not allow direct conclusions regarding their attached GAG chains. Only a couple of studies aimed to describe the spatial distribution of GAGs in atherosclerotic plaques in relation to morphological and cellular components[225,246]. Curren et al. showed that alcian blue- and toluidine blue staining, both directed against acidic mucopolysaccharides, was more intense in regions with high cellularity as compared to hyaline-like, acellular and necrotic areas[225]. Later, Völker et al. used cuprolinic blue for electron microscopic visualization of GAGs in the atherosclerotic arteries of 13 human subjects. In line with Curren and colleagues, the authors noticed an increased accumulation of large cuprolinic blue-PG precipitates in cell-rich areas around both foam cells and VSMCs, but only the latter cell type contained cuprolinic blue-PG-filled vesicles[246]. However, these were the only studies since the 1980s which described the spatial distribution of GAGs in atherosclerotic plaques and associated with stability- and instability- related morphological features. One aim of the current study was to investigate the intensity of alcian blue staining in macrophage-rich areas (identified as regions with positive anti-CD68 immunoreactivity), in NCs (identified within the Movat pentachrome staining), and in VSMC-sparse locations (identified by weak anti-αSMA immunoreactivity), as well as to describe its relation towards collagen-rich- (identified by picro-sirius red stain) and calcified regions (as identified by the Movat pentachrome staining).

4.2.1 The distribution of GAGs is inversely correlated to inflammation, necrosis and loss of vascular smooth muscle cells

The majority of atherosclerotic plaques that were analyzed in the current study presented with a very weak to weak alcian blue staining intensity around or inside CD68-abundant regions. Infiltrating macrophages and other immune cells (e.g. neutrophils, mast cells etc.) are well-known producers of extracellular proteases (e.g. metalloproteinases, cysteine- and serine proteases) in atherosclerotic disease and these molecules are pivotal in the process of vascular remodeling[24]. It is likely that macrophages also secrete GAG-degrading glycosidases and sulfatases that contribute to vascular remodeling.

On the other hand, in four cases representing a PIT and three fibrous plaques, the alcian blue staining intensity was detected to be moderate to strong within CD68-abundant regions. In other cases, although the observers evaluated the alcian blue staining intensity in CD68-positive areas as weak to mild, certain CD68-rich spots were found to be more intensely stained with alcian blue. It was not further investigated, however, what plaque characteristics could lead to this histological result. One possible explanation derives from the fact that in early and stable lesion types (i.e., PITs and fibrous plaques) the inflammatory burden is relatively low, and the amount and catabolism pace of degrading enzymes might not exceed the biosynthesis rate of GAGs by adjacent cell types. This suggestion is supported by the fact that VSMCs, one of the main ECM producers in human atherosclerotic plaques[7], are present around or inside CD68-positively stained areas in these sections. Additionally, macrophages are highly plastic and can adopt various microenvironment-dependent phenotypes during a process that has been termed "polarization". At the one pole of this phenotypic spectrum, classically activated, pro-inflammatory cell types (M1) functionally oppose alternatively activated, anti-inflammatory, immune response resolution-promoting types (e.g. M2) of the other pole[276]. However, CD68 is not exclusively present on the surface of pro-inflammatory M1 spectrum-associated macrophages. M2-type macrophages can express CD68, and such cells are capable of producing ECM molecules during the process of tissue healing[277,278]. Interestingly, dedifferentiated VSMCs and endothelial cells of atherosclerotic lesions can also express macrophage-related surface markers such as CD68 while assuming macrophage-like functional states[279,280]. The increased colocalization of GAGs and CD68-rich areas in certain cases might be due to an increased content of these cell types. Pro-inflammatory macrophages might also be capable of producing and secreting PGs and GAGs, the presence of which would sustain or even enhance a prevailing pro-inflammatory milieu. The positive correlation of decorin, HA, fibromodulin and lumican with macrophage-rich areas, as reported by Evanko et al., Onda et al. and Shami et al., might be related to this process[96,113]. Some of these molecules have been found to be upregulated and secreted from macrophages under pro-inflammatory conditions[281,282], and in a very recent study it was shown that macrophage polarization directly affects the type and structure of the synthesized PGs[283].

In the present study, the amount of GAGs tended to be less in NCs as compared to non-necrotic areas of the same section. In most of the samples the absence of alcian blue staining indicates a complete lack of GAGs inside NCs of LFAs, whereas in four plaque sections, classified as EFAs, GAGs were clearly detectable in the NCs. This is in agreement with the findings of Otsuka et al., who noticed a difference of PG core protein immunostaining between the NCs of EFAs and

LFAs[119]. In this study, 151 coronary plaque sections were used in order to detect the distribution of certain core proteins (versican, biglycan and decorin) and HA in atherosclerotic lesions, and a reduction in the immunostaining of these molecules in NCs and especially between EFAs and LFAs was detected[119]. These observations indicate that PGs and their GAG side chains decrease with the progression of necrosis. Areas with ongoing necrosis are characterized by protease- and glycosidase-filled dying cells, by toxic cellular products such as reactive oxygen species that facilitate protein- and carbohydrate degradation, by an acidic microenvironment that optimally supports the action of such enzymes, and by numerous pro-inflammatory cytokines that perpetuate the process of immune cell attraction, death and enzyme secretion[18,24,284-286]. Such an environment favors the successive degradation of GAG and other ECM molecules.

It was found that the amount of GAGs was reduced in most regions with low anti-αSMA immunoreactivity compared to VSMC-rich areas in the same plaque. This result most probably relates to the fact that dedifferentiated, synthetic VSMCs are one of the main producers of ECM molecules in atherosclerosis[284]. Unexpectedly, in several α-SMA-poor areas, the alcian blue staining intensity was mild to strong. In this case, the high VSMC phenotypic plasticity has to be taken into account. Dedifferentiation of plaque VSMCs can lead to a decrease or even loss of VSCM markers such as αSMA and other cytoskeletal proteins[279]. It is conceivable that some of the VSMCs that may have contributed to the production of GAGs in certain areas of the plaques lost their anti-α-SMA immunogenicity. Alternatively, the decreased amount of macrophages that was detected in or adjacent to such regions of low VSMC content may be responsible for the incongruence between α-SMA immunoreactivity and alcian blue staining intensity. It is conceivable that a few numbers of macrophages produce less extracellular matrix degrading enzymes, and under these circumstances even a small number of VSMCs can effectively counteract the degradation rate, leading to alcianophilia in regions with low VSMC content and reduced macrophage density.

4.2.2 Collagen and GAGs mostly colocalize in atherosclerotic plaques

In the present study, the plaque percentage covered by GAGs (as identified by alcian blue staining) and collagen molecules (as identified by picro-sirius red staining) revealed an overlapping distribution in most cases. Polarization microscopy was additionally used to compare the GAG distribution with areas of various collagen fiber thickness, according to which GAGs are more abundantly found in areas with small-caliber collagen fibers.

Previous histological and immunohistochemical studies have reported overlapping spatial distributions between certain collagen types and PGs. Biglycan-, decorin-, fibromodulin- and lumican core proteins have been found to colocalize with collagens type I and III in human atherosclerotic lesions[113,226]. The coexistence of various PGs (e.g. perlecan, collagen type XV and -XVIII) with collagens type IV, -V and XIV in basement membranes is wellknown[50,286]. Collagens and PGs comprise the majority of the ECM molecules in atherosclerotic lesions[63]. The interaction of certain PGs of the SLRP family with the collagen matrix is indispensable for proper ECM assembly (i.e., collagen fibrillogenesis) and regulation of the plaque microenvironment (e.g. calcification, tissue remodeling etc.)[287].

Despite the plethora of information demonstrating a strong functional connection of PG and collagen molecules, there has not yet been a study with its main aim being the investigation of the histological relationship of GAGs and collagen fibers in atherosclerotic plaques.

In this study the amount of alcian blue in collagen-rich areas was high. However, in several cases there was an incongruence between the spatial distributions of GAGs and collagens. More specifically, it was found that the amount of GAGs in some FCs that contained abundant collagen molecules was very low to non-existent, especially in areas with thick collagen fibers. And these areas mostly contained considerable amounts of CD68-positive cells. These observations might provide an explanation as to why higher collagen content is required to withstand a given amount of biomechanical strength in FCs of atherosclerotic lesions[288]. The loss or reduced amount of PGs/GAGs as compared to collagen molecules might influence the geometry and architecture of the collagen network, thus reducing its resistance[288]. Indeed, many SLRPs such as biglycan, decorin, lumican and fibromodulin are known to be involved in the structural organization and assembly of fibrillar and non-fibrillar collagen types[287]. From a diagnostic point of view, these findings might indicate GAGs as a novel marker for early detection of FC destabilization. The thickness of a fibrous cap has long been considered to be one of the major factors that influences whether a plaque is prone to rupture[8]. Proinflammatory conditions promote thinning of the cap by ECM degradation and the loss of collagen is a well investigated marker of plaque instability[289,290]. The observations of this study suggest that GAGs may be degraded faster than collagens under inflammatory conditions. This would be highly interesting for diagnostic purposes and warrants further investigations.

4.2.3 GAGs accumulate around calcified regions

Intimal calcification is an important process in atherosclerotic vessel pathology. It reflects the total plaque burden, and its CT-based visualization and quantification in terms of coronary artery calcium score calculation is used clinically for future cardiac event prediction[291]. Depending on the extent, size, location and morphology of the calcified matrix, calcification is thought to promote both plaque stability and instability. The presence of microcalcifications in fibrous caps modifies their biomechanical properties, making them more prone to rupture, while the fusion of numerous microcalcifications into calcified fragments, and later into calcified sheets, is thought to promote plaque stability[292,293]. Taking the crucial role of this process in influencing atherosclerotic plaque vulnerability into account, it was investigated whether GAGs histologically correlate with calcified regions.

In this study, GAGs were found to be abundant adjacent to calcified regions, suggesting a potential association of these molecules with the calcification process. These observations are in line with those of several histopathological and ultrastructural studies on human and swine atherosclerotic specimens, in which calcium/calcified matrix and acidic mucopolysaccharides/GAGs were found to colocalize[294-298]. Duer et al. used solid-state nuclear magnetic resonance to examine the mineral-organic interface of calcium deposits in carotid atherosclerotic plaques and observed that GAGs link the inorganic part of calcification nodules with the surrounding organic matrix[298]. Similarly, the organic-mineral interface in bone, in teeth, in the calcified cartilage zone of joints and in urinary stones, as well as in the surface of cell-derived calcifying matrix vesicles, is also covered by negatively charged GAGs, and it was suggested that these polysaccharides may play an universal role in mineral crystallization in both health and disease[293,297-303]. In one analyzed plaque section that exhibited remnants of a calcified fragment (as identified by alizarin red staining), the calcified structure was intensely alcianophilic. Although the analysis of undecalcified plaque segments is mandatory in order to make safer conclusions, this study provides an additional supportive hint towards the link between GAGs and calcification. It would be tempting to investigate whether this connection is based purely on the negative charge of GAGs as already known[293,297-302], or whether various sulfation patterns exhibit different affinities towards calcified areas.

The individual instability-related plaque features influence the intra-plaque distribution of GAGs. Determining the status of necrosis, the degree of inflammation, the extent of calcification and the degradation pace of GAG to collagen by visualizing GAGs might be a novel approach in the field of non-invasive atherosclerotic plaque imaging.

4.3 PG-/GAG-related transcripts associate to stability and instability-inferring criteria

Our preliminary histological observations suggest that the distribution of GAGs relate to atherosclerotic plaque features associated with plaque (in)-stability. However, conventional histology did not allow for the specification of GAG molecules that might relate to these features. The histological results do not allow for any estimation with respect to the PG core proteins to which GAG are usually attached. Microarray analysis was performed as a technique for the measurement of mRNA expression levels of 64 PG core proteins and 77 GAG metabolism-associated enzymes in search of instability-related patterns. For this purpose, plaques were classified according to their histomorphology (vulnerability score and anti-CD68-immunoreactivity) in two groups prior to subsequent differential expression analysis. The mRNA signal intensities of the PG core protein- and GAG metabolism-related enzymes were correlated to the mRNA signal intensities of well-established inflammation-, VSMC-, calcification- and collagen markers. Despite the small sample size of this pilot study, the integration of both approaches enabled the preliminary identification of 20 candidates that may be related to plaque stability. Although this pilot study only allows for the formulation of working hypotheses, the preliminary results are partially consistent with the results of previous microarray- and proteomics-based studies, which will be discussed in detail in the following subchapters.

4.3.1 SRGN eventually relates to plaque instability

The mRNA signal intensities of the core proteins SRGN and NRP1, as well as the GAG metabolism-related enzymes NDST3, B3GNT3, HS6ST3, HPSE and ARSK, were at least more than two-fold higher in lesions that presented with a high vulnerability score and a high inflammatory burden, as compared to lesions with a low vulnerability score and a low anti-CD68 immunoreactivity. Their mRNA signal intensities showed a positive correlation with those of well-established inflammation- and immune cell-associated markers. The fold change of SRGN in the HV vs. LV comparison group was considered statistically significant. As representatives of GAG-catabolism associated enzymes, HPSE and ARSK, which exhibited similar behaviour to SRGN, are discussed in this chapter.

SRGN codes for the small PG serglycin, consisting of a 158 amino acid-long core protein with eight serine-/glycine repeats, which serve as attachment sites for heparin and/or chondroitin sulfate-4S/-4S6S[304]. Various studies have reported SRGN to be present in unstable atherosclerotic

plaques at both an mRNA- and a protein level. Tabibiazar et al. aimed to find gene sets that are shared between murine and human atherosclerotic lesions, hypothesizing that these might have an important regulatory function in atherosclerosis[262]. Among other PG core protein- and GAG-metabolism associated enzymes, SRGN (referre to in the study as PRG1) was found to be upregulated in human coronary segments with signs of atherosclerosis as compared to non-atherosclerotic coronary lesions[262]. Papaspyridonos et al. investigated three CEA specimens after macroscopical selection of stable and unstable plaque segments via microarray analysis and reported SRGN (PRG1) to be upregulated in unstable areas[263]. The mRNA signal intensity of SRGN was found to be increased in atherosclerosis-susceptible vascular beds (e.g. aorta, carotid- and femoral arteries) as compared to the more atherosclerosis-resistant internal thoracic arteries[263]. In line with this result, Steenman et al. identified the mRNA levels of SRGN to be increased in carotid atherosclerotic arteries as compared to femoral- and intra-popliteal arteries that mostly exhibit a stable histological phenotype[276]. These observations also agree with the results of other studies that have linked SRGN to various inflammatory conditions including cutaneous autoimmune diseases[305], as well as various haematological and solid tumor entities[306]. In cancer, SRGN has been related to patient prognosis, tumor aggressiveness and metastatic behaviour, and it is considered as a biomarker and a potential therapeutical target[306].

HPSE was identified to be upregulated in unstable and advanced atherosclerotic lesions[263,276]. Perisic et al. compared 87 CEA specimens from symptomatic patients with 40 CEA specimens derived from asymptomatic patients and identified increased mRNA levels of HPSE in the first group[270]. HPSE was found to be overexpressed in M1-macrophages as compared to M2-macrophages[307]. Macrophages that were isolated from the blood of patients with a diagnosed cardiovascular disease contained increased mRNA signal intensity levels of HPSE as compared to macrophages from healthy donors[307]. HPSE codes for the glycosidase heparanase that is involved in the post-translational modification and/or degradation of HS[41]. At a functional level HPSE is able to modify and regulate immune responses by direct cell interaction or by alteration of the microenvironment[308]. The enzyme was found to have a major role in various chronic inflammatory disorders including atherosclerosis[308] and a recently published study showed that HPSE inhibition was able to reduce or even reverse atherosclerosis-induced vascular effects[309]. Similarly to SRGN, HPSE has been in the focus of cancer research due to its relevance as a patient prognosis-related marker and as a regulator metastasis[308].

ARSK had an almost three-fold change both in high vs. low vulnerability sections and between sections that exhibited a high- vs. low anti-CD68 immunoreactivity. The mRNA expression levels

of this gene also positively correlated with various inflammatory markers such as CD80, MACP, CD68, ALOX5 and CCL2. It was not until 2017 that arylsulfatase K was discovered to be the enzyme that fulfils the glucoronate-2-sulfatase activity in GAG catabolism[310]. It is responsible for the detachment of the sulfate group of the C2-atom of a glucuronic acid moiety, and theoretically arylsulfatase K is engaged in the degradation of CS-/DS-2S, CS-/DS-2S/4S, CS-/DS-2S/6S, HS-IA, HS-IIIA, HS-IS, HS-IIIS, HS-IH and HS-IIIH. This migh perhaps be one of the reasons why the HPLC peaks that were analyzed for the purpose of this thesis were found to have low values, especially in sections with high vulnerability and high anti-CD68 immunoreactivity. A study by Theocharis et al. that glycoanalytically compared type II to type V atherosclerotic plaque lesions (according to the American Heart Association Classification of 1995) also found a decrease in CS-/DS-2S6S and CS-/DS-2S4S moieties when comparing early to later stages[250]. Interestingly, there are no studies that support the connection of ARSK with any condition that is related to atherosclerosis, such as a defective inflammatory response or fibrotic remodelling. There is no evidence that ARSK is associated to other non-atherosclerotic diseases that share common pathophysiological processes such as cancer or autoimmunity. According to phylogenetic studies, arylsulfatase K represents an "ancient protein" that appeared early in vertebrate evolution, and thus the constellation of ARSK´s recent functional definition, its evolutionary background, as well as the working hypothesis that was formulated by the preliminary results of this thesis, make ARSK an intriguing candidate to keep track of in future experiments.

4.3.2 ASPN, CHADL, CHST10 and CHSY3 eventually relate to plaque stability

The differential mRNA expression- and correlation analyses of the current study also revealed higher mRNA signal intensities of the core proteins ASPN, CHADL, HAPLN1, PODNL1 and IMPG1, as well as of the GAG-metabolism-associated enzymes CHSY3, DSEL, EXTL2, CHST12, CHST10 and CHPF2 in sections with a low vulnerability score and a low anti-CD68 immunoreactivity, as compared to other sections with a high vulnerability score and a high anti-CD68 immunoreactivity. The signal intensities of these molecules displayed a positive correlation with the mRNA signal intensities of well-known smooth muscle cell-, calcification- and collagen-markers. ASPN, CHADL, CHST10 and CHSY3 showed statistical significance, but due to the central role of the enzymes coded by DSEL and EXTL2 with respect to DS- and HS-anabolism, as well as the importance of carbohydrate sulfotransferase 12 (coded by CHST12) for the formation of CS/DS-4S moieties, which were found to be one of the main peaks in the HPLC results of this study, these candidates are discussed in this subchapter.

ASPN encodes for the core protein asporin, an SLRP family member that possesses an aspartate-rich amino terminus and has similarities to the PGs biglycan and decorin, the latter especially[312]. The mRNA expression levels of ASPN were two- to three-fold higher in lesions that showed low anti-CD68 immunoreactivity in this pilot study. Similar observations were reported by Puig et al.[266] who conducted a microarray analysis on macrophage- or VSMC-rich laser microdissected regions of atherosclerotic sections and found a low expression of ASPN in macrophage-rich areas[266]. In line with these results, ASPN was found to be upregulated in stable atherosclerotic plaques in comparison to vulnerable plaques, as identified by histopathology, by the patient's clinical presentation and by magnetic resonance angiography[313]. A downregulation of ASPN in CEA specimens obtained from symptomatic patients with carotid artery disease was reported by Perisic et al.[270]. Wang et al. found a decreased mRNA signal intensity of ASPN when comparing microarray results obtained from human ruptured atherosclerotic plaques as compared to those retrieved from stable lesions[270]. At a protein level, Langley et al. reported that asporin was less abundant in CEA specimens that were retrieved from symptomatic patients as compared to asymptomatic individuals[314]. In the correlation analyses of the current study, ASPN not only clustered with VSMC-related markers, but also with markers associated with the process of calcification and with collagen markers. In a very recent work by Karlöf et al., CEA specimens exhibiting a high calcification burden were found to show increased ASPN mRNA levels as compared to specimens with low calcification[315]. ASPN contains both calcium- and collagen-binding regions[316] and has been found to negatively regulate mineralization[317,318]. Interestingly, Lyck Hansen et al. reported a downregulation in the protein expression of asporin in patients presenting with high pulse-wave velocities and thus explainable increased arterial stiffness[319].

CHADL codes for the chondroadherin-like protein, a recently characterized SLRP for which it is known to be mostly abundant in cartilage tissue, where it binds collagen and influences chondrocyte differentiation[320]. In this study, CHADL showed a 3-4 fold decrease in its mRNA signal intensity values when comparing HV versus LV and HI versus LI lesions. Chondroadherin-like protein was found to bind collagen molecules in in vitro experiments leading to regulation of collagen production and thus extracellular matrix stabilization[320]. Therefore, it might not be surprising that CHADL was found to be in the same cluster group as COL1A1 and COL9A1. There are no known studies that have examined a possible role of chondroadherin-like protein in an atherosclerotic context.

CHST10, also known as HNK-1 sulfotransferase, due to its involvement in the biosynthesis of the carbohydrate epitope HNK-1, which was originally detected on human natural killer cells and later

found to be expressed on the surface of many neuroectoderm-derived cells, is a mammalian sulfotransferase that is located in the lumina of the Golgi apparatus and is responsible for the 3-O sulfation of glucuronic acid moieties[321]. The certain sulfation signal is considered to act in an inhibitory way towards GAG chain biosynthesis as was exemplarily shown on the CS-carrying PG α-thrombomodulin. Although the exact molecular interactions that lead to this inhibition are still unknown, it was suggested that both the glucuronic acid of the tetrasaccharide linker and those of the CS chains are involved[38]. The reduced levels of CHST10 were unexpected considering its proposed function as a negative regulator of GAG biosynthesis and the fact that GAGs were less to be found in HV lesions in comparison to LV lesions. A negative feedback mechanism that would sense the loss of GAGs inside the plaque leading to an inhibition of biosynthesis-terminating mechanisms could be hypothesized; however, after its discovery and characterization in 1997 and 1998, respectively, publications regarding the molecular interactions and pathways that lead to regulation of CHST10 are scarce[321, 322]. Its important role in the synthesis of the carbohydrate epitope HNK-1 and the impact of the HNK-1 sulfation on hippocampal synaptic plasticity was tested in CHST10-null mice suggesting regulatory functions in learning and memory[321]. Taking the current microarray results into account it would be very tempting to breed CHST10- and ApoE-double knockout mice and compare differences in atherosclerotic lesion formation with ApoE-single knockout littermates. Previously, there have been gene expression analyses that have focused on differences between asymptomatic and symptomatic plaques, between inflamed and non-inflamed areas, between histologically stable and unstable regions as well as between atherosclerotic regions and disease-free areas[251-275], but CHST10 was never found to be differentially expressed in any of them.

CHSY3 refers to a gene that codes for chondroitin sulfate synthase 3, one of the four known CS-related polymerizing enzymes[323]. Chondroitin sulfate synthase-3 possesses a dual glycosyltransferase activity and is responsible for the initiation and elongation of CS chains[323]. In this study the mRNA signal intensity of CHSY3 was more than two-fold decreased in lesions with high anti-CD68 immunoreactivity versus lesions with low anti-CD68 immunostaining coverage. In a microarray study conducted by Wang et al., the signal intensity of CHSY3 was decreased in ruptured atherosclerotic plaques as compared to stable atherosclerotic plaques[270]. Our correlation analyses, however, revealed a clustering of CHSY3 with inflammation-related markers, albeit conversely, Puig et al. identified the mRNA expression levels of CHSY3 to anti-correlate with CD68, ALOX5 and CCL2[266]. To date, no studies have reported correlating CHSY3 with atherosclerosis or inflammation.

Little is known about DSEL in the context of atherosclerosis. Sulkava et al. reported a reduced mRNA signal intensity in atherosclerosis-susceptible aortas and femoral arteries as compared to internal mammary arteries[273], but subsequently no other data have been published. DSEL is responsible for the epimerization of glucuronic acid found inside CS chains, leading to the formation of DS chains[324]. In this study, the mRNA signal intensities of DSEL correlated positively to those of VSMC- and calcification-related markers. The mRNA signal intensities of DSEL were higher in lesions exhibiting with a low anti-CD68 immunoreactivity as compared to sections that were strongly immunostained for anti-CD68. It might be conceivable to hypothesize that DSEL associates to plaque stability.

The mRNA signal intensities of EXTL2 were found to be up to 4-fold lower in lesions with a high vulnerability score and a low anti-CD68 immunoreactivity as compared to lesions with low vulnerability score and a high anti-CD68 immunoreactivity. Similar results were reported by Puig et al.[266], who reported high EXTL2 signal intensities in VSMC-related regions as compared to inflammation-rich sites[266]. In another microarray analysis that aimed to identify differences in the mRNA expression levels of genes between various vascular beds, it was shown that the atherosusceptible artery regions exhibited reduced EXTL2 mRNA signals as compared to atherosclerosis-resistant internal mammary arteries[273]. Interestingly, the EXTL2 mRNA expression levels of M1 macrophages were lower than those measured in M2 macrophages[307]. Accordingly, macrophages that were isolated from the synovial fluid of rheumatoid arthritis patients also presented with lower EXTL2 mRNA levels as compared to those measured in macrophages that were retrieved from the synovial fluid of healthy subjects[307]. EXTL2 is part of the exostosin-like gene family and its protein product is considered to be involved in the inhibition of GAG chain elongation by the addition of a nonproductive, α1, 4-linked monosaccharide to the tetrasaccharide linkage region[325]. Exostosin-like 2 most probably acts as a balancing agent between the synthesis of the tetrasaccharide linkage region occurring at a faster pace and the GAG chain polymerization. The aim is to avoid the production of abnormally modified GAG chains with various sulfation patterns that have been reported to have a negative impact in tissue healing[325]. The positive correlations of the mRNA signal intensities of EXTL2 with those of calcification markers was another observation of this study. In a recent study, Purnomo et al. demonstrated that EXTL2-knockout mice with chronic kidney disease-imitating conditions exhibit increased vascular calcification and this was explained by the parallel absence of exostosin-like 2 enzymatic activity that led to an increase of HS- and CS chains[326]. Based on the observations of reduced EXTL2 mRNA levels in atherosclerotic lesions with higher inflammatory burden and low

VSMC content, as well as the positive associations with calcification-related markers, it would be very attractive to further examine whether this molecule is capable of reflecting plaque stability.

Lower mRNA levels of CHST12 were found in lesions exhibiting a high vulnerability score as well as a high inflammatory burden in comparison to sections classified as such with a low vulnerability score and a low anti-CD68 immunoreactivity. CHST12 encodes for the second isoform of the chondroitin 4-sulfotransferases that catalyze the transfer of a sulfate group on the hydroxyl group of the fourth C atom of the N-acetylgalactosamine moieties of CS and thus facilitates the formation of CS/DS-4S and CS-4S6S[327]. There have been no atherosclerotic studies that have measured differences in the transcription- or protein levels of CHST12. Certain studies have reported decreases in the mRNA and/or protein levels of CHST12 under inflammatory conditions[328,329]. In addition, the mRNA signal intensities of CHST12 showed positive correlations towards those of calcification-related markers, but no studies exist that link CHST12 with the process of calcification.

The individual atherosclerotic plaque characteristics seem to influence the mRNA signal intensity levels of PG- and GAG- metabolism-related molecules. The identification of morphology-, cell- and process-related transcription patterns via microarray analysis will aid the selection of appropriate candidates for the visualization of specific aspects of atherosclerotic plaque stability-/instability.

4.4 CS/DS-4S and -6S units seem to be abundant in atherosclerotic lesions, and alterations in their ratio might signal changes in plaque morphology and stability

The experimental design of this study was created in order to facilitate a precise correlation of plaque histomorphology, mRNA expression analysis and glycoanalysis by using only a few μms of carotid vessel wall, and one of the main goals was to search for biochemical differences in the GAG composition as eventually detected between atherosclerotic plaque sections with varying vulnerability score and anti-CD68 immunoreactivity.

Satisfying amounts of extracted and purified GAGs from 100 μm-thick segments of FFPE-pretreated tissue were obtained. The controlled acquisition of glycoanalytical information between sections representing a specific, unalternating plaque morphology as part of the experimental design was successful. However, the use of a one batch analysis technique during the HPLC disaccharide unit analysis led to the overlapping of chromatogram peaks.

Peaks 5 (CS/DS-4S/HS-IVH) and -7 (CS/DS-6S/HS-IVH/HS-IIA/HS-IIIA) have been identified to possess the highest values, followed by peaks 9, -8 and -10 respectively. Due to the overlapping of the disaccharide units, no safe conclusions can be drawn and it is not clear as to what extent peak 5 consists of CS, DS and HS-IVH, or to what extent peak 7 is composed of CS/DS-6S, HS-IVH, HS-IIA or HS-IIIA.

Previous studies that investigated the chemical identity of vascular GAGs in atherosclerosis exist (Table 14). These studies reported CS-4S, CS-6S, DS, and HS (no further specification of the analyzed subunits) to be present in atherosclerotic lesions. A few studies presented results regarding CS-0S and the double-sulfated CS-4S6S, CS/DS-2S4S and CS-2S6S[158,240,245,250]. All studies revealed that the amount of GAGs increases in the initial stages, but decreases during advanced stages of the disease (Table 14). Monosulfated CS units (CS-4S and CS-6S) show an increase until the stage of advanced lesion formation prior to a subsequent decline, while HS-associated disaccharide units reach a maximum during the early stages of the disease and decline thereafter[231,234,238-239,241,245,248]. The decline of HS precedes that of CS-associated units. Similar results were reported for DS units[158,231,233,234,238], although others have reported contradictory results[236,238,240,241,245,248]. The more recent studies that were based on strict histomorphological criteria reported that no changes occur throughout lesion progression for DS, and that only in advanced plaques was there a marked decline of this GAG subtype[158,250].

On the basis of these results and the fact that this study reported peaks 5 and -7 to be the highest in atherosclerotic lesions, one can hypothesize that the majority of the disaccharide units included in peaks 5 and -7 are mainly CS-4S and CS-6S accompanied by a smaller amount of DS-4S and DS-6S, while the amount of HS-IV could be considered negligible or very small.

The glycoanalytical studies reported HA to behave in a similar manner as HS (Table 14). In the present study, peaks 8, -9 and -10, depicting HA, HS-IVA and HV-IVS disaccharide units respectively, possessed low values in comparison to peaks 5 and -7. Our classification was based on well-defined instability associated criteria and on the introduction of a vulnerability scoring system. Low vulnerability score plaques were by no means considered to represent early atherosclerotic lesions such as fatty streaks. Thus, the low percentage of HA and the HS-subtypes HS-IVA and HS-IVS may be associated with the fact that the degradation process for HA and HS had already progressed in lesions that were classified as LV or LI. HS-IVA was also found to be higher in LV/LI lesions as compared to HV/HI lesions, although as a nonsignificant trend. Thus,

our results are in line with the results of other glycoanalytical studies presented in Table 14 and provide additional indications regarding the fate of HS and HA in human atherosclerotic lesions.

It was further investigated whether GAG-peak trends are observed between sections of different or similar plaque morphology, between sections of different or similar vulnerability and between sections of different or similar anti-CD68 immunoreactivity, all of which was derived from the same CEA specimen. Although the GAG analysis results of these pairs and triplets of sections were solitary and not indicative of a certain trend, it can be hypothesized that the ratio of peak 5/peak 7 is higher in lesions with higher vulnerability score and/or lesions that are morphologically characterized by the formation of a thrombus or hemorrhage. Lesions that presented with similar morphology and vulnerability score did not seem to display this hypothetical trend. Considering the working hypothesis that CS/DS-4S and CS/DS-6S are mainly responsible for the creation of peaks 5 and -7, then one could further hypothesize that such an alteration could be a sign of plaque instability and evolving vulnerability. The most recent glycoanalytical study by Theocharis et al., that was based on the AHA classification of 1995, is in line with this hypothesis and the authors of the paper have shown that the ratio of CS-6S to CS-4S is decreased in advanced atherosclerotic plaque stages as compared to early lesions[250].

Future experiments should investigate the working hypothesis that the ratio between CS/DS-4S and CS/DS-6S might signal changes in plaque morphology and/or vulnerability.

Table 14. Glycoanalytical studies on human atherosclerotic lesions.

Study/Material	Comparison and classification methodology prior to pooling and glycoanalysis	GAG analysis results*
Budecke et al.[230] (Aorta)	Classification with exclusion of necrotic and calcification areas as identified macroscopically (not further specified)	-CS-DS: no changes -DS: ↑ -HA: ↓ -HS: ↑
Klynstra et al.[231] (Aorta)	Macroscopical classification according to WHO Study Group (1958), pooling (n=2-91) of fatty streaks, plaques, atheromas, ulcerated lesions and comparison between these stages	-CS-6S: initially ↑, then ↑↑, then ↓ -DS: unrelated to stage, although ↓ in later stages -HA: ↓ with increasing stage -HS: initially ↑, then ↓
Kumar et al.[233] (Aorta)	Macroscopical classification and pooling (n=56) in fatty streaks, fibrous plaques and complicated lesions and comparison between these stages	-CS-4S: ↑, ↑↑, ↓ in advanced lesions -CS-6S: ↑ in fatty streaks, ↓ in advanced lesions

		-DS: ↑↑ in fatty streaks, but almost absent in fibrous plaques -HA, HS: no changes
Nakamura et al.[234] (Aorta)	Macroscopical classification according to the WHO Study Group (1958) and comparison of grade II lesions with adjacent normal tissue (n=26)	- HA, HS, CS6S and DS: ↓
Murata et al.[236] (Aorta)	Macroscopical classification into three grades: Grade 0-I: free lesions, grade II: fatty streaks, grade III: lipid fibrous plaques without ulcerations or calcification	- total CS (=CS4S and CS6S): ↓ in advanced atherosclerosis DS: unchanged
Dalferes et al.[237] (Aorta)	Combinational macroscopical and microscopical classification: Comparison between normal lesions and lesions with invisible and visible fatty streaks and microscopically confirmed foam cell infiltration (n=28)	CS/HS: ↑ in fatty streaks HA: no changes
Stevens et al.[238] (Aorta)	Macroscopical classification according to the WHO Study Group (1958) and comparison between the grades	-CS-4S: no changes -CS-6S: ↓ -DS: slightly ↑ -HA: no changes -HS: ↓
Tammi et al.[239] (Coronary arteries)	Macroscopical classification into three groups: Group A: visually disease-free samples, group B: fatty streaks and plaques without stenosis, group C: arteries of advanced atherosclerosis and severe stenosis	- CS: no changes - DS: ↑ in advanced lesions - HA: ↓ in mild to advanced lesions - HS: ↓ in advanced lesions
Murata et al.[240] (Coronary arteries)	Macroscopical classification into four grades: Grade 0: grossly normal, grade I: yellowish, flat lesions; grade II: fatty fibrous plaques; grade III: ulceration and hemorrhage (n=48)	- total GAG: ↓ - CS-6S: ↑ with increasing lesion progression - DS: ↑ with increasing lesion progression -CS-0S: ↓ with increasing lesion progression - HA: ↓ with increasing lesion progression
Murata et al.[241] (Cerebral arteries)	Macroscopical classification: Comparison between normal and atherosclerotic parts	- CS-6S: ↑ with progressing atherosclerosis - DS: ↑ with progressing atherosclerosis - HS: ↓ with progressing atherosclerosis

Murata et al.[245] (Cerebral arteries)	Classification in disease-free and atherosclerotic areas (not further specified) (n=332)	- CS-4S: ↓ - CS-6S: ↑ - CS-0S: ↓ - DS: ↑ - CS/DS-2S4S: ↑ - HS: ↓↓ - HA: ↓
Cherchi et al.[247] (Aorta)	Comparison between normal and adjacent atherosclerotic lesions (not further specified)	- DS: ↑ in atherosclerotic plaques
Wasty et al.[248] (Aorta)	Macroscopical classification: Comparison between normal and plaque areas without ulcerations/calcifications	- DS: ↑ - HS: ↓
Shirk et al.[158] (Aorta)	Classification according to the AHA Classification (1995): Changes between normal and atherosclerotic lesions (type II-VI)	- DS: ↓ (biglycan-bound) - CS/DS-2S4S: ↓ (referring to biglycan and not decorin) - CS/DS-4S6S: ↓ (referring to biglycan and not decorin)
Theocharis et al.[250] (Aorta)	Comparison between type II and type V lesions (AHA Classification 1995) (n=4 for each group)	-CS-6S/CS-4S ↓ - DS: no changes - CS-4S6S: no changes - CS/DS-2S6S: ↓ - CS-2S4S ↓

* ↑: increased, ↑↑ very increased

4.5 Future perspectives

Several aspects should be taken into consideration for future experiments.

One of the questions is whether formalin fixation, EDTA-mediated decalcification and the process of paraffin embedding affects the carbohydrate content of the examined specimens. A couple of studies addressed this issue and partly controversial results have been reported[330,331]. It is possible that prolonged times of EDTA action might lead to PG/GAG losses and thus it might be beneficial to minimize the action of the EDTA solution by determination of the exact point at which decalcification is complete[332].

Alcian blue staining was used to depict GAGs at a histological level. The polyvalent basic dye allows an interaction with the negatively charged carboxyl- and sulfate groups of GAGs[333]. But alcian blue is not a GAG-specific staining method. Under certain conditions the dye partly interacts with polynucleotides or other aromatic ring-containing molecules[334]. Negatively charged sialic acid residues and sulfated aminoacids that are present in the vessel can also be stained with alcian blue[335,336]. The use of low pH can mask GAGs by the attachment of proteins via salt links[334] and

therefore part of the GAGs inside the sections can escape staining[337]. Alcian blue staining provides no information about the different GAG classes and sulfation patterns. Alternative methods should be considered for the acquisition of more detailed information. For example, the critical electrolyte concentration method that takes advantage of different concentrations of $MgCl_2$ to selectively stain carboxylate-, sulfate- and phosphate groups might be helpful in increasing the specificity of the alcian blue staining. Highly specific GAG-targeting immunohistochemistry is hampered by the limited commercial availability and high cost of specific antibodies. The use of single-domain antibodies (known as nanobodies) with a very small size and higher tissue penetration might be more suitable[338].

The use of a whole slide scanner with integrated storage management would reduce the acquisition time and allow the retrieval of a greater number of images with a resolution of up to 100x.

This study was based on the classification of atherosclerotic sections according to well-known morphological criteria[8,339,340] that were summarized in a vulnerability scoring system. The criteria for awarding the vulnerability points were based on well-established histopathological parameters that encounter certain changes with progression of atherosclerosis[8,339,340]. However, the definition of the morphometrical criteria according to which vulnerability points were awarded, although partly inspired by previous studies[339-343], was newly proposed, and no correlations between histopathology and clinical imaging exist. The validation of the score has yet to be performed as an independent experiment. The broadly used criterion of stenosis could not be taken into account due to the opening of the vessel during the surgical procedure, and thus no vulnerability points were awarded to plaques that were highly stenotic. High resolution imaging measurements of the carotid vessel diameter prior to the intervention might be used to estimate stenosis. This can be subsequently integrated as an additional vulnerability criterion.

The definition of controls was based on the assumption that a low vulnerability score is considered to morphologically resemble the nearest towards a non-atherosclerotic phenotype. Purely non-atherosclerotic segments would only be found inside the vessels of newborns and children. The use of internal thoracic arteries that are considered atheroresistant is common in experimental studies, but these arteries possess a distinct GAG-related biochemical signature[344] and represent a different vascular bed area than the one from which the diseased segment is retrieved from. The proximal and distal parts of the extracted CEA specimen can be considered as being "almost controls" and could further be used as a reference.

Newly collected CEA specimens could be scanned by an experimental 7T-MRI scanner. In combination with the special nature of the experimental design (Figure 3, Chapter 1.6), one can directly combine high quality MRI images of the CEA specimens with the subsequently acquired multi-omics data. The experimental design allows the addition of further research methodologies (e.g. MALDI imaging, immunohistochemistry of PG core proteins or even X-ray absorption spectroscopy for the identification of sulfation density patterns) that could provide useful information to generate or validate working hypotheses.

For the detection of inflammation-related PG-/GAG-related patterns, the atherosclerotic plaques were classified according to their inflammatory burden as identified by immunohistochemistry and the use of anti-CD68- antibodies prior to grouping and subsequent interpretation of the HPLC- and microarray results. However, CD68 is not exclusively expressed by pro-inflammatory macrophages and various studies have revealed that in both mouse- and human atherosclerosis more than 30 % of CD68+ cells and foam cells derive from VSMCs[345]. Various cell types (e.g. VSMCs, macrophages, fibroblasts etc.) exhibit high cellular plasticity that is influenced by the atherosclerotic plaque microenvironment[9,280,346]. Taking this into account, and in an attempt to display the underlying morphology and pathophysiology of each plaque section in a broader way, multiple representative markers for each group (e.g. inflammation, calcification etc.) and cell subtype (e.g. VSMC, macrophages etc.) could be used. For example general pro- (e.g. Interleukin 1-beta, interleukin 6) and anti-inflammatory (e.g. Interleukin 10) markers could be combined with immune cell-specific molecules such as M1- and/or M2-macrophage-asociated antigens in order to acquire a better estimation of the prevailing inflammatory conditions of each plaque section.

The performance of the microarray analyses on RNA extracted from FFPE tissues has to be taken into account due to the strong degradation of the RNA, and results should be treated with caution. This renders the addition of multiple validation methods (e.g. qRT-PCR and Western blot) necessary. The differential expression analysis methodology that was followed by this study accords with the well-established procedure that is part of the 'limma' R package[218]. For future experiments, a batch effect correction should be performed in order to avoid a dependence of the signal variance on alternating experimental conditions (e.g. differences in the time and procedure of the RNA extraction between samples 1-10, 11-20 etc.). The R package 'limma'[218] offers the necessary tools to accomplish this task.

The extraction of sufficient amounts of GAGs from within μms of FFPE-pretreated atherosclerotic tissue and the subsequent GAG composition analysis was another aim of the study. The lack of

estimation of potential GAG losses during extraction is one aspect that should be tested as part of a quality assessment procedure. The performance of the extraction procedure of technical samples with GAG standards of known quality would help standardize the extraction process. The chromatogram peak overlapping and the need to identify more individual disaccharide units suggests changes in the HPLC protocol. Efforts should be made to optimize the GAG extraction procedure so that less than 100 µm-thick segments can be used for GAG extraction. An optimized enzymatic digestion algorithm is needed. For example, after the extraction of GAGs from an atherosclerotic plaque section, five solutions containing equal amounts of extracted GAG material could be created. Enzymatic digestion should then be performed in a way that each aliquot contains one GAG class. Subsequent multiple enzymatic digestions (e.g. via sulfatases and lyases) could further produce individual disaccharide units. In a nutshell, the goal should be to create guided digestions and acquire aliquots containing highly specific disaccharide units from each GAG class.

5. Conclusion

This study introduces a suitable research platform to obtain histologically-, immunohistochemically-, glycoanalytically- and molecular-biologically-derived data from only 600 μm-thick segments of formalin-fixed paraffin-embedded tissue.

The first preliminary data suggest that the individual instability-related plaque features influence the intra-plaque distribution of GAGs and affect the mRNA signal intensity levels of PG- and GAG-metabolism-related molecules, which seem to form instability- and process-specific transcription patterns.

The distribution of GAGs in atherosclerotic plaques was influenced by instability- or stability-associated morphological factors (i.e., inflammation, necrosis, VSMCs, calcification and collagen). Using microarray technology, the histological patterns were partially translated into specific patterns that associate to instability (vulnerability, inflammation) or stability (content of VSMC, calcification).

The mRNA expression analysis implied that SRGN may associate to increased vulnerability and high anti-CD68 immunoreactivity, in comparison to ASPN, CHADL, CHST10 and CHSY3. mRNA signal intensity correlation analyses identified clusters between those of PG-/GAG-associated genes and those that code for inflammation-, vascular smooth muscle cell-, calcification and collagen markers.

Preliminary HPLC results suggest that CS/DS-4S and -6S units seem to be abundant in atherosclerotic lesions, and alterations in their ratio might signal changes in plaque morphology and stability.

Increase of the analyzed sample size to 60-70 samples, optimization of the HPLC analysis with eventual extension of the number of types of disaccharide units that can be analyzed, as well as the addition of validation methods would provide a precise picture as to which PG-/GAG patterns relate to plaque stability and instability. Out of these patterns, candidates that correlate to certain disease processes or to certain plaque morphologies can be chosen to represent novel molecular imaging targets for atherosclerosis.

6. References

1. Cardiovascular Diseases. 2017. (Accessed August 6, 2018, at http://www.who.int/en/news-room/fact-sheets/detail/cardiovascular-diseases-(cvds).)

2. About Cardiovascular Diseases. 2017. (Accessed August 6, 2018, at http://www.who.int/cardiovascular_diseases/about_cvd/en/.)

3. Bloom DE, Cafiero ET. The Global Economic Burden of Non-communicable Diseases. Geneva: World Economic Forum; 2011.

4. Herrington W, Lacey B, Sherliker P, Armitage J, Lewington S. Epidemiology of Atherosclerosis and the Potential to Reduce the Global Burden of Atherothrombotic Disease. Circ Res 2016;118:535-46.

5. McPherson R, Tybjaerg-Hansen A. Genetics of Coronary Artery Disease. Circ Res 2016;118:564-78.

6. Gimbrone MA, Jr., Garcia-Cardena G. Endothelial Cell Dysfunction and the Pathobiology of Atherosclerosis. Circ Res 2016;118:620-36.

7. Bennett MR, Sinha S, Owens GK. Vascular Smooth Muscle Cells in Atherosclerosis. Circ Res 2016;118:692-702.

8. Yahagi K, Kolodgie FD, Otsuka F, Finn AV, Davis HR, Joner M, Virmani R. Pathophysiology of native coronary, vein graft, and in-stent atherosclerosis. Nature Reviews Cardiology 2015;13:79.

9. Cybulsky MI, Cheong C, Robbins CS. Macrophages and Dendritic Cells: Partners in Atherogenesis. Circ Res 2016;118:637-52.

10. Tabas I, Williams KJ, Boren J. Subendothelial lipoprotein retention as the initiating process in atherosclerosis: update and therapeutic implications. Circulation 2007;116:1832-44.

11. Boren J, Williams KJ. The central role of arterial retention of cholesterol-rich apolipoprotein-B-containing lipoproteins in the pathogenesis of atherosclerosis: a triumph of simplicity. Curr Opin Lipidol 2016;27:473-83.

12. Toth PP. Triglyceride-rich lipoproteins as a causal factor for cardiovascular disease. Vascular health and risk management 2016;12:171-83.

13. Ferretti G, Bacchetti T, Johnston TP, Banach M, Pirro M, Sahebkar A. Lipoprotein(a): A missing culprit in the management of athero-thrombosis? J Cell Physiol 2018;233:2966-81.

14. Tabas I, Bornfeldt KE. Macrophage Phenotype and Function in Different Stages of Atherosclerosis. Circ Res 2016;118:653-67.

15. Sorci-Thomas MG, Thomas MJ. Microdomains, Inflammation, and Atherosclerosis. Circ Res 2016;118:679-91.

16.   Tabas I, Lichtman AH. Monocyte-Macrophages and T Cells in Atherosclerosis. Immunity 2017;47:621-34.

17.   Tabas I, Garcia-Cardena G, Owens GK. Recent insights into the cellular biology of atherosclerosis. J Cell Biol 2015;209:13-22.

18.   Rayner KJ. Cell Death in the Vessel Wall: The Good, the Bad, the Ugly. Arterioscler Thromb Vasc Biol 2017;37:e75-e81.

19.   Tabas I. 2016 Russell Ross Memorial Lecture in Vascular Biology: Molecular-Cellular Mechanisms in the Progression of Atherosclerosis. Arterioscler Thromb Vasc Biol 2017;37:183-9.

20.   Frink RJ. Inflammatory Atherosclerosis: Characteristics of the Injurious Agent. Sacramento (CA): Heart Research Foundation; 2002. Chapter 5 CAPDAfhw.

21.   Yurdagul A, Jr., Doran AC, Cai B, Fredman G, Tabas IA. Mechanisms and Consequences of Defective Efferocytosis in Atherosclerosis. Frontiers in cardiovascular medicine 2017;4:86.

22.   Grootaert MOJ, Roth L, Schrijvers DM, De Meyer GRY, Martinet W. Defective Autophagy in Atherosclerosis: To Die or to Senesce? Oxid Med Cell Longev 2018;2018:12.

23.   Garrido AM, Bennett M. Assessment and consequences of cell senescence in atherosclerosis. Curr Opin Lipidol 2016;27:431-8.

24.   Garcia-Touchard A, Henry TD, Sangiorgi G, Spagnoli LG, Mauriello A, Conover C, Schwartz RS. Extracellular proteases in atherosclerosis and restenosis. Arterioscler Thromb Vasc Biol 2005;25:1119-27.

25.   Camare C, Pucelle M, Negre-Salvayre A, Salvayre R. Angiogenesis in the atherosclerotic plaque. Redox biology 2017;12:18-34.

26.   Quillard T, Franck G, Mawson T, Folco E, Libby P. Mechanisms of erosion of atherosclerotic plaques. Curr Opin Lipidol 2017;28:434-41.

27.   Bentzon JF, Otsuka F, Virmani R, Falk E. Mechanisms of plaque formation and rupture. Circ Res 2014;114:1852-66.

28.   Naghavi M, Libby P, Falk E, Casscells SW, Litovsky S, Rumberger J, Badimon JJ, Stefanadis C, Moreno P, Pasterkamp G, Fayad Z, Stone PH, Waxman S, Raggi P, Madjid M, Zarrabi A, Burke A, Yuan C, Fitzgerald PJ, Siscovick DS, de Korte CL, Aikawa M, Juhani Airaksinen KE, Assmann G, Becker CR, Chesebro JH, Farb A, Galis ZS, Jackson C, Jang IK, Koenig W, Lodder RA, March K, Demirovic J, Navab M, Priori SG, Rekhter MD, Bahr R, Grundy SM, Mehran R, Colombo A, Boerwinkle E, Ballantyne C, Insull W, Jr., Schwartz RS, Vogel R, Serruys PW, Hansson GK, Faxon DP, Kaul S, Drexler H, Greenland P, Muller JE, Virmani R, Ridker PM, Zipes DP, Shah PK, Willerson JT. From vulnerable plaque to vulnerable patient: a call for new definitions and risk assessment strategies: Part I. Circulation 2003;108:1664-72.

29.   Lindahl U CJ, Kimata K, et al. Proteoglycans and Sulfated Glycosaminoglycans. 2017. In: Varki A, Cummings RD, Esko JD, Freeze HH, Stanley P, Bertozzi CR, Hart GW, Etzler ME,

editors. Essentials of Glycobiology [Internet]. 3rd edition. Cold Spring Harbor (NY): Cold Spring Harbor Laboratory Press; 2015-2017. Chapter 17. Available from: https://www.ncbi.nlm.nih.gov/books/NBK453033/ doi: 10.1101/glycobiology.3e.017.

30.   Hascall V, Cummings RD, Esko JD, et al., editors. Essentials of Glycobiology [Internet]. 3rd edition. Cold Spring Harbor (NY): Cold Spring Harbor Laboratory Press; 2015-2017. Chapter 16. Available from: https://www.ncbi.nlm.nih.gov/books/NBK453025/ doi: 10.1101/glycobiology.3e.016.

31.   Hynes RO, Naba A. Overview of the matrisome--an inventory of extracellular matrix constituents and functions. Cold Spring Harb Perspect Biol 2012;4:a004903.

32.   Iozzo RV, Schaefer L. Proteoglycan form and function: A comprehensive nomenclature of proteoglycans. Matrix Biol 2015;42:11-55.

33.   Prydz K, Dalen KT. Synthesis and sorting of proteoglycans. J Cell Sci 2000;113 Pt 2:193-205.

34.   Aono S, Keino H, Ono T, Yasuda Y, Tokita Y, Matsui F, Taniguchi M, Sonta S, Oohira A. Genomic organization and expression pattern of mouse neuroglycan C in the cerebellar development. J Biol Chem 2000;275:337-42.

35.   Chen S, Birk DE. The regulatory roles of small leucine-rich proteoglycans in extracellular matrix assembly. The FEBS journal 2013;280:2120-37.

36.   Schaefer L, Iozzo RV. Biological functions of the small leucine-rich proteoglycans: from genetics to signal transduction. J Biol Chem 2008;283:21305-9.

37.   Sotoodehnejadnematalahi F, Burke B. Structure, function and regulation of versican: the most abundant type of proteoglycan in the extracellular matrix. Acta Med Iran 2013;51:740-50.

38.   Prydz K. Determinants of Glycosaminoglycan (GAG) Structure. Biomolecules 2015;5:2003-22.Cate

39.   Caterson, Bruce, and James Melrose. Keratan sulfate, a complex glycosaminoglycan with unique functional capability. Glycobiology 2018; 28.4: 182-206.

40.   Mikami T, Kitagawa H. Biosynthesis and function of chondroitin sulfate. Biochim Biophys Acta 2013;1830:4719-33.

41.   Li JP, Kusche-Gullberg M. Heparan Sulfate: Biosynthesis, Structure, and Function. Int Rev Cell Mol Biol 2016;325:215-73.

42.   Kusche-Gullberg M, Kjellen L. Sulfotransferases in glycosaminoglycan biosynthesis. Curr Opin Struct Biol 2003;13:605-11.

43.   Hammond E, Khurana A, Shridhar V, Dredge K. The Role of Heparanase and Sulfatases in the Modification of Heparan Sulfate Proteoglycans within the Tumor Microenvironment and Opportunities for Novel Cancer Therapeutics. Front Oncol 2014;4.

44.   Itano N, Kimata K. Mammalian hyaluronan synthases. IUBMB life 2002;54:195-9.

45.   Freeze HH. Genetic Disorders of Glycan Degradation. In: Varki A CR, Esko JD, Cummings RD, Esko JD, Freeze HH, Stanley P, Bertozzi CR, Hart GW, Etzler ME, editors. Essentials of Glycobiology. 2nd edition. Cold Spring Harbor (NY): Cold Spring Harbor Laboratory Press; 2009. Chapter 41. Available from: https://www.ncbi.nlm.nih.gov/books/NBK1934/.

46.   Griffin LS, Gloster TM. The Enzymatic Degradation of Heparan Sulfate. Protein Pept Lett 2017;24:710-22.

47.   Triggs-Raine B, Natowicz MR. Biology of hyaluronan: Insights from genetic disorders of hyaluronan metabolism. World J Biol Chem 2015;6:110-20.

48.   Reitsma S, Slaaf DW, Vink H, van Zandvoort MAMJ, oude Egbrink MGA. The endothelial glycocalyx: composition, functions, and visualization. Pflügers Archiv - European Journal of Physiology 2007;454:345-59.

49.   Fu BM, Tarbell JM. Mechano-sensing and transduction by endothelial surface glycocalyx: composition, structure, and function. Wiley Interdiscip Rev Syst Biol Med 2013;5:381-90.

50.   Eble JA, Niland S. The extracellular matrix of blood vessels. Curr Pharm Des 2009;15:1385-400.

51.   Merrilees MJ, Beaumont B, Scott LJ. Comparison of deposits of versican, biglycan and decorin in saphenous vein and internal thoracic, radial and coronary arteries: correlation to patency. Coron Artery Dis 2001;12:7-16.

52.   van den Berg B, Vink H. Glycocalyx perturbation: cause or consequence of damage to the vasculature? Am J Physiol Heart Circ Physiol 2006;290:H2174-5.

53.   Cancel LM, Ebong EE, Mensah S, Hirschberg C, Tarbell JM. Endothelial glycocalyx, apoptosis and inflammation in an atherosclerotic mouse model. Atherosclerosis 2016;252:136-46.

54.   McDonald KK, Cooper S, Danielzak L, Leask RL. Glycocalyx Degradation Induces a Proinflammatory Phenotype and Increased Leukocyte Adhesion in Cultured Endothelial Cells under Flow. PLoS One 2016;11:e0167576.

55.   Voyvodic PL, Min D, Liu R, Williams E, Chitalia V, Dunn AK, Baker AB. Loss of syndecan-1 induces a pro-inflammatory phenotype in endothelial cells with a dysregulated response to atheroprotective flow. J Biol Chem 2014;289:9547-59.

56.   Baeyens N, Mulligan-Kehoe MJ, Corti F, et al. Syndecan 4 is required for endothelial alignment in flow and atheroprotective signaling. Proc Natl Acad Sci U S A 2014;111:17308-13.

57.   Ebong EE, Lopez-Quintero SV, Rizzo V, Spray DC, Tarbell JM. Shear-induced endothelial NOS activation and remodeling via heparan sulfate, glypican-1, and syndecan-1. Integr Biol (Camb) 2014;6:338-47.

58.   Sieve I, Munster-Kuhnel AK, Hilfiker-Kleiner D. Regulation and function of endothelial glycocalyx layer in vascular diseases. Vascul Pharmacol 2018;100:26-33.

59.   Zeng Y. Endothelial Glycocalyx: Novel Insight into Atherosclerosis. J Biomed 2017;2:109-16.

60.   Nonaka R, Iesaki T, de Vega S, Daida H, Okada T, Sasaki T, Arikawa-Hirasawa E. Perlecan deficiency causes endothelial dysfunction by reducing the expression of endothelial nitric oxide synthase. Physiological reports 2015;3.

61.   Kennett EC, Rees MD, Malle E, Hammer A, Whitelock JM, Davies MJ. Peroxynitrite modifies the structure and function of the extracellular matrix proteoglycan perlecan by reaction with both the protein core and the heparan sulfate chains. Free Radic Biol Med 2010;49:282-93.

62.   Chuang CY, Degendorfer G, Hammer A, Whitelock JM, Malle E, Davies MJ. Oxidation modifies the structure and function of the extracellular matrix generated by human coronary artery endothelial cells. Biochem J 2014;459:313-22.

63.   Wight TN. A role for proteoglycans in vascular disease. Matrix Biol 2018;71-72:396-420.

64.   Moulton KS, Olsen BR, Sonn S, Fukai N, Zurakowski D, Zeng X. Loss of collagen XVIII enhances neovascularization and vascular permeability in atherosclerosis. Circulation 2004;110:1330-6.

65.   Fritze LM, Reilly CF, Rosenberg RD. An antiproliferative heparan sulfate species produced by postconfluent smooth muscle cells. J Cell Biol 1985;100:1041-9.

66.   Bingley JA, Hayward IP, Campbell JH, Campbell GR. Arterial heparan sulfate proteoglycans inhibit vascular smooth muscle cell proliferation and phenotype change in vitro and neointimal formation in vivo. J Vasc Surg 1998;28:308-18.

67.   Koyama N, Kinsella MG, Wight TN, Hedin U, Clowes AW. Heparan sulfate proteoglycans mediate a potent inhibitory signal for migration of vascular smooth muscle cells. Circ Res 1998;83:305-13.

68.   Fukai N, Kenagy RD, Chen L, Gao L, Daum G, Clowes AW. Syndecan-1: an inhibitor of arterial smooth muscle cell growth and intimal hyperplasia. Arterioscler Thromb Vasc Biol 2009;29:1356-62.

69.   Tran-Lundmark K, Tannenberg P, Rauch BH, Ekstrand J, Tran PK, Hedin U, Kinsella MG. Perlecan Heparan Sulfate Is Required for the Inhibition of Smooth Muscle Cell Proliferation by All-trans-Retinoic Acid. J Cell Physiol 2015;230:482-7.

70.   Chaterji S, Lam CH, Ho DS, Proske DC, Baker AB. Syndecan-1 regulates vascular smooth muscle cell phenotype. PLoS One 2014;9:e89824.

71.   Gotha L, Lim SY, Osherov AB, Wolff R, Qiang B, Erlich I, Nili N, Pillarisetti S, Chang YT, Tran PK, Tryggvason K, Hedin U, Tran-Lundmark K, Advani SL, Gilbert RE, Strauss BH. Heparan sulfate side chains have a critical role in the inhibitory effects of perlecan on vascular smooth muscle cell response to arterial injury. Am J Physiol Heart Circ Physiol 2014;307:H337-45.

72.   Tran PK, Tran-Lundmark K, Soininen R, Tryggvason K, Thyberg J, Hedin U. Increased intimal hyperplasia and smooth muscle cell proliferation in transgenic mice with heparan sulfate-deficient perlecan. Circ Res 2004;94:550-8.

73.   Lundmark K, Tran PK, Kinsella MG, Clowes AW, Wight TN, Hedin U. Perlecan inhibits smooth muscle cell adhesion to fibronectin: role of heparan sulfate. J Cell Physiol 2001;188:67-74.

74.   Ikesue M, Matsui Y, Ohta D, Danzaki K, Ito K, Kanayama M, Kurotaki D, Morimoto J, Kojima T, Tsutsui H, Uede T. Syndecan-4 deficiency limits neointimal formation after vascular injury by regulating vascular smooth muscle cell proliferation and vascular progenitor cell mobilization. Arterioscler Thromb Vasc Biol 2011;31:1066-74.

75.   Rauch BH, Millette E, Kenagy RD, Daum G, Fischer JW, Clowes AW. Syndecan-4 is required for thrombin-induced migration and proliferation in human vascular smooth muscle cells. J Biol Chem 2005;280:17507-11.

76.   Newby AC, Zaltsman AB. Molecular mechanisms in intimal hyperplasia. J Pathol 2000;190:300-9.

77.   Levesque H, Girard N, Maingonnat C, Delpech A, Chauzy C, Tayot J, Courtois H, Delpech B. Localization and solubilization of hyaluronan and of the hyaluronan-binding protein hyaluronectin in human normal and arteriosclerotic arterial walls. Atherosclerosis 1994;105:51-62.

78.   Gutierrez P, O'Brien KD, Ferguson M, Nikkari ST, Alpers CE, Wight TN. Differences in the distribution of versican, decorin, and biglycan in atherosclerotic human coronary arteries. Cardiovasc Pathol 1997;6:271-8.

79.   O'Brien KD, Olin KL, Alpers CE, Chiu W, Ferguson M, Hudkins K, Wight TN, Chait A. Comparison of apolipoprotein and proteoglycan deposits in human coronary atherosclerotic plaques: colocalization of biglycan with apolipoproteins. Circulation 1998;98:519-27.

80.   Radhakrishnamurthy B, Tracy RE, Dalferes ER, Berenson GS. Proteoglycans in Human Coronary Arteriosclerotic Lesions. Exp Mol Pathol 1998;65:1-8.

81.   Nakashima Y, Fujii H, Sumiyoshi S, Wight T, Sueishi K. Early Human Atherosclerosis: Accumulation of Lipid and Proteoglycans in Intimal Thickenings Followed by Macrophage Infiltration2007.

82.   Wight TN, Merrilees MJ. Proteoglycans in Atherosclerosis and Restenosis Key Roles for Versican. Circulation Research: Journal of the American Heart Association 2004;94:1158-67.

83.   Wight TN, Kinsella MG, Evanko SP, Potter-Perigo S, Merrilees MJ. Versican and the regulation of cell phenotype in disease. Biochimica et Biophysica Acta (BBA)-General Subjects 2014;1840:2441-51.

84.   Evanko SP, Angello JC, Wight TN. Formation of hyaluronan-and versican-rich pericellular matrix is required for proliferation and migration of vascular smooth muscle cells. Arterioscler Thromb Vasc Biol 1999;19:1004-13.

85.   Evanko SP, Johnson PY, Braun KR, Underhill CB, Dudhia J, Wight TN. Platelet-derived growth factor stimulates the formation of versican–hyaluronan aggregates and pericellular matrix expansion in arterial smooth muscle cells. Arch Biochem Biophys 2001;394:29-38.

86.   Fischer JW. Role of hyaluronan in atherosclerosis: Current knowledge and open questions. Matrix Biol 2018.

87.   Shimizu-Hirota R, Sasamura H, Kuroda M, Kobayashi E, Hayashi M, Saruta T. Extracellular matrix glycoprotein biglycan enhances vascular smooth muscle cell proliferation and migration. Circ Res 2004;94:1067-74.

88.   Papakonstantinou E, Roth M, Block L-H, Mirtsou-Fidani V, Argiriadis P, Karakiulakis G. The differential distribution of hyaluronic acid in the layers of human atheromatic aortas is associated with vascular smooth muscle cell proliferation and migration. Atherosclerosis 1998;138:79-89.

89.   Hwang J-Y, Johnson PY, Braun KR, Hinek A, Fischer JW, O'Brien KD, Starcher B, Clowes AW, Merrilees MJ, Wight TN. Retrovirally mediated overexpression of glycosaminoglycan-deficient biglycan in arterial smooth muscle cells induces tropoelastin synthesis and elastic fiber formation in vitro and in neointimae after vascular injury. The American journal of pathology 2008;173:1919-28.

90.   Lemire JM, Merrilees MJ, Braun KR, Wight TN. Overexpression of the V3 variant of versican alters arterial smooth muscle cell adhesion, migration, and proliferation in vitro. J Cell Physiol 2002;190:38-45.

91.   Kang I, Barth JL, Sproul EP, Yoon DW, Braun KR, Argraves WS, Wight TN. Expression of V3 versican by rat arterial smooth muscle cells promotes differentiated and anti-inflammatory phenotypes. J Biol Chem 2015:jbc. M115. 657486.

92.   Fischer JW, Kinsella MG, Levkau B, Clowes AW, Wight TN. Retroviral overexpression of decorin differentially affects the response of arterial smooth muscle cells to growth factors. Arterioscler Thromb Vasc Biol 2001;21:777-84.

93.   Nili N, Cheema AN, Giordano FJ, Barolet AW, Babaei S, Hickey R, Eskandarian MR, Smeets M, Butany J, Pasterkamp G. Decorin inhibition of PDGF-stimulated vascular smooth muscle cell function: potential mechanism for inhibition of intimal hyperplasia after balloon angioplasty. The American journal of pathology 2003;163:869-78.

94.   Talusan P, Bedri S, Yang S, Kattapuram T, Silva N, Roughley PJ, Stone JR. Analysis of intimal proteoglycans in atherosclerosis-prone and atherosclerosis-resistant human arteries by mass spectrometry. Mol Cell Proteomics 2005;4:1350-7.

95.   Didangelos A, Yin X, Mandal K, Baumert M, Jahangiri M, Mayr M. Proteomic characterization of extracellular space components in the human aorta. Mol Cell Proteomics 2010:mcp. M110. 001693.

96.   Onda M, Ishiwata T, Kawahara K, Wang R, Naito Z, Sugisaki Y. Expression of lumican in thickened intima and smooth muscle cells in human coronary atherosclerosis. Exp Mol Pathol 2002;72:142-9.

97.   Hutter R, Speidl W, Huang L, Gianarelli C, Badimon J, Klotman P. the Novel Small Leucine-rich Repeat Protein Podocan Inhibits Smooth Muscle Cell Activation And Neointima Formation Via Modulation Of The Canonical Wnt-pathway And Is Differently Expressed In Human Primary Versus Restenotic Coronary Lesions: 259. Cardiology 2014;128:273.

98.   Shanahan CM, Cary NR, Osbourn JK, Weissberg PL. Identification of osteoglycin as a component of the vascular matrix: differential expression by vascular smooth muscle cells during neointima formation and in atherosclerotic plaques. Arterioscler Thromb Vasc Biol 1997;17:2437-47.

99.   Kampmann A, Fernández B, Deindl E, Kubin T, Pipp F, Eitenmüller I, Hoefer IE, Schaper W, Zimmermann R. The proteoglycan osteoglycin/mimecan is correlated with arteriogenesis. Mol Cell Biochem 2009;322:15-23.

100.   Zhang HJ, Wang J, Liu HF, Zhang XN, Zhan M, Chen FL. Overexpression of mimecan in human aortic smooth muscle cells inhibits cell proliferation and enhances apoptosis and migration. Exp Ther Med 2015;10:187-92.

101.   Moncayo-Arlandi J, López-García A, Fernández MC, Durán AC, Fernández B. Osteoglycin deficiency does not affect atherosclerosis in mice. Atherosclerosis 2014;237:418-25.

102.   Yanagishita M. A brief history of proteoglycans. Experientia 1993;49:366-8.

103.   Williams KJ, Tabas I. The response-to-retention hypothesis of early atherogenesis. Arterioscler Thromb Vasc Biol 1995;15:551-61.

104.   Gustafsson M, Borén J. Mechanism of lipoprotein retention by the extracellular matrix. Curr Opin Lipidol 2004;15:505-14.

105.   Thompson JC, Tang T, Wilson PG, Yoder MH, Tannock LR. Increased atherosclerosis in mice with increased vascular biglycan content. Atherosclerosis 2014;235:71-5.

106.   O'Brien KD, Lewis K, Fischer JW, Johnson P, Hwang J-Y, Knopp EA, Kinsella MG, Barrett PHR, Chait A, Wight TN. Smooth muscle cell biglycan overexpression results in increased lipoprotein retention on extracellular matrix: implications for the retention of lipoproteins in atherosclerosis. Atherosclerosis 2004;177:29-35.

107.   Neufeld EB, Zadrozny LM, Phillips D, Aponte A, Yu Z-X, Balaban RS. Decorin and biglycan retain LDL in disease-prone valvular and aortic subendothelial intimal matrix. Atherosclerosis 2014;233:113-21.

108.   Pentikäinen MO, Öörni K, Lassila R, Kovanen PT. The proteoglycan decorin links low density lipoproteins with collagen type I. J Biol Chem 1997;272:7633-8.

109.   Tran-Lundmark K, Tran P-K, Paulsson-Berne G, Fridén V, Soininen R, Tryggvason K, Wight TN, Kinsella MG, Borén J, Hedin U. Heparan sulfate in perlecan promotes mouse

atherosclerosis: roles in lipid permeability, lipid retention, and smooth muscle cell proliferation. Circ Res 2008;103:43-52.

110.   Vikramadithyan RK, Kako Y, Chen G, Hu Y, Arikawa-Hirasawa E, Yamada Y, Goldberg IJ. Atherosclerosis in perlecan heterozygous mice. J Lipid Res 2004;45:1806-12.

111.   Boyanovsky BB, Shridas P, Simons M, van der Westhuyzen DR, Webb NR. Syndecan-4 mediates macrophage uptake of group V secretory phospholipase A2-modified LDL. J Lipid Res 2009;50:641-50.

112.   She Z-G, Chang Y, Pang H-B, Han W, Chen H-Z, Smith JW, Stallcup WB. NG2 proteoglycan ablation reduces foam cell formation and atherogenesis via decreased low-density lipoprotein retention by synthetic smooth muscle cells. Arterioscler Thromb Vasc Biol 2016;36:49-59.

113.   Shami A, Tengryd C, Asciutto G, Bengtsson E, Nilsson J, Hultgårdh-Nilsson A, Gonçalves I. Expression of fibromodulin in carotid atherosclerotic plaques is associated with diabetes and cerebrovascular events. Atherosclerosis 2015;241:701-8.

114.   Shami A, Gustafsson R, Kalamajski S, Krams R, Segers D, Rauch U, Roos G, Nilsson J, Oldberg Å, Hultgårdh-Nilsson A. Fibromodulin Deficiency Reduces Low-Density Lipoprotein Accumulation in Atherosclerotic Plaques in Apolipoprotein E–Null Mice. Arterioscler Thromb Vasc Biol 2013;33:354-61.

115.   Kunjathoor VV, Chiu DS, O'brien KD, LeBoeuf RC. Accumulation of biglycan and perlecan, but not versican, in lesions of murine models of atherosclerosis. Arterioscler Thromb Vasc Biol 2002;22:462-8.

116.   Stefanovich V, Akiyama K. Comparative studies of aortic acid mucopolysaccharides in fifteen species. Comp Biochem Physiol 1970;34:125-30.

117.   Gardais A, Picard J, Hermelin B. Glycosaminoglycan (GAG) distribution in aortic wall from five species. Comparative Biochemistry and Physiology Part B: Comparative Biochemistry 1973;44:507-15.

118.   Tran P-K, Agardh HE, Tran-Lundmark K, Ekstrand J, Roy J, Henderson B, Gabrielsen A, Hansson GK, Swedenborg J, Paulsson-Berne G. Reduced perlecan expression and accumulation in human carotid atherosclerotic lesions. Atherosclerosis 2007;190:264-70.

119.   Otsuka F, Kramer MC, Woudstra P, Yahagi K, Ladich E, Finn AV, de Winter RJ, Kolodgie FD, Wight TN, Davis HR. Natural progression of atherosclerosis from pathologic intimal thickening to late fibroatheroma in human coronary arteries: a pathology study. Atherosclerosis 2015;241:772-82.

120.   Cardoso LE, Mourao PA. Glycosaminoglycan fractions from human arteries presenting diverse susceptibilities to atherosclerosis have different binding affinities to plasma LDL. Arteriosclerosis and thrombosis: a journal of vascular biology 1994;14:115-24.

121.   E Karangelis D, Kanakis I, P Asimakopoulou A, Karousou E, Passi A, D Theocharis A, Triposkiadi F, B Tsilimingas N, K Karamanos N. Glycosaminoglycans as key molecules in atherosclerosis: the role of versican and hyaluronan. Curr Med Chem 2010;17:4018-26.

122.   Little PJ, Osman N, D O'Brien K. Hyperelongated biglycan: the surreptitious initiator of atherosclerosis. Curr Opin Lipidol 2008;19:448-54.

123.   Little PJ, Ballinger ML, Osman N. Vascular wall proteoglycan synthesis and structure as a target for the prevention of atherosclerosis. Vascular health and risk management 2007;3:117.

124.   Sambandam T, Baker J, Christner J, Ekborg S. Specificity of the low density lipoprotein-glycosaminoglycan interaction. Arteriosclerosis and thrombosis: a journal of vascular biology 1991;11:561-8.

125.   Qiang B, Lim SY, Lekas M, Kuliszewski MA, Wolff R, Osherov AB, Rudenko D, Leong-Poi H, Noyan H, Husain M. Perlecan heparan sulfate proteoglycan is a critical determinant of angiogenesis in response to mouse hind-limb ischemia. Can J Cardiol 2014;30:1444-51.

126.   Durgin BG, Cherepanova OA, Gomez D, et al. Smooth muscle cell-specific deletion of Col15a1 unexpectedly leads to impaired development of advanced atherosclerotic lesions. American Journal of Physiology-Heart and Circulatory Physiology 2017;312:H943-H58.

127.   Li Q, Olsen BR. Increased angiogenic response in aortic explants of collagen XVIII/endostatin-null mice. The American journal of pathology 2004;165:415-24.

128.   Mao W, Kong J, Dai J, Huang Z-q, Wang D-z, Ni G-b, Chen M-l. Evaluation of recombinant endostatin in the treatment of atherosclerotic plaques and neovascularization in rabbits. Journal of Zhejiang University SCIENCE B 2010;11:599-607.

129.   Moulton KS, Heller E, Konerding MA, Flynn E, Palinski W, Folkman J. Angiogenesis inhibitors endostatin or TNP-470 reduce intimal neovascularization and plaque growth in apolipoprotein E–deficient mice. Circulation 1999;99:1726-32.

130.   Mongiat M, Andreuzzi E, Tarticchio G, Paulitti A. Extracellular matrix, a hard player in angiogenesis. Int J Mol Sci 2016;17:1822.

131.   Jian J, Zheng Z, Zhang K, Rackohn TM, Hsu C, Levin A, Enjamuri DR, Zhang X, Ting K, Soo C. Fibromodulin promoted in vitro and in vivo angiogenesis. Biochem Biophys Res Commun 2013;436:530-5.

132.   Adini I, Ghosh K, Adini A, Chi Z-L, Yoshimura T, Benny O, Connor KM, Rogers MS, Bazinet L, Birsner AE. Melanocyte-secreted fibromodulin promotes an angiogenic microenvironment. The Journal of clinical investigation 2014;124:425-36.

133.   Zheng Z, Jian J, Velasco O, Hsu C-y, Zhang K, Levin A, Murphy M, Zhang X, Ting K, Soo C. Fibromodulin enhances angiogenesis during cutaneous wound healing. Plastic and Reconstructive Surgery Global Open 2014;2.

134. Asano K, Nelson CM, Nandadasa S, Aramaki-Hattori N, Lindner DJ, Alban T, Inagaki J, Ohtsuki T, Oohashi T, Apte SS. Stromal versican regulates tumor growth by promoting angiogenesis. Sci Rep 2017;7:17225.

135. Rauch U, Bengtsson E, Gonçalves I, Hultgårdh-Nilsson A. Distinctive peri-luminal presence of agrin in murine and human carotid atherosclerotic plaques. Histol Histopathol 2018:11970-.

136. Xu X, Mao W, Chai Y, Dai J, Chen Q, Wang L, Zhuang Q, Pan Y, Chen M, Ni G. Angiogenesis inhibitor, endostar, prevents vasa vasorum neovascularization in a swine atherosclerosis model. Journal of atherosclerosis and thrombosis 2015;22:1100-12.

137. van Hinsbergh VW. Osteoglycin's embracement of VEGF receptor-2 limits angiogenesis and collateralization. Oxford University Press; 2017.

138. Gomez-Outes A, Luisa Suarez-Gea M, Calvo-Rojas G, Lecumberri R, Rocha E, Pozo-Hernández C, Isabel Terleira-Fernandez A, Vargas-Castrillón E. Discovery of anticoagulant drugs: a historical perspective. Current drug discovery technologies 2012;9:83-104.

139. Sobczak AI, Pitt SJ, Stewart AJ. Glycosaminoglycan Neutralization in Coagulation Control. Arterioscler Thromb Vasc Biol 2018;38:1258-70.

140. Morrison L, Rucker P, Ershoff B. Prolongation of thrombus-formation time in rabbits given chondroitin sulfate A. J Atheroscler Res 1968;8:319-27.

141. Bjornsson T, Nash P, Schaten R. The anticoagulant effect of chondroitin-4-sulfate. Thromb Res 1982;27:15-21.

142. Silver FH, Yannas IV, Salzman EW. Glycosaminoglycan inhibition of collagen induced platelet aggregation. Thromb Res 1978;13:267-77.

143. Teien AN, Abildgaard U, Höök M. The anticoagulant effect of heparan sulfate and dermatan sulfate. Thromb Res 1976;8:859-67.

144. Ofosu F, Modi G, Blajchman M, Buchanan M, Johnson E. Increased sulphation improves the anticoagulant activities of heparan sulphate and dermatan sulphate. Biochem J 1987;248:889-96.

145. Murata K, Nakazawa K, Hamai A. Distribution of acidic glycosaminoglycans in the intima, media and adventitia of bovine aorta and their anticoagulant properties. Atherosclerosis 1975;21:93-103.

146. Hatton M, Berry L, Ragoeczl E. Inhibition of thrombin by antithrombin III in the presence of certain glycosaminoglycans found in the mammalian aorta. Thromb Res 1978;13:655-70.

147. Eisenstein R. Combined effect of prostaglandins and an aortic proteoglycan on platelet aggregation and plasma clotting. Prostaglandins Med 1979;3:159-66.

148. Izuka K, Murata K. Inhibitory effects of human aortic and venous acid glycosaminoglycans on thrombus formation. Atherosclerosis 1972;16:217-24.

149.   Tovar AM, de Mattos DA, Stelling MP, Sarcinelli-Luz BS, Nazareth RA, Mourão PA. Dermatan sulfate is the predominant antithrombotic glycosaminoglycan in vessel walls: implications for a possible physiological function of heparin cofactor II. Biochimica et Biophysica Acta (BBA)-Molecular Basis of Disease 2005;1740:45-53.

150.   Shworak NW, Kobayashi T, de Agostini A, Smits NC. Anticoagulant heparan sulfate: to not clot—or not? Prog Mol Biol Transl Sci: Elsevier; 2010:153-78.

151.   Tollefsen DM. Vascular dermatan sulfate and heparin cofactor II. Prog Mol Biol Transl Sci: Elsevier; 2010:351-72.

152.   Kolodgie FD, Burke AP, Farb A, Weber DK, Kutys R, Wight TN, Virmani R. Differential accumulation of proteoglycans and hyaluronan in culprit lesions: insights into plaque erosion. Arterioscler Thromb Vasc Biol 2002;22:1642-8.

153.   Koshiishi I, Shizari M, Underhill C. CD44 can mediate the adhesion of platelets to hyaluronan. Blood 1994;84:390-6.

154.   Mazzucato M, Cozzi MR, Pradella P, Perissinotto D, Malmsttröm A, Mörgelin M, Spessotto P, Colombatti A, De Marco L, Perris R. Vascular PG-M/versican variants promote platelet adhesion at low shear rates and cooperate with collagens to induce aggregation. The FASEB journal 2002;16:1903-16.

155.   Zheng P-S, Reis M, Sparling C, Lee DY, La Pierre DP, Wong C-KA, Deng Z, Kahai S, Wen J, Yang BB. Versican G3 domain promotes blood coagulation through suppressing the activity of tissue factor pathway inhibitor-1. J Biol Chem 2006;281:8175-82.

156.   McGee M, Wagner WD. Chondroitin sulfate anticoagulant activity is linked to water transfer: relevance to proteoglycan structure in atherosclerosis. Arterioscler Thromb Vasc Biol 2003;23:1921-7.

157.   Grandoch M, Kohlmorgen C, Melchior-Becker A, Feldmann K, Homann S, Müller J, Kiene L-S, Zeng-Brouwers J, Schmitz F, Nagy N. Loss of biglycan enhances thrombin generation in apolipoprotein E-deficient mice: Implications for inflammation and atherosclerosis. Arterioscler Thromb Vasc Biol 2016;36:e41-e50.

158.   Shirk RA, Parthasarathy N, San Antonio JD, Church FC, Wagner WD. Altered dermatan sulfate structure and reduced heparin cofactor II stimulating activity of biglycan and decorin from human atherosclerotic plaque. J Biol Chem 2000.

159.   Hultgardh-Nilsson A, Boren J, Chakravarti S. The small leucine-rich repeat proteoglycans in tissue repair and atherosclerosis. J Intern Med 2015;278:447-61.

160.   Binno S, Hoes AW, Piepoli MF, Group ESD, Cosyns B, Deaton C, Richter DJ, Prescott E, Graham I, Perk J, Løchen M-L, Cooney M-T, Tiberi M, Marques-Vidal P, Agewall S, Corrà U, Verschuren WMM, Smulders Y, Brotons C, Hobbs FDR, Sattar N, Catapano AL, van Dis I, Redon J, van der Worp HB, Hall MS, Löllgen H, Albus C. 2016 European Guidelines on cardiovascular disease prevention in clinical practice: The Sixth Joint Task Force of the European Society of Cardiology and Other Societies on Cardiovascular Disease Prevention in Clinical Practice

(constituted by representatives of 10 societies and by invited experts)Developed with the special contribution of the European Association for Cardiovascular Prevention & Rehabilitation (EACPR). Eur Heart J 2016;37:2315-81.

161.   Naylor AR, Vlachopoulos C, Espinola-Klein C, Tepe G, Desormais I, Collet J-P, Röther J, Mazzolai L, Venermo M, De Carlo M, Roffi M, Brodmann M, Bartelink M-LEL, Björck M, Czerny M, Tendera M, Sprynger M, Debus S, Kownator S, Kahan T, Cohnert T, Ricco J-B, Aboyans V, Group ESD. 2017 ESC Guidelines on the Diagnosis and Treatment of Peripheral Arterial Diseases, in collaboration with the European Society for Vascular Surgery (ESVS): Document covering atherosclerotic disease of extracranial carotid and vertebral, mesenteric, renal, upper and lower extremity arteriesEndorsed by: the European Stroke Organization (ESO)The Task Force for the Diagnosis and Treatment of Peripheral Arterial Diseases of the European Society of Cardiology (ESC) and of the European Society for Vascular Surgery (ESVS). Eur Heart J 2017;39:763-816.

162.   Torbicki A, Linhart A, Budaj A, Gitt AK, Hoes AW, Gersh BJ, Di Mario C, Erol C, Arden C, Deaton C, Vrints CJM, Hasdai D, Taggart DP, van der Wall EE, Prescott E, Andreotti F, Crea F, Ruschitzka F, Montalescot G, Bueno H, Baumgartner H, Ferreira JR, Hulot J-S, Bax JJ, Zamorano JL, Tamargo JL, Knuuti J, Opie LH, Sabaté M, Piepoli MF, Pfisterer M, Tendera M, Marx N, Lancellotti P, Kirchhof P, Sirnes PA, Nihoyannopoulos P, Kolh P, Ponikowski P, Bugiardini R, Fagard R, Ferrari R, Senior R, Achenbach S, Achenbach S, Windecker S, Cuisset T, Sechtem U, Dean V, Wijns W, Reviewers D, Guidelines ECfP, Members TF, Timmis A, Maggioni AP, Pries AR, Yildirir A, Erol C, Funck-Brentano C, Hasdai D, Romeo F, Bueno H, Frank H, Zamorano JL, Gonzalez-Juanatey JR, Knuuti J, Kervinen K, Rydén L, Simoons ML, Claeys MJ, Valgimigli M, Piepoli MF, Hamilos M, Donner-Banzhoff N, Gaemperli O, Lancellotti P, Sirnes PA, Steg PG, Kolh P, Husted S, Kristensen SD, James SK, Windecker S, Wijns W. 2013 ESC guidelines on the management of stable coronary artery disease: The Task Force on the management of stable coronary artery disease of the European Society of Cardiology. Eur Heart J 2013;34:2949-3003.

163.   Kastrati A, Caforio ALP, Bucciarelli-Ducci C, Varenhorst C, Prescott E, Crea F, Hindricks G, Bueno H, Goudevenos JA, Antunes MJ, Roffi M, Valgimigli M, Lenzen MJ, Vranckx P, Widimský P, Halvorsen S, Agewall S, Ibanez B, James S, Group ESD. 2017 ESC Guidelines for the management of acute myocardial infarction in patients presenting with ST-segment elevation: The Task Force for the management of acute myocardial infarction in patients presenting with ST-segment elevation of the European Society of Cardiology (ESC). Eur Heart J 2017;39:119-77.

164.   Gencer B, Brotons C, Mueller C, Mukherjee D, Chew DP, Andreotti F, Hasenfuss G, Collet J-P, Bax JJ, Mehilli J, Kjeldsen K, Valgimigli M, Borger MA, Lancellotti P, Storey RF, Windecker S, Landmesser U, Patrono C, Roffi M, Group ESD. 2015 ESC Guidelines for the management of acute coronary syndromes in patients presenting without persistent ST-segment elevation: Task Force for the Management of Acute Coronary Syndromes in Patients Presenting without Persistent ST-Segment Elevation of the European Society of Cardiology (ESC). Eur Heart J 2016;37:267-315.

165.   Kastrati A, Banning AP, Koller A, Ahlsson A, Richter DJ, Sibbing D, Alfonso F, Stefanini GG, Collet J-P, Niebauer J, Zembala MO, Seferović PM, Jüni P, Yadav R, Byrne RA, Kristensen SD, Windecker S, Head SJ, Benedetto U, Falk V, Neumann F-J, Sousa-Uva M, Group ESD. 2018 ESC/EACTS Guidelines on myocardial revascularization. Eur Heart J 2018;40:87-165.

166.   Dweck MR, Doris MK, Motwani M, Adamson PD, Slomka P, Dey D, Fayad ZA, Newby DE, Berman D. Imaging of coronary atherosclerosis - evolution towards new treatment strategies. Nat Rev Cardiol 2016;13:533-48.

167.   Finn AV, Nakano M, Narula J, Kolodgie FD, Virmani R. Concept of vulnerable/unstable plaque. Arterioscler Thromb Vasc Biol 2010;30:1282-92.

168.   Arbab-Zadeh A, Fuster V. The myth of the "vulnerable plaque": transitioning from a focus on individual lesions to atherosclerotic disease burden for coronary artery disease risk assessment. J Am Coll Cardiol 2015;65:846-55.

169.   Stefanadis C, Antoniou CK, Tsiachris D, Pietri P. Coronary atherosclerotic vulnerable plaque: Current perspectives. Journal of the American Heart Association 2017;6:e005543.

170.   Motoyama S, Sarai M, Harigaya H, Anno H, Inoue K, Hara T, Naruse H, Ishii J, Hishida H, Wong ND, Virmani R, Kondo T, Ozaki Y, Narula J. Computed tomographic angiography characteristics of atherosclerotic plaques subsequently resulting in acute coronary syndrome. J Am Coll Cardiol 2009;54:49-57.

171.   Noguchi T, Yamada N, Higashi M, Goto Y, Naito H. High-intensity signals in carotid plaques on T1-weighted magnetic resonance imaging predict coronary events in patients with coronary artery disease. J Am Coll Cardiol 2011;58:416-22.

172.   Otsuka K, Fukuda S, Tanaka A, Nakanishi K, Taguchi H, Yoshikawa J, Shimada K, Yoshiyama M. Napkin-ring sign on coronary CT angiography for the prediction of acute coronary syndrome. JACC Cardiovasc Imaging 2013;6:448-57.

173.   Versteylen MO, Kietselaer BL, Dagnelie PC, Joosen IA, Dedic A, Raaijmakers RH, Wildberger JE, Nieman K, Crijns HJ, Niessen WJ, Daemen MJ, Hofstra L. Additive value of semiautomated quantification of coronary artery disease using cardiac computed tomographic angiography to predict future acute coronary syndrome. J Am Coll Cardiol 2013;61:2296-305.

174.   Noguchi T, Kawasaki T, Tanaka A, Yasuda S, Goto Y, Ishihara M, Nishimura K, Miyamoto Y, Node K, Koga N. High-intensity signals in coronary plaques on noncontrast T1-weighted magnetic resonance imaging as a novel determinant of coronary events. J Am Coll Cardiol 2014;63:989-99.

175.   Saam T, Hetterich H, Hoffmann V, Yuan C, Dichgans M, Poppert H, Koeppel T, Hoffmann U, Reiser MF, Bamberg F. Meta-analysis and systematic review of the predictive value of carotid plaque hemorrhage on cerebrovascular events by magnetic resonance imaging. J Am Coll Cardiol 2013;62:1081-91.

176.   Puchner SB, Liu T, Mayrhofer T, Truong QA, Lee H, Fleg JL, Nagurney JT, Udelson JE, Hoffmann U, Ferencik M. High-risk plaque detected on coronary CT angiography predicts acute

coronary syndromes independent of significant stenosis in acute chest pain: results from the ROMICAT-II trial. J Am Coll Cardiol 2014;64:684-92.

177.   Motoyama S, Ito H, Sarai M, Kondo T, Kawai H, Nagahara Y, Harigaya H, Kan S, Anno H, Takahashi H, Naruse H, Ishii J, Hecht H, Shaw LJ, Ozaki Y, Narula J. Plaque Characterization by Coronary Computed Tomography Angiography and the Likelihood of Acute Coronary Events in Mid-Term Follow-Up. J Am Coll Cardiol 2015;66:337-46.

178.   Conte E, Annoni A, Pontone G, Mushtaq S, Guglielmo M, Baggiano A, Volpato V, Agalbato C, Bonomi A, Veglia F, Formenti A, Fiorentini C, Bartorelli AL, Pepi M, Andreini D. Evaluation of coronary plaque characteristics with coronary computed tomography angiography in patients with non-obstructive coronary artery disease: a long-term follow-up study. Eur Heart J Cardiovasc Imaging 2017;18:1170-8.

179.   Ferencik M, Mayrhofer T, Bittner DO, Emami H, Puchner SB, Lu MT, Meyersohn NM, Ivanov AV, Adami EC, Patel MR, Mark DB, Udelson JE, Lee KL, Douglas PS, Hoffmann U. Use of High-Risk Coronary Atherosclerotic Plaque Detection for Risk Stratification of Patients With Stable Chest Pain: A Secondary Analysis of the PROMISE Randomized Clinical Trial. JAMA cardiology 2018;3:144-52.

180.   Saba L, Yuan C, Hatsukami TS, Balu N, Qiao Y, DeMarco JK, Saam T, Moody AR, Li D, Matouk CC, Johnson MH, Jager HR, Mossa-Basha M, Kooi ME, Fan Z, Saloner D, Wintermark M, Mikulis DJ, Wasserman BA. Carotid Artery Wall Imaging: Perspective and Guidelines from the ASNR Vessel Wall Imaging Study Group and Expert Consensus Recommendations of the American Society of Neuroradiology. AJNR Am J Neuroradiol 2018;39:E9-e31.

181.   Williams MC, Moss AJ, Dweck M, Adamson PD, Alam S, Hunter A, Shah ASV, Pawade T, Weir-McCall JR, Roditi G, van Beek EJR, Newby DE, Nicol ED. Coronary Artery Plaque Characteristics Associated With Adverse Outcomes in the SCOT-HEART Study. J Am Coll Cardiol 2019;73:291-301.

182.   Andrews JPM, Fayad ZA, Dweck MR. New methods to image unstable atherosclerotic plaques. Atherosclerosis 2018;272:118-28.

183.   Newby DE, Adamson PD. Non-invasive imaging of the coronary arteries. 2018.

184.   Min JK, Leipsic J, Pencina MJ, Berman DS, Koo BK, van Mieghem C, Erglis A, Lin FY, Dunning AM, Apruzzese P, Budoff MJ, Cole JH, Jaffer FA, Leon MB, Malpeso J, Mancini GB, Park SJ, Schwartz RS, Shaw LJ, Mauri L. Diagnostic accuracy of fractional flow reserve from anatomic CT angiography. JAMA 2012;308:1237-45.

185.   Norgaard BL, Leipsic J, Gaur S, Seneviratne S, Ko BS, Ito H, Jensen JM, Mauri L, De Bruyne B, Bezerra H, Osawa K, Marwan M, Naber C, Erglis A, Park SJ, Christiansen EH, Kaltoft A, Lassen JF, Botker HE, Achenbach S. Diagnostic performance of noninvasive fractional flow reserve derived from coronary computed tomography angiography in suspected coronary artery disease: the NXT trial (Analysis of Coronary Blood Flow Using CT Angiography: Next Steps). J Am Coll Cardiol 2014;63:1145-55.

186.	Douglas PS, Pontone G, Hlatky MA, Patel MR, Norgaard BL, Byrne RA, Curzen N, Purcell I, Gutberlet M, Rioufol G, Hink U, Schuchlenz HW, Feuchtner G, Gilard M, Andreini D, Jensen JM, Hadamitzky M, Chiswell K, Cyr D, Wilk A, Wang F, Rogers C, De Bruyne B. Clinical outcomes of fractional flow reserve by computed tomographic angiography-guided diagnostic strategies vs. usual care in patients with suspected coronary artery disease: the prospective longitudinal trial of FFR(CT): outcome and resource impacts study. Eur Heart J 2015;36:3359-67.

187.	Patel K, Tarkin J, Serruys PW, Tenekecioglu E, Foin N, Zhang YJ, Crake T, Moon J, Mathur A, Bourantas CV. Invasive or non-invasive imaging for detecting high-risk coronary lesions? Expert Rev Cardiovasc Ther 2017;15:165-79.

188.	Tarkin JM, Dweck MR, Evans NR, Takx RA, Brown AJ, Tawakol A, Fayad ZA, Rudd JH. Imaging Atherosclerosis. Circ Res 2016;118:750-69.

189.	Friedrich MG. The Future of Cardiovascular Magnetic Resonance Imaging. Eur Heart J 2017;38:1698-701.

190.	Iozzo RV, Gubbiotti MA. Extracellular matrix: The driving force of mammalian diseases. Matrix Biol 2018.

191.	Reimann C, Brangsch J, Colletini F, Walter T, Hamm B, Botnar RM, Makowski MR. Molecular imaging of the extracellular matrix in the context of atherosclerosis. Adv Drug Deliv Rev 2017;113:49-60.

192.	Makowski MR, Varma G, Wiethoff AJ, Smith A, Mattock K, Jansen CH, Warley A, Taupitz M, Schaeffter T, Botnar RM. Noninvasive assessment of atherosclerotic plaque progression in ApoE−/− mice using susceptibility gradient mapping. Circ Cardiovasc Imaging 2011;4:295-303.

193.	Ludwig A, Poller WC, Westphal K, Minkwitz S, Lättig-Tünnemann G, Metzkow S, Stangl K, Baumann G, Taupitz M, Wagner S. Rapid binding of electrostatically stabilized iron oxide nanoparticles to THP-1 monocytic cells via interaction with glycosaminoglycans. Basic Res Cardiol 2013;108:328.

194.	Wagner S, Schnorr J, Ludwig A, Stangl V, Ebert M, Hamm B, Taupitz M. Contrast-enhanced MR imaging of atherosclerosis using citrate-coated superparamagnetic iron oxide nanoparticles: calcifying microvesicles as imaging target for plaque characterization. International journal of nanomedicine 2013;8:767.

195.	Poller WC, Löwa N, Wiekhorst F, Taupitz M, Wagner S, Möller K, Baumann G, Stangl V, Trahms L, Ludwig A. Magnetic particle spectroscopy reveals dynamic changes in the magnetic behavior of very small superparamagnetic iron oxide nanoparticles during cellular uptake and enables determination of cell-labeling efficacy. J Biomed Nanotechnol 2016;12:337-46.

196.	Ariza de Schellenberger A, Bergs J, Sack I, Taupitz M. The Extracellular Matrix as a Target for Biophysical and Molecular Magnetic Resonance Imaging. In: Sack I, Schaeffter T, eds. Quantification of Biophysical Parameters in Medical Imaging. Cham: Springer International Publishing; 2018:123-50.

197.   Garvey W, Fathi A, Bigelow F, Carpenter B, Jimenez C. Improved Movat pentachrome stain. Stain Technol 1986;61:60-2.

198.   Carson F. Alcian blue, p.H 2.5. Histotechnology: A Self-Instructional Text. Chicago: American Society for Clinical Pathology; 2015:147-9.

199.   Junqueira LCU, Bignolas G, Brentani RR. Picrosirius staining plus polarization microscopy, a specific method for collagen detection in tissue sections. Histochem J 1979;11:447-55.

200.   Carson F. Alizarin Red S Calcium Stain. Histotechnology, A Self-Instructional Text. Chicago: American Society for Clinical Pathology; 2015:257-8.

201.   Schindelin J, Arganda-Carreras I, Frise E, Kaynig V, Longair M, Pietzsch T, Preibisch S, Rueden C, Saalfeld S, Schmid B, Tinevez JY, White DJ, Hartenstein V, Eliceiri K, Tomancak P, Cardona A. Fiji: an open-source platform for biological-image analysis. Nature methods 2012;9:676-82.

202.   Bonin S, Hlubek F, Benhattar J, Denkert C, Dietel M, Fernandez PL, Hofler G, Kothmaier H, Kruslin B, Mazzanti CM, Perren A, Popper H, Scarpa A, Soares P, Stanta G, Groenen PJ. Multicentre validation study of nucleic acids extraction from FFPE tissues. Virchows Arch 2010;457:309-17.

203.   Boeckx C, Wouters A, Pauwels B, Deschoolmeester V, Specenier P, Lukaszuk K, Vermorken JB, Pauwels P, Peeters M, Lardon F, Baay MF. Expression analysis on archival material: comparison of 5 commercially available RNA isolation kits for FFPE material. Diagn Mol Pathol 2011;20:203-11.

204.   Deben C, Zwaenepoel K, Boeckx C, et al. Expression analysis on archival material revisited: isolation and quantification of RNA extracted from FFPE samples. Diagn Mol Pathol 2013;22:59-64.

205.   Uyama T KH, Sugahara K. Biosynthesis of Glycoaminoglycans and Proteoglycans. In: Kamerling JP, ed. Comprehensive Glycoscience (From Chemistry to Systems Biology). Amsterdam: Elsevier; 2007:79–104.

206.   Silbert JE, Sugumaran G. Biosynthesis of chondroitin/dermatan sulfate. IUBMB life 2002;54:177-86.

207.   Sugahara K, Kitagawa H. Heparin and heparan sulfate biosynthesis. IUBMB life 2002;54:163-75.

208.   Sasisekharan R, Venkataraman G. Heparin and heparan sulfate: biosynthesis, structure and function. Curr Opin Chem Biol 2000;4:626-31.

209.   Boeriu CG, Springer J, Kooy FK, van den Broek LAM, Eggink G. Production Methods for Hyaluronan. International Journal of Carbohydrate Chemistry 2013;2013:14.

210.   Pomin VH. Keratan sulfate: an up-to-date review. Int J Biol Macromol 2015;72:282-9.

211. Seko A, Yamashita K. Biosynthesis of Keratan Sulfate. In: Taniguchi N, Suzuki A, Ito Y, Narimatsu H, Kawasaki T, Hase S, eds. Experimental Glycoscience: Glycobiology. Tokyo: Springer Japan; 2008:67-9.

212. Fabregat A, Sidiropoulos K, Viteri G, Marin-Garcia P, Ping P, Stein L, D'Eustachio P, Hermjakob H. Reactome diagram viewer: Data structures and strategies to boost performance. Bioinformatics 2017.

213. RStudio Team (2020). RStudio: Integrated Development for R. RStudio P, Boston, MA URL http://www.rstudio.com/.

214. Ritchie ME, Phipson B, Wu D, Hu Y, Law CW, Shi W, Smyth GK. limma powers differential expression analyses for RNA-sequencing and microarray studies. Nucleic Acids Res 2015;43:e47.

215. Huber W, von Heydebreck A, Sültmann H, Poustka A, Vingron M. Variance stabilization applied to microarray data calibration and to the quantification of differential expression. Bioinformatics 2002;18 Suppl 1:S96-104.

216. Wickham H. ggplot2: elegant graphics for data analysis: springer; 2016.

217. Blighe K RS, Lewis M (2020). EnhancedVolcano: Publication-ready volcano plots with enhanced colouring and labeling. R package version 1.6.0, https://github.com/kevinblighe/EnhancedVolcano.

218. Metsalu T, Vilo J. ClustVis: a web tool for visualizing clustering of multivariate data using Principal Component Analysis and heatmap. Nucleic Acids Res 2015;43:W566-70.

219. Tibshirani R. A simple method for assessing sample sizes in microarray experiments. BMC Bioinformatics 2006;7:106.

220. Tusher VG, Tibshirani R, Chu G. Significance analysis of microarrays applied to the ionizing radiation response. Proceedings of the National Academy of Sciences 2001;98:5116-21.

221. van Wijk XM, Vallen MJ, van de Westerlo EM, Oosterhof A, Hao W, Versteeg EM, Raben J, Wismans RG, Smetsers TF, Dijkman HB, Schalkwijk J, van Kuppevelt TH. Extraction and structural analysis of glycosaminoglycans from formalin-fixed, paraffin-embedded tissues. Glycobiology 2012;22:1666-72.

222. Ambrosius M. Analyse von Glykosaminoglykanen in humanen Zellen und Körperflüssigkeiten. 2008.

223. Takegawa Y, Araki K, Fujitani N, Furukawa J, Sugiyama H, Sakai H, Shinohara Y. Simultaneous analysis of heparan sulfate, chondroitin/dermatan sulfates, and hyaluronan disaccharides by glycoblotting-assisted sample preparation followed by single-step zwitter-ionic-hydrophilic interaction chromatography. Anal Chem 2011;83:9443-9.

224. Bolstad BM, Irizarry RA, Astrand M, Speed TP. A comparison of normalization methods for high density oligonucleotide array data based on variance and bias. Bioinformatics 2003;19:185-93.

225.   Curran R, Crane W. Mucopolysaccharides in the atheromatous aorta. The Journal of pathology and bacteriology 1962;84:405-12.

226.   Riessen R, Isner JM, Blessing E, Loushin C, Nikol S, Wight TN. Regional differences in the distribution of the proteoglycans biglycan and decorin in the extracellular matrix of atherosclerotic and restenotic human coronary arteries. The American journal of pathology 1994;144:962.

227.   Evanko SP, Raines EW, Ross R, Gold LI, Wight TN. Proteoglycan distribution in lesions of atherosclerosis depends on lesion severity, structural characteristics, and the proximity of platelet-derived growth factor and transforming growth factor-beta. The American journal of pathology 1998;152:533.

228.   Müller-Spreer H-C, Werber U, Voigt K. Untersuchungen über die Höhe und Zusammensetzung der eiweißgebundenen kohlenhydrathaltigen Bestandteile in Serum und Gefäßwand von Normalpersonen und Arteriosklerotikern. Klin Wochenschr 1960;38:28-32.

229.   Berenson G. Studies of "ground substance" of the vessel wall and alterations in atherosclerosis and related diseases. J Atheroscler Res 1961;1:386-93.

230.   Buddecke E. Chemical changes in the ground substance of the vessel wall in arteriosclerosis. J Atheroscler Res 1962;2:32-46.

231.   Klynstra F, Böttcher C, Van Melsen J, Van der Laan E. Distribution and composition of acid mucopolysaccharides in normal and atherosclerotic human aortas. J Atheroscler Res 1967;7:301-9.

232.   Manley G, Mullinger R. Mucopolysaccharides of atherosclerotic plaques and platelets. Br J Exp Pathol 1967;48:529.

233.   Kumar V, Berenson G, Ruiz H, Dalferes Jr E, Strong J. Acid mucopolysaccharides of human aorta: Part 2. Variations with atherosclerotic involvement. J Atheroscler Res 1967;7:583-90.

234.   Nakamura T, Tokita K, Tateno S, Kotoku T, Ohba T. Human aortic acid mucopolysaccharides and glycoproteins: Changes during ageing and in atherosclerosis. J Atheroscler Res 1968;8:891-902.

235.   Sanwald R, Ritz E, Hug B. Untersuchungen zum Stoffwechsel der sauren Mucopolysaccharide in normalen und arteriosklerotisch veränderten frischen menschlichen Arterien. J Atheroscler Res 1968;8:433-44.

236.   Murata K, Oshima Y. Chondroitin sulfates in atherosclerotic human aorta. Atherosclerosis 1971;14:121-9.

237.   Dalferes Jr E, Ruiz H, Kumar V, Radhakrishnamurthy B, Berenson G. Acid mucopolysaccharides of fatty streaks in young, human male aortas. Atherosclerosis 1971;13:121-31.

238.   Stevens R, Colombo M, Gonzales J, Hollander W, Schmid K. The glycosaminoglycans of the human artery and their changes in atherosclerosis. The Journal of Clinical Investigation 1976;58:470-81.

239.   Tammi M, Seppälä P, Lehtonen A, Möttönen M. Connective tissue components in normal and atherosclerotic human coronary arteries. Atherosclerosis 1978;29:191-4.

240.   Murata K, Yokoyama Y. Acidic glycosaminoglycan, lipid and water contents in human coronary arterial branches. Atherosclerosis 1982;45:53-65.

241.   Murata K, Hashimoto N. Acidic glycosaminoglycans, water and lipids in normal and atherosclerotic human cerebral arteries. Atherosclerosis 1984;51:307-11.

242.   Wagner WD, Salisbury G, Rowe HA. A proposed structure of chondroitin 6-sulfate proteoglycan of human normal and adjacent atherosclerotic plaque. Arteriosclerosis: An Official Journal of the American Heart Association, Inc 1986;6:407-17.

243.   Dalferes Jr ER, Radhakrishnamurthy B, Ruiz HA, Berenson GS. Composition of proteoglycans from human atherosclerotic lesions. Exp Mol Pathol 1987;47:363-76.

244.   Alavi MZ, Moore S. Proteoglycan composition of rabbit arterial wall under conditions of experimentally induced atherosclerosis. Atherosclerosis 1987;63:65-74.

245.   Murata K, Yokoyama Y. Acidic glycosaminoglycans in human atherosclerotic cerebral arterial tissues. Atherosclerosis 1989;78:69-79.

246.   Völker W, Schmidt A, Buddecke E. Cytochemical changes in a human arterial proteoglycan related to atherosclerosis. Atherosclerosis 1989;77:117-30.

247.   Cherchi G, Coinu R, Demuro P, Formato M, Sanna G, Tidore M, Tira M, De Luca G. Structural and functional modifications of human aorta proteoglycans in atherosclerosis. Matrix 1990;10:362-72.

248.   Wasty F, Alavi M, Moore S. Distribution of glycosaminoglycans in the intima of human aortas: changes in atherosclerosis and diabetes mellitus. Diabetologia 1993;36:316-22.

249.   Heickendorff L, Ledet T, Rasmussen L. Glycosaminoglycans in the human aorta in diabetes mellitus: a study of tunica media from areas with and without atherosclerotic plaque. Diabetologia 1994;37:286-92.

250.   Theocharis AD, Theocharis DA, De Luca G, Hjerpe A, Karamanos NK. Compositional and structural alterations of chondroitin and dermatan sulfates during the progression of atherosclerosis and aneurysmal dilatation of the human abdominal aorta. Biochimie 2002;84:667-74.

251.   Faber BC, Cleutjens KB, Niessen RL, Aarts PL, Boon W, Greenberg AS, Kitslaar PJ, Tordoir JH, Daemen MJ. Identification of genes potentially involved in rupture of human atherosclerotic plaques. Circ Res 2001;89:547-54.

252.   Hiltunen MO, Tuomisto TT, Niemi M, Bräsen JH, Rissanen TT, Törönen P, Vajanto I, Ylä-Herttuala S. Changes in gene expression in atherosclerotic plaques analyzed using DNA array. Atherosclerosis 2002;165:23-32.

253.   Faber BC, Heeneman S, Daemen MJ, Cleutjens KB. Genes potentially involved in plaque rupture. Curr Opin Lipidol 2002;13:545-52.

254.   Tyson KL, Weissberg PL, Shanahan CM. Heterogeneity of gene expression in human atheroma unmasked using cDNA representational difference analysis. Physiol Genomics 2002;9:121-30.

255.   Randi A, Biguzzi E, Falciani F, Merlini P, Blakemore S, Bramucci E, Lucreziotti S, Lennon M, Faioni E, Ardissino D. Identification of differentially expressed genes in coronary atherosclerotic plaques from patients with stable or unstable angina by cDNA array analysis. J Thromb Haemost 2003;1:829-35.

256.   Tuomisto TT, Korkeela A, Rutanen J, Viita H, Brasen JH, Riekkinen MS, Rissanen TT, Karkola K, Kiraly Z, Kolble K, Yla-Herttuala S. Gene expression in macrophage-rich inflammatory cell infiltrates in human atherosclerotic lesions as studied by laser microdissection and DNA array: overexpression of HMG-CoA reductase, colony stimulating factor receptors, CD11A/CD18 integrins, and interleukin receptors. Arterioscler Thromb Vasc Biol 2003;23:2235-40.

257.   Archacki SR, Angheloiu G, Tian XL, Tan FL, DiPaola N, Shen GQ, Moravec C, Ellis S, Topol EJ, Wang Q. Identification of new genes differentially expressed in coronary artery disease by expression profiling. Physiol Genomics 2003;15:65-74.

258.   Archacki S, Wang Q. Expression profiling of cardiovascular disease. Human genomics 2004;1:355.

259.   Satterthwaite G, Francis SE, Suvarna K, Blakemore S, Ward C, Wallace D, Braddock M, Crossman D. Differential gene expression in coronary arteries from patients presenting with ischemic heart disease: further evidence for the inflammatory basis of atherosclerosis. Am Heart J 2005;150:488-99.

260.   King JY, Ferrara R, Tabibiazar R, Spin JM, Chen MM, Kuchinsky A, Vailaya A, Kincaid R, Tsalenko A, Deng DX, Connolly A, Zhang P, Yang E, Watt C, Yakhini Z, Ben-Dor A, Adler A, Bruhn L, Tsao P, Quertermous T, Ashley EA. Pathway analysis of coronary atherosclerosis. Physiol Genomics 2005;23:103-18.

261.   Tabibiazar R, Wagner RA, Ashley EA, King JY, Ferrara R, Spin JM, Sanan DA, Narasimhan B, Tibshirani R, Tsao PS. Signature patterns of gene expression in mouse atherosclerosis and their correlation to human coronary disease. Physiol Genomics 2005;22:213-26.

262.   Papaspyridonos M, Smith A, Burnand KG, Taylor P, Padayachee S, Suckling KE, James CH, Greaves DR, Patel L. Novel candidate genes in unstable areas of human atherosclerotic plaques. Arterioscler Thromb Vasc Biol 2006;26:1837-44.

263.   Sluimer JC, Kisters N, Cleutjens KB, Volger OL, Horrevoets AJ, van den Akker LH, Bijnens AP, Daemen MJ. Dead or alive: gene expression profiles of advanced atherosclerotic plaques from autopsy and surgery. Physiol Genomics 2007;30:335-41.

264.   Hägg DA, Jernås M, Wiklund O, Thelle DS, Fagerberg B, Eriksson P, Hamsten A, Olsson B, Carlsson B, Carlsson L. Expression profiling of macrophages from subjects with atherosclerosis to identify novel susceptibility genes. Int J Mol Med 2008;21:697-704.

265.   Puig O, Yuan J, Stepaniants S, Zieba R, Zycband E, Morris M, Coulter S, Yu X, Menke J, Woods J, Chen F, Ramey DR, He X, O'Neill EA, Hailman E, Johns DG, Hubbard BK, Yee Lum P, Wright SD, Desouza MM, Plump A, Reiser V. A gene expression signature that classifies human atherosclerotic plaque by relative inflammation status. Circ Cardiovasc Genet 2011;4:595-604.

266.   Razuvaev A, Ekstrand J, Folkersen L, Agardh H, Markus D, Swedenborg J, Hansson G, Gabrielsen A, Paulsson-Berne G, Roy J. Correlations between clinical variables and gene-expression profiles in carotid plaque instability. Eur J Vasc Endovasc Surg 2011;42:722-30.

267.   Saksi J, Ijäs P, Nuotio K, Sonninen R, Soinne L, Salonen O, Saimanen E, Tuimala J, Lehtonen-Smeds EM, Kaste M. Gene expression differences between stroke-associated and asymptomatic carotid plaques. J Mol Med 2011;89:1015-26.

268.   Levula M, Oksala N, Airla N, Zeitlin R, Salenius JP, Jarvinen O, Venermo M, Partio T, Saarinen J, Somppi T, Suominen V, Virkkunen J, Hautalahti J, Laaksonen R, Kahonen M, Mennander A, Kytomaki L, Soini JT, Parkkinen J, Pelto-Huikko M, Lehtimaki T. Genes involved in systemic and arterial bed dependent atherosclerosis--Tampere Vascular study. PLoS One 2012;7:e33787.

269.   Wang J, Wei B, Cao S, Xu F, Chen W, Lin H, Du C, Sun Z. Identification by microarray technology of key genes involved in the progression of carotid atherosclerotic plaque. Genes Genet Syst 2014;89:253-8.

270.   Perisic L, Aldi S, Sun Y, Folkersen L, Razuvaev A, Roy J, Lengquist M, Akesson S, Wheelock CE, Maegdefessel L, Gabrielsen A, Odeberg J, Hansson GK, Paulsson-Berne G, Hedin U. Gene expression signatures, pathways and networks in carotid atherosclerosis. J Intern Med 2016;279:293-308.

271.   Aavik E, Lumivuori H, Leppanen O, Wirth T, Hakkinen SK, Brasen JH, Beschorner U, Zeller T, Braspenning M, van Criekinge W, Makinen K, Yla-Herttuala S. Global DNA methylation analysis of human atherosclerotic plaques reveals extensive genomic hypomethylation and reactivation at imprinted locus 14q32 involving induction of a miRNA cluster. Eur Heart J 2015;36:993-1000.

272.   Nai W, Threapleton D, Lu J, Zhang K, Wu H, Fu Y, Wang Y, Ou Z, Shan L, Ding Y, Yu Y, Dai M. Identification of novel genes and pathways in carotid atheroma using integrated bioinformatic methods. Sci Rep 2016;6:18764.

273.   Sulkava M, Raitoharju E, Levula M, Seppala I, Lyytikainen LP, Mennander A, Jarvinen O, Zeitlin R, Salenius JP, Illig T, Klopp N, Mononen N, Laaksonen R, Kahonen M, Oksala N,

Lehtimaki T. Differentially expressed genes and canonical pathway expression in human atherosclerotic plaques - Tampere Vascular Study. Sci Rep 2017;7:41483.

274. Kashyap S, Kumar S, Agarwal V, Misra DP, Phadke SR, Kapoor A. Gene expression profiling of coronary artery disease and its relation with different severities. Journal of Genetics:1-15.

275. Steenman M, Espitia O, Maurel B, Guyomarch B, Heymann MF, Pistorius MA, Ory B, Heymann D, Houlgatte R, Goueffic Y, Quillard T. Identification of genomic differences among peripheral arterial beds in atherosclerotic and healthy arteries. Sci Rep 2018;8:3940.

276. Mosser DM, Edwards JP. Exploring the full spectrum of macrophage activation. Nature reviews immunology 2008;8:958.

277. Stöger JL, Gijbels MJ, van der Velden S, Manca M, van der Loos CM, Biessen EA, Daemen MJ, Lutgens E, de Winther MP. Distribution of macrophage polarization markers in human atherosclerosis. Atherosclerosis 2012;225:461-8.

278. Wynn TA, Vannella KM. Macrophages in tissue repair, regeneration, and fibrosis. Immunity 2016;44:450-62.

279. Allahverdian S, Chaabane C, Boukais K, Francis GA, Bochaton-Piallat M-L. Smooth muscle cell fate and plasticity in atherosclerosis. Cardiovasc Res 2018;114:540-50.

280. Souilhol C, Harmsen MC, Evans PC, Krenning G. Endothelial–mesenchymal transition in atherosclerosis. Cardiovasc Res 2018;114:565-77.

281. Chang MY, Chan CK, Braun KR, Green PS, O'Brien KD, Chait A, Day AJ, Wight TN. Monocyte to macrophage differentiation: Synthesis and secretion of a complex extracellular matrix. J Biol Chem 2012:jbc. M111. 324988.

282. Chang MY, Tanino Y, Vidova V, Kinsella MG, Chan CK, Johnson PY, Wight TN, Frevert CW. A rapid increase in macrophage-derived versican and hyaluronan in infectious lung disease. Matrix Biol 2014;34:1-12.

283. Martinez P, Denys A, Delos M, Sikora A-S, Carpentier M, Julien S, Pestel J, Allain F. Macrophage polarization alters the expression and sulfation pattern of glycosaminoglycans. Glycobiology 2014;25:502-13.

284. Katsuda S, Kaji T. Atherosclerosis and extracellular matrix. Journal of atherosclerosis and thrombosis 2003;10:267-74.

285. McCullagh K, Duance V, Bishop KA. The distribution of collagen types I, III and V (AB) in normal and atherosclerotic human aorta. The Journal of pathology 1980;130:45-55.

286. Theocharis AD, Skandalis SS, Gialeli C, Karamanos NK. Extracellular matrix structure. Advanced drug delivery reviews 2016;97:4-27.

287. Kalamajski S, Oldberg Å. The role of small leucine-rich proteoglycans in collagen fibrillogenesis. Matrix Biol 2010;29:248-53.

288.   Burleigh MC, Brigfs AD, Lendon CL, Davies MJ, Born GV, Richardson PD. Collagen types I and III, collagen content, GAGs and mechanical strength of human atherosclerotic plaque caps: span-wise variations. Atherosclerosis 1992;96:71-81.

289.   Adiguzel E, Ahmad PJ, Franco C, Bendeck MP. Collagens in the progression and complications of atherosclerosis. Vasc Med 2009;14:73-89.

290.   Rekhter MD. Collagen synthesis in atherosclerosis: too much and not enough. Cardiovasc Res 1999;41:376-84.

291.   Blaha MJ, Mortensen MB, Kianoush S, Tota-Maharaj R, Cainzos-Achirica M. Coronary artery calcium scoring: is it time for a change in methodology? JACC Cardiovasc Imaging 2017;10:923-37.

292.   Mori H, Torii S, Kutyna M, Sakamoto A, Finn AV, Virmani R. Coronary Artery Calcification and its Progression: What Does it Really Mean? JACC Cardiovasc Imaging 2018;11:127-42.

293.   Panh L, Lairez O, Ruidavets J-B, Galinier M, Carrié D, Ferrières J. Coronary artery calcification: From crystal to plaque rupture. Arch Cardiovasc Dis 2017.

294.   Walton K, Williamson N. Histological and immunofluorescent studies on the evolution of the human atheromatous plaque. J Atheroscler Res 1968;8:599-624.

295.   Hale A, Hall T, Curran R. Electron-microprobe analysis of calcium phosphorus and sulphur in human arteries. The Journal of pathology and bacteriology 1967;93:1-17.

296.   Hollander W. Unified concept on the role of acid mucopolysaccharides and connective tissue proteins in the accumulation of lipids, lipoproteins, and calcium in the atherosclerotic plaque. Exp Mol Pathol 1976;25:106-20.

297.   Daoud A, Frank A, Jarmolych J, Franco W, Fritz K. Ultrastructural and elemental analysis of calcification of advanced swine aortic atherosclerosis. Exp Mol Pathol 1985;43:337-47.

298.   Duer MJ, Friščić T, Proudfoot D, Reid DG, Schoppet M, Shanahan CM, Skepper JN, Wise ER. Mineral surface in calcified plaque is like that of bone: further evidence for regulated mineralization. Arterioscler Thromb Vasc Biol 2008;28:2030-4.

299.   Wise ER, Maltsev S, Davies ME, Duer MJ, Jaeger C, Loveridge N, Murray RC, Reid DG. The organic− mineral interface in bone is predominantly polysaccharide. Chem Mater 2007;19:5055-7.

300.   Reid DG, Duer MJ, Murray RC, Wise ER. The Organic− Mineral Interface in Teeth Is Like That in Bone and Dominated by Polysaccharides: Universal Mediators of Normal Calcium Phosphate Biomineralization in Vertebrates? Chem Mater 2008;20:3549-50.

301.   Duer MJ, Friščić T, Murray RC, Reid DG, Wise ER. The mineral phase of calcified cartilage: its molecular structure and interface with the organic matrix. Biophys J 2009;96:3372-8.

302.   Reid DG, Jackson GJ, Duer MJ, Rodgers AL. Apatite in kidney stones is a molecular composite with glycosaminoglycans and proteins: evidence from nuclear magnetic resonance spectroscopy, and relevance to Randall's plaque, pathogenesis and prophylaxis. The Journal of urology 2011;185:725-30.

303.   New SE, Aikawa E. Role of extracellular vesicles in de novo mineralization: an additional novel mechanism of cardiovascular calcification. Arterioscler Thromb Vasc Biol 2013;33:1753-8.

304.   Kolset SO, Pejler G. Serglycin: a structural and functional chameleon with wide impact on immune cells. J Immunol 2011;187:4927-33.

305.   Kim JS, Werth VP. Identification of specific chondroitin sulfate species in cutaneous autoimmune disease. J Histochem Cytochem 2011;59:780-90.

306.   Korpetinou A, Skandalis SS, Labropoulou VT, Smirlaki G, Noulas A, Karamanos NK, Theocharis AD. Serglycin: at the crossroad of inflammation and malignancy. Front Oncol 2014;3:327.

307.   Swart M, Troeberg L. Effect of Polarization and Chronic Inflammation on Macrophage Expression of Heparan Sulfate Proteoglycans and Biosynthesis Enzymes. J Histochem Cytochem 2019;67:9-27.

308.   Jin H, Zhou S. The Functions of Heparanase in Human Diseases. Mini Rev Med Chem 2017;17:541-8.

309.   Muhammad RS, Abu-Saleh N, Kinaneh S, Agbaria M, Sabo E, Grajeda-Iglesias C, Volkova N, Hamoud S. Heparanase inhibition attenuates atherosclerosis progression and liver steatosis in E0 mice. Atherosclerosis 2018;276:155-62.

310.   Dhamale OP, Lawrence R, Wiegmann EM, Shah BA, Al-Mafraji K, Lamanna WC, Lübke T, Dierks T, Boons GJ, Esko JD. Arylsulfatase K is the Lysosomal 2-Sulfoglucuronate Sulfatase. ACS Chem Biol 2017;12:367-73.

311.   Holmes R. Vertebrate Arylsulfatase K (ARSK): Comparative and Evolutionary Studies of the Lysosomal 2-Sulfoglucuronate Sulfatase. Journal of Data Mining in Genomics & Proteomics 2018;8:1-6.

312.   Lorenzo P, Aspberg A, Onnerfjord P, Bayliss MT, Neame PJ, Heinegard D. Identification and characterization of asporin. a novel member of the leucine-rich repeat protein family closely related to decorin and biglycan. J Biol Chem 2001;276:12201-11.

313.   Lee KSY. A genomic approach to atherosclerotic plaque vulnerability: Newcastle University; 2012.

314.   Langley SR, Willeit K, Didangelos A, Matic LP, Skroblin P, Barallobre-Barreiro J, Lengquist M, Rungger G, Kapustin A, Kedenko L, Molenaar C, Lu R, Barwari T, Suna G, Yin X, Iglseder B, Paulweber B, Willeit P, Shalhoub J, Pasterkamp G, Davies AH, Monaco C, Hedin U, Shanahan CM, Willeit J, Kiechl S, Mayr M. Extracellular matrix proteomics identifies molecular signature of symptomatic carotid plaques. J Clin Invest 2017;127:1546-60.

315.	Karlof E, Seime T, Dias N, Lengquist M, Witasp A, Almqvist H, Kronqvist M, Gadin JR, Odeberg J, Maegdefessel L, Stenvinkel P, Matic LP, Hedin U. Correlation of computed tomography with carotid plaque transcriptomes associates calcification with lesion-stabilization. Atherosclerosis 2019.

316.	Kalamajski S, Aspberg A, Lindblom K, Heinegard D, Oldberg A. Asporin competes with decorin for collagen binding, binds calcium and promotes osteoblast collagen mineralization. Biochem J 2009;423:53-9.

317.	Lee EH, Park HJ, Jeong JH, Kim YJ, Cha DW, Kwon DK, Lee SH, Cho JY. The role of asporin in mineralization of human dental pulp stem cells. J Cell Physiol 2011;226:1676-82.

318.	Yamada S, Tomoeda M, Ozawa Y, Yoneda S, Terashima Y, Ikezawa K, Ikegawa S, Saito M, Toyosawa S, Murakami S. PLAP-1/asporin, a novel negative regulator of periodontal ligament mineralization. J Biol Chem 2007;282:23070-80.

319.	Lyck Hansen M, Beck HC, Irmukhamedov A, Jensen PS, Olsen MH, Rasmussen LM. Proteome analysis of human arterial tissue discloses associations between the vascular content of small leucine-rich repeat proteoglycans and pulse wave velocity. Arterioscler Thromb Vasc Biol 2015;35:1896-903.

320.	Tillgren V, Ho JC, Önnerfjord P, Kalamajski S. The novel small leucine-rich protein chondroadherin-like (CHADL) is expressed in cartilage and modulates chondrocyte differentiation. J Biol Chem 2015;290:918-25.

321.	Bakker H. Carbohydrate Sulfotransferase 10 (CHST10). Handbook of Glycosyltransferases and Related Genes: Springer; 2014:1035-45.

322.	Zhao X, Graves C, Ames SJ, Fisher DE, Spanjaard RA. Mechanism of regulation and suppression of melanoma invasiveness by novel retinoic acid receptor-γ target gene carbohydrate sulfotransferase 10. Cancer Res 2009;69:5218-25.

323.	Kitagawa H, Nadanaka S. Chondroitin Polymerizing Factor, Chondroitin Polymerizing Factor 2, Chondroitin Sulfate Synthase 1,3 (CHPF, CHPF2, CHSY1, CHSY3). In: Taniguchi N, Honke K, Fukuda M, Narimatsu H, Yamaguchi Y, Angata T, eds. Handbook of Glycosyltransferases and Related Genes. Tokyo: Springer Japan; 2014:947-63.

324.	Maccarana M, Malmström A. Dermatan Sulfate Epimerases (DSE, DSEL). In: Taniguchi N, Honke K, Fukuda M, Narimatsu H, Yamaguchi Y, Angata T, eds. Handbook of Glycosyltransferases and Related Genes. Tokyo: Springer Japan; 2014:935-45.

325.	Nadanaka S, Zhou S, Kagiyama S, Shoji N, Sugahara K, Sugihara K, Asano M, Kitagawa H. EXTL2, a member of the EXT family of tumor suppressors, controls glycosaminoglycan biosynthesis in a xylose kinase-dependent manner. J Biol Chem 2013;288:9321-33.

326.	Purnomo E, Emoto N, Nugrahaningsih DA, Nakayama K, Yagi K, Heiden S, Nadanaka S, Kitagawa H, Hirata K. Glycosaminoglycan overproduction in the aorta increases aortic calcification in murine chronic kidney disease. J Am Heart Assoc 2013;2:e000405.

327.   Habuchi O. Carbohydrate (Chondroitin 4) Sulfotransferase 11-13 (CHST11-13). In: Taniguchi N, Honke K, Fukuda M, Narimatsu H, Yamaguchi Y, Angata T, eds. Handbook of Glycosyltransferases and Related Genes. Tokyo: Springer Japan; 2014:1025-33.

328.   Han J, Li D, Qu C, Wang D, Wang L, Guo X, Lammi MJ. Altered expression of chondroitin sulfate structure modifying sulfotransferases in the articular cartilage from adult osteoarthritis and Kashin-Beck disease. Osteoarthritis Cartilage 2017;25:1372-5.

329.   Willhauck-Fleckenstein M, Moehler TM, Merling A, Pusunc S, Goldschmidt H, Schwartz-Albiez R. Transcriptional regulation of the vascular endothelial glycome by angiogenic and inflammatory signalling. Angiogenesis 2010;13:25-42.

330.   Kiviranta J, Tammi M, Jurvelin J, Säämänen A-M, Helminen H. Fixation, decalcification, and tissue processing effects on articular cartilage proteoglycans. Histochemistry 1984;80:569-73.

331.   Ippolito E, Velle SL, Pedrini V. The effect of various decalcifying agents on cartilage proteoglycans. Stain Technol 1981;56:367-72.

332.   Rosen AD. Notes on technic: End-point determination in edta decalcification using ammonium oxalate. Stain Technol 1981;56:48-9.

333.   Quintarelli G. The chemical and histochemical properties of Alcian Blue. II. Dye binding of tissue polyanions. Histochemie 1964;4:86-98.

334.   Scott JE. Histochemistry of Alcian blue. Histochemie 1972;32:191-212.

335.   Spicer S, Warren L. The histochemistry of sialic acid containing mucoproteins. J Histochem Cytochem 1960;8:135-7.

336.   Murata K, Kirk J. Sialic acid content of human arterial and venous tissue. J Atheroscler Res 1962;2:452-8.

337.   Scott JE, Dorling J. Differential staining of acid glycosaminoglycans (mucopolysaccharides) by Alcian blue in salt solutions. Histochemie 1965;5:221-33.

338.   Beghein E, Gettemans J. Nanobody Technology: A Versatile Toolkit for Microscopic Imaging, Protein–Protein Interaction Analysis, and Protein Function Exploration. Front Immunol 2017;8.

339.   Howard DP, van Lammeren GW, Rothwell PM, Redgrave JN, Moll FL, de Vries JP, de Kleijn DP, den Ruijter HM, de Borst GJ, Pasterkamp G. Symptomatic carotid atherosclerotic disease: correlations between plaque composition and ipsilateral stroke risk. Stroke 2015;46:182-9.

340.   Carter-Monroe N, Yazdani SK, Ladich E, Kolodgie FD, Virmani R. Introduction to the Pathology of Carotid Atherosclerosis: Histologic Classification and Imaging Correlation. In: Suri JS, Kathuria C, Molinari F, eds. Atherosclerosis Disease Management. New York, NY: Springer New York; 2011:3-35.

341.   Kolodgie FD, Yahagi K, Mori H, Romero ME, Trout HHR, Finn AV, Virmani R. High-risk carotid plaque: lessons learned from histopathology. Semin Vasc Surg 2017;30:31-43.

342.   Redgrave JN, Lovett JK, Gallagher PJ, Rothwell PM. Histological assessment of 526 symptomatic carotid plaques in relation to the nature and timing of ischemic symptoms: the Oxford plaque study. Circulation 2006;113:2320-8.

343.   Verhoeven BA, Velema E, Schoneveld AH, de Vries JP, de Bruin P, Seldenrijk CA, de Kleijn DP, Busser E, van der Graaf Y, Moll F, Pasterkamp G. Athero-express: differential atherosclerotic plaque expression of mRNA and protein in relation to cardiovascular events and patient characteristics. Rationale and design. Eur J Epidemiol 2004;19:1127-33.

344.   Otsuka F, Yahagi K, Sakakura K, Virmani R. Why is the mammary artery so special and what protects it from atherosclerosis? Ann Cardiothorac Surg 2013;2:519-26.

345.   Basatemur GL, Jørgensen HF, Clarke MCH, Bennett MR, Mallat Z. Vascular smooth muscle cells in atherosclerosis. Nature Reviews Cardiology 2019.

346.   Durham AL, Speer MY, Scatena M, Giachelli CM, Shanahan CM. Role of smooth muscle cells in vascular calcification: implications in atherosclerosis and arterial stiffness. Cardiovasc Res 2018;114:590-600.

Eidesstattliche Versicherung und Anteilserklärung

„Ich, Vasileios Karampelas, versichere an Eides statt durch meine eigenhändige Unterschrift, dass ich die vorgelegte Dissertation mit dem Thema: „Identification of stability- and instability-associated proteoglycan/ glycosaminoglycan patterns in human atherosclerotic lesions"/ „Identifizierung von stabilitäts- und instabilitätsassoziierten Proteoglykan-/ Glykosaminoglykanmuster in humanen atherosklerotischen Läsionen" selbstständig und ohne nicht offengelegte Hilfe Dritter verfasst und keine anderen als die angegebenen Quellen und Hilfsmittel genutzt habe.

Alle Stellen, die wörtlich oder dem Sinne nach auf Publikationen oder Vorträgen anderer Autoren/innen beruhen, sind als solche in korrekter Zitierung kenntlich gemacht. Die Abschnitte zu Methodik (insbesondere praktische Arbeiten, Laborbestimmungen, statistische Aufarbeitung) und Resultaten (insbesondere Abbildungen, Graphiken und Tabellen) werden von mir verantwortet.

Ich versichere ferner, dass ich die in Zusammenarbeit mit anderen Personen generierten Daten, Datenauswertungen und Schlussfolgerungen korrekt gekennzeichnet und meinen eigenen Beitrag sowie die Beiträge anderer Personen korrekt kenntlich gemacht habe (siehe Anteilserklärung). Texte oder Textteile, die gemeinsam mit anderen erstellt oder verwendet wurden, habe ich korrekt kenntlich gemacht.

Meine Anteile an etwaigen Publikationen zu dieser Dissertation entsprechen denen, die in der untenstehenden gemeinsamen Erklärung mit dem/der Erstbetreuer/in, angegeben sind. Für sämtliche im Rahmen der Dissertation entstandenen Publikationen wurden die Richtlinien des ICMJE (International Committee of Medical Journal Editors; www.icmje.og) zur Autorenschaft eingehalten. Ich erkläre ferner, dass ich mich zur Einhaltung der Satzung der Charité – Universitätsmedizin Berlin zur Sicherung Guter Wissenschaftlicher Praxis verpflichte.

Weiterhin versichere ich, dass ich diese Dissertation weder in gleicher noch in ähnlicher Form bereits an einer anderen Fakultät eingereicht habe.

Die Bedeutung dieser eidesstattlichen Versicherung und die strafrechtlichen Folgen einer unwahren eidesstattlichen Versicherung (§§156, 161 des Strafgesetzbuches) sind mir bekannt und bewusst."

Datum: Unterschrift:

Anteilserklärung an erfolgten Publikationen

Vasileios Karampelas had the following share in the following publications:

1. **V.Karampelas**, A. Ludwig, A. Stach, K. Biskup, A. S. Kasper S, S. Malinka, P. et al. Identification of instability-associated glycosaminoglycan patterns in human atherosclerotic lesions as potential diagnostic targets for the non-invasive detection of vulnerable plaques. Poster presented at: Rhythm for life. 83rd Annual Meeting of the German Cardiac Society; 2017 April 19-22; Mannheim.

Contribution: Presentation of preliminary results at the "Otto-Hess poster session 2"

2. Poller WC, Pieber M, Boehm-Sturm P, Ramberger E, **Karampelas V**, Moller K, et al. Very small superparamagnetic iron oxide nanoparticles: Long-term fate and metabolic processing in atherosclerotic mice. Nanomedicine. 2018.

Contribution: Preprocessing and paraffin-embedding of spleen and liver tissue from LDLR-/- mice that received VSOP (3h, 7 days, 28 days), generation of 6 µm-thick cross sections and use of conventional histology (Prussian blue sections that were counterstained with Nuclear Fast Red) in order to identify Prussian blue positive cells. Images were acquired via Axiocam MrC (Zeiss) (Figure 2, page 2579).

_____

Unterschrift, Datum und Stempel des/der erstbetreuenden Hochschullehrers/in

_____

Unterschrift des Doktoranden/der Doktorandin

Curriculum vitae

The CV is in the digital version of this thesis for reasons of personal data protection not included.

List of publications

1. **V.Karampelas**, A. Ludwig, A. Stach, K. Biskup, A. S. Kasper S, S. Malinka, P. Olschewski, I. Klempert, V. Blanchard, K. Stangl, V. Stangl, W. Poller. Identification of instability-associated glycosaminoglycan patterns in human atherosclerotic lesions as potential diagnostic targets for the non-invasive detection of vulnerable plaques. Poster presented at: Rhythm for life. 83rd Annual Meeting of the German Cardiac Society; 2017 April 19-22; Mannheim.

2. Poller WC, Pieber M, Boehm-Sturm P, Ramberger E, **Karampelas V**, Moller K, et al. Very small superparamagnetic iron oxide nanoparticles: Long-term fate and metabolic processing in atherosclerotic mice. Nanomedicine. 2018.

Acknowledgements